

Influence of dimensional accuracy and tooth flank surface texturing on worm wheel pitting formation

Mašović, Robert

Doctoral thesis / Disertacija

2024

Degree Grantor / Ustanova koja je dodijelila akademski / stručni stupanj: **University of Zagreb, Faculty of Mechanical Engineering and Naval Architecture / Sveučilište u Zagrebu, Fakultet strojarstva i brodogradnje**

Permanent link / Trajna poveznica: <https://urn.nsk.hr/urn:nbn:hr:235:060058>

Rights / Prava: [In copyright](#) / [Zaštićeno autorskim pravom.](#)

Download date / Datum preuzimanja: **2025-03-29**

Repository / Repozitorij:

[Repository of Faculty of Mechanical Engineering and Naval Architecture University of Zagreb](#)





University of Zagreb
Faculty of Mechanical Engineering and Naval Architecture

Robert Mašović

**INFLUENCE OF DIMENSIONAL
ACCURACY AND TOOTH FLANK
SURFACE TEXTURING ON WORM
WHEEL PITTING FORMATION**

DOCTORAL THESIS

Zagreb, 2024.



University of Zagreb
Faculty of Mechanical Engineering and Naval Architecture

Robert Mašović

**INFLUENCE OF DIMENSIONAL
ACCURACY AND TOOTH FLANK
SURFACE TEXTURING ON WORM
WHEEL PITTING FORMATION**

DOCTORAL THESIS

Supervisor:
Prof. Dragan Žeželj, PhD

Zagreb, 2024.



Sveučilište u Zagrebu
Fakultet strojarstva i brodogradnje

Robert Mašović

**UTJECAJ DIMENZIJSKE TOČNOSTI
PUŽNOGA KOLA I TEKSTURE POVRŠINE
BOKA ZUBA NA RAZVOJ RUPičENJA**

DOKTORSKI RAD

Mentor:
prof. dr. sc. Dragan Žeželj

Zagreb, 2024.

Bibliography data

UDK: 621.8

Keywords: worm pair; pitting; deviations; 3D optical scanning; surface texturing; electropolishing; efficiency; finite element method

Scientific area: Technical Sciences

Institution: University of Zagreb, Faculty of Mechanical Engineering and Naval Architecture

Thesis supervisor: prof. Dragan Žeželj, PhD

Number of pages: 209

Number of figures: 140

Number of tables: 47

Number of references: 154

Date of examination: 7th June 2024

Dissertation Defense Committee:

Prof. Suzana Jakovljević, PhD – Chairman of the Dissertation Defense Committee

Assoc. Prof. Ivica Galić, PhD – member

Prof. Robert Basan, PhD – external member

Archive: University of Zagreb, Faculty of Mechanical Engineering and Naval Architecture

Acknowledgment

Prvenstveno bih se zahvalio mentoru prof. dr. sc. Draganu Žeželju na strpljenju, vodstvu, razumijevanju te pruženoj pomoći prilikom izrade ovog rada.

Zahvaljujem se prof. dr. sc. Suzani Jakovljević, izv. prof. dr. sc. Ivici Galiću i prof. dr. sc. Robertu Basanu na dobronamjnim komentarima i sugestijama kojima su doprinijeli kvaliteti ovog doktorskog rada.

Veliko hvala prijateljima i kolegama Ivanu i Danielu na svim korisnim savjetima prilikom izrade ovog rada. Također, za isto bih se zahvalio i svim ostalim kolegama sa Zavoda za konstruiranje.

Zahvalio bih se razvojno-edukacijskom centru Metalska jezgra Čakovec te poduzećima Neo Dens d.o.o. i DMB Product d.o.o. na stručnoj pomoći kojom su mi uvelike pomogli u provedenom istraživanju. Također, zahvalio bih se Zavodu za procesne tehnike Fakulteta šumarstva i drvne tehnologije, a posebice kolegi Juraju Jovanoviću na velikom trudu i vremenu koje je uloženo u mjerenje i obradu uzoraka.

Enormnu zahvalu dugujem svojoj majci za sva odricanja, žrtve i vjeru u mene bez kojih danas ne bih bio gdje jesam. Od srca hvala bratu na bezuvjetnoj potpori i razumijevanju.

U konačnici, zahvalu dugujem supruzi. Sve ostvareno ne bi bilo moguće bez tvojeg razumijevanja, podrške i motivacije. Ovo je i tvoj rad.

*U spomen na baku i djeda, njihovu veliku ljubav i predivno
djetinjstvo.*

Table of Contents

Bibliography data	II
Acknowledgment	III
Table of Contents	I
Abstract	V
Prošireni sažetak.....	VI
Abbreviations	X
List of Figures	XI
List of Tables.....	XVII
Nomenclature	XIX
1. INTRODUCTION.....	1
1.1 Motivation	2
1.2 Defining the research gap.....	4
1.3 Hypotheses	8
1.4 Methodology.....	9
1.5 Expected scientific contribution	12
1.6 Thesis layout.....	12
2. WORM PAIR PROPERTIES.....	15
2.1 General characteristics.....	16
2.2 Geometry and manufacturing of ZN worm pairs	18
2.3 Materials	22
2.3.1 Worm material	22
2.3.2 Worm wheel material.....	22
2.4 Lubrication	24
2.4.1 Contact conditions.....	25
2.4.2 Lubricant selection.....	27

3. PITTING AND WEAR IN WORM PAIRS	29
3.1 Pitting	31
3.1.1 Theoretical basis	31
3.1.2 Pitting resistance calculation.....	34
3.1.3 Relevant pitting resistance calculation studies in literature	39
3.2 Sliding Wear.....	42
3.2.1 Abrasive wear	42
3.2.2 Adhesive wear.....	45
3.2.3 Wear load capacity calculation	46
4. WORM PAIR DIMENSIONAL ACCURACY	51
4.1 Deviations.....	51
4.2 Three dimensional (3D) optical scanning	55
4.3 Worm pair scanning process	59
4.4 Processing of scanned data.....	61
5. SURFACE TEXTURING	66
5.1 Surface texturing methods.....	66
5.2 Surface texturing in gears.....	71
5.3 Selection of surface texturing method.....	72
6. TRIBOLOGICAL BEHAVIOR OF ELECTROPOLISHED STEEL-BRONZE PAIR IN MIXED AND BOUNDARY LUBRICATION REGIMES	74
6.1 Electropolishing process	74
6.2 Electropolishing setup	76
6.3 Experimental setup	77
6.4 Surface characteristics of electropolished steel.....	78
6.4.1 Surface profile and hardness	78
6.4.2 Chemical composition and pit area density	82
6.5 Contact characteristics and variable selection.....	84
6.6 Results and discussion.....	86

6.6.1 Friction and wear	86
6.6.2 State of surfaces after the tests	91
6.7 Summary	93
7. FINITE ELEMENT MODEL.....	95
7.1 Finite element method model.....	95
7.1.1 Contact definition	98
7.1.2 Simulation steps and boundary conditions	99
7.1.3 Element selection.....	99
7.2 Model verification.....	100
8. WORM PAIR EXPERIMENTAL SETUP	103
8.1 Experimental setup.....	103
8.1.1 Gearbox and worm pair material combinations.....	103
8.1.2 Experimental stand	105
8.1.3 Digital imaging equipment and requirements.....	107
8.2 Testing procedure.....	109
8.2.1 Contact pattern adjustment and running-in procedure.....	110
8.2.2 Digital image acquisition and post-processing	112
9. RESULTS AND DISCUSSION.....	115
9.1 Influence of surface texturing.....	115
9.1.1 Overall efficiency and running-in effect.....	115
9.1.2 Surface topography	119
9.2 Pitting	123
9.2.1 Worm pair 1	128
9.2.2 Worm pair 2 (EP).....	143
9.2.3 Worm pair 3 (EP).....	153
9.2.4 Worm pair 4 (AlSn6 worm wheel)	160
9.3 Finite element analysis results.....	168

9.3.1 Initial load distribution and contact pattern	169
9.3.2 Contact pattern, stress, and load distribution at the end of the test.....	174
10. CONCLUSIONS	181
10.1 Research limitations	185
10.2 Scientific contributions	186
10.3 Outlook and future work	186
References	188
Curriculum Vitae.....	198
Appendix	201

Abstract

Pitting of worm wheel flanks is one of the main damage mechanisms that occur in worm pairs. Due to their geometry, worm pairs are sensitive to manufacturing errors, and their influence on damage mechanisms, namely pitting, has not yet been thoroughly studied. This doctoral thesis investigates the influence of worm pair dimensional accuracy on pitting formation and development. The goal was to correlate worm pair deviations with the occurrence of pitting and to predict worm wheel flanks susceptible to pitting based on measured deviations. Also, three-dimensional optical scans were employed in developing a finite element method model based on real worm pair geometry. The model was used to obtain contact patterns and load and stress distribution in worm pairs. If a specific worm wheel deviation distribution is present, it will govern the pitting formation and development. However, if worm threads have distinct differences, the unfavorable deviation present in one of the worm threads will induce the majority of pitting on worm wheel flanks. If there is no specific distribution of deviations, the locations of the most damaged and least damaged flanks can be explained by radial and axial runout. Besides deviations, established contact patterns have a large influence on pitting formation.

In worm pairs, a high degree of sliding paired with unfavorable oil-entraining geometry leads to poor lubrication conditions and lower overall efficiency compared to other gear types. In order to improve lubrication conditions in worm pairs, surface texturing was conducted through electropolishing at higher current densities which produced surface texture in the form of dimples and pits on a steel surface. Electropolishing, as a surface texturing method, was verified through model testing of an electropolished steel-bronze pair. Results showed a reduced coefficient of friction and faster running-in. Electropolishing was then applied to steel worms to investigate the effects of surface texturing in worm pairs. Obtained results indicated improved lubrication conditions as both worm pairs with electropolished worms showed higher overall efficiencies and higher initial bronze wear, demonstrating a faster running-in process. Surface texture with larger and shallower pits displayed better results in terms of efficiency and pitting. Overall results indicate that surface texturing improves lubrication conditions in worm pairs with possible promising applications in other machine elements characterized by highly loaded non-conformal contacts.

Keywords: *worm pair; pitting; deviations; 3D optical scanning; surface texturing; electropolishing; efficiency; finite element method*

Prošireni sažetak

Pužni parovi su strojni elementi koji se koriste u prijenosu snage i gibanja. Pužni par sastoji se od puža i pužnog kola. Puž je najčešće pogonski, dok je kolo gonjeni element pužnog para. Pužni parovi karakteristični su po visokom prijenosnom omjeru u jednom stupnju prijenosa te kompaktnoj izvedbi. Kao i ostali strojni elementi, podložni su mehanizmima oštećenja među kojima su najizraženiji klizno trošenje i rupičenje (*eng. pitting*). Rupičenje je posljedica umora površine uslijed velikog broja ciklusa izmjena opterećenja koji su popraćeni visokim kontaktnim pritiscima. Manifestira se u odvajanju i ispadanju čestica materijala s površine boka pužnog kola što dovodi do pojave rupica. Rupičenje je tip oštećenja koje je teško izbjeći čak i u pravilnom radu pužnog para. Pužno kolo može normalno raditi čak do 60% površine boka zuba oštećene rupičenjem. Općenito, mehanizam i razvoj rupičenja dobro je poznat te detaljno istražen u području zupčanika s ravnim zubima, no u području pužnih parova nedostaje saznanja o različitim materijalima, radnim uvjetima te utjecaju geometrije na sam nastanak i razvoj rupičenja. Kako je dosad u istraživanjima pokazano da je rupičenje izrazito neujednačeno te je teško uspostaviti određene zakonitosti, prvi cilj ovog istraživanja je pobliže povezati utjecaj grešaka izrade, odnosno dimenzijske točnosti pužnog para, s pojavom i razvojem rupičenja. Greške u izradi mogu nepovoljno utjecati na raspodjelu opterećenja i naprezanja te na sliku nošenja što u konačnici može utjecati na razmjer oštećenja bokova pužnog kola rupičenjem.

Drugi cilj ovog istraživanja temelji se na nepovoljnim uvjetima podmazivanja, a koji predstavljaju jedan od glavnih nedostataka pužnih parova. Nepovoljna geometrija pužnog para popraćena s pretežito kliznim gibanjem u zahvatu rezultira lošijim uvjetima podmazivanja. Nedostatno podmazivanje uzorkuje povećane gubitke u sustavu, ubrzano trošenje, a u ekstremnim slučajevima rezultira naglim zatajenjem pužnog para uslijed zaribavanja. Također, uvjeti podmazivanja jedan su od glavnih razloga manje iskoristivosti pužnih parova naspram ostalih tipova zupčanika. Rješenje u pogledu povećanja iskoristivosti i općenito boljeg podmazivanja dosad se pokušalo riješiti upotrebom novih materijala pužnih parova ili varijacijama u samoj geometriji. U ovom radu cilj je promjenom teksture površine poboljšati uvjete podmazivanja te time povećati iskoristivost pužnih parova. Umjetno stvorene teksture sastoje se od jamica koje mogu biti različitih oblika i dimenzija te raspoređene u specifičnim rasporedima. Uloge takvih tekstura prvenstveno se očituju u funkcijama kao što su: sekundarno podmazivanje, povećanje debljine uljnog filma, poboljšano odvođenje topline iz mjesta kontakta, zadržavanje čestica nastalih trošenjem i smanjenje trenja. Teksture na površinama

kreiraju se procesima kao što su lasersko graviranje, jetkanje, sačmarenje ili mehaničko utiskivanje. Iako je primjena različitih površinskih tekstura čest predmet triboloških istraživanja, sama primjena i istraživanje tekstura na zupčanicima je vrlo rijetka i ograničena. Razlog tomu su prvenstveno kompleksna geometrija i priroda dodira zupčanika u zahvatu popraćena visokim dodirnim pritiscima. Izuzev par istraživanja provedenih na čelnicima s ravnim zubima, primjena površinskih tekstura na pužnim parovima dosad je neistražena.

Kako bi se ispunila oba opisana cilja, istraživanje je započeto paralelno u oba smjera. Stvarna geometrija proizvedenih pužnih parova dobivena je pomoću trodimenzionalnog (3D) optičkog skeniranja. Dobiveni podaci sadrže informacije o potpunoj geometriji puža i pužnog kola iz kojih su se naknadnom programskom obradom odredila odstupanja stvarne geometrije od idealne, odnosno definirale devijacije izrađenih pužnih parova. Također, samo kućište pužnog prijenosnika je 3D optički skenirano kako bi se utvrdile eventualne greške odstupanja osi pužnog para. Paralelno je provedena evaluacija postojećih metoda za kreiranje površinskih tekstura. Odabir najprikladnije metode proveden je uzimajući u obzir geometriju pužnog para, jednostavnost i brzinu primjene, točnost proizvedene geometrije te u konačnici cijene samog postupka. Kao najprikladnija metoda odabrano je elektropoliranje pri povišenim gustoćama struje. Elektropoliranjem pri povišenim gustoćama struje dolazi do nastanka jamica i kanalića na površini obrađivanog uzorka stvarajući tako svojevrsnu površinsku teksturu. Za materijal primjene odabran je cementirani čelik, odnosno materijal puža. Kako u radu pužnog para dolazi do izrazitog trošenja brončanog kola zbog manje tvrdoće i lošijih mehaničkih svojstava (posebice u procesu uhodavanja), logično je bilo površinsku teksturu proizvesti na tvrđoj komponenti, odnosno čeličnom pužu. Iz istog razloga, tekstura proizvedena na čeličnom pužu trajat će znatno duže nego ista proizvedena na brončanom kolu. Verifikacija odabrane metode provedena je modelskim ispitivanjem na paru materijala čelik (16MnCr5)-bronca (CuSn12) koji je ujedno i najučestaliji par materijala pužnih parova. Rezultati ispitivanja ukazali su na smanjeni faktor trenja i ubrzano uhodavanje para elektropolirani čelik-bronca u usporedbi s konvencionalnim parom brušeni čelik-bronca. Kako je elektropoliranje polučilo pozitivne rezultate modelskog ispitivanja, odlučeno je da će se elektropoliranjem proizvesti površinska tekstura na pužu kako bi se utvrdio utjecaj promjene teksture površine na ponašanje pužnog para u radnim uvjetima.

Ispitivanje pužnih parova provedeno je u sklopu Laboratorija za elemente strojeva Fakulteta brodogradnje i strojarstva u Zagrebu. Ukupno je provedeno ispitivanje na šest pužnih parova (četiri pužna kola od materijala CuSn12, jedno pužno kolo od materijala AlSn6 i jedno pužno

kolo od materijala CuAl10Fe5Ni5) od kojih su četiri obuhvaćena u analizu rupičenja (tri pužna kola od materijala CuSn12 i jedno pužno kolo od materijala AlSn6). Tijekom ispitivanja, vrijednosti opterećenja, brzine vrtnje te temperature ulja bile su konstantne te kontinuirano praćene. Dodatno, periodički se ispitivanje zaustavljalo kako bi se provelo fotografsko dokumentiranje bokova pužnog kola u svrhu određivanja površine boka zahvaćene rupičenjem. Za cijelo vrijeme ispitivanja posebna pozornost bila je usmjerena na praćenje iskoristivosti pužnog para.

Rezultati praćenja iskoristivosti korišteni su kao generalni pokazatelj poboljšanja uvjeta podmazivanja u pužnim parovima s elektropoliranim pužem. Svi pužni parovi obuhvaćeni ovim dijelom ispitivanja su bili od materijala čelik (16MnCr5)-bronca (CuSn12). Oba pužna para s elektropoliranim pužem imala su veću iskoristivost od konvencionalnog pužnog para. Spomenuto je posebice bilo vidljivo kod elektropoliranog puža s većim, ali plićim jamicama. Također, oba pužna para imala su veće trošenje brončanog kola, što je opet posebice bilo prisutno kod ranije spomenutog puža. Povećano trošenje može se pripisati periodu uhodavanja i kao takvo ne smatra se lošom pojavom. Dapače, pužni par s najvećim trošenjem imao je najvišu iskoristivost te najmanje rupičenje bokova. Povrh povećane iskoristivosti, jedan od pužnih parova s elektropoliranim pužem radio je s punom slikom nošenja koja se u pravilu izbjegava zbog onemogućenog ulaska ulja u područje zahvata što drastično povećava opasnost od pojave zaribavanja. Za potrebe usporedbe i potvrde teorije, provedeno je dodatno ispitivanje jednog konvencionalnog pužnog para s uspostavljenom punom slikom nošenja. Na navedenom pužnom paru došlo je do zaribavanja u dva navrata, prilikom čega je drugi put bio i katastrofalan te je rezultirao prijevremenim prekidom ispitivanja. Na temelju rezultata iskoristivosti i uspostave funkcionalne pune slike nošenja može se zaključiti da površinska tekstura proizvedena elektropoliranjem poboljšava uvjete podmazivanja pužnih parova.

Rupičenje je praćeno na ukupno četiri pužna para preko fotografija oštećenih bokova u relativno jednakim vremenskim intervalima. Zbog same geometrije istraživanih pužnih parova, svaki pojedini voj dvovojnog puža bio je konstantno u zahvatu s istim bokovima pužnog kola (parnim ili neparnim). Takva specifičnost pužnog para je donekle istaknula razlike u procesu rupičenja na pojedinim bokovima. Svaki od pužnih parova obrađen ja zasebno zbog specifičnosti koje su bile prisutne bilo u rasporedu grešaka, razlici ispitivanih materijala pužnog kola ili površinskoj teksturi puža (brušeni puž; elektropolirani puž). Rezultati rupičenja ukazuju na povezanost s greškama u izradi puža ili pužnog kola. Ukoliko postoji jasna razlika između dva voja puža, kao što je slučaj greške profila boka na jednom od puževa, tada će ta greška diktirati zakonitost

pojave rupičenja na bokovima pužnog kola. Ako ne postoje razlike u vojevima puža, a postoji specifična raspodjela greške koraka pužnog kola, razvoj rupičenja bit će uvjetovan upravo specifičnom raspodjelom spomenute greške. Općenito je za očekivati da greška koraka igra veliku ulogu u nastanku rupičenja jer direktno utječe na raspodjelu opterećenja među zubima u zahvatu. Ukoliko ne postoji zakonitost ili specifičnost u raspodjeli neke od grešaka, već su greške stohastički distribuirane, razlike među zubima s najvećim i najmanjim udjelom rupičenja mogu se povezati s raspodjelom radijalne i aksijalne točnosti vrtnje. Općenito se u literaturi rupičenje predviđa pomoću broja ciklusa opterećenja te se razmatra u obliku prosječnog rupičenja svih bokova pužnog kola. U ovom istraživanju predstavljeni su linearni modeli koji opisuju rupičenje pojedinog boka pužnog kola pomoću broja ciklusa opterećenja i izmjerenih grešaka pužnog kola.

Koristeći 3D optičke skenove pužnih parova uspostavljen je numerički model pomoću metode konačnih elemenata. Model je korišten za analizu slike nošenja i raspodjele opterećenja i naprezanja na bokovima pužnog kola. Predloženi model verificiran je s aktualnom normom te validiran na temelju slika nošenja ostvarenih u eksperimentalnim istraživanjima. Rezultati dobiveni modelom ukazuju na velike razlike naspram teoretskih pretpostavki te upućuju na kontinuiranu promjenu slike nošenja uslijed trošenja bokova pužnog kola. Za razliku od modela koji u pravilu koriste idealnu geometriju promatranih komponenti, cilj ovog modela bilo je prikazati stanje pužnih parova temeljeno na stvarnoj geometriji te tako omogućiti realniju simulaciju uvjeta rada.

Posljednje poglavlje sažima provedeno istraživanje, sadrži zaključke i ograničenja istraživanja te prijedloge mogućih smjerova budućih istraživanja. Također, izneseni su znanstveni doprinosi ovog doktorskog rada.

Ključne riječi: *pužni par; rupičenje; greške; 3D optičko skeniranje; površinska tekstura; elektropoliranje; iskoristivost; metoda konačnih elemenata*

Abbreviations

AGMA	American Gear Manufacturers Association
ASTM	American Society for Testing and Materials
CAD	Computer-aided design
CMM	Coordinate measuring machine
DIN	German: <i>Deutsches Institut für Normung</i>
EP	Electropolished
EP additives	Extreme pressure additives
ESD	Electropolished steel disc
FEM	Finite element method
GBS	Ground bronze specimen
GMI	Gear measuring instrument
GSD	Ground steel disc
ISO VG	International Standards Organization Viscosity Grade
ISO/TS	International Organization for Standardization/Technical specification
LST	Laser surface texturing
MBS	Milled bronze specimen
MV	Measuring volume
rpm	Revolutions Per Minute
VDI/VDE	German: Verein Deutscher Ingenieure

List of Figures

Figure 1. Schematic representation of the research plan	9
Figure 2. Worm pair	16
Figure 3. Worm pair configurations [47]	17
Figure 4. Worm wheel face width	17
Figure 5. ZN worm – tool geometry [52]	18
Figure 6. Basic dimensions of ZN worm pair [25].....	18
Figure 7. Split contact pattern due to hob undersize [52].....	19
Figure 8. Contact pressure distribution for a) fully conjugated pair, b) worm pair processed by a 5% oversized hob, c) hob angle error of 0.1° [22]	20
Figure 9. Types of contact patterns [5].....	20
Figure 10. Worm pair - technical drawings [25]	21
Figure 11. Comparison between AlSn6 vs. CuSn12: a) Comparison of coefficients of friction; b) Comparison of wear track surface [53].....	24
Figure 12. Stribeck curve and lubrication regimes.....	25
Figure 13. Detailed model of mixed lubrication regime	26
Figure 14. Contact analysis: a) film thickness, μm ; b) wheel tooth surface temperature, $^\circ\text{C}$ [12]	26
Figure 15. Output torque limitations for small center distances [3].....	30
Figure 16. A schematic representation of pitting and spalling, according to [66]	31
Figure 17. Stress distribution between contacting surfaces under rolling-sliding conditions [68]	32
Figure 18. Surface distress leading to spalling in CuSn12 worm wheel	33
Figure 19. Visual representation of a) Micropitting, b) Pitting.....	34
Figure 20. Mechanisms of abrasive wear [60]	43
Figure 21. Worm wheel abrasion due to irregularities in working conditions [25]	43
Figure 22. Schematic representation of the characteristic wear periods, according to [74]....	44
Figure 23. Process of adhesive wear [60].....	45
Figure 24. First signs of scuffing on the bronze worm wheel	46
Figure 25. Single pitch deviation (axial)	52
Figure 26. Single pitch deviation	53
Figure 27. Adjacent pitch difference and total cumulative pitch deviation, according to [76]53	

Figure 28. Total profile deviation.....	54
Figure 29. Representation of runout, according to [77]	54
Figure 30. Representation of single flank composite inspection.....	55
Figure 31. Gear measurement using CMM/GMI [80]	56
Figure 32. a) Schematic of fringe projection profilometry, according to [82], b) Two camera system, according to [79]	57
Figure 33. Scanning process: a) System calibration, b) Anti-reflective coating and reference point application, c) Worm wheel on the rotary table during the scanning process	60
Figure 34. 3D optical scans of a) worm, b) worm wheel assembly, c) housing.....	61
Figure 35. Worm wheel assembly alignment.....	62
Figure 36. Pitch deviation measurement on scanned data.....	62
Figure 37. Tooth flank profile used for evaluation	63
Figure 38. Tooth flank evaluation	64
Figure 39. Runout deviation measurement on scanned data	64
Figure 40. Axial runout	65
Figure 41. Dimple profile	67
Figure 42. Laser surface textures: a) dimples of 40 μm in diameter (polished after LST) [98], b) dimple obtained with laser wavelength of 532 nm (non-polished after LST, visible bulges and debris) [99]	68
Figure 43. Etched surfaces: a) photolithography [104], b) MECT [103], c) chemically etched spur gear teeth [44].....	69
Figure 44. Surface textures created by mechanical indentation: a) micro-dimple rolling operation [106], b) roller surface indented using a Rockwell indenter [34]	69
Figure 45. Shot peened surface: a) ground surface, b) shot peened surface, c) shot peened surface after polishing [108].....	70
Figure 46. Electropolished surfaces: a) carbon gear steel ground vs. electropolished surface [109], b) stainless steel surfaces electropolished with various current densities and time duration [110].....	70
Figure 47. Fundamentals of electropolishing: a) electropolishing mechanism, b) electropolishing curve [119].....	75
Figure 48. Electropolishing setup [18]	76
Figure 49. Block-on-disc experimental rig [18]	78
Figure 50. Kurtosis R_{ku} and skewness R_{sk} [18].....	79
Figure 51. Hardness profile of steel discs [18].....	81

Figure 52. Surface roughness of a) ground steel disc, b) electropolished steel disc [18]	81
Figure 53. EDS spectrum of a) ground steel disc, b) electropolished steel disc [18].....	82
Figure 54. The appearance of electropolished steel disc (ESD) vs. ground steel disc (GSD)	83
Figure 55. Sem image of a) ground steel surface, b) electropolished steel surface	84
Figure 56. Results of sliding test ($t = 180$ s): a) the ground bronze specimen in the mixed lubrication regime, b) the milled bronze specimen in the boundary lubrication regime, c) the milled bronze specimen in the boundary lubrication regime [18].....	88
Figure 57. Comparison of coefficients of friction [18]	88
Figure 58. Results of the sliding test ($t = 21\ 600$ s): a) the ground bronze specimen in the mixed lubrication regime, b) the milled bronze specimen in the boundary lubrication regime, c) the milled bronze specimen in the boundary lubrication regime [18].....	89
Figure 59. Comparison of bronze specimen wear [18]	90
Figure 60. Bronze specimen after the test: a) rectangular contact patch [18], b) SEM image of the surface	91
Figure 61. Electropolished steel surface after the test: a) visible pits on wear track, b) marked locations analyzed by EDS [18]	91
Figure 62. The surface profile of electropolished steel wear track [18].....	92
Figure 63. Stribeck curve for electropolished vs ground steel [18]	93
Figure 64. Surface model deviations	96
Figure 65. Worm wheel model creation [1]	96
Figure 66. Schematic representation of finite element model.....	97
Figure 67. Housing deviations.....	97
Figure 68. Pressure-overclosure relationship	98
Figure 69. Worm pair mesh.....	100
Figure 70. Bearing spacing according to ISO/TS 14521 [3].....	100
Figure 71. Worm deflection obtained by developed FEM model.....	101
Figure 72. Comparison of contact patterns	102
Figure 73. Gearbox CAD model [25].....	104
Figure 74. Experimental stand - scheme	106
Figure 75. Experimental stand.....	107
Figure 76. Camera and worm wheel positioning assemblies [25]	108
Figure 77. Photographing of worm wheel tooth flank	109
Figure 78. Initial “no load” contact pattern on worm wheel 3	111
Figure 79. Contact pattern development during running-in	112

Figure 80. Defining the image scale.....	112
Figure 81. Worm pair efficiency comparison	116
Figure 82. Visual comparison of worm wheel wear.....	117
Figure 83. Worm pair 6 – efficiency and scuffing	119
Figure 84. Worm wheel 6 - worn out and pointed teeth due to scuffing.....	119
Figure 85. Surface profiles: a) worm wheel 3, b) worm 1, c) worm 2 (EP), d) worm 3 (EP)	120
Figure 86. Surface profile measurement after the test: a) worm wheel 3, b) worm 3 (EP), c) worm wheel 3 surface profile, d) worm 3 (EP) surface profile.....	123
Figure 87. Worm pair 1 - efficiency and pitting percentage	124
Figure 88. Worm pair 2 (EP) - efficiency and pitting percentage	124
Figure 89. Worm pair 3 (EP) - efficiency and pitting percentage	125
Figure 90. Worm pair 4 - efficiency and pitting percentage	125
Figure 91. Worm pair 5 - efficiency	126
Figure 92. Pitting comparison - CuSn12 worm wheels.....	126
Figure 93. Pitting comparison of AlSn6 worm wheel.....	127
Figure 94. Pitting percentages for worm wheel 1	129
Figure 95. Flank No. 22 – initial pitting location.....	129
Figure 96. Pitting development on flank No. 11	130
Figure 97. Pitting location (overlapped) on flanks of worm wheel 1.....	131
Figure 98. Pitting correlation for worm wheel 1	132
Figure 99. Worm wheel 1 – deviations	134
Figure 100. Pitch error in double contact [152]	135
Figure 101. Worm 1 – axial profile curvature.....	136
Figure 102. Worm pair contact.....	137
Figure 103. Worm wheel 1 - Correlation between wear, pitting, and deviations	139
Figure 104. Worm wheel 1 - deviation distribution among the least and the most damaged flanks	142
Figure 105. Axial runout – definition of positive and negative axial runout	142
Figure 106. Pitting percentages for worm wheel 2	143
Figure 107. Pitting formation and development on flank No. 35.....	144
Figure 108. Pitting correlation for worm wheel 2	144
Figure 109. Pitting formation and development on worm wheel 2 flanks	145
Figure 110. Pitting depth analysis of flank No. 35.....	146

Figure 111. Worm wheel 2 - deviations	147
Figure 112. Worm 2 – axial profile curvature	148
Figure 113. Worm wheel 2 - Correlation between wear, pitting, and deviations	150
Figure 114. Overlap of nine consecutive flanks: a) large F_r , b) small F_r	152
Figure 115. Worm wheel 2 - deviation of most damaged and least damaged flanks.....	153
Figure 116. Pitting on worm wheel 3	154
Figure 117. Pitting location (overlapped) on flanks of worm wheel 3.....	154
Figure 118. An example of micropitting and pitting.....	155
Figure 119. Worm wheel 3 – deviations	157
Figure 120. Worm 3 – axial profile curvature	158
Figure 121. Worm wheel 3 – pitting at the end of the test	159
Figure 122. Pitting on worm wheel 4	160
Figure 123. Pitting formation and development on AlSn6 worm wheel flanks.....	161
Figure 124. CT scan of AlSn6 worm wheel: a) detected shrinkage volume, b) porosity defects	162
Figure 125. Pit depth across different axial sections.....	162
Figure 126. Worm wheel 4 – deviations	163
Figure 127. Worm 4 – axial profile curvature	164
Figure 128. Pitting corresponding to criterion $A_{P10} = 2\%$	166
Figure 129. Pitting correlation for worm wheel 4	167
Figure 130. Worm wheel 4 - deviation distribution among the least and the most damaged flanks	167
Figure 131. Initial load distribution on worm wheel 1	169
Figure 132. Initial contact of worm wheel 1: a) contact pattern defined by variable <i>CSTATUS</i> , b) contact pressure, c) initial contact pattern on worm wheel 1, d) average contact pressure	170
Figure 133. Theoretical worm wheel contact ($T_2 = 300$ Nm): a) load distribution, b) contact pattern, c) contact pressure.....	172
Figure 134. Theoretical average contact pressures on worm wheel 2.....	173
Figure 135. Average contact pressure among flanks with large F_r and small F_r	173
Figure 136. Contact patterns at the end of test runs (variable <i>CSTATUS</i>): a) worm wheel 1, b) worm wheel 2, c) worm wheel 3	174
Figure 137. Contact pressures at the end of test runs (variable <i>CPRESS</i>): a) worm wheel 1, b) worm wheel 2, c) worm wheel 3	175

Figure 138. Average contact pressures at the end of the test: a) worm wheel 2, b) worm wheel 3.....	177
Figure 139. Load distribution in worm wheels	178
Figure 140. FEM results: a) average contact pressure, b) contact area.....	179

List of Tables

Table 1. Advantages and disadvantages of worm pairs.....	16
Table 2. Chemical composition of 16MnCr5 steel, wt.%	22
Table 3. Mechanical properties of 16MnCr5 steel	22
Table 4. Chemical composition of worm wheel materials, wt.%	23
Table 5. Mechanical properties of worm wheel materials.....	23
Table 6. Recommendation for oil selection based on oil kinematic viscosity at 100°C [25,53]	28
Table 7. Main properties of the Alpha SP 150 lubrication oil.....	28
Table 8. Failure mode according to influence factors	30
Table 9. Boundary conditions for pitting resistance calculation procedure	34
Table 10. Pitting resistance for contact stress (materials used in this research).....	36
Table 11. Pitting resistance calculation values and results.....	36
Table 12. Number of load cycles N_L needed for pitting formation, according to ISO/TS 14521 [3]	39
Table 13. Number of cycles required for first pitting, according to [53]	40
Table 14. Comparison of the number of load cycles according to [3,25,53]	41
Table 15. Wear load capacity calculation values and results	49
Table 16. Worm pair deviations	52
Table 17. Acceptance test values.....	60
Table 18. Summary of presented surface texturing methods	72
Table 19. Surface parameters of electropolished steel surfaces [18]	80
Table 20. Average surface profile values of investigated steel discs and bronze specimens..	82
Table 21. Comparison of surface chemical compositions [18]	83
Table 22. Parameters used for the calculation of H_{min}	85
Table 23. Sliding test setups	86
Table 24. EDS inspection of surfaces after the test.....	91
Table 25. Values used for calculation of deflection of the worm.....	101
Table 26. Tested worm pair combinations	105
Table 27. Image post-processing errors.....	114
Table 28. Average worm wheel tooth thickness “as manufactured” vs. “end of test”	117
Table 29. Results of 16MnCr5-CuSn12 worm pair tests by Huber [57].....	118

Table 30. Electropolishing parameters of worm 2 and worm 3	121
Table 31. Worm 1 - deviations	134
Table 32. Worm pair 1 – quality grades (Q).....	135
Table 33. Worm wheel 1 - tooth thickness difference after the test	137
Table 34. Pitting linear models for worm wheel 1	140
Table 35. Pitting linear model for worm wheel 1 - alternative beginning of pitting criterion	141
Table 36. Worm 2 - deviations	148
Table 37. Worm pair 2 (EP) – quality grades (Q)	148
Table 38. Worm wheel 2 - tooth thickness difference after the test	149
Table 39. Pitting linear models for worm wheel 2	151
Table 40. Pitting linear model for worm wheel 2 - alternative “Beginning of pitting” criterion	151
Table 41. Worm wheel 3 - tooth thickness difference after the test	155
Table 42. Worm 3 - deviations	157
Table 43. Worm pair 3 (EP) – quality grades (Q)	158
Table 44. Worm 4 - deviations	164
Table 45. Worm pair 4 – quality grades (Q).....	164
Table 46. Pitting linear models for worm wheel 4	165
Table 47. Pitting linear model for worm wheel 4 - alternative “Beginning of pitting” criterion	166

Nomenclature

A_{fl}	approximate tooth flank surface, mm ²
A_P	flank pitting area, %
$A_{P,avg}$	average flank pitting area, %
A_{P10}	average flank pitting area of the 10 % of most damaged teeth, %
$A_{P10,max}$	maximum flank pitting area, %
a	center distance, mm
b_{2H}	effective wheel facewidth, mm
c_α	proximity value for the viscosity pressure exponent α , m ² /N
c_0	clearance at zero pressure, mm
d_{a1}	worm tip diameter, mm
d_{f1}	worm root diameter, mm
d_{disc}	diameter of steel disc, mm
d_{m1}	worm reference diameter, mm
E'	equivalent modulus of elasticity, N/mm ²
E_1	Young modulus of steel disc, N/mm ²
E_2	Young modulus of bronze specimen, N/mm ²
E_{red}	equivalent modulus of elasticity, N/mm ²
$F_{friction}$	Frictional force, N
F_{i1}'	total single flank composite deviation (worm), mm
F_{i2}'	total single flank composite deviation (worm wheel), mm
F_{pz}	total pitch deviation, mm
F_N	Normal force, N
F_{p2}	total cumulative pitch deviation, mm
F_{r1}	radial runout (worm), mm
F_{r2}	radial runout (worm wheel), mm
F_{tm2}	circumferential or tangential force to the worm wheel, N
$F_{\alpha1}$	total profile deviation (worm), mm
$F_{\alpha2}$	total profile deviation (worm wheel), mm

f_{px}	single pitch deviation (axial, worm), mm
f_{p2}	single pitch deviation (worm wheel), mm
f_{ux}	adjacent pitch difference (worm), mm
f_{u2}	adjacent pitch difference (worm wheel), mm
h^*	parameter for the mean lubricant film thickness, -
h_{a1}	worm tooth reference addendum in axial section, mm
G	dimensionless materials parameter, -
H_{min}	dimensionless film thickness parameter for line contact, -
h_{min}	minimum oil film thickness, mm
$h_{min m}$	minimum mean oil film thickness, mm
i	nominal ratio, -
J_w	wear intensity, -
J_{WP}	wear intensity, -
J_{0T}	reference wear intensity, -
J_{0I}	reference wear intensity for stage I, -
J_{0II}	reference wear intensity for stage II, -
J_{0III}	reference wear intensity for stage III, -
K_w	lubricant film thickness parameter, -
L_h	lifetime, h
l_1	spacing of the worm shaft bearings, mm
l_{11}	bearing spacing of the worm shaft, mm
l_{12}	bearing spacing of the worm shaft, mm
m_{x1}	axial module, mm
Δm_{lim}	material loss limit, mg
N_L	number of load cycles of the worm wheel, -
N_{LI}	number of load cycles of the worm wheel for stage I, -
N_{LII}	number of load cycles of the worm wheel for stage II, -
N_{LIII}	number of load cycles of the worm wheel for stage III, -
N_{LI}^*	number of load cycles required for first pitting, -

N_s	number of starts per hour, -
n_1	rotational speed of the worm shaft, min^{-1}
p_x	axial pitch, mm
p_m^*	parameter for the mean Hertzian stress, -
p_0	pressure at zero clearance, N/mm^2
Q	quality grade, -
q_1	diameter quotient, mm
R'	reduced radius of curvature, m
R_a	average surface roughness, μm
R_k	core roughness, μm
R_{ku}	kurtosis, -
R_{pk}	reduced peak height, μm
R_q	root mean square roughness, μm
R_{q1}	root mean square roughness of steel disc, μm
R_{q2}	root mean square roughness of bronze specimen, μm
R_{sk}	skewness, -
R_{vk}	reduced valley depth, μm
r_{a2}	addendum radius, mm
r_b	base radius, mm
r_{m2}	referent radius, mm
S_{Fmin}	minimum tooth breakage safety factor, -
S_H	pitting safety factor, -
S_{Hmin}	minimum pitting safety factor, -
S_W	wear safety factor, -
S_{Wmin}	minimum wear safety factor, -
s^*	parameter for the mean sliding path, -
s_{Wm}	wear path inside of the required life expectancy, mm
Δs_{m2}	tooth thickness reduction in the middle of the flank, μm
Δs_2	tooth thickness reduction on the leaving side of the flank, μm

Δs_{lim}	allowable tooth thickness loss, mm
$T_{friction}$	torque due to frictional force, Nm
T_{oil}	oil temperature, °
T_1	input torque, Nm
T_2	output torque, Nm
U	dimensionless speed parameter, -
u	gear ratio, -
u_{vel}	entraining surface velocity, m/s
u_1	entraining surface velocity of steel disc, m/s
u_2	entraining surface velocity of bronze specimen, m/s
v_g	sliding velocity at mean reference diameter, m/s
v_{gm}	mean sliding velocity, m/s
W	dimensionless load parameter, -
W_H	pressure factor, -
W_{ML}	material-lubricant factor, -
W_{NS}	start factor, -
W_S	lubricant structure factor, -
w	load per unit length, N/m
x_A	coordinate x of theoretical profile value, -
x_m	coordinate x of measured profile value, -
x_2	worm wheel profile shift coefficient, mm
y_A	coordinate y of theoretical profile value, -
y_m	coordinate y of measured profile value, -
Z_h	life factor, -
Z_{oil}	lubricant factor, -
Z_S	size factor, -
Z_u	gear ratio factor, -
Z_v	velocity factor, -
z_1	number of teeth/threads in worm, -

z_2 number of teeth in worm wheel, -

Greek symbols

α pressure-viscosity coefficient, m^2/N

α_0 normal pressure angle, $^\circ$

γ_{m1} reference lead angle of worm, $^\circ$

δ_m deflection of the worm, mm

δ_{Wn} flank loss from wheel through abrasive wear in the normal section, mm

δ_{WPn} flank loss from wheel through abrasive wear in the normal section, mm

δ_{Wlim} limiting value of flank loss, mm

$\delta_{Wlim,n}$ limiting value of flank loss in normal section, mm

ε_m contact ratio, -

η overall efficiency, %

η' viscosity at atmospheric pressure and temperature, Pas

η_{0M} dynamic viscosity of lubricant at ambient pressure and wheel bulk temperature, Ns/m^2

λ film thickness parameter, -

μ_{zm} mean tooth coefficient of friction, -

ν_1 Poisson's ratio for steel, -

ν_2 Poisson's ratio for bronze, -

ν_M kinematic viscosity at wheel bulk temperature, mm^2/s

θ_M wheel bulk temperature, $^\circ\text{C}$

ρ_{oilM} lubricant density at wheel bulk temperature, kg/dm^3

ρ_{Rad} material density of the wheel, mg/mm^3

σ_H contact stress, N/mm^2

σ_{HlimT} pitting resistance, N/mm^2

σ_{Hm} mean contact stress, N/mm^2

σ_{HG} limiting value for the mean contact stress, N/mm^2

Expressions

$$E' \quad \frac{1}{E'} = \frac{1}{2} \left[\frac{1 - v_1^2}{E_1} + \frac{1 - v_2^2}{E_2} \right]$$

$$G \quad G = \alpha E'$$

$$h_{\min} \quad h_{\min} = H_{\min} \cdot R'$$

$$R' \quad \frac{1}{R'} = \frac{1}{R_1} + \frac{1}{R_2}$$

$$U \quad U = \frac{\eta \cdot u}{E' \cdot R'}$$

$$u_{\text{vel}} \quad u_{\text{vel}} = \frac{u_1 + u_2}{2}$$

$$W \quad W = \frac{w}{E' \cdot R'}$$

1

Introduction

Worm pairs are commonly used machine elements for power transmission, especially where a high transmission ratio in a single gear stage is required. A worm is often driving, and a worm wheel is a driven part of a worm pair. As in other gear types, damage mechanisms that occur in worm pairs are wear, pitting, tooth breakage, and scuffing. While tooth breakage and scuffing rarely occur, wear and pitting are common during regular working conditions. Due to their geometry, worm pairs are sensitive to manufacturing and assembly errors [1], and their influence on damage mechanisms, namely pitting, has not been thoroughly studied yet. Therefore, further investigation is required to address the influence of the dimensional accuracy of worm pairs on pitting formation more accurately. Additionally, worm pair meshing is characterized by prevailing sliding action which enables smooth running but results in considerable frictional power loss and lower efficiency than other gear types. Furthermore, specific worm pair geometry causes unfavorable lubricating conditions, contributing to the abovementioned problems. Surface modification, such as surface texturing, changes the topography of the surface with the goal of improving lubrication conditions. Applying surface texturing in worm pairs is challenging due to complex geometry, tight tolerances, and high loads. However, potential benefits would result in better lubrication conditions and consequently higher gearbox efficiency. Therefore, an opportunity arises to investigate the surface modification approach and its influence on worm pair operating conditions.

1.1 Motivation

As mentioned in the previous section, pitting is a common damage mechanism that could occur even in normal operating conditions [2]. Pitting occurs on worm wheel tooth flanks as the worm wheel is usually made from a softer material, mostly bronze, and paired with a hardened steel worm. The existing standards [3,4] address pitting durability by limiting the value of contact stress. Such calculation requires a complete contact pattern which is rarely the case in practice as worm wheels are produced using an oversized hob. Such a concept results in an incomplete contact pattern, but on the other hand, improves lubrication conditions and reduces sensitivity to manufacturing and assembly errors [5]. The ISO TS/14521 standard [3] provides calculation for three stages of pitting: the beginning of pitting (defined by pitting area $A_{P10} = 2\%$), the pitting growth stage, and the wear stage. Worm pairs can operate even when pitted areas exceed 60% of worm wheel tooth flank area which is an interesting phenomenon compared to other types of damage mechanisms. Also, pitting may or may not directly impact efficiency loss [6]. However, the provided calculation is relevant for specific materials and boundary conditions while the data for other material combinations, lubrication types, and worm pair geometry are scarce.

Pitting formation and development are usually uneven across worm wheel tooth flanks. This phenomenon is supported through standards [3,4] where the referent value of pitted area A_{P10} is defined as the mean value of the pitting percentage of 10% of the most damaged teeth. Other research showed that pitting overlap on multiple teeth can be as low as 1.39% or as high as 50% [7]. Also, the pitting percentage on different tooth flanks of the same worm wheel can range from 1% to 30% [8]. In contrast, the pitting can also diminish through excessive worm wheel wear. Due to sliding wear, material defects, operating conditions, and dimensional accuracy of the worm pair, contact geometry changes throughout the worm pair lifetime, and pitting formation can theoretically occur anywhere on the worm wheel tooth flank.

To better understand the uneven occurrence of pitting in worm wheels, further research should be conducted to interpret the influence of worm pair dimensional accuracy on pitting formation. While the effect of tooth spacing errors and shaft misalignments has been addressed through a computational model [9], other errors mentioned in standards concerning the accuracy of worms and worm wheels [10,11] have not been researched and thoroughly discussed. This provides an opportunity to better define and understand the correlation between worm pair

dimensional accuracy and pitting formation to provide new guidelines regarding worm pair inspection and damage prevention.

One of the major drawbacks of worm pairs compared to other gear types is significantly lower efficiency primarily caused by dominant sliding action during meshing. Typical high-ratio designs are characterized by mechanical efficiency of 70-80% compared to 95% in parallel axis gear units [12]. A high degree of sliding paired with unfavorable oil-entraining geometry leads to poor lubrication conditions. Worm pair geometry is well known, and several flank types are commonly used (e.g., ZA, ZN, ZE, ZK flank types). A typical worm pair consists of a steel worm and a bronze wheel. This material pair is characterized by a low coefficient of friction and low metallic compatibility which makes it resistant to scuffing. Intending to improve lubrication conditions, researchers investigated new material pairs with better tribological properties [13,14]. In addition, researchers have focused on new geometry types characterized by better load-carrying capabilities and better lubricating conditions [15–17]. However, among available studies, there has not been any effort to employ surface modification as a potential method to achieve better lubrication in worm pairs, namely steel-bronze material pair.

Surface modification of metal surfaces is often conducted to reduce wear and friction and subsequently improve lubrication conditions. Surfaces are usually modified by employing surface coatings or by altering surface topography. The change in surface topography is frequently achieved by producing a surface texture [18]. If surface modification would result in better lubrication conditions, the benefits would be mainly visible in higher worm pair efficiency. It was estimated that an increase of 5% in the overall efficiency of worm drives in the United States would save approximately 0.6 billion USD per annum. This estimation does not include worm drives rated under 5 HP [19]. Implementing surface texturing on gears is relatively challenging due to complex geometry, tight tolerances, high loads, and roughness requirements. Additionally, many gears are case-carburized and the impact of surface texturing methods, such as laser surface texturing, may severely reduce surface hardness [20]. These limitations present a challenge in finding and applying appropriate surface modification techniques to complex worm pair geometry while being sufficiently simple, fast, and cost-effective.

1.2 Defining the research gap

As portrayed in the previous section, a relationship between worm pair dimensional accuracy and pitting is required to better understand pitting formation and development as pitting is a common damage mechanism that occurs on worm wheel tooth flanks even in normal operating conditions.

Many studies on load distribution, pitting, and wear in worm wheels have been conducted. Simon [9,21–23] researched load distribution in worm pairs. The tooth spacing error worsens the load sharing among tooth pairs, possibly eliminating one of the tooth pairs from contact [9]. Modifications induced by manufacturing the worm wheel with an oversized hob considerably increase contact pressures, load distribution, and transmission error. Nevertheless, such modifications reduce the sensitivity of worm pairs to misalignments and errors [21]. An oversized hob accompanied by a machine tool setting angle error can increase contact stresses up to 100% [22]. Falah et al. [24] concluded that assembly errors worsen load distribution among worm wheel teeth which can lead to premature pitting failure at the tooth surface. While the effect of center distance error can be reduced using an oversized hob, the angular misalignment of either worm or wheel shafts tends to increase contact stresses on one side of the tooth flank and reduce them on the other. Opalić et al. [7] formulated the dependence of a pitted area with the number of load cycles and identified uneven pitting on worm wheel teeth flanks. Žeželj [25] investigated pitting location and pitted area percentage on AlSn6 and CuSn12 bronze worm wheel teeth flanks using digital imaging and computer vision applications. The difference in the pitted area between teeth of the same worm wheel was up to 50%. Stahl et al. [26] investigated pitting on larger center distance worm pairs. The pitting location on the worm wheel tooth flank was influenced by the minimum equivalent radius of curvature and the highest Hertzian stress found on the leaving side of the flank. Additionally, pitting growth in the affected areas of the tooth flanks was very consistent. Oppositely to Stahl et al. [26], Sievers et al. [8] investigated the pitting of bronze worm wheels. Results showed uneven pitting area distribution between 1% and 30% for teeth flanks of the same worm wheel. Multiple investigations reported that with an increase in pitting percentage, the worm pair efficiency remained the same or even increased [6,8,25]. This suggests pitting might be favorable regarding pits acting like oil micro reservoirs, thus improving lubrication conditions. Jbily et al. [27] created a model based on the abrasive wear of a worm wheel. The model was evaluated with experimental results and showed a good correlation. However, the pitting

phenomenon was not considered. As pitting reduces tooth contact area, the increased contact stresses can induce even more pitting or a faster wear rate. Sharif et al. [28] developed a wear model based on EHL elastohydrodynamic analysis and concluded that the wear pattern was mainly influenced by oil film thickness. Oil film thickness is expected to be the thinnest or even non-existent in the middle part of the wheel tooth flank area where the highest wear rate occurs until sufficient material is removed to relieve the pressure locally and thereby reduce the wear rate. Octrue [29] studied the relationship between wear and pitting phenomena in worm gears. Increased wear can eliminate the pitted area from the tooth flank. Moreover, material heterogeneity can produce non-homogeneity of tooth-to-tooth wear and result in pitch errors, leading to bad load sharing between teeth.

Based on earlier sections, the conclusion arises that lubrication conditions in worm pairs are poor compared to other gear types. Relatively unfavorable entraining geometry of typical worm pair designs creates poor film-forming characteristics and causes main limitations of lower load capacity and efficiency [12]. Sharif et al. [12,30] and Kong et al. [31] developed the elastic contact model and elastohydrodynamic (EHD) lubrication of worm pairs. According to the proposed model, the authors pointed out a zone of dry contact on the worm wheel teeth flank where temperature increased by 45°C compared to the outer regions of the contact zone. While commonly paired hardened worm steel and bronze worm wheel is a well-known material combination, some authors conducted studies towards improving lubrication conditions by employing new materials. Fontanari et al. [2,13] investigated wear damage mechanisms in steel-bronze and alloy steel-cast iron pairs under a mixed lubrication regime, commonly used to describe the tribological system in worm pairs. Cast iron showed a lower wear rate, suggesting that an alternative material may perform better than bronze. Benedetti et al. [14] investigated various coatings on steel-steel tribo-pairs. The results showed improved wear resistance compared to conventionally used bronze. Simon [17] proposed the improved geometry of worm drives to improve load distribution and lubrication. The new type of worm gearing had higher EHD load-carrying capacity and lower power losses.

From the earlier paragraph, it is evident that various studies were conducted to understand and improve lubrication conditions in worm pairs and consequently to investigate wear mechanisms in different material pairs. However, no studies were found where surface modification was employed to improve lubrication properties in steel-bronze, or worm pairs. Surface modification of metal surfaces is carried out to reduce wear and friction between contacting surfaces. This is often correlated with improving lubrication conditions, characterized by better

lubricant supply, improved film thickness, debris entrapment, enhanced heat dissipation, etc. Surfaces are usually modified by changing surface topography or employing surface coatings. The change in surface topography is frequently achieved by producing a surface texture. Common techniques used for surface texturing include laser surface texturing (LST), electrochemical etching, and micro-machining [20,32,33]. Surface textures are characterized by micro-cavities with multiple beneficial functions: entrapment of wear debris, secondary oil effect, friction reduction, and an increase in the oil film thickness [20]. Since worm and worm wheel contact can be described as a tribological system characterized by non-conformal contact under a mixed lubrication regime [2,13], it is important to acknowledge the corresponding advantages of surface texturing in such a system. Surface textures have been frequently investigated in boundary and mixed lubrication regimes. Vrbka et al. [34,35] investigated the effect of surface texturing in mixed lubricated non-conformal contacts. The authors observed that shallow micro-dents and textures increased the oil film thickness and the rolling contact fatigue life. Krupka et al. [36] observed that shallow pits work as lubricant micro-reservoirs, while deep grooves cause oil film thickness reduction in mixed lubricated non-conformal contacts. Ali et al. [37] investigated textured surfaces in high load boundary lubrication conditions. Textured surfaces reduced the friction and contributed to the creation of an extra hydrodynamic lift effect. Galda et al. [38] studied surfaces textured with spherical oil pockets. Results showed an increase in the oil film thickness and a reduction of the coefficient of friction compared to the untextured surface. Dimple density smaller than 20% of the area and dimple depth-to-length ratios between 0.03 and 0.08 proved beneficial. Kovalchenko et al. [32] explored laser textured surface behavior under non-conformal sliding contact. The textured surface substantially reduced friction coefficients and increased the sliding speed under mixed lubrication. The dimple density area was either 12% or 15%, while the dimple depth-to-length ratios were 0.07 and 0.086. In addition to surface texturing techniques mentioned earlier, other techniques such as shot peening (shot blasting), and electropolishing can also produce surface textures. Li et al. [39] shot peened specimens made of gear steel. A positive influence on the friction coefficient reduction was attributed to the dimpled surface, particularly if fine particle peening is used. Nakatsuji and Mori [40,41] investigated the electropolished surfaces of medium-carbon steel. The produced surface had many pores/pits and shallow dimples that encouraged the creation of the oil film, consequently exhibiting longer pitting durability.

Implementing surface texturing in gears is challenging due to relatively complex geometry, tight tolerances, high loads, and surface roughness requirements. Additionally, many gears are

case-carburized. Therefore, the impact of a certain surface texturing method, such as the laser source, may severely reduce surface hardness [20]. Usually, lubrication conditions in gears are improved by grinding or superfinishing [42]. However, gear surface texture can also be indirectly achieved, i.e., by electropolishing. Nakatsuji and Mori [41,43] applied previous findings in electropolished surfaces to medium carbon steel gears. The produced surface had many micropores and oxidized and phosphoric compounds that encouraged the creation of the oil film, consequently improving the pitting and scuffing durability. Some recent studies focused on the surface texturing of gears or gear steel. Gupta et al. chemically etched [44] and laser textured [45] spur gear teeth flanks, producing a dimpled surface. Results showed reduced wear and a significant decrease in vibration amplitudes. Petare et al. [46] laser textured helical and straight bevel gears. The results showed friction reduction and higher wear resistance than untextured gears. Based on the literature overview, most of the research was conducted on spur gears, presumably because the spur gear tooth flank is the most “approachable” (from the geometrical standpoint) for laser texturing or etching. The application of surface texturing in other types of gears and materials, apart from steel spur gears, has yet to be more thoroughly investigated.

After carrying out a detailed overview of the existing studies related to this investigation, it can be concluded that besides a few analytical studies, the relationship between dimensional accuracy and pitting in worm pairs is not sufficiently investigated. Even though there are some indications and reports on the influence of certain errors on increased contact stresses, there is a gap in quantitative and qualitative relation between dimensional accuracy and pitting formation. Furthermore, the problem of poor lubrication conditions in worm pairs has been addressed by investigating and developing wear and contact models, proposing improved geometry, and employing new material pairs to reduce friction and wear. Although researched in various types of contacts, materials and spur gears, the surface modification approach has not yet been applied to worm pairs, focusing on improving lubrication conditions and overall efficiency.

By measuring and investigating specific worm pair deviations, their influence on pitting formation and development on worm wheel tooth flanks is presented. Moreover, differentiation between influential and less important deviations in terms of pitting formation is made. Models of pitting formation based on the number of load cycles and worm pair dimensional accuracy are provided based on experimental investigation. Also, the finite element method (FEM) model based on a real, non-ideal, worm pair geometry is developed to investigate load and stress

distribution and influence of deviations on values of contact pressures. Additionally, model testing is used to verify the selected surface texturing method in a steel-bronze pair to gain further insight into surface texturing possibilities in worm pairs. Lastly, surface texturing is applied to a steel-bronze worm pair, and the results, focusing on pitting formation and gearbox efficiency, are compared to a conventional worm pair.

1.3 Hypotheses

This doctoral thesis has two main objectives, each supported by its appropriate hypothesis formulation.

The first objective is to analyze the dimensional accuracy of the worm pair, namely the worm wheel, and relate the deviations and errors with pitting formation and development. This objective aims to improve the understanding of the uneven pitting phenomenon in worm wheels.

Hypothesis 1:

By analyzing worm wheel dimensional accuracy and its influence on load and stress distribution, it is possible to define worm wheel tooth flank pitting initial location and pitting formation more accurately.

The second objective is to apply surface modification in the form of surface texturing on either the worm or worm wheel tooth flank. The aim is to improve poor lubrication conditions present in worm pairs. Improved lubrication conditions should be manifested in better efficiency, lower wear, or lower pitting percentage.

Hypothesis 2:

By employing surface texturing on a worm or worm wheel tooth flank, it is possible to improve worm pair lubrication conditions.

1.4 Methodology

The research conducted within the scope of this doctoral thesis started with a dimensional inspection of worm pairs and the selection of a surface texturing method that can successfully be applied to worm pairs. Then, the model testing on simple steel-bronze geometry was conducted to validate the selected method and its applicability in steel-bronze pair. This was followed by experimental testing of conventional and textured worm pairs and concluded with evaluation of the results. The research plan is schematically shown in Figure 1.

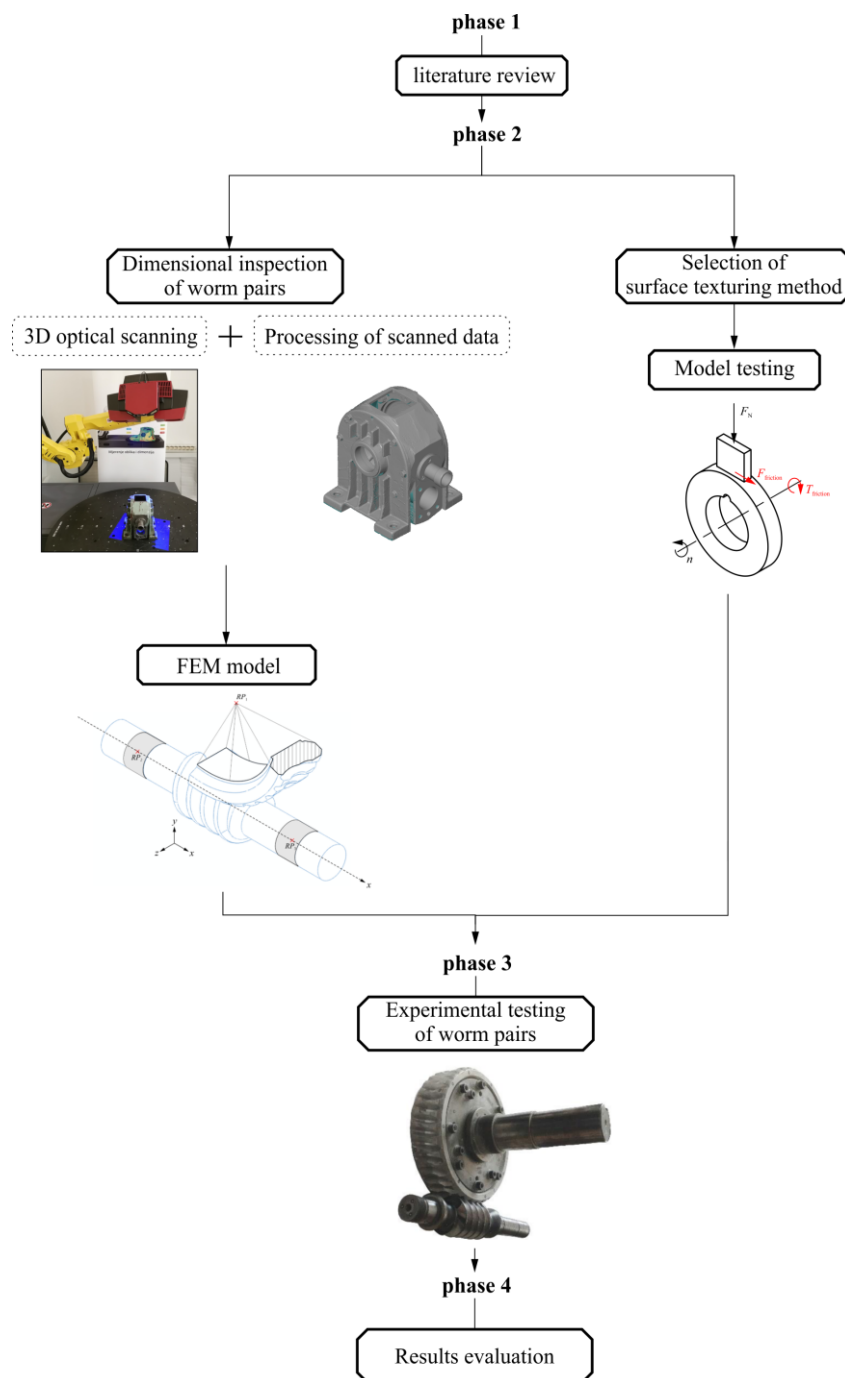


Figure 1. Schematic representation of the research plan

This research is divided into four main phases:

1) *Phase 1: Literature review*

Defining the research gap refers to choosing an area that has not been sufficiently investigated in the field of study. This was carried out through an extensive literature overview of the relevant studies. Based on the literature overview, a motivation for investigating the influence of dimensional accuracy on pitting formation and implementation of surface texturing in worm pairs appeared. However, the literature overview is a continuous process in which the latest and most relevant studies are always kept track of.

2) *Phase 2: Dimensional inspection of worm pairs and selection of surface texturing method. Verification of selected surface texturing method by model testing.*

Dimensional inspection of worm pairs was conducted using 3D optical scanning. It provided an ability to capture the entire geometry of complex parts, such as worm pairs, with sufficient accuracy and precision. Additionally, the worm pairs housing was scanned which enabled the inclusion of housing errors into future evaluation. The scanned data was processed and deviations concerning the accuracy of worms and worm wheels were measured according to standards [10,11]. Obtained 3D optical scans were used in developing the finite element method (FEM) model. The model was used for analyzing load and stress distribution, contact pattern, and contact ratio in worm pairs represented by actual geometry.

Alongside dimensional inspection, the appropriate surface texturing method was carefully selected. Among many available methods, electropolishing at high current potentials was chosen as it is relatively simple and easily applicable to complex geometry. Such method produces surface topography with many pits and canals that function as oil reservoirs and micro-hydrodynamic bearings. The electropolishing was applied to the steel worm as the bronze worm wheel wears significantly more than steel. Therefore, any surface texture introduced on steel will last considerably longer, producing longer-lasting benefits of a surface topography change. The model testing on simple geometry (block-on-disc setup) was conducted to validate the chosen method. The results of model testing will be presented in detail in the thesis and can be found in published paper [18].

3) *Phase 3: Experimental testing of worm pairs*

Worm pairs, both conventional and surface textured, were experimentally tested using an already developed testing rig [25] which was further upgraded as a part of this research. Pitting formation and development were monitored using digital image acquisition and post-processing. Besides pitting, gearbox efficiency was constantly monitored as it is one of the main indicators of improved lubrication conditions. In addition to tests carried out on 16MnCr5 steel and CuSn12 bronze pairs, tests with 16MnCr5-AlSn6 and 16MnCr5-CuAl10Fe5Ni5 pairs were also conducted. Following the experimental tests, the worm pairs were once more 3D optically scanned.

4) *Phase 4: Results evaluation*

As mentioned earlier, the pitting percentage on worm wheel tooth flanks was measured through digital image processing and correlated with measured deviations. Locations of pitting formation were investigated based on digital images, measured deviations, and developed FEM model. A model of pitting formation based on the number of load cycles and worm pair dimensional accuracy is provided upon experimental tests carried out in phase 3. Worm wheel wear was investigated in terms of worm wheel tooth thickness measured before and after experimental tests. The comparison between conventional and surface textured worm pairs was presented.

To summarize, the dimensional inspection of worm pairs was conducted after defining the research gap (phase 1). Alongside the inspection, electropolishing was selected as the appropriate surface texturing method. The model testing on simple geometry (block-on-disc setup) was carried out to validate the selected method (phase 2). Worm pairs, both conventional and surface textured, were experimentally tested while pitting formation was constantly monitored through digital image acquisition. Besides the usual steel-bronze, additional material pairs were also tested (phase 3). Lastly, the acquired data was evaluated and interpreted. Pitting percentage and location were correlated with measured worm pair deviations, and the model of pitting formation based on the number of load cycles and worm pair dimensional accuracy was provided. Furthermore, the comparison between conventional and surface textured worm pairs was presented (phase 4).

1.5 Expected scientific contribution

The measured deviations will be used to model worm wheel tooth flank pitting by analyzing worm pair dimensional accuracy. The model will consider the number of load cycles and dimensional accuracy of the worm pair to model and predict pitting on worm wheel tooth flanks. This will enable qualitative and quantitative representation of the influence of worm pair dimensional accuracy on tooth flank pitting. A better understanding of the abovementioned relation will help outline the deviations that have a greater impact on pitting formation and therefore should be more carefully considered during worm pair manufacturing and inspection.

Employing surface texturing in worm pairs will improve lubrication conditions manifested primarily through higher efficiency. Higher efficiency results in lower energy losses and therefore cost savings. As higher efficiency is directly linked to lower friction in the contact zone, lower damage in terms of wear and pitting can be expected. This would prolong the worm pair service life and improve the cost-effectiveness of the gear design. Moreover, as surface texturing will be carried out through electropolishing at elevated potentials, the surface topography change of electropolished case-carburized 16MnCr5 steel will be presented. This will establish a foundation for possible future experimental studies focused on electropolishing other gear materials, namely hardened steels, which are not usually considered or investigated in such a manner.

1.6 Thesis layout

This doctoral thesis consists of ten chapters. The research gap regarding the pitting and poor lubrication conditions in worm pairs along with research motivation was presented in the introductory chapter. Existing studies that helped define the research methodology and formulate the hypotheses were portrayed. Lastly, the expected scientific contribution of the doctoral thesis was conveyed.

The second chapter presents a more detailed description of the worm pair geometry, materials, lubrication, and worm wheel manufacturing is presented. Mechanical properties and chemical composition of worm and worm wheel materials are provided. Also, the properties of lubrication oil used in the experimental tests are presented. Lastly, the specifics of worm wheel manufacturing are discussed.

The third chapter describes the damage mechanisms in worm pairs, focusing on pitting and wear. The pitting and wear resistance calculation procedures are carried out according to the

ISO/TS 14521 standard. Other relevant pitting resistance calculation studies from the literature are presented and mutually compared.

The fourth chapter deals with dimensional accuracy in worm pairs. The deviations of worm pairs outlined in the DIN 3974 standard are covered in detail in this chapter. The 3D optical scanning method used for dimensional inspection of worm pairs is presented and compared to other methods commonly employed in gear inspection. The worm pair scanning process is described. Finally, scanned data processing is explained through examples of scan alignment and deviation measurements.

The fifth chapter deals with the topic of surface texturing. Most common surface texturing methods are presented. The emphasis is placed on surface texturing in gears due to their complex geometry that is not equally suited for all surface texturing methods. The selection of an appropriate surface texturing method to be applied in worm pairs was carried out. Based on evaluation criteria, electropolishing was chosen as a promising method that first needs to be evaluated through model testing.

The sixth chapter presents the model testing results of the electropolished steel-bronze pair. The electropolishing procedure and the effect of electropolishing parameters on the surface topography of case-carburized 16MnCr5 steel are presented and explained. The results are compared to the results of the ground steel-bronze pair in terms of coefficient of friction, wear, surface topography, and chemical composition modifications.

In the seventh chapter, the finite element method (FEM) model developed for evaluating load and stress distribution in worm pairs is presented. The model is focused on real geometry worm pairs, meaning it is used to investigate worm pairs “as manufactured”, rather than ideal worm pair geometry. The goal of the FEM model is to gain a better understanding of how real geometry affects load and stress distribution in worm pairs. The FEM model is verified with ISO/TS 14521 standard.

The eighth chapter covers the experimental setup employed for worm pair testing. Also, the worm pair testing procedure, running-in process, digital imaging of the worm wheel flank, and image post-processing are explained in detail.

In the ninth chapter, the results of worm pair experimental tests are presented and compared to existing literature. The results include worm pair efficiency, pitting, and worm wheel tooth flank wear. Also, the influence of dimensional accuracy on worm wheel pitting formation is

presented by analyzing worm pair deviations obtained through 3D optical scanning. Lastly, the results obtained through developed the FEM model are used to analyze the contact pattern, contact ratio, and load and stress distribution in worm pairs.

In the tenth and final chapter, the conclusions are drawn, research limitations are presented, and future work is discussed.

2

Worm pair properties

In this chapter, a more detailed description of the worm pair geometry, materials, lubrication, and worm wheel manufacturing is presented. In the geometry section, a brief overview of the ZN-type worm pair used in this research is provided. In the materials section, the mechanical properties and chemical composition of worm and worm wheel materials are given. The lubrication section deals with problematic and poor lubrication conditions in worm pairs and the expected types of lubrication regimes that occur in worm pairs. Also, the properties of lubrication oil used in the experimental tests are provided. Lastly, the specifics of worm wheel manufacturing are discussed. The advantages and disadvantages of the oversized hob/fly cutter manufacturing method are described and details regarding expected contact patterns are outlined.

2.1 General characteristics

The worm pair consists of a worm and worm wheel (Figure 2). The worm is usually manufactured as a shaft, while the worm wheel is manufactured as a separate part and assembled with a hub on its shaft. They are widely used for systems with non-parallel axes, primarily perpendicular, although different angles are achievable. Some examples include lifts and elevators, presses, conveyor belts, automotive steering systems, rotary tables, and speed reducers in motors. The advantages and disadvantages of worm pairs are listed in Table 1 [47–50]:

Table 1. Advantages and disadvantages of worm pairs

Advantages:

-
- A large transmission ratio in one gear stage allows for a compact design.
 - Low noise and vibration due to dominant sliding motion
 - Relatively high load-bearing capacity as multiple teeth are usually in the mesh.
 - The capacity for heavy shock loading
 - The ability to self-lock which can be exploited in lifting equipment, rapid braking, or holding the desired position
 - Relatively good efficiency in worm pairs with multiple worm threads

Disadvantages:

-
- Lower efficiency compared to cylindrical and bevel gears
 - Frictional heat generation requires continuous lubrication and heat dissipation
 - Highly sensitive to assembly errors (center distance change, shaft angles, and axial displacements).



Figure 2. Worm pair

Based on the shape, the worm and/or worm wheel can be cylindrical or throated (globoidal). If one member is throated the designation *single-enveloping*. In contrast, if both members are throated the designation *double-enveloping* is used [50]. There are three possible configurations of the worm pair (Figure 3):

- a) Cylindrical worm and throated worm wheel (single-enveloping worm pair)
- b) Throated worm and cylindrical worm wheel (single-enveloping worm pair)
- c) Throated worm and throated worm wheel (double-enveloping worm pair)

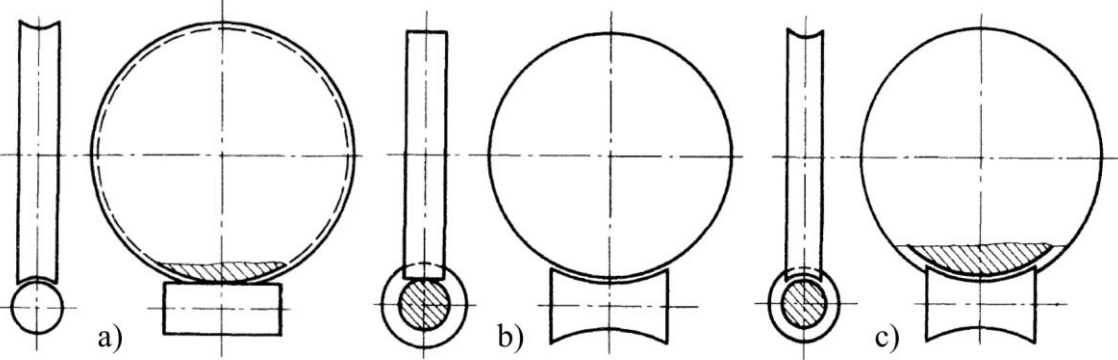


Figure 3. Worm pair configurations [47]

Additionally, based on the worm wheel design, the active worm wheel face width may differ from the worm wheel rim width [51]. The three possible designs are shown in Figure 4. The worm can have one or multiple threads which can be left or right-hand oriented. The worm pair ratio is calculated as the ratio of worm wheel teeth z_2 and worm threads z_1 .

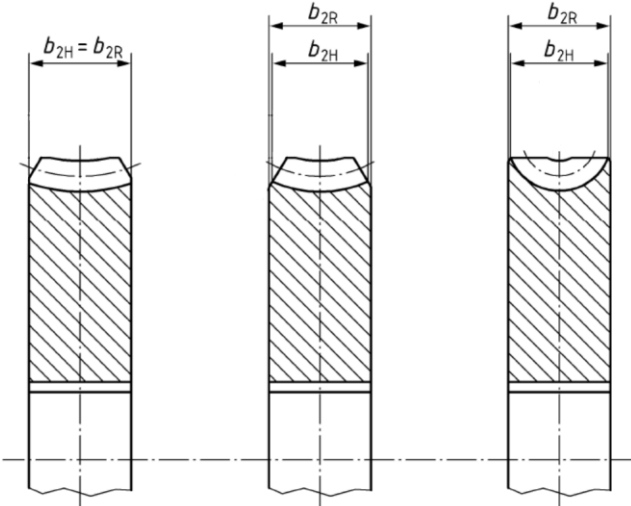


Figure 4. Worm wheel face width, according to [51]

Depending on the method of generation and geometry of cylindrical worms, typical profiles of cylindrical worms are: type A (ZA worm), type I (ZI worm), type N (ZN worm), type K (ZK worm) and type C (ZC worm) [51]. This research uses double-threaded right-hand ZN worms and throated (globoidal) worm wheels. A further mention of the worm pair in this thesis refers to the configuration mentioned above.

2.2 Geometry and manufacturing of ZN worm pairs

The ZN worm is typically cut in a lathe by a straight-edged trapezoidal turning tool, although the form can be obtained by milling and skiving. The tool with normal pressure angle α_0 is inclined for a lead angle γ_{m1} from the worm axis; thus, the tool edge angle equals the pressure angle in the normal section ($\alpha_0 = \alpha_n$) (Figure 5). The resulting profile is straight-lined in a normal section and slightly concave in an axial plane [47–49,51,52]. The basic dimensions of the ZN worm pair are presented in Figure 6.

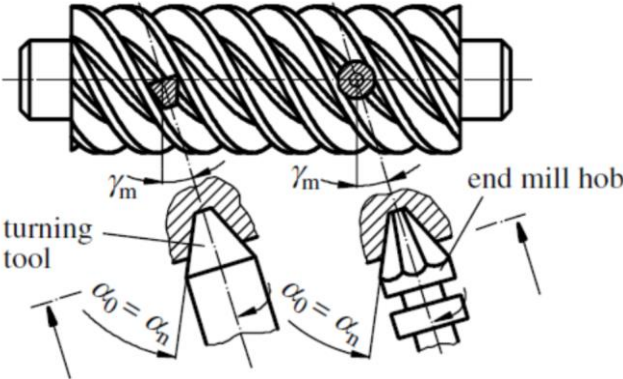


Figure 5. ZN worm – tool geometry [52]

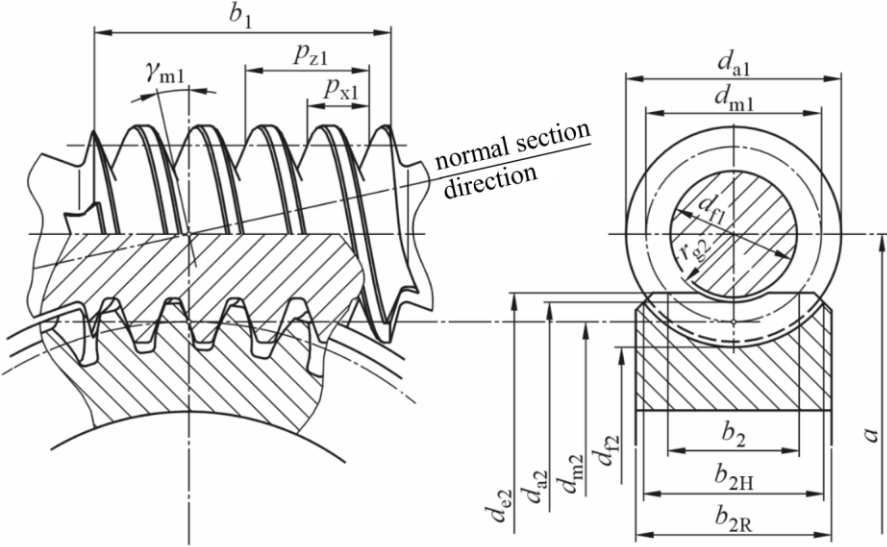


Figure 6. Basic dimensions of ZN worm pair [25]

The worm wheel is usually produced by hob using the radial feed method (the hob is radially fed into the worm wheel blank until full cutting is completed). Theoretically, if the hob has the same dimensions, number of threads, and lead angle as a mating worm, the result is a fully conjugated worm pair. This produces instantaneous line contacts between worm and worm wheel tooth surfaces. However, since the hob sharpening reduces its dimensions, the worm wheel produced by the undersized hob creates an unacceptable split outer edge contact pattern (Figure 7).

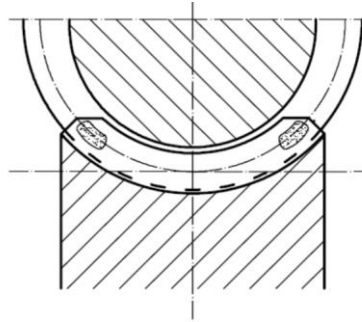


Figure 7. Split contact pattern due to hob undersize [52]

Additionally, such a manufacturing method would be uneconomical and impractical as hob life would be limited, and the produced worm pair would be highly sensitive to manufacturing and assembly errors. The oversized hob is used in worm wheel manufacturing to mitigate the abovementioned problems. An oversized hob reduces the sensitivity of the worm pair to alignment errors and transforms line contacts into localized elliptical contacts; thus, the worm pair becomes “mismatched” [22]. Also, the hob is often adjusted at a small angle to position the contact toward the leaving side of the worm wheel tooth. This improves the oil supply in the contact zone. On the other hand, employing oversized hob worsens meshing characteristics. The contact pressures in worm pair processed with oversized hob are significantly higher than in conjugated pair (Figure 8). Additionally, small tool settings errors greatly impact maximum contact pressure and the transmission error of the worm pair [22,23]. Nevertheless, the worm pair is always adjusted at the start of the operation in a process known as the running-in. Under lighter loads, the softer worm wheel conforms to a harder worm until the desired contact pattern is achieved (Figure 9). Therefore, the modifications induced using an oversized hob are somewhat mitigated and more uniform contact pressure distribution is achieved. However, the use of an oversized hob creates meshing conditions far from theoretical, especially regarding contact pressure values, which are not accounted for in calculations in present standards.

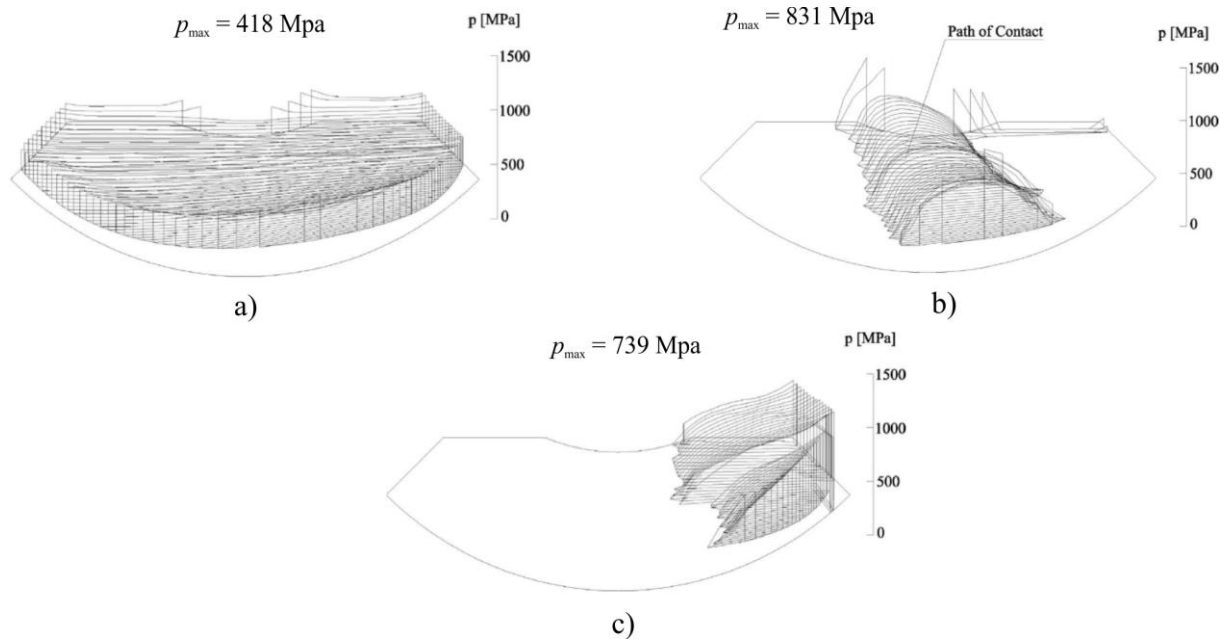


Figure 8. Contact pressure distribution for a) fully conjugated pair, b) worm pair processed by a 5% oversized hob, c) hob angle error of 0.1° [22]

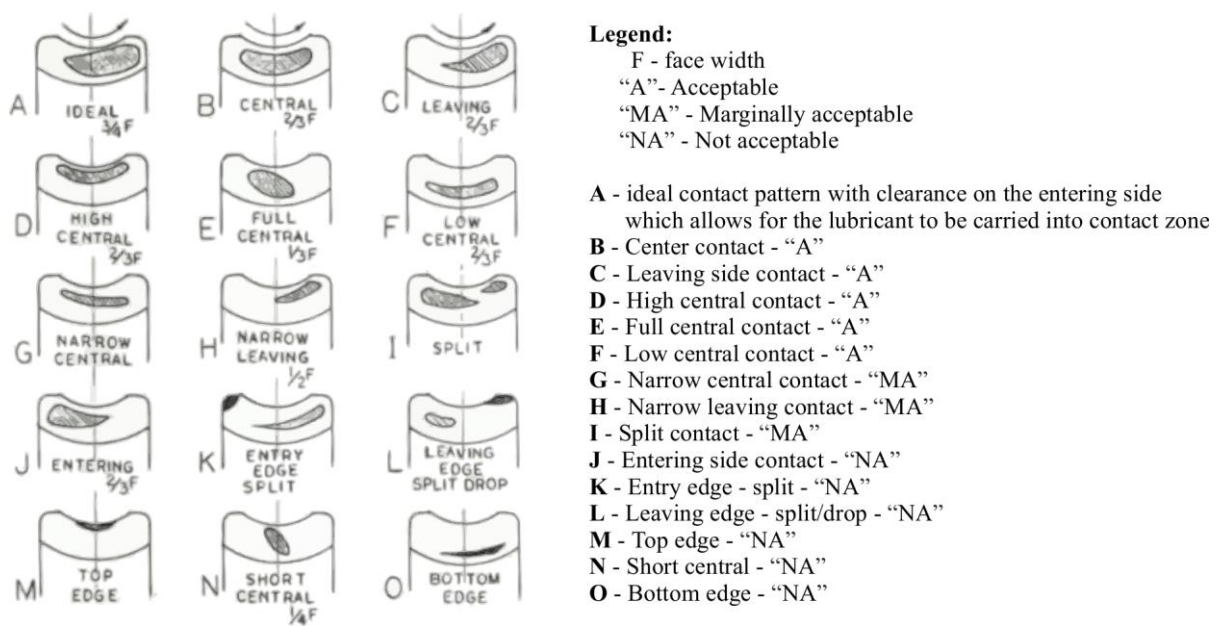
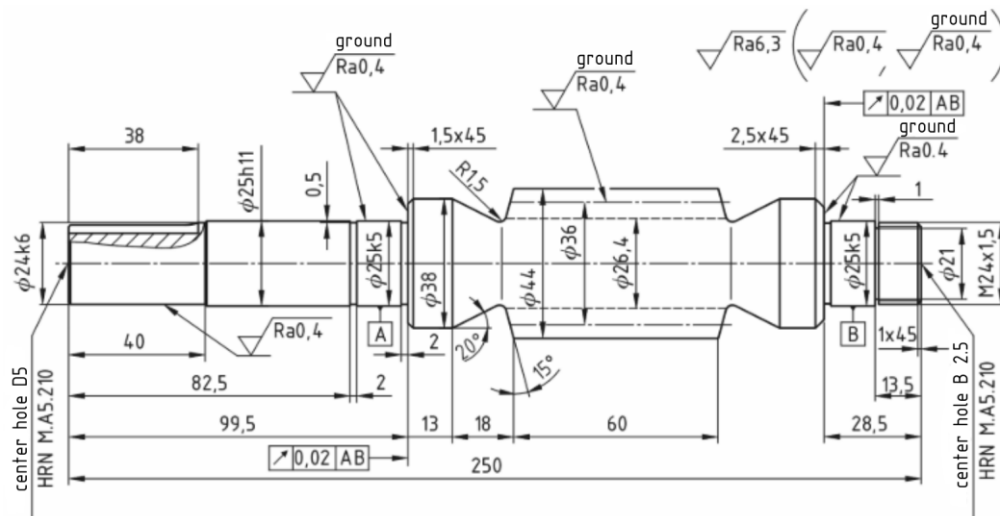


Figure 9. Types of contact patterns [5]

The worm pair used in this research was also used in many previous studies. Žeželj [25] and Opalić [53] investigated pitting areas and the correlation between pitting and the number of load cycles in worm wheels made of CuSn12 and AlSn6. Rakamarić [54] studied the influence of oil on sliding wear in worm wheels made of CuSn12, AlSn6, and CuAl10Fe5Ni5. Panić [55] researched the wear and tribocorrosion of worm wheels made of CuAl10Fe5Ni5. Technical

drawings of the worm and worm wheel used in previous studies, and this research, are presented in Figure 10.



Worm		
Number of threads	z_1	2
Thread direction		right
Module	m	4
Pitch diameter	d_{v1}	36
Pressure angle	α_n	20°
Axial pitch	p_x	12.566
Lead	P	25.132
Lead angle	γ_{m1}	12.529°
Tooth thickness	s_{m1}	6.134
Addendum	h_s	4
Center distance	a	90
Profile type		ZN
Number of teeth - worm wheel		36
Pitch diameter	d_{v2}	144

Worm wheel		
Number of teeth	z_2	36
Thread direction		right
Module	m	4
Pitch diameter	d_{v2}	144
Reference diameter	d_{r2}	144
Profile shift	$x_2 \cdot m$	0
Pitch	p_2	25.132
Worm profile type		ZN
Number of threads	z_1	2
Pitch diameter	d_{v1}	36
Center distance	a	90

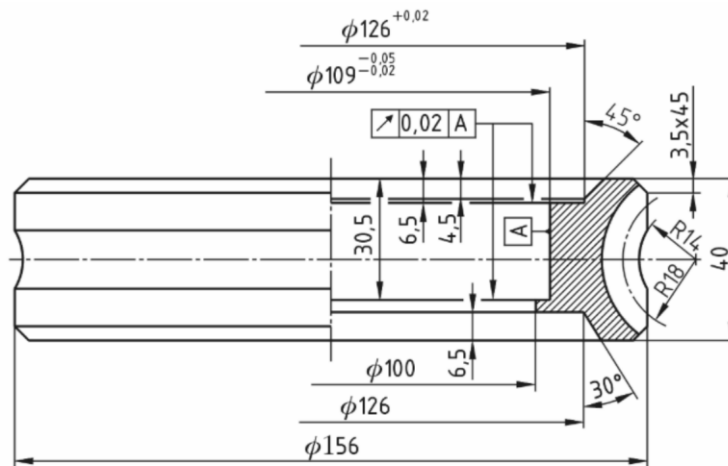


Figure 10. Worm pair - technical drawings [25]

2.3 Materials

In worm pairs, it is a known practice to pair ‘hard’ and ‘soft’ material, i.e., a hardened steel worm and a bronze wheel. This pair is characterized by a low coefficient of friction and resistance to scuffing due to low metallic compatibility [2,3,56]. Since bronze has considerably lower mechanical properties than steel, most damage and failure, mainly sliding wear and pitting, occur on the worm wheel. This section will provide a detailed description of worm and worm wheel materials used in experimental procedures conducted in this research.

2.3.1 Worm material

The worm is made from surface-hardened (case-carburized) 16MnCr5 steel. The surface was finely ground to achieve low surface roughness. This particular steel is often used as a standard reference worm material [3,4]. The chemical composition of 16MnCr5 steel is given in Table 2 while mechanical properties are presented in Table 3.

Table 2. Chemical composition of 16MnCr5 steel, wt.%

16MnCr5	C	Si	Mn	P	S	Cr	Ni	Mo	As	Al	Cu
	0.19	0.31	1.11	0.02	0.01	1.01	0.08	0.01	0.03	0.03	0.15

Table 3. Mechanical properties of 16MnCr5 steel

Tensile strength, N/mm ²	800-1100
Yield point, N/mm ²	600
Hardness	HB 207
Case carburizing depth, mm	0.5
Hardness after case carburizing and grinding	HRC 59±2
Tensile strength, N/mm ²	800-1100

2.3.2 Worm wheel material

Worm pairs exhibit dominant sliding contact conditions; therefore, friction has a more important role than in other gear types. To account for such working conditions, which are similar to sliding bearings, an appropriate material combination should be selected. Frequently, softer material such as centrifugally or continuously cast bronze is paired with hardened steel worm. For lower and medium loads, CuSn12/CuSn14 or CuSn12Ni2 bronzes are used, while

aluminum bronzes, e.g., CuAl10Fe5Ni5 bronze, can be employed for higher loads. Also, worm wheels made of cast irons are in use due to good scuffing and wear resistance. Lastly, the use of alternative worm wheel materials such as coated steel [14] or aluminum alloy AlSn6 [53] can be found in the literature. In this research, the focus was on worm wheels made of CuSn12, although experimental tests were also conducted on worm wheels made of AlSn6 and CuAl10Fe5Ni5. The chemical composition of worm wheels obtained through X-ray diffraction analysis (XRD) is given in Table 4. and some mechanical properties [53,57] are presented in Table 5.

Table 4. Chemical composition of worm wheel materials, wt.%

	CuSn12	CuAl10Fe5Ni5	AlSn6
Cu	86.15	80.32	2.25
Sn	12.1	-	6.03
Pb	0.67	-	0.08
Al	-	8.01	86.36
Fe	-	5.74	0.54
Mg	-	-	2.73
Ni	0.4	5.32	1.23
Si	0.005	0.007	0.48
Cr	0.08	0.1	0.09
Co	0.08	-	0.08
Zn	0.36	-	0.04
S	0.14	0.15	-
other	<0.2	<0.4	<0.1

Table 5. Mechanical properties of worm wheel materials

	CuSn12	CuAl10Fe5Ni5	AlSn6
$R_{p0.2}$, N/mm ²	207	371	120
R_m , N/mm ²	330	746	150
E, N/mm ²	88300	122600	100000
A_5 , %	10	17	-
HB	100	202	71
ρ , kg/m ³	8800	7400	2840

Bronzes are the most common and most investigated of all worm wheel materials [6–8,25,26,55,57]. Their properties as worm wheel materials are covered by the relevant standard for worm pair load calculation [3]. On the other hand, aluminum alloy AlSn6 was first used as a bushing material in sliding bearings. Due to good scuffing and wear resistance, it was thoroughly studied by Opalić [53] as a worm wheel material. Antifriction properties of AlSn6 are based on the thin tin film that forms on the surface under the influence of load, temperature, and sliding speed, thus providing self-lubrication characteristics. The AlSn6 material was compared to the CuSn12 bronze through block-on-disc experimental tests (Figure 11). The initial contact pressure was $\sigma_H = 300 \text{ N/mm}^2$. Compared to CuSn12, AlSn6 has a lower coefficient of friction for sliding speeds up to 1.5 m/s while the observed wear was relatively similar. Based on the results, it can be concluded that aluminum alloy AlSn6 is suitable as worm wheel material, especially for lower sliding speeds.

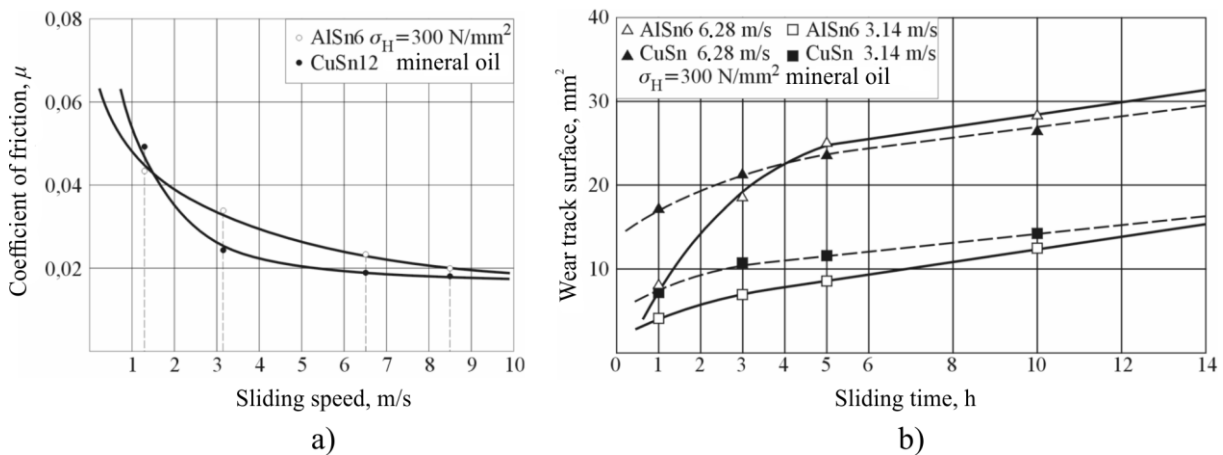


Figure 11. Comparison between AlSn6 vs. CuSn12: a) Comparison of coefficients of friction; b) Comparison of wear track surface [53]

2.4 Lubrication

The influence of proper lubrication is much more significant in worm pairs than in spur, helical, or bevel gears. There are a few reasons for this. A high ratio of sliding-to-rolling velocity paired with unfavorable oil-entraining geometry results in poor film-forming characteristics limiting load and efficiency [31]. Sliding friction in contact zones causes a large amount of frictional heating. When paired with the fact that worm pair gearboxes have a compact design and high power/volume ratio, all generated heat in a smaller assembly size must be addressed by properly and constantly cooling the oil. In order to prevent scuffing, it is necessary to pair metallurgically dissimilar materials. The steel-bronze pair is the most common combination used for that purpose. Additionally, due to the geometry of worm pairs, the gearing

efficiency is considerably lower in worm pairs with high transmission ratios. Although these limitations have been tolerated in the past, in the ever-developing gearing world, power/weight ratio and better thermal and efficiency ratings are key selling points that need to be constantly improved. Proper lubrication is one of the most important factors contributing to better thermal and efficiency ratings. Hence, it is one of the main research areas in worm pairs.

2.4.1 Contact conditions

Worm pair contact is often described as a tribological system that operates in a mixed lubrication regime [2,13,14,58,59]. Mixed or partial lubrication is governed by a mixture of boundary and hydrodynamic regimes acting simultaneously. In other words, the applied load is supported by hydrodynamic (fluid film) lubrication and by occasional asperity contacts. In most cases, this lubrication regime prevents any severe forms of wear. However, sudden lubrication failure, known as scuffing, can occur [60–62]. It is worth noting that if the effects of elastic deformation of the metal surfaces and the increase in the oil viscosity under high pressure are considered, hydrodynamic lubrication is often referred to as elastohydrodynamic lubrication (EHL). The Stribeck curve and corresponding lubrication regimes are shown in Figure 12. A detailed model of the mixed lubrication model is presented in Figure 13.

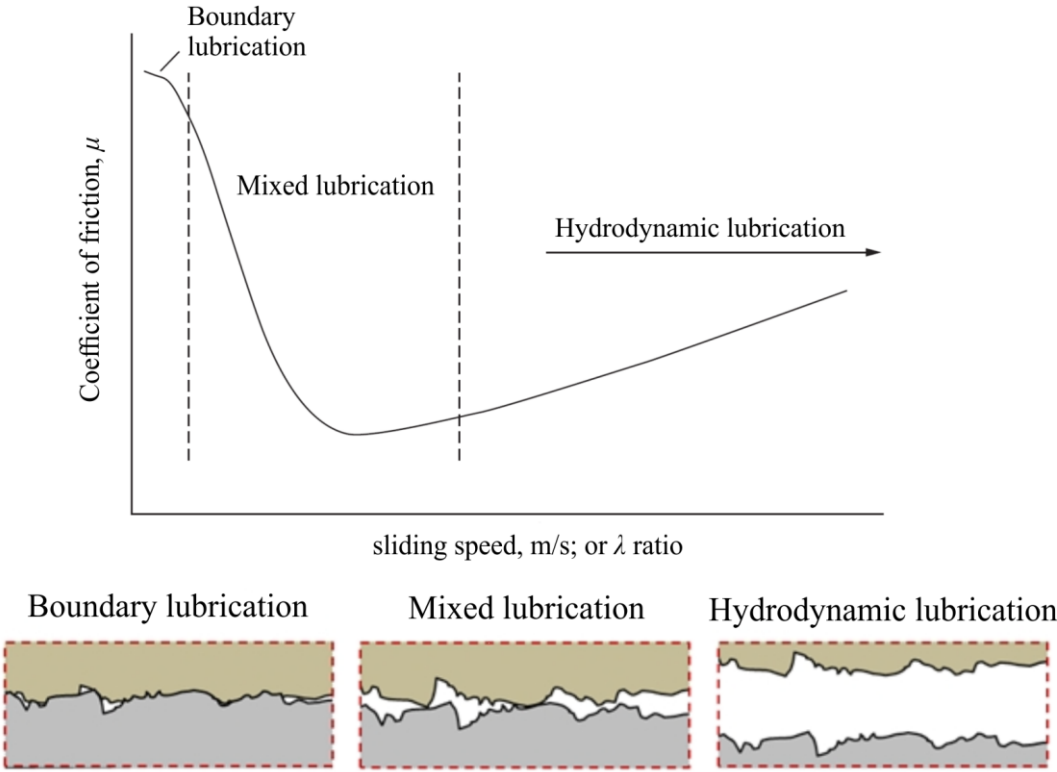


Figure 12. Stribeck curve and lubrication regimes

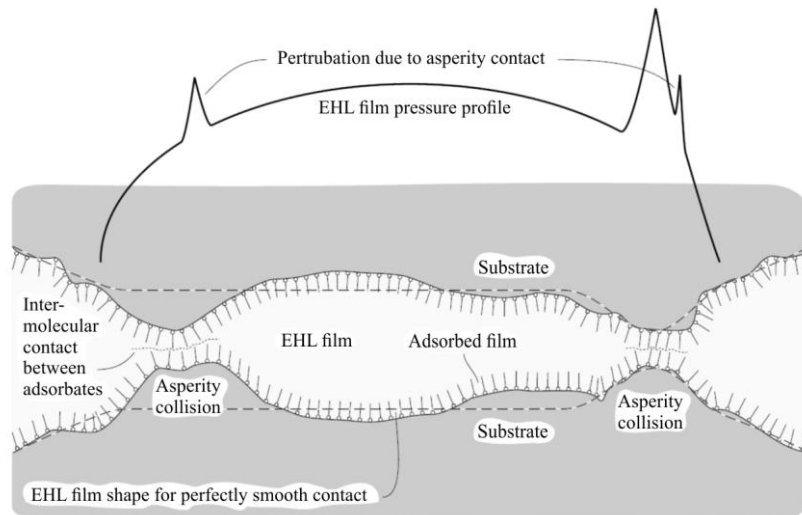


Figure 13. Detailed model of mixed lubrication regime

Another important parameter governing the contact conditions in worm pairs is temperature. Sharif et al. [12,30] and Kong et al. [31] investigated elastohydrodynamic contact properties in worm pairs. Predicted minimum film thickness was of order $0.5 \mu\text{m}$ or less. Additionally, very high shear rates due to prevailing sliding motion are imposed on the lubricant [12]. The main features of the contact are elongated asymmetrical contact shapes, resulting in relatively poor film generation and oil entrainment in a longitudinal direction accompanied by the division of contact into two regions separated by a band of severely thin film. It was also observed that significant solid convection of temperature by the worm wheel tooth into the oil inlet tooth zone takes place which tends to produce a thinning effect usually not common in contact with both surfaces moving in the relatively same direction [30]. An example of calculated film thickness contours and worm wheel tooth surface temperatures is presented in Figure 14.

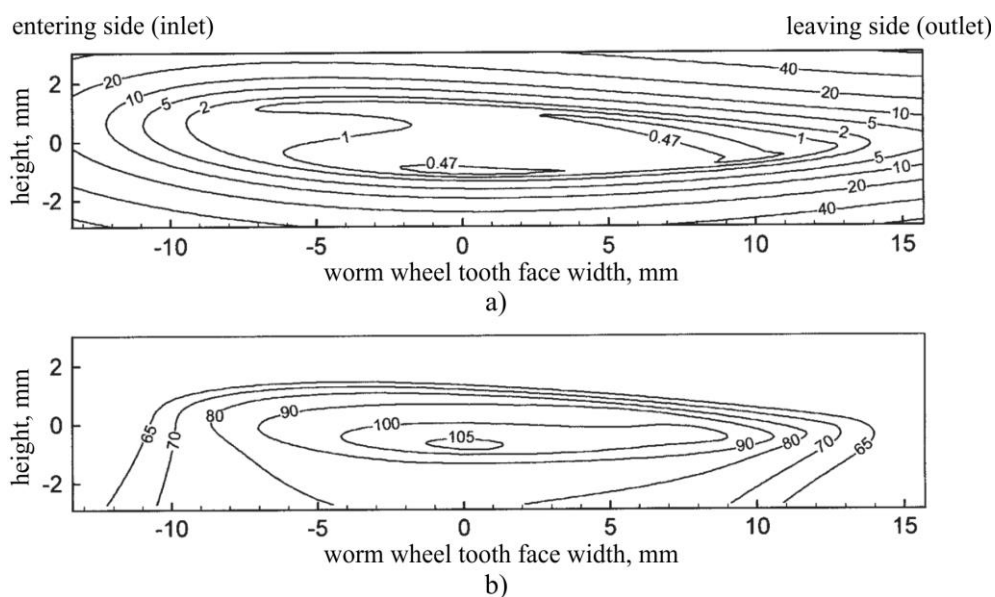


Figure 14. Contact analysis: a) film thickness, μm ; b) wheel tooth surface temperature, $^{\circ}\text{C}$ [12]

2.4.2 Lubricant selection

Worm pairs are lubricated by oils of mineral or synthetic bases. The oil can also have additives that can increase efficiency, lower temperatures through lower coefficient of friction, and reduce worm wheel wear and running-in time. Extreme pressure (EP) additives form inorganic compounds (sulfur, chlorine, or phosphorous compounds) on sliding surfaces. Under high pressures, the chemical reaction occurs at locations of small sliding surface irregularities and prevents micro welding phenomenon. This results in improved lubrication in locations of potential abrasive wear [63]. Some additives, such as ZDDP anti-wear additive (zinc dialkyl dithiophosphate), form protective tribofilms that act as sacrificial layers, reducing wear. Solid lubricant additives, e.g. MoS₂ (molybdenum disulfide) nanoparticles, that improve worm pair running-in process, reduce oil temperature, and increase worm pair efficiency [19].

Gearbox oil must have a reliable viscosity-temperature relationship due to high temperature variations such as inlet vs. contact zone temperature (see Figure 14). Additionally, it is important to reliably account for oil churning losses primarily affected by oil level and viscosity. It is known that high-viscosity oils, if compared at the same temperature, provide better pitting resistance. Viscosity-temperature dependence is usually defined through standards (e.g., ISO VG at 40°C or 100°C).

Several studies were conducted to define the influence of oil on the operational characteristics of worm pairs and gears in general. Höhn and Michaelis [64] investigated the influence of oil temperature on gear failures. High temperatures lead to lower viscosity and thin oil film thickness formation while improving chemical activity and protective tribological layer formation. Also, the results suggest a trend towards lower pitting resistance with increased oil temperature. Muminović et al. [65] compared oils of mineral and synthetic bases. Worm pairs lubricated by synthetic oils provided higher levels of efficiency and less heat, especially at higher sliding speeds. Such findings were explained by increased hydrodynamic lubrication and better adhesion than mineral oil. These differences were less obvious at lower sliding speeds because of deterioration in the hydrodynamic conditions. Rakamarić [54] studied wear rates on worm wheels made of AlSn6, CuSn12, and CuAl10Fe5Ni5 lubricated by mineral and synthetic oils. Higher wear rates were observed for all materials when lubricated with mineral oils. Material AlSn6 was much more wear-resistant than CuSn12 and CuAl10Fe5Ni5 bronzes for all load and oil combinations. Additionally, tribocorrosion can be expected if CuAl10Fe5Ni5 is paired with mineral oils [55]. Mautner et al. [6] studied the efficiency of large worm gearboxes.

Slightly lower efficiencies were recorded with the use of lower-viscosity oils. Moreover, mineral oils led to approximately 3% lower efficiency than synthetic oils.

Many parameters such as material combination, sliding speed, load, temperature, and geometry play an important role in oil selection. Therefore, it is impossible to select the oil optimally for every given case. Usually, the oil is selected either by the oil manufacturer's recommendation or through recommendations given by relevant standards. The recommendations for worm gearboxes based on worm speed and output power are presented in Table 6.

Table 6. Recommendation for oil selection based on oil kinematic viscosity at 100°C [25,53]

P , kW	Worm speed, rpm			
	100-250	250-750	100-250	2000
1-15	17	1-15	17	1-15
15-75	25-40	15-75	25-40	15-75
75	-	75	-	75

The Worm gearbox used in this research is characterized by input worm speed $n_1 = 1480$ rpm and output power $P_2 = 2.5$ kW. The employed lubricant was Castrol Alpha SP 150 mineral oil (Table 7). This lubricating oil is intended for industrial gearboxes with forced circulation, splash, or bath lubrication. The oil is enhanced with EP additives for good thermal and load-carrying stability. The EP additives are compatible with both ferrous and non-ferrous materials. The quality of the employed oil complies with AGMA 9005 - E02 and DIN 51517 Part 3 (CLP).

Table 7. Main properties of the Alpha SP 150 lubrication oil

Density at 15 °C, kg/m ³	Kinematic viscosity, mm ² /s		Viscosity index (-)	Open flash point, °C	Pour point, °C
	40 °C	100 °C			
890	150	14.5	> 95	223	890

Based on a literature review presented earlier, synthetic oils are superior to mineral oils regarding load-carrying capability, wear rates, and efficiency of worm pairs. However, mineral oils are more affordable, widely available and more environmentally sustainable (mineral oils are obtained from refining crude oil). Furthermore, much research on worm pairs in the Laboratory for Machine Elements (Faculty of Engineering and Naval Architecture, University of Zagreb) was conducted using mineral oils as a lubricant [25,53–55]. The latter was an additional reason for employing mineral oil in this research as it allows one to compare the results with previous studies more reliably.

3

Pitting and wear in worm pairs

All machine elements, especially those characterized by heavily loaded contact surfaces found in gears, are subject to various types of damage mechanisms. The damage that occurs can be a consequence of irregular working conditions (insufficient lubrication, system overload, or assembly errors) or, which is more often the case, the damage is an expected feature of that system that is taken into consideration during the design phase. The most common damage mechanisms in worm pairs encountered in service are [2,48,60,62,66]:

- Surface fatigue (pitting): a consequence of repeated surface overloads resulting in shallow craters at contact surfaces,
- Spalling: similar to pitting, subsurface originated large irregularly shaped pits of larger depth
- Scoring: involves the surface welding and formation of grooves and scratches in the direction of sliding and can also imply scratching by abrasive particles
- Scuffing: a serious surface deterioration due to the breakdown of lubrication resulting in metal-to-metal welding, high temperature rise, rapid adhesive wear, and subsequent surface roughening,
- Abrasive wear in the running-in phase and later, in case of lubrication with unfiltered oil (mainly experienced at lower sliding velocities).

- Adhesive wear: metal-to-metal transfer from one surface to another during relative sliding motion. In worm pairs, severe adhesion can result in scuffing if insufficient lubrication is provided to the contact zone.

The presented damage mechanism can be divided into two main categories, fatigue-based wear (pitting and spalling) and sliding wear. The term *adhesive wear* is often used to describe *sliding wear*. However, it is only one of the several physical and chemical processes that may be involved [62]. Therefore, as the scuffing, scoring, and abrasive wear are associated with the overall sliding wear, the term *sliding wear* will be used for the remainder of this thesis. An overview of influence factors on failure modes in worm pairs is shown in Table 8 [3]. Limitations based on output torque T_2 for small center distance worm pairs (applicable to worm pair in this research; $a = 90$ mm) are presented in Figure 15.

Table 8. Failure mode according to influence factors

Influence factors	Failure modes					
	Wear	Pitting	Tooth-breakage	Worm shaft deflection	Scuffing	Low efficiency
Hertzian pressure	x	x	x	x	x	x
Worm speed	x	x			x	x
Oil film thickness	x	x			x	x
Oil	x	x			x	x
Contact pattern	x	x	x		x	x
Worm surface	x	x			x	x
Shearing value			x			

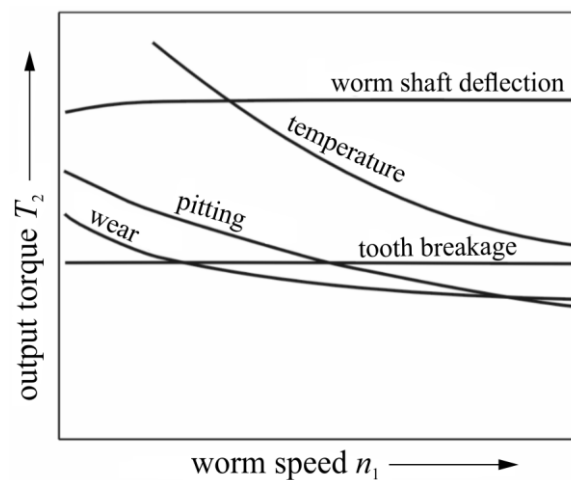


Figure 15. Output torque limitations for small center distances [3]

3.1 Pitting

Pitting is a manifestation of rolling-sliding contact fatigue (RSCF) characterized by shallow surface craters due to prolonged and repeated contact loads that exceed local Hertzian contact fatigue stress limits. Pitting formation on the flanks of worm wheel teeth is a phenomenon that occurs even under proper lubrication conditions, since oil, as incompressible fluid, transmits the load between contacting surfaces. In some cases, pitting appears in the form of micropitting as early as the running-in phase of the worm pair. Pitting initial location and initiation depend on material microstructure, contact stresses, micro and macro geometry, and rolling-sliding conditions. Generally, three processes lead to pitting: crack initiation, propagation, and failure. The crack initiates from surface irregularity, inclusions, inhomogeneities, or other surface and material defects. After the crack initiation, cyclic loading produced by rolling-sliding contact conditions grows and propagates the crack. Finally, crack failure will take place and result in surface damage. The initial crack can be at or below the surface [60,64,66–68]. The surface initial crack results in a pitting phenomenon while the subsurface initial crack yields a spalling phenomenon (Figure 16).

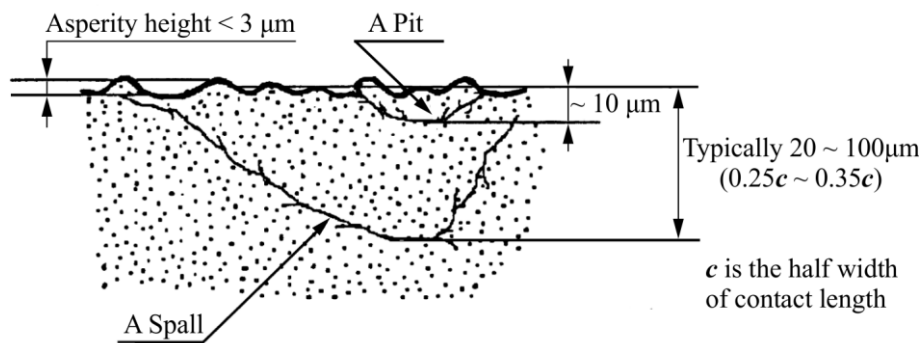


Figure 16. A schematic representation of pitting and spalling, according to [66]

3.1.1 Theoretical basis

Pitting results from the surface-originated crack that forms due to surface irregularities such as surface roughness, machining marks, or surface inclusions. Formed craters are usually of shallow depth ($< 10 \mu\text{m}$). The crack growth is driven by either mode I (tension) propagation or mode II (shear) propagation [66,68–70]. In mode I, the lubricating oil is squeezed between crack surfaces in every loading cycle. Therefore, the hydraulic pressure of the oil opens and closes the crack and gradually extends the crack tip. In mode II, the induced shear (Hertzian) stresses at and near the surface are the main contributors to crack propagation. The crack

initiates at the point of maximum stress and propagates parallel to the surface. Mode II is further emphasized in rolling-sliding contacts, where the sliding component moves the position of maximum shear stress towards the surface, initiating surface crack. This applies to gear contacts and especially to worm pairs due to the high degree of sliding. The shear stress distribution in rolling-sliding contact is shown in Figure 17.

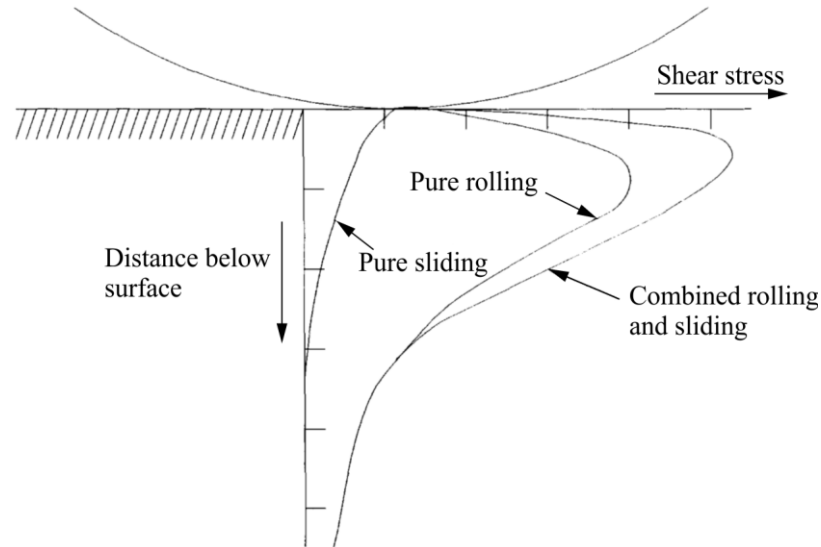


Figure 17. Stress distribution between contacting surfaces under rolling-sliding conditions [68]

As mentioned, pitting is heavily affected by the roughness of the contacting surfaces i.e., metallic asperity contacts through the corresponding oil film thickness. Dawson [71] correlated the surface roughness and oil film thickness in a D ratio, nowadays known as λ ratio, and found that the number of revolutions to pitting decreases when λ increases.

$$\lambda = \frac{\text{minimum oil film thickness}}{\text{composite surface roughness}} = \frac{h_{min}}{\sqrt{R_{q1}^2 + R_{q2}^2}} \quad (1)$$

Spalling (or *macropitting*), on the other hand, is a result of subsurface-originated cracks. The cracks are initiated at the location of maximum shear stress under the surface. At the same time, the growth of the subsurface crack is in mode II parallel to the contacting surface (as already explained in the paragraph above; also see Figure 17). Spalling appears as larger, deeper pits (typically 20-100 μm) at contact surfaces [66]. Spalling may also occur as the continuation of pitting as smaller pits serve as locations of high-stress concentrations. The cracks initiated in this way may propagate into the material and result in the loss of large pieces of metal from the contacting surfaces [68]. A common indicator of expected spalling damage is a distressed surface characterized by a mesh of surface cracks. Surface cracks can also be linked to

subsurface crack propagation onto the surface. The amount of material removed through this process is substantial. If pieces of the metal are carried into the worm pair mesh, it can result in accelerated abrasive wear of the worm wheel tooth flank. The example of surface distress leading to spalling in the CuSn12 worm wheel is presented in Figure 18. It can be observed that surface damage happens abruptly (in terms of a number of load cycles) creating large surface pits that also tend to grow progressively.

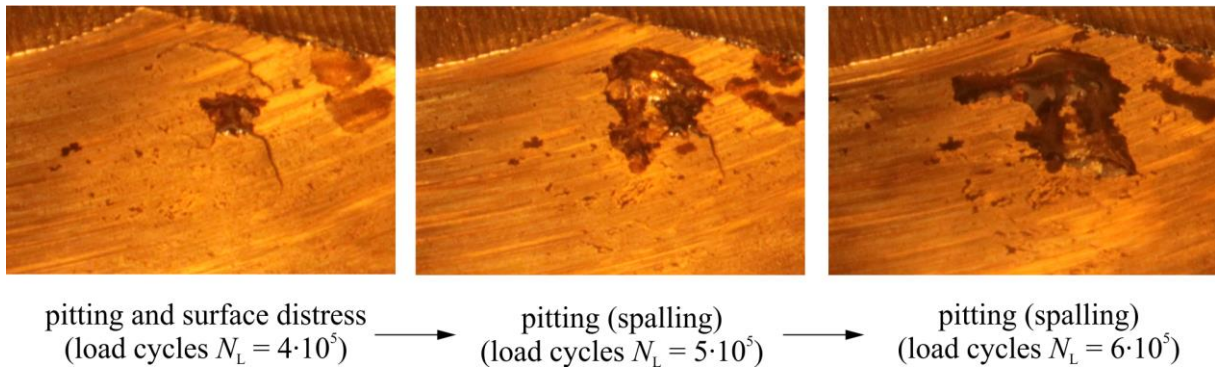


Figure 18. Surface distress leading to spalling in CuSn12 worm wheel

In literature, *micropitting*, *pitting*, and *spalling* have distinguished differences regarding crack initiation and propagation, pit depth, size, and general appearance. Although the literature distinguishes *pitting* from *spalling*, and *pitting* from *micropitting*, the terms are often used interchangeably under the general term *pitting*. The same is true for worm pairs as the literature and standard [3] use the terminology *pitting* or *pitting damage* when considering the surface durability of worm wheel tooth flanks. Therefore, the terminology used for the remainder of this thesis will be as follows:

- *Micropitting* – surface damage due to asperity microcracks resulting in small and shallow pits ($< 10 \mu\text{m}$). It usually occurs during the running-in phase and early phases of the operation in worm pairs when the lubrication regime is not yet fully established due to surface irregularities and a partially developed contact pattern. An example of micropitting developing on the leaving side of the CuSn12 worm wheel tooth flank is presented in Figure 19.
- *Pitting* – damage due to collapse of subsurface cracks resulting in larger and deeper pits (typically $20\text{-}100 \mu\text{m}$). This refers to spalling (macropitting) as described earlier in this section. Pitting can occur as initial pitting during earlier phases of operation and stabilize or diminish due to increased and/or continual wear. In later phases, the pitting phenomenon is expected even in normal operating conditions. If pitting development progresses, it significantly reduces the tooth flank surface, increasing contact stresses.

In turn, this leads to higher wear intensity when the wear capacity limits the life endurance and can lead to failure.

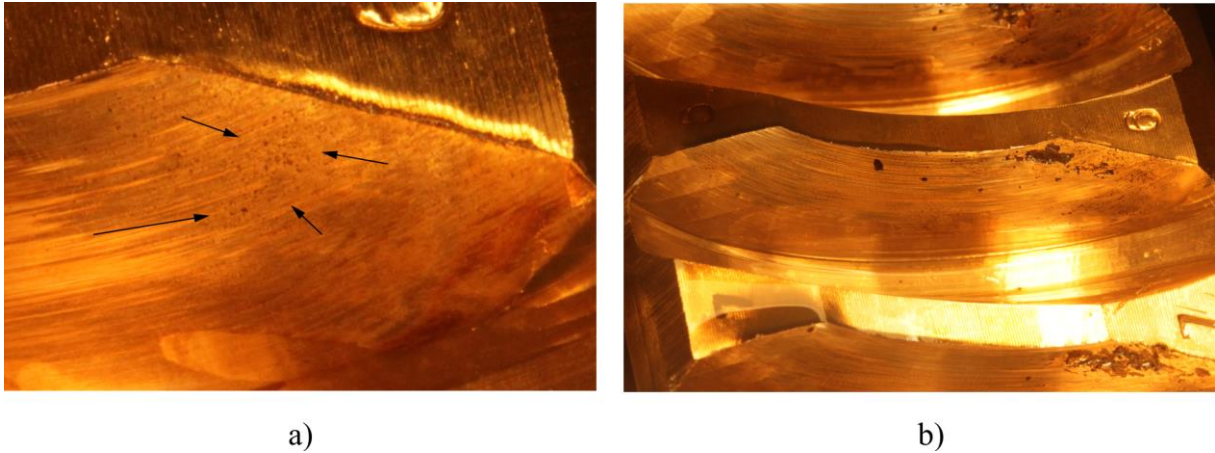


Figure 19. Visual representation of a) Micropitting, b) Pitting

3.1.2 Pitting resistance calculation

In this section, the calculation procedure regarding surface durability (pitting resistance) according to the ISO/TR 14521 standard [3] will be presented and discussed. The current calculation is based on existing literature (experimental tests) and its applicability is defined by the boundary conditions. Boundary conditions defined in standard and boundary conditions applicable to worm pairs in this research are comparatively given in Table 9.

Table 9. Boundary conditions for pitting resistance calculation procedure

	ISO/TR 14521	Worm pairs in this research
Working mode	Constant with running-in	Constant with running-in
Mean contact stress σ_{Hm}	330...620 N/mm ²	≈ 300 N/mm ²
Mean sliding velocity v_{gm}	1...7.5 m/s	3 m/s
Center distance a	65...160 mm	90 mm
Nominal ratio i	10...20	18
Surface roughness R_a	0.4...0.5 μ m	0.25...0.6 μ m
Material combination	16MnCr5 / CuSn12Ni2-C-GZ	16MnCr5 / CuSn12 16MnCr5 / CuAl10Fe5Ni5 16MnCr5 / AlSn6
Lubrication	Polyglycol ISO VG 220 at $T_{oil} = 80$ °C	Mineral oil ISO VG 150 at $T_{oil} = 60$ °C

For worm pairs that are in between these boundary conditions, the calculation procedure should show good results, and for worm pairs that are out of scope, the calculation results should be verified [3]. This indicates that there is no universally accepted or standardized procedure for pitting resistance calculation for all profile types, material combinations, and lubrication oils used in worm pairs. The same is true for worm pairs used in this research as some boundary conditions are the same as in the standard, while others, such as material combinations and oil used, differ significantly.

Firstly, a non-dimensional parameter for the mean Hertzian stress p_m^* and mean contact stress σ_{Hm} are defined as follows:

$$p_m^* = 0.1794 + 0.2389 \cdot \frac{a}{d_{m1}} + 0.0761 \cdot x_2 \cdot |x_2|^{3.18} + 0.0536 \cdot q_1 - 0.00369 \cdot z_2 \quad (2)$$

$$- 0.01136 \cdot \alpha_0 + 44.9814 \cdot \frac{x_2 + 0.005657}{z_2} \cdot \left(\frac{z_1}{q_1}\right)^{2.6872}$$

$$\sigma_{Hm} = \frac{4}{\pi} \left(\frac{p_m^* \cdot T_2 \cdot 10^3 \cdot E_{red}}{a^3} \right)^{0.5} \quad (3)$$

Pitting safety factor S_H is defined as follows:

$$S_H = \frac{\sigma_{HG}}{\sigma_{Hm}} \geq S_{Hmin} \quad (4)$$

- σ_{HG} – limit value for the mean contact stress
- σ_{Hm} – mean contact stress
- $S_{Hmin} = 1.0$ – minimum safety factor

The limiting value for contact stress σ_{HG} is determined based on pitting resistance σ_{HlimT} for a given material (see Table 10) and five empirical factors that define the working conditions:

$$\sigma_{HG} = \sigma_{HlimT} \cdot Z_h \cdot Z_v \cdot Z_s \cdot Z_u \cdot Z_{oil} \quad (5)$$

- $Z_h = (25000/L_h)^{\frac{1}{6}} \leq 1.6$ – life factor
- $Z_v = \sqrt{\frac{5}{4+v_g}}$ – velocity factor where v_g is sliding velocity at mean reference diameter
calculated as $v_g = \frac{d_{m1} \cdot n_1}{19098 \cdot \cos \gamma_{m1}}$
- $Z_s = \sqrt{\frac{3000}{2900+a}}$ – size factor

- $Z_u = \left(\frac{u}{20.5}\right)^{\frac{1}{6}}$ – gear ratio factor
- $Z_{oil} = 0,89$ – lubricant factor for mineral oils

Table 10. Pitting resistance for contact stress (materials used in this research)

Worm wheel material	CuSn12	CuAl10Fe5Ni5	AlSn6
σ_{HlimT} , N/mm ²	425	660 ¹⁾	300*
¹⁾ for low sliding velocities, $v_g < 0.5$ m/s * according to [53]			
NOTE: The given endurance limits for contact stress are valid for pitting areas accounting for approximately 50% of the worm wheel tooth flank			

Table 11. Pitting resistance calculation values and results

Worm material	16MnCr5		
Worm wheel material	CuSn12	CuAl10Fe5Ni5	AlSn6
a , mm	90	90	90
d_{m1} , mm	36	36	36
x_2 , mm	0	0	0
q_1 , mm	9	9	9
z_1 , -	2	2	2
z_2 , -	36	36	36
α_0 , °	20	20	20
p_m^* , -	1.122	1.122	1.122
T_2 , Nm	300	300	200
E_{red} , N/mm ²	139 322	172 787	150 813
v_g , m/s	2.82	2.82	2.82
L_h , hours	5 000	5 000	5 000
Z_h , -	1.308	1.308	1.308
Z_v , -	0.856	0.856	0.856
Z_s , -	1.002	1.002	1.002
Z_u , -	0.979	0.979	0.979
Z_{oil} , -	0.89	0.89	0.89
σ_{HlimT} , N/mm ²	425	660	300
σ_{Hm} , N/mm ²	323	360	275
σ_{HG} , N/mm ²	415	645	293
S_H	1.285	1.791	1.067

The values used for the calculation as well as calculation results (based on expressions (2)-(5)) for worm pairs investigated in this research are given in

Table 11. The value of required life expectancy with continuous operation L_h is arbitrarily set as $L_h = 5\,000$ hours. The purpose was to demonstrate that worm pairs tested in this research have structural integrity far greater than the testing time of approximately 400 hours (corresponding to the number of load cycles $N_L = 2 \cdot 10^6$). The same can be seen from calculated pitting safety factor values S_H . However, it is important to note that practical L_h values used in worm pair calculations are generally $L_h > 20,000$ hours.

The presented results are relevant for already mentioned boundary conditions of the calculation procedure and the assumption/simplification of mean contact stress σ_{Hm} . The standard states that the calculation of contact stresses is not derived from experimental and measurement data (method A) yet it is calculated using numerical methods that are sufficiently precise under corresponding assumptions (method B) and for some factors additional simplified approximation procedures are specified (method C) [3]. In summary, the mean Hertzian stress is calculated assuming equal Hertzian pressure for all simultaneously meshed contact lines. The calculation implies a fully conjugated worm pair which is not true if the worm wheel is manufactured using an oversized hob (see section 2.2). In working practice, the full contact pattern may or may not be achieved due to the possible problem of insufficient lubrication; instead, incomplete but acceptable contact patterns are frequently present (Figure 9). Incomplete contact patterns are therefore subjected to significantly higher contact stresses compared to fully conjugated worm pairs as assumed in this calculation.

It is a known fact that worm pairs can normally operate under heavily pitted worm wheel tooth flanks without significant efficiency loss [6,8,25]. The pitting resistance σ_{HlimT} mentioned in Table 10 is valid for pitting areas accounting for approximately 50% of the worm wheel tooth flank. The given value is relatively high, and the basic calculation does not account for more details in terms of pitting formation and development. However, the annex in the standard considers a lifetime estimation for worm wheels with a high risk of pitting damage in more detail. The lifetime based on the number of load cycles is divided into three characteristic stages:

- Stage I: stage of beginning of pitting, number of load cycles N_{LI}
- Stage II: pitting growth stage, number of load cycles N_{LII}

- Stage III: wear stage, number of load cycles N_{LIII}

The allowed number of load cycles can be combined into a total number of load cycles N_L :

$$N_L = N_{LI} + N_{LII} + N_{LIII} \quad (6)$$

Stage I covers the time up to the development of the first significant pitted areas. This is defined by pitting area $A_{P10} = 2\%$. A_{P10} represents the average pitting area of 10% of most damaged teeth. For example, four teeth will be considered for the A_{P10} value in the case of worm wheel with the number of teeth $z_2 = 36$. In the case of $A_{P10} = 2\%$, the pitted area value must be higher or equal to 2% of the total worm wheel tooth flank surface area. The number of load cycles N_{LI} can be calculated based on the expression:

$$N_{LI} = 10^6 \cdot \left(1 + 0.860 \cdot \ln\left(3 \cdot \frac{v_g}{v_{ref}}\right)\right) \cdot \exp\left[28.078 - 4.666 \cdot \ln\left(520 \cdot \frac{\sigma_{Hm}}{\sigma_{HlimT}}\right)\right] \quad (7)$$

(with $v_{ref} = 3$ m/s, σ_{HlimT} from Table 10, and σ_{Hm} according to expression (3))

Stage II is called the pitting growth stage and stops when the maximum pitting area $A_{P10,max}$ is reached. For allowable pitting area $A_{P10,max} = (2...60 \%)$ the number of load cycles N_{LII} can be calculated by the expression:

$$N_{LII} = \frac{(A_{P10,max} - 2) \cdot 10^6}{16.212 \cdot \frac{(\sigma_{Hm} - 180)}{\sigma_{HlimT}} \cdot \exp\left[1.541 \cdot \frac{\sigma_{Hm}}{\sigma_{HlimT}} - 0.581 \cdot \frac{v_g}{v_{ref}}\right]} \quad (8)$$

The plausibility check must be made:

$$N_{LI} + N_{LII} \leq N_{L(I+II)} \quad (9)$$

where $N_{L(I+II)}$:

$$N_{L(I+II)} = 3 \cdot 10^6 \cdot \frac{v_g}{v_{ref}} \cdot \exp\left[24.924 - 4.047 \cdot \ln\left(520 \cdot \frac{\sigma_{Hm}}{\sigma_{HlimT}}\right)\right] \quad (10)$$

Stage III is characterized by wear behavior. As a large portion of the worm wheel tooth surface is damaged, its load-carrying ability is significantly reduced resulting in increased wear. The number of load cycles N_{LIII} is determined by expression (6). The number of load cycles N_{LIII} is only reached if there is sufficient wear safety. Instead of the wear intensity J_W and flank loss δ_{Wn} (expressions (31) and (32)), the wear intensity J_{WP} and flank loss δ_{WPn} must be used:

$$J_{WP} = W_{ML} \cdot W_{NS} \cdot \left[J_{OI} \cdot \frac{N_{LI}}{N_L} + 0.5 \cdot (J_{OI} + J_{OIII}) \cdot \frac{N_{LII}}{N_L} + J_{OIII} \cdot \frac{N_{LIII}}{N_L} \right] \quad (11)$$

$$J_{OIII} = W_P \cdot J_{OI} \quad (12)$$

$$W_P = 25 \cdot K_W^{0.75} \quad (13)$$

For calculation purposes, pitting area value $A_{P10,max}$ is set at 10%. Such value represents a meaningful increase in pitting percentage from $A_{P10} = 2\%$. It enables enough time, measured in the number of load cycles, to study pitting formation and development in CuSn12 and AlSn6 worm wheels. The worm wheel made of CuAl10Fe5Ni5 is investigated for comparison in terms of efficiency only, as its mechanical properties are significantly higher than those of CuSn12 and AlSn6. For investigated worm wheels, the calculated number of cycles N_{LI} , N_{LII} , and N_{LIII} are given in Table 12. The number of load cycles for CuAl10Fe5Ni5 needed to achieve $A_{P10} = 10\%$ does not pass the plausibility check as this material is not intended to work under high sliding speeds due to intensive wear (recommended $v_g < 0.5$ m/s; the calculation was conducted with $v_g < 2.82$ m/s).

Table 12. Number of load cycles N_L needed for pitting formation, according to ISO/TS 14521 [3]

Worm wheel material	CuSn12	AlSn6	CuAl10Fe5Ni5
T_2 , Nm	300	200	300
N_{LI} ($A_{P10} = 2\%$)	2 260 479	942 753	10 625 790
N_{LII} ($A_{P10,max} = 10\%$)	784 990	655 178	11 973 717
$N_{LI} + N_{LII}$	3 045 469	1 597 931	22 599 507
$N_{L(I+II)}$	5 824 875	2 728 158	22 298 586

3.1.3 Relevant pitting resistance calculation studies in literature

Besides the calculation in the ISO/TS 14521 standard, several studies were focused on relating the pitting formation with the number of load cycles. Due to the nature of pitting formation, experimental tests are inevitably long and there is a tendency to reduce the number of factors, especially those considered irrelevant for pitting. The idea is to control certain factors such as keeping the oil and gearbox temperature constant through the cooling system, oil filtration to reduce abrasive wear, or conducting proper running-in of the worm pair. Additionally, multiple damage mechanisms occur simultaneously, for instance sliding wear and pitting. However, even with the effort to reduce the influence of certain factors, it is impossible to completely ignore the mutual influence of one damage mechanism on another.

Opalić [53] investigated pitting and sliding wear in worm wheels made of AlSn6. The worm pair's geometry and tooth flank profile (ZN) were identical as in this research. The experimental tests were carried out up to $N_L = 7.5 \cdot 10^6$ cycles, the output torque was in the range $T_2 = 150 \dots 310$ Nm, and worm pairs were lubricated with mineral oil at $T_{oil} = 60$ °C. Based on the experimental results, the number of load cycles N_L related to the pitting area A_p in %/100 and the number of cycles required for the first pitting N_{LI}^* was proposed:

$$N_L \approx \frac{12.5 \cdot 10^{14} \cdot A_p^{1.5}}{T_2^3} + N_{LI}^* \quad (14)$$

Table 13. Number of cycles required for first pitting, according to [53]

T_2 , Nm	150	180	260	310
N_{LI}^*	$6.5 \cdot 10^5$	$5 \cdot 10^5$	$3.7 \cdot 10^5$	$3 \cdot 10^5$

Žeželj [25] focused on the influence of measurement of pitting areas and the empirical correlation between pitting, load, and number of load cycles. The research was conducted on worm wheels made of CuSn12 and AlSn6 subjected to $N_L = 5 \cdot 10^6$ cycles lubricated with mineral oil at $T_{oil} = 60$ °C. The identical tooth flank profile ZN and similar worm pair geometry were employed as in [53] and this research. The number of load cycles N_L in relation to pitting area A_p in %/100, and the number of cycles required for first pitting N_{LI}^* for AlSn6 and CuSn12 worm wheels were formulated:

$$N_L \approx \frac{8.57 \cdot 10^{13} \cdot A_p^{1.5}}{T_2^3} + N_{LI}^* \quad (15)$$

– valid for AlSn6 with $N_{LI}^* = 5.3 \cdot 10^5$ cycles

$$N_L \approx \frac{7.18 \cdot 10^{14} \cdot A_p^{1.5}}{T_2^3} + N_{LI}^* \quad (16)$$

– valid for CuSn12 with $N_{LI}^* = 7.26 \cdot 10^5$ cycles

Stahl et al. [26] experimentally and theoretically analyzed worm pairs of different sizes, contact patterns, and flank types (ZI, ZC). The findings suggested that pitting occurs at the minimum equivalent radius of curvature where contact Hertzian stresses are the highest. These locations are found on the leaving side of the worm wheel tooth flank. The tests were conducted on CuSn12Ni2 worm wheels lubricated with synthetic oil (Polyglycol). The relation between number of cycles required for first pitting N_{LI} and mean Hertzian stress σ_{Hm} was described with the expression:

$$N_{LI} = \left(\frac{2650}{\sigma_{Hm}}\right)^{7.8} - \text{valid for } \sigma_{Hm} \leq 500 \text{ N/mm}^2 \quad (17)$$

Although the expression (17) does not apply to worm pairs in this research (different worm wheel material, geometry, and lubrication oil), the expressions derived from studies of Opalić [53] and Žeželj [25] can serve as orientation values in combination with the values already obtained from the ISO/TS 14521 standard [3]. The comparison of the number of load cycles N_{LI} and $N_{L(I+II)}$ (equivalent to the number of cycles N_L for $A_P = 10\%$) is presented in Table 14.

Table 14. Comparison of the number of load cycles according to [3,25,53]

Worm wheel material	CuSn12	AlSn6
Output torque T_2 , Nm	300	200
According to ISO/TS 14521 [3]		
$N_{LI} (A_{P10} = 2\%)$	2 260 479	942 753
$N_{LII} (A_{P10,max} = 10\%)$	784 990	655 178
$N_L = N_{LI} + N_{LII} (A_{P10,max} = 10\%)$	3 045 469	1 597 931
According to Opalić [53]		
$N_L (A_P = 2\%)$	-	909 442
$N_L (A_P = 10\%)$	-	5 408 558
According to Žeželj [25]		
$N_L (A_P = 2\%)$	801 215	560 300
$N_L (A_P = 10\%)$	1 566 932	868 759
Percentage change compared to ISO/TS 14521 [3]		
Opalić [53]		
$N_{LI} (A_{P10} = 2\%)$ vs. $N_L (A_P = 2\%)$	-	- 3.5 %
$N_L (A_{P10,max} = 10\%)$ vs. $N_L (A_P = 10\%)$	-	+ 238.5 %
Žeželj [25]		
$N_{LI} (A_{P10} = 2\%)$ vs. $N_L (A_P = 2\%)$	- 64.6 %	- 40.6 %
$N_L (A_{P10,max} = 10\%)$ vs. $N_L (A_P = 10\%)$	- 48.5 %	- 45.6 %
NOTE: the value of $N_{LI}^* = 467\,500$ for the AlSn6 worm wheel was linearly interpolated for $T_2 = 200$ Nm according to values in Table 13.		

It must be noted that a comparison in Table 14 is conducted between values that are to some extent different: A_{P10} represents the average pitting area of the 10 % of most damaged flanks while A_P represents the average pitting area of all measured flanks. Compared to the ISO/TS

14521 standard, Opalić [53] slightly underestimates the number of load cycles for the AlSn6 worm wheel for $A_P = 2\%$ by 3.5% and overestimates the number of load cycles for $A_P = 10\%$ by + 238.5%. On the other hand, Žeželj [25] estimated the required number of load cycles for $A_P = 2\%$ and $A_P = 10\%$ to be lower by 40.6% and 45.6% compared to the ISO/TS 14521 [3], respectively. For the CuSn12 worm wheel, Žeželj [25] underestimates the required number of load cycles for $A_P = 2\%$ and $A_P = 10\%$ by 64.6% and 48.5%, respectively. The comparison of the number of load cycles N_L suggests no fair agreement between the ISO/TS 14521 standard and available literature. The main causes for such discrepancy in results is due to restrictive boundary conditions for which the pitting calculation procedure is validated in the ISO/TS 14521 standard (see Table 9). Also, there is a difference in representations of pitted area, either average pitted area, A_P , or the average pitting area of the 10% of most damaged teeth, A_{P10} . As available results in the literature are scarce and not in good agreement, the conclusion arises that further investigations regarding worm wheel pitting should be conducted to provide values for different material/lubrication/load combinations.

3.2 Sliding Wear

In addition to pitting, sliding wear is one of the main damage mechanisms occurring in worm pairs. The damage usually appears on bronze worm wheel's tooth flanks. Sliding wear in worm pairs takes place in two main forms: abrasive wear and adhesive wear. In this chapter, the abrasive and adhesive wear will be covered in more detail, and wear load capacity calculation according to the ISO 14521 standard will be presented.

3.2.1 Abrasive wear

Abrasive wear is the removal of material by the passage of hard particles over a surface. It occurs whenever a solid object is loaded against particles of a material with equal or greater hardness [60]. In the case of worm pairs, the harder part is the case-hardened steel worm, while the softer component is usually the bronze worm wheel. Mechanisms of abrasive wear are depicted in Figure 20.

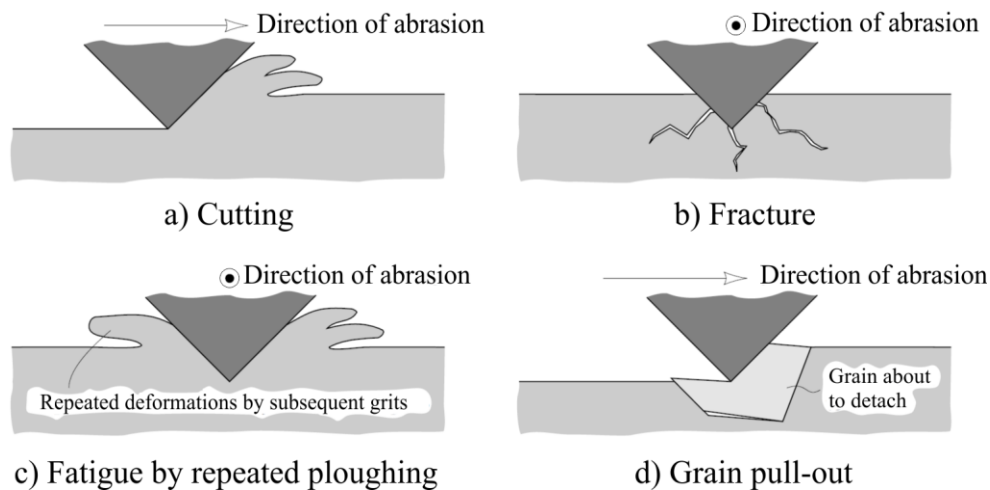


Figure 20. Mechanisms of abrasive wear [60]

The literature recognizes two basic modes of abrasive wear: two-body and three-body abrasive wear. In two-body mode, the hard asperities or grits pass over the surface like a cutting tool. In three-body mode, the grits are free to roll in between the surfaces since they are not held rigidly [60]. In worm pairs, the example of two-body abrasive wear would be a hardened steel worm passing over a bronze worm wheel, while three-body abrasive wear would manifest itself in abrasive particles, namely already detached bronze particles, found in unfiltered oil therefore constantly wearing the bronze surfaces through lubrication. Notably, the repeated strain caused by grits deforming the contact area on the surface can also cause material fatigue. This indicates that abrasive wear and pitting can have a strong mutual influence and often act simultaneously. The example of abrasive wear on the worm wheel tooth flank due to increased system vibrations can be seen in Figure 21.

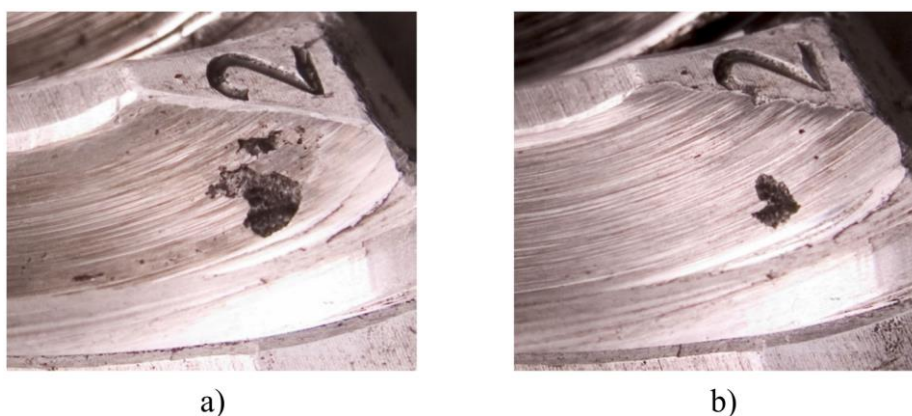


Figure 21. Worm wheel abrasion: a) before, b) after $N_L = 4.9 \cdot 10^4$ [25]

The wear process can generally be divided into three characteristic periods (see Figure 22):

- The *running-in* period at the start of the operation of two surfaces in relative sliding motion. It is characterized by smoothing of surface asperities, achieving better conformity of contacting surfaces, and increasing efficiency before reaching steady-state operation [72,73]. The absence of running-in results in local contact loads many times higher than expected. Therefore, running-in is carried out under lighter loads as higher contact pressures can result in premature damage [74]. Mallipeddi et al. [73] showed that higher running-in loads result in more micropitting. When one of the contacting surfaces is comparatively hard and the lubrication conditions prevent metallic transfer during running-in, wear will be principally confined to the softer surface [72]. Worm pairs are the prime example of machine elements heavily influenced by proper running-in. During the running-in period, the goal is to achieve an acceptable contact pattern on worm wheel tooth flanks to distribute the load evenly and smoothen the contacting surfaces. This process is also accompanied by gradually lower coefficient of friction resulting in increase in the worm pair efficiency.
- *Steady-state wear* period onsets when the system attains the constant wear rate until it reaches the severe wear state leading to component failure. The conditions of steady-state wear are strongly affected by the running-in process. The coefficient of friction in the steady-state is constant. This period typically represents most of the component's life expectancy.
- *Severe wear* period distinguished by rapid wear rate, lubricant breakdown, and abrupt failure. The amount of wear becomes unacceptable since the worn-out surfaces produce large clearances leading to increased system vibrations. During design phase, the goal is to predict and avoid this period.

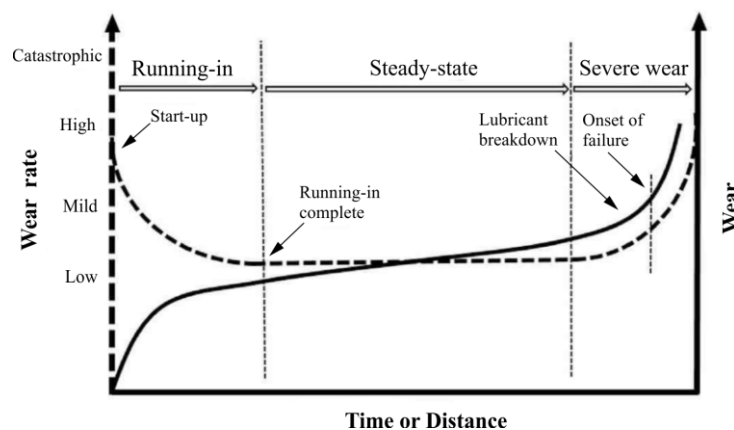


Figure 22. Schematic representation of the characteristic wear periods, according to [74]

3.2.2 Adhesive wear

Due to solid-phase welding, adhesive wear is characterized by metal-to-metal transfer from one surface to the other during relative sliding motion [63]. Generally, the same or similar metals tend to adhere at the contact. The practice is to pair different metals as a contacting pair to mitigate the adhesion, especially ones with low metallic compatibility. Moreover, adhesion is reduced when sufficient lubricant film thickness is present to eliminate direct metal-to-metal contact. Adhesion is also reduced with increasing surface roughness or hardness of the contacting bodies [60]. In worm pairs, this is achieved by a combination of hardened steel worm and bronze worm wheel. This material pair is characterized by very low metallic compatibility, low coefficient of friction, and particular resistance to scuffing [2]. The result of adhesive wear is a removed metal particle that remains either “glued” to one of the contacting surfaces or eventually leaves the contact zone through oil flow, thus acting as an abrasive particle if the oil is unfiltered. A simple schematic of the adhesion process is presented in Figure 23.

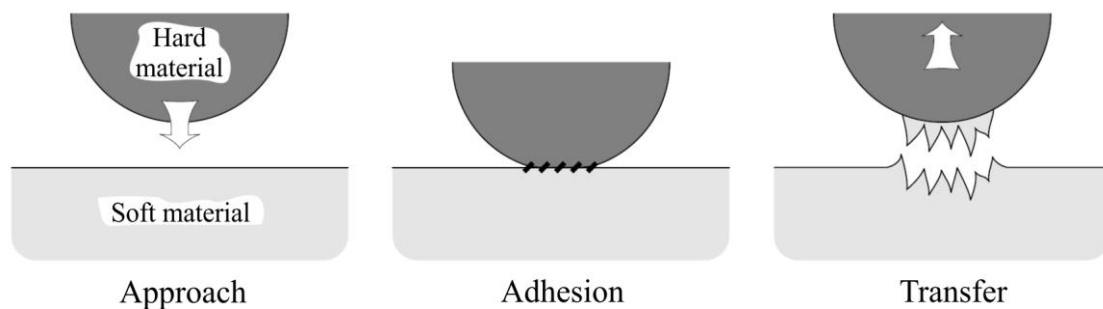


Figure 23. Process of adhesive wear, according to [60]

The most severe form of adhesive wear is scuffing. Scuffing usually occurs when there is a breakdown of lubrication. The temperature in the contact zone rises significantly accompanied by a high coefficient of friction. Contact zone overheats and rapid adhesion and adhesive wear occur, leading to sudden failure. Gears are very susceptible to scuffing, worm pairs in particular. Due to dominant sliding motion and unfavorable geometry, the shear stresses and rise in oil temperature in the middle of the worm wheel tooth flank result in oil film thinning. Oil film thinning is a precondition for lubrication breakdown (see Figure 14). The addition of EP additives in the oil can prevent the onset of scuffing. The signs of scuffing on the worm wheel can be observed in a significant amount of material removed (clearly visible at the lower portion of the worm wheel tooth flank, Figure 24), darkened oil due to exposure to high temperatures, and a large number of bronze particles visible in oil.



Figure 24. First signs of scuffing on the bronze worm wheel

3.2.3 Wear load capacity calculation

The calculation in ISO 14521 [3] is based on permissible wear that is set following several criteria:

- a) The thickness in the normal section on the outside diameter of the wheel teeth must not become pointed

$$\delta_{Wlim\ n} = m_{x1} \cdot \cos \gamma_{m1} \cdot \left(\frac{\pi}{2} - 2 \cdot \tan \alpha_0 \right) \quad (18)$$

- b) Allowable tooth thickness loss Δs_{lim} is defined through tooth breakage safety factor S_{Fmin} .

$$\delta_{Wlim\ n} = \Delta s_{lim} \cdot \cos \gamma_{m1} \quad (19)$$

- c) The material loss Δm_{lim} should not exceed a pre-set limit dependent on oil change intervals and bearing lubrication. This criterion is based on the approximate tooth flank surface A_{fl} .

$$\delta_{Wlim\ n} = \frac{\Delta m_{lim}}{A_{fl} \cdot \rho_{Rad}} \quad (20)$$

$$A_{fl} \approx \frac{z_2 \cdot 2m_{x1} \cdot d_{m1} \cdot \arcsin \left(\frac{b_{2H}}{d_{a1}} \right)}{\cos \gamma_{m1} \cdot \cos \alpha_0} \quad (21)$$

d) The wheel tooth flank loss reaches a pre-set value indicated by the backlash. Frequently

$\delta_{Wlim} = 0.3 \cdot m_{x1}$ is applied. In the normal section, the expression becomes:

$$\delta_{Wlim n} = 0.3 \cdot m_{x1} \cdot \cos \gamma_{m1} \quad (22)$$

The safety against wear S_W is defined as follows:

$$S_W = \frac{\delta_{Wlim n}}{\delta_{Wn}} \geq S_{Wmin} \quad (23)$$

- $\delta_{Wlim n}$ – limiting value of worm wheel tooth flank loss in the normal section
- δ_{Wn} – worm wheel tooth flank loss through abrasive wear in the normal section
- $S_{Wmin} = 1.1$ – minimum safety factor

Firstly, the minimum mean lubricant thickness $h_{min m}$ and corresponding non-dimensional parameter for the mean lubricant film thickness h^* are calculated:

$$h_{min m} = 21 \cdot h^* \cdot \frac{c_\alpha^{0.6} \cdot \eta_{0M}^{0.7} \cdot n_1^{0.7} \cdot a^{1.39} \cdot E_{red}^{0.03}}{T_2^{0.13}} \quad (24)$$

$$c_\alpha = 1.7 \cdot 10^{-8} \text{ m}^2/\text{N} \text{ – for mineral oils} \quad (25)$$

$$\eta_{0M} = 0.04815 \text{ Ns/m}^2 \text{ – for } \theta_M = 70 \text{ }^\circ\text{C}, \rho_{oilM} = 0.857 \text{ kg/dm}^3, \nu_M = 56.18 \text{ mm}^2/\text{s} \quad (26)$$

$$h^* = -0.393 + 2.9157 \cdot 10^{-6} \cdot (z_2)^{-0.0847} \cdot \alpha_0^{0.0595} \cdot (7.947 \cdot 10^{-7} \cdot x_2 + 5.927 \cdot 10^{-5}) \cdot ((1 - 0.038 \cdot q_1) \cdot q_1 + 65.576) \cdot \left(\left(108.8547 \cdot \frac{z_1}{q_1} - 1 \right) \cdot \frac{z_1}{q_1} - 3294.921 \right) \cdot ((3.291 \cdot 10^{-3} \cdot B + 1) \cdot B - 13064.58) \quad (27)$$

$$\text{– with } B = \sqrt{6 \cdot m_{x1} \cdot d_{m1} - 9 \cdot (m_{x1})^2} + m_{x1}$$

Then, the wear path s_{Wm} is calculated from the number of stress cycles N_L and parameter for the mean sliding path s^* :

$$s_{Wm} = s^* \cdot \frac{\sigma_{Hm} \cdot a}{E_{red}} \cdot N_L \quad (28)$$

$$N_L = L_h \cdot \frac{n_1 \cdot 60}{u} \quad (29)$$

$$s^* = 0.78 + 0.21 \cdot u + \frac{5.6}{\tan \gamma_{m1}} \quad (30)$$

Lastly, flank loss due to wear δ_{Wn} based on wear intensity J_W is derived:

$$\delta_{Wn} = J_W \cdot s_{Wm} \quad (31)$$

$$J_W = J_{OT} \cdot W_{ML} \cdot W_{NS} \quad (32)$$

The reference wear intensity J_{OT} in expression (32) is derived from available equations based on the worm wheel material and the type of lubrication oil used. For worm wheels used in this study, J_{OT} can be calculated for CuSn12 and CuAl10Fe5Ni5 worm wheel materials:

$$J_{OT} = 2.4 \cdot 10^{-11} \cdot K_W^{-3.1} \leq 400 \cdot 10^{-9} \quad (33)$$

– valid for bronze wheels (e.g., CuSn12) lubricated with mineral oil

$$J_{OT} = 5.45 \cdot 10^{-9} \cdot K_W^{-1.23} \leq 400 \cdot 10^{-9} \quad (34)$$

– valid for aluminum bronze wheels (e.g., CuAl10Fe5Ni5) lubricated with mineral oil

The lubricant film thickness parameter K_W used in expressions (33) and (34) is calculated using lubricant structure factor $W_S = 1$ (for mineral oils) and pressure factor $W_H = 1$ (for bronze materials for $\sigma_{Hm} < 450 \text{ N/mm}^2$):

$$K_W = h_{\min m} \cdot W_S \cdot W_H \quad (35)$$

The value of material/lubricant factor W_{ML} is only available for three types of oil and a small number of materials. In the case of mineral oil and material combination 16MnCr5/CuSn12, $W_{ML} = 1.6$, while for combination 16MnCr5/CuAl10Fe5Ni5 $W_{ML} = 1.0$.

The start factor W_{NS} considers the influence of the number of starts per hour, N_S , on the wear rate:

$$W_{NS} = 1 + 0.015 \cdot N_S \quad (36)$$

Ultimately, the flank loss due to wear δ_{Wn} is compared to δ_{Wlim} values based on criteria a) - d) with minimum safety factor $S_{Wmin} = 1.1$.

The values used for the wear load capacity calculation for worm pairs investigated in this research are given in Table 15.

Table 15. Wear load capacity calculation values and results

Worm material	16MnCr5	
Worm wheel material	CuSn12	CuAl10Fe5Ni5
a , mm	90	90
d_{m1} , mm	36	36
x_2 , mm	0	0
q_1 , mm	9	9
z_1 , -	2	2
z_2 , -	36	36
u	18	18
α_0 , °	20	20
n_1 , min ⁻¹	1460	1460
T_2 , Nm	300	300
E_{red} , N/mm ²	139 322	172 787
c_α , m ² /N	$1.7 \cdot 10^{-8}$	$1.7 \cdot 10^{-8}$
η_{0M} , Ns/m ²	0.04815	0.04815
B , -	26.907	26.907
h^* , -	0.074	0.074
$h_{min m}$, μm	0.235	0.237
L_h , hours	5 000	5 000
N_L , -	24 333 333	24 333 333
σ_{Hm} , N/mm ²	323	360
s^* , -	29.760	29.760
s_{Wm} , mm	151 098 397	135 790 214
W_S , -	1	1
W_H , -	1	1
K_W , -	0.235	0.237
J_{OT} , -	$2.137 \cdot 10^{-9}$	$3.202 \cdot 10^{-8}$
W_{ML} , -	1.6	1
N_S , -	0.1	0.1
W_{NS} , -	1.0015	1.0015
J_W , -	$3.426 \cdot 10^{-9}$	$3.207 \cdot 10^{-8}$
δ_{Wn} , mm	0.517	4.355
$\delta_{Wlim n}$, mm (criterion d))	1.171	1.171
S_W	2.265	0.269

Based on calculation results, the wear load capacity, for an arbitrary value of $L_h = 5\ 000$ hours is achieved for CuSn12 worm wheels and not for CuAl10Fe5Ni5 worm wheel. The latter worm wheel material is not intended for high sliding speeds. The recommended sliding speed for CuAl10Fe5Ni5 should be $v_g = 0.5$ m/s. The calculation could not be conducted for the AlSn6 worm wheel as no relevant factors are available for that material. Thus, one of the main limitations of wear load capacity calculation becomes evident: it is relevant only for a few material-lubricant combinations. The presented calculation assumes that a full contact pattern is established and that wear calculation is independent of the pitting capacity calculation. This means there is no consideration of any correlation between those two damage mechanisms. This simplifies real working conditions as a full contact pattern may or may not be achieved, as already discussed in Section *Geometry and manufacturing of ZN worm pairs*. Furthermore, pitting development accelerates wear. This is mostly apparent in the wear stage of pitting calculation (Stage III) as the contact surface becomes smaller, increasing the contact stresses on the remainder of the tooth flank surface, resulting in an increased wear rate.

4

Worm pair dimensional accuracy

Gear dimensional accuracy refers to how closely the manufactured geometrical features resemble the theoretical geometry and design. Manufacturing errors in gears typically result in increased contact pressures, amplified noise and vibrations, and problems with inaccurate motion transfer [75]. As with many other machine elements, the dimensional accuracy of gears is defined through allowable deviations divided into accuracy grades. Allowable deviations and advice regarding inspection methods are usually outlined in relevant standards. The same holds for worm pairs which are one of many gear types. The deviations of worm pairs are outlined in the DIN 3974 standard [10,11] and will be covered in detail in this chapter. Also, the 3D optical scanning method used for dimensional inspection of worm pairs will be presented and discussed.

4.1 Deviations

Worm pair deviations are presented in the standard DIN 3974-1 Accuracy of worms and worm gears - Part 1: General bases (in original: *DIN 3974-1 Toleranzen für Schneckengetriebe-Verzahnungen - Teil 1: Grundlagen* [10]) and in the standard DIN 3974-2 Accuracy of worms and worm gears - Part 2: Tolerances for individual errors (in original: *DIN 3974-2 Toleranzen für Schneckengetriebe-Verzahnungen - Teil 2: Toleranzen für Abweichungen einzelner Bestimmungsgrößen* [11]). The outlined deviations are valid for worm pairs with rectangular

crossing shafts, worm wheel pitch diameters up to 2500 mm, and modules up to 40 mm. An overview of worm and worm wheel deviations is presented in Table 16.

Table 16. Worm pair deviations

Deviation	Abbreviations	
	Worm	Wheel
Single pitch deviation (axial)	f_{px}	-
Single pitch deviation	-	f_{p2}
Adjacent pitch difference	f_{ux}	f_{u2}
Total pitch deviation	F_{pz}	-
Total cumulative pitch deviation	-	F_{p2}
Total profile deviation	$F_{\alpha 1}$	$F_{\alpha 2}$
Runout	F_{r1}	F_{r2}
Total single flank composite deviation	$F'_{i 1}$	$F'_{i 2}$

Single pitch deviation (axial) (f_{px})

The axial single pitch deviation is the algebraic difference between the actual pitch and the corresponding theoretical pitch in the axial section of the worm. The deviation is evaluated on the cylinder approximately at the mid-depth of the tooth (typically on the pitch cylinder). In the case of a worm with multiple threads (teeth), the measurement must be carried out in further axial sections until all threads have been recorded (Figure 25).

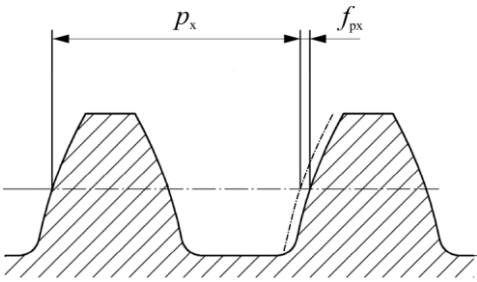


Figure 25. Single pitch deviation (axial)

Single pitch deviation (f_{p2})

The single pitch deviation is the algebraic difference between the actual and corresponding theoretical pitch in the transverse plane on the circle concentric with the worm wheel axis. The deviation is evaluated approximately at the mid-depth of the tooth (typically on pitch diameter).

In the case of a worm with multiple threads, the measurement must be carried out in further axial sections until all threads have been recorded (Figure 26).

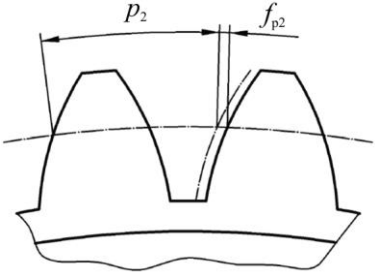


Figure 26. Single pitch deviation

Adjacent pitch difference (f_{ux}, f_{u2})

The adjacent pitch difference is the algebraic difference between the actual dimensions of two successive individual pitches of the right or left flanks. It is specified without a sign. For evaluation purposes, the largest adjacent pitch difference is reported (Figure 27).

Total pitch deviation (F_{pz})

The algebraic difference between the actual and nominal dimension of the worm pitch, measured over the gauge length l .

Total cumulative pitch deviation (F_{p2})

The difference between the algebraically largest and the algebraically smallest value of all corresponding single pitch deviations of the worm wheel (Figure 27).

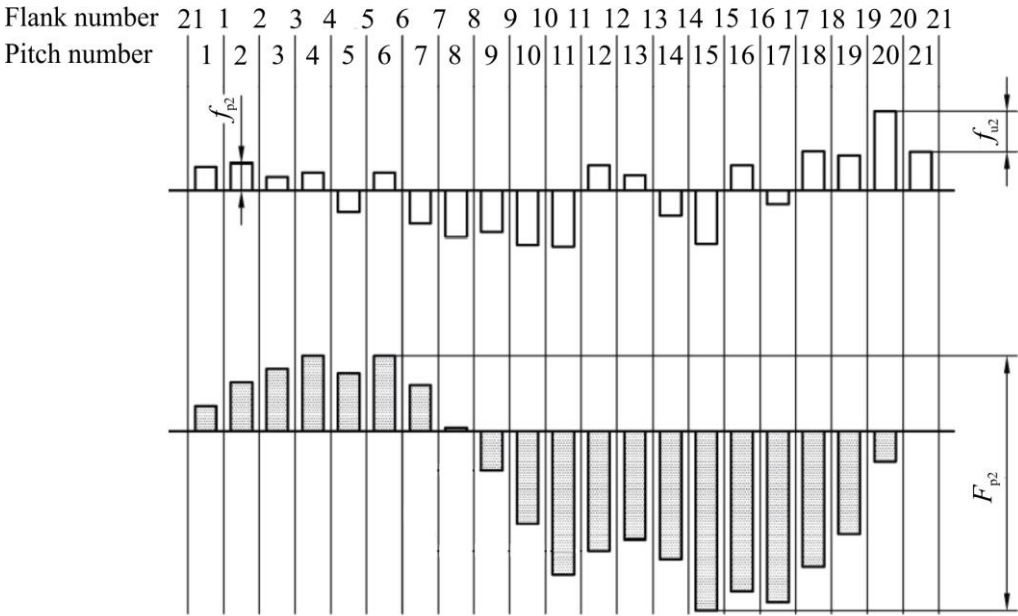


Figure 27. Adjacent pitch difference and total cumulative pitch deviation, according to [76]

Total profile deviation ($F_{\alpha 1}, F_{\alpha 2}$)

Distance between two design profile traces which enclose the actual profile trace over the evaluation range defined by the start of active profile and the end of active profile diameter. The tolerances of the total profile deviation refer to the worm’s axial section and the worm wheel’s center axial plane (Figure 28).

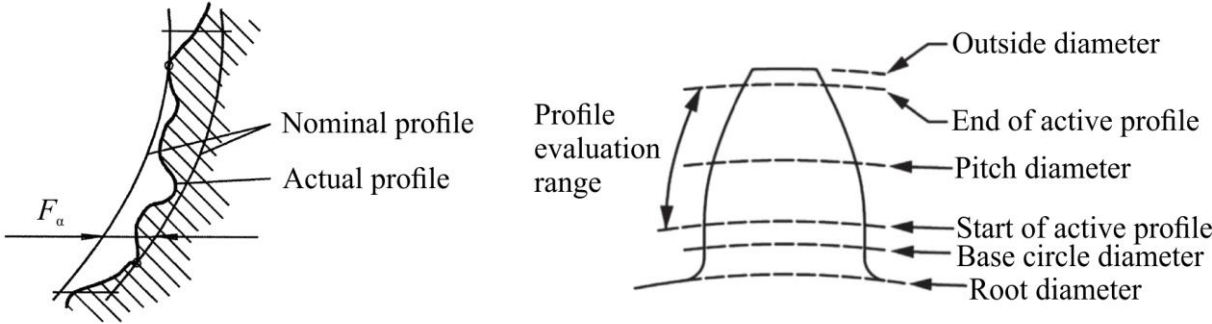


Figure 28. Total profile deviation

Runout (F_{r1}, F_{r2})

The algebraic difference between the maximum and the minimum radial distance from the worm or worm wheel axis, of a probe (e.g., ball or cylinder) which is placed successively in each tooth space. During each check, the probe contacts the right and left flanks at approximately mid-tooth depth. The measurement is conducted in the axial section of the worm and preferably in the center axial plane of the worm wheel.

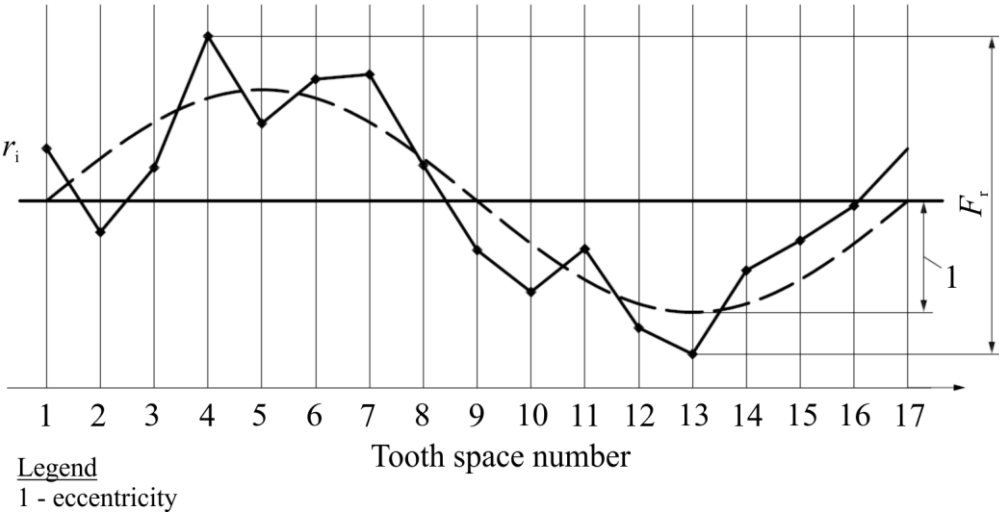


Figure 29. Representation of runout, according to [77]

Total single flank composite deviation (F_i' , F_i'')

The deviation F_i' is the difference between the actual rotational positions of a master (reference) gear and the rotational positions of the gear under inspection, measured at the pitch circle. It is calculated as the difference between the largest leading and the largest remaining rotational position deviation within one revolution of the inspected gear (i.e. transmission error, Figure 30). Both gears are rolled under the prescribed center distance without load. During inspection, contact occurs on only one set of corresponding flanks.

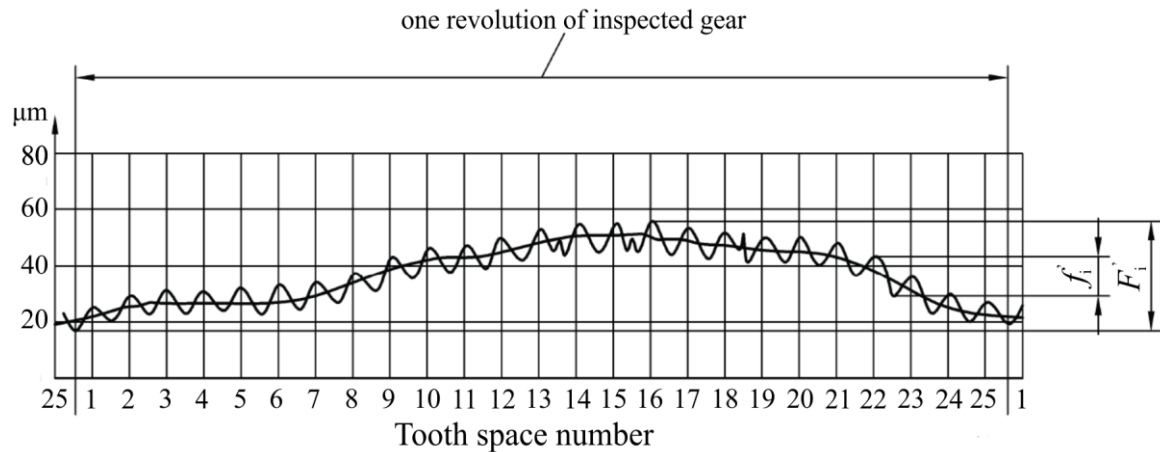


Figure 30. Representation of single flank composite inspection

4.2 Three dimensional (3D) optical scanning

Dimensional inspection of gears is commonly carried out by contact measuring machines such as coordinate measuring machines (CMMs) or gear measuring instruments (GMIs) [78] (Figure 31). CMMs are universal measuring machines that can measure various workpieces. At the same time, GMIs have additional rotary tables and specially designed probing systems for easier and more precise measurements in gears. CMMs and GMIs perform tactile measurements of selected surfaces, and the result of such measurements is usually recorded as measuring points or profiles. However, these devices have reached state-of-the-art, and significant accuracy and measurement speed improvements are hardly expected [78]. Nonetheless, CMMs and GMIs still have the best measurement accuracy and repeatability. They are considered as a referent measurement method for gear quality control.

On the other hand, CMMs and GMIs have certain drawbacks. Data acquisition is time-consuming; therefore, providing three-dimensional (3D) data of the entire geometry is not feasible since every point on the surface should be probed. Additionally, the recorded points

are further postprocessed due to signal delay, inaccuracy of measurement coordinate system and radius of the probe. In the case of gear measurement, the border areas of tooth surfaces (tooth gap) cannot be measured accurately since the probe would touch multiple locations at once [79]. Multiple contact measuring machines or systems are sometimes needed to inspect a gear pair fully according to standards. Lastly, a controlled environment is needed for contact measuring systems to operate properly due to high sensitivity to vibrations and temperature variations.

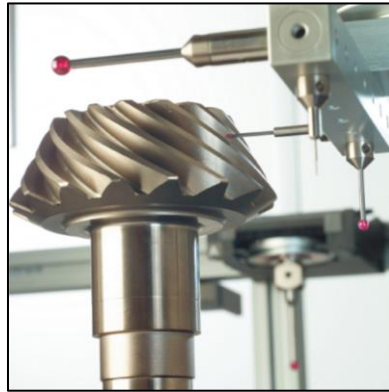


Figure 31. Gear measurement using CMM/GMI [80]

In recent years, non-contact measurement methods capable of fast data acquisition that results in 3D scans of complex workpieces have become an alternative. Such methods include laser incorporated in CMM, computed tomography (CT), and 3D optical scanning. Amongst the mentioned methods, 3D optical scanning provides certain advantages compared to contact measurement methods. These advantages are evident in a high sampling rate, the ability to scan objects made from any material, relatively high measurement accuracy, measuring hard-to-reach spaces and features (e.g., gear tooth gap/flanks), and it is relatively simple to use [1].

3D optical scanning can be based on different optical metrology approaches, such as optical interferometry, stereo vision, time-of-flight (TOF) technique, and structured light. The structured light technique is among the most popular due to its high measurement accuracy, point density, speed, simple hardware configuration, and low cost. In optical metrology, structured light is used in the form of fringe projection patterns with sinusoidal form and is often referred to as fringe projection profilometry (FPP). Firstly, fringe patterns are projected onto the scanned object and then captured from different angles, usually by two cameras. The original fringes would be captured as deformed due to the geometry of the scanned object (i.e. the difference in the height of the measured object) thus encoding the object's depth into the phase of the fringe images. Then, the images are processed by algorithms to obtain phase

distribution which is used to recreate the surface of the scanned object based on the triangulation process to determine the location of a point in space [79,81,82]. A schematic of fringe projection profilometry is presented in Figure 32.

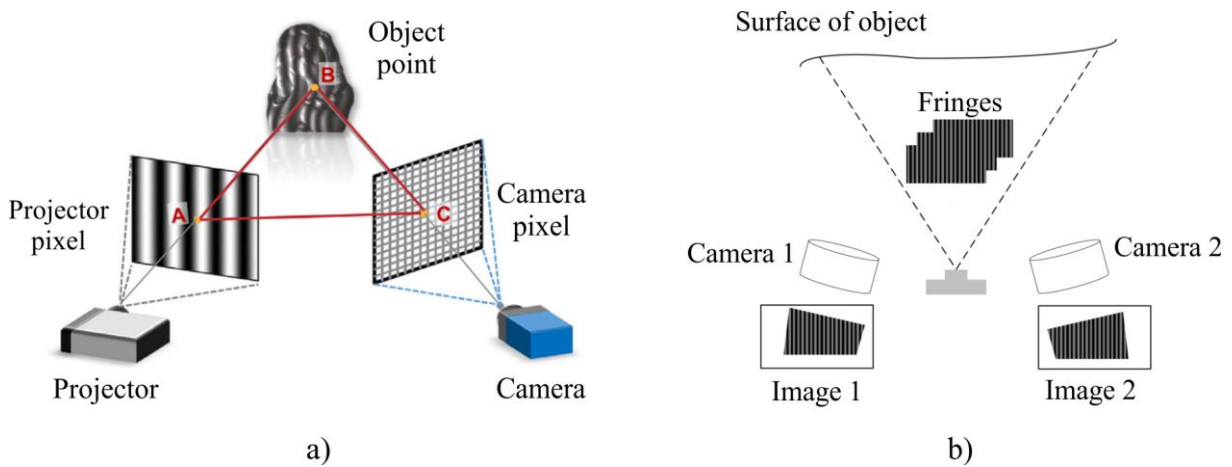


Figure 32. a) Schematic of fringe projection profilometry, according to [82], b) Two camera system, according to [79]

Recent studies have focused on comparing 3D optical scanning to contact measurement methods (mainly CMMs), estimating measurement uncertainty and accuracy, and employing 3D optical scanning in gear inspection.

Matache et al. [83] compared 3D optical scanning and CMM in the dimensional gas turbine inspection. The findings suggested that CMM had slightly higher accuracy with a downside of higher workload and inability to capture whole geometry compared to 3D optical scanning. Gapinski et al. [84] compared CMM, 3D optical scanning, and 3D computed tomography (CT). Based on observed geometry types such as plane flatness and angles, spheres, and holes, CMM and CT performed more precisely when measuring small narrow holes while 3D optical scanning excelled in positional measurements. Barbero and Ureta [85] compared different digitalization techniques and their accuracy. Among other non-contact measurement methods, the 3D optical scanner with fringe projection system (ATOS scanner) had accuracy and measurement uncertainty comparable with the laser mounted in the CMM system.

One of the major drawbacks of 3D optical scanning is the lack of universally accepted standards for the performance evaluation of such systems. Currently, VDI/VDE 2634 is the only general guideline related to 3D optical systems. Some recent studies were therefore directed towards estimating measurement uncertainty and accuracy in 3D optical scanning. Urbas et al. [86] obtained a combined measurement uncertainty of 4.24 μm for 3D optical scanning and 2.82 μm for the CMM while conducting gear inspection. Ghandali et al. [87] determined expanded uncertainty for structured-light 3D scanners based on novel reference artifacts. Estimated

expanded uncertainties were $4.42\ \mu\text{m}$ for distance and $1.28\ \mu\text{m}$ for size and form. Mendricky [88] dealt with the measurement accuracy of ATOS 3D scanners. The author developed a new calibration etalon and compared it to the so-called “Acceptance test” based on VDI 2634 (currently the only way to express the accuracy of an ATOS 3D scanner explicitly). The comparison showed that in the case of a scanner with a smaller measuring volume (MV 55), the errors were slightly larger than those in the “Acceptance test”. However, the magnitude of errors was not higher than $0.01\ \text{mm}$ suggesting that the system is still measuring properly. In the case of scanners with large measuring volumes (MV 250 and MV 700) the results were even better than those officially reported in the “Acceptance test”. Additionally, it was concluded that the device should be calibrated often regardless of its non-problematic operation. After calibration, the measured values were much closer to nominal values. Lastly, the influence of anti-reflective coating, which must be applied when scanning highly reflective objects, is analyzed. The application of coating, usually in the form of a sprayed powder, increases measured values uniformly by $5\text{-}10\ \mu\text{m}$. The difference in spraying one or two layers resulted in an average difference of $3\ \mu\text{m}$ in measured values. As the coating is applied manually, the quality of the scanned results depends highly on the operator’s competence. The insufficient coating represents a much more serious problem as local reflections may cause irregularities leading to local errors thus decreasing the objectivity of the measurement.

Gear inspection is an interesting topic for 3D optical scanning applications due to the complex geometry in gears and strict requirements for their dimensional accuracy. Urbas et al. [86,89] conducted a dimensional inspection of polymer gears according to ISO 1328-1 standard. They concluded that 3D optical scanning is suitable for evaluating injection molded gears. Additionally, Urbas et al. [90] compared different alignment methodologies in the gear inspection process based on point clouds obtained from 3D optical scanning. Results showed that the global alignment method used in commercially available GOM Inspect software for dimensional inspection of point clouds obtained through 3D optical scanning underperformed compared to the newly developed four sequential step method. Lu et al. [79] optically scanned face gears. The authors managed to obtain the model of complete gear tooth surfaces used to develop a finite element method model. The results showed that gear deviations caused edge contact, significantly reducing the gear’s contact and bending strength.

To sum up, 3D optical scanning has some distinct advantages over CMM while still falling somewhat behind in terms of accuracy and repeatability. The high sampling rate and ability to capture the whole geometry of the scanned object represent significant benefits when inspecting

large and/or complex geometry compared to CMM's low sampling rate and ability to capture only specific points or sections. When it comes to accuracy, CMM still represents the gold standard. However, research data suggest that accuracy and measurement uncertainty in 3D scanners are almost on par with CMM, implying that 3D optical scanning represents a reliable alternative to conventional contact measurement methods.

4.3 Worm pair scanning process

Worm pairs were 3D optically scanned by ATOS scanners based on structured light in the form of fringe projection patterns. Worm and worm wheels were scanned using the ATOS 5 400 MV 320 system, while worm pair housing was scanned using the ATOS III 400 MV 320 system. Both are stereo systems with one projector and two cameras and have measuring volumes of 320 mm x 240 mm x 240 mm. The scanning process consisted of:

1. Calibrating the system.
2. Placing reference points on the scanned object. Most features of scanned objects are not visible from a single measurement position. Therefore, partial scans from different angles are needed to obtain the complete geometry of the scanned object. Reference points enable the scanner to accurately position during the scans and combine partial scans into the final point cloud of the scanned object.
3. Applying anti-reflection coating on the scanned object (both worm and worm wheel have highly reflective surfaces).
4. Removing the coating from reference points to enable accurate recognition of object's positions during the scanning process.
5. Scanning the object from multiple angles/positions as it is being incrementally rotated on the rotary table.

The scanning process is depicted in Figure 33. The acceptance test values, which are used to verify the accuracy of the scanners, are provided in Table 17.

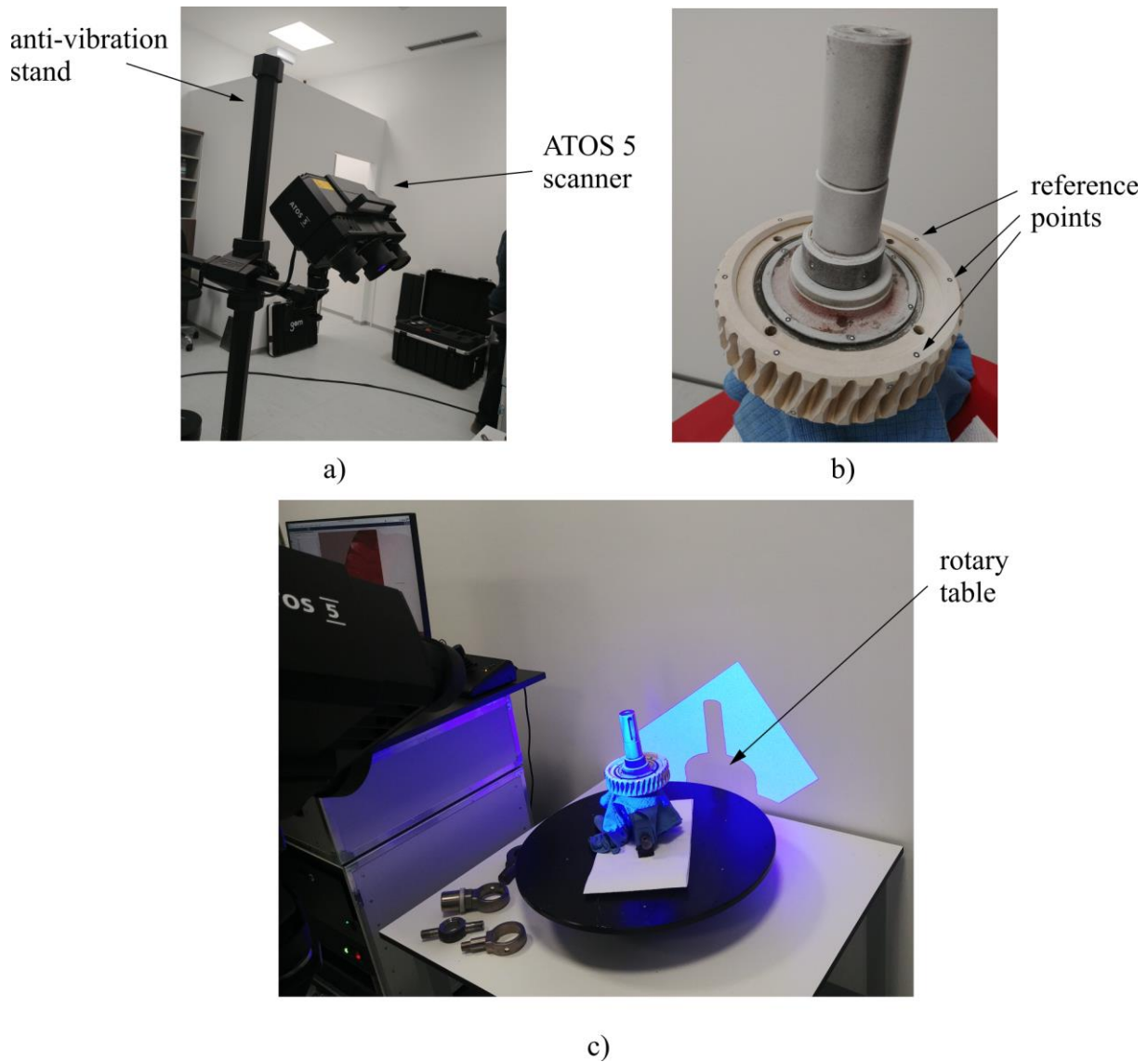


Figure 33. Scanning process: a) System calibration, b) Anti-reflective coating and reference point application, c) Worm wheel on the rotary table during the scanning process

Table 17. Acceptance test values

Scanner	ATOS 5 400 MV 320	ATOS 3 MV 320	
Parameter	Maximum deviation, mm	Maximum deviation, mm	Limit, mm
Probing error form (sigma)	0.001	0.001	0.004
Probing error (size)	0.004	0.004	0.015
Sphere spacing error	-0.008	0.006	0.012
Length measurement error	-0.006	-0.006	0.027

4.4 Processing of scanned data

The result of the scanning process is a triangulated surface file based on the point cloud of the object. While the worm was scanned as a single part, the worm wheel was scanned in an assembly with a hub and shaft. The goal was to consider possible assembly errors that hub and shaft connections induced. These errors can greatly affect the worm wheel position inside the gearbox, changing the meshing conditions and load sharing during worm pair operation. On average, the worm scan had 500 000 points, the worm wheel scan had 1 100 000 points, and the housing scan had 5 000 000 points (Figure 34). The scans were analyzed in GOM Inspect software [91] specialized for geometric dimensioning and tolerancing (GD&T) and post-processing of scanned data. The software has been tested and certified by PTB (*Physikalisch-Technische Bundesanstalt* is the National Metrology Institute of Germany) and NIST (*The National Institute of Standards and Technology*, United States of America) to ensure precise measurement accuracy.

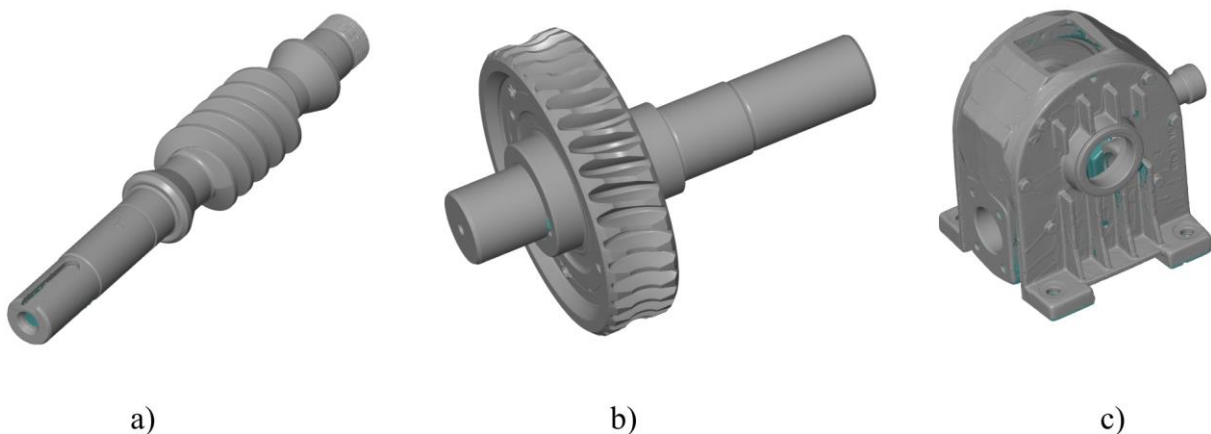


Figure 34. 3D optical scans of a) worm, b) worm wheel assembly, c) housing

Before any measurements, the scan alignment must be carried out. The procedure of the worm wheel assembly alignment will be presented. Similar procedures were undertaken for worm and housing alignment. The alignment was conducted to replicate the working conditions as accurately as possible:

1. *Plane 1* and *Plane 2* were fitted on the sides of the worm wheel, thus serving for the creation of symmetrical *Plane 3*
2. The axis of rotation was defined by fitting the cylinder using *Bearing location 1* and *Bearing location 2* on the shaft
3. The intersection between *Plane 3* and the axis of rotation was set up as *Origin*
4. *Mid-plane* was created as normal to the axis of rotation, positioned by the *Origin*

5. *Plane 5* was created as normal to the *Plane 4* (key slot plane)
6. 3-2-1 alignment (*ZZZ-XX-Y*) was carried out. Three points (z_1 , z_2 , and z_3) were selected in *Mid-plane* (now *Plane Z*), two points (x_1 and x_2) in *Plane 5* (now *Plane X*), and one point (y) in *Origin*

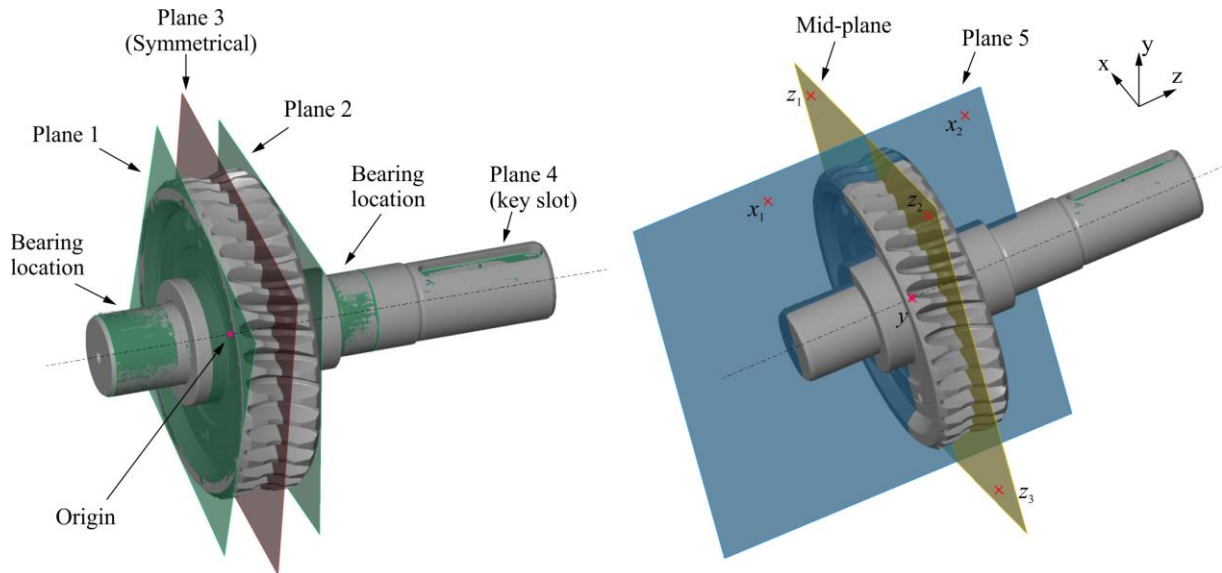


Figure 35. Worm wheel assembly alignment

Mid-plane was used to create a worm wheel mid-section where most deviations are inspected, as the standard suggests [10,11]. The pitch circle was constructed in *Mid-plane* and its intersection with the mid-section resulted in a point cloud suitable for pitch evaluation. Pitch deviation was measured between two points on two neighboring active flanks of the teeth, as presented in Figure 36.

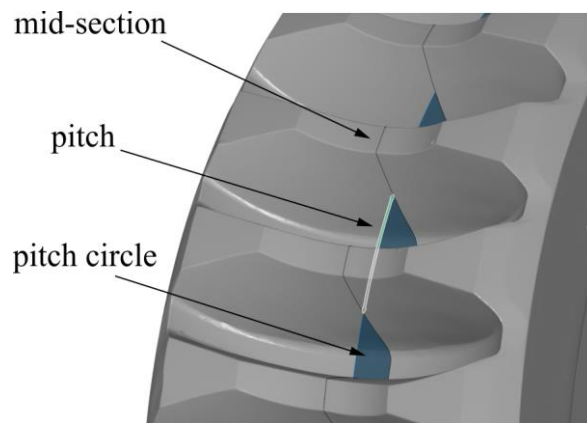


Figure 36. Pitch deviation measurement on scanned data

Total profile deviation F_α was evaluated on each tooth's active flank over the evaluation range defined by the start and end of the active profile diameter. The start of the active profile was calculated according to [92] and is approximately 136.58 mm while the end of the active profile

diameter is at 152 mm as no tooth tip alternations were present in worm wheel tooth geometry (Figure 37).

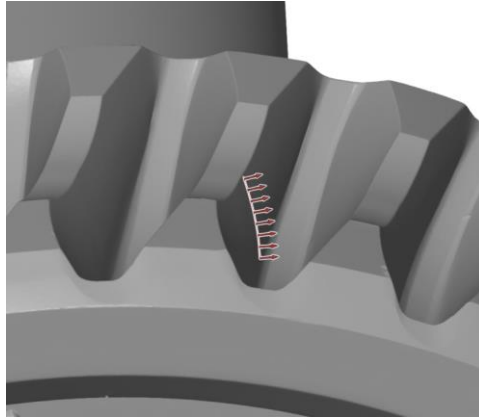


Figure 37. Tooth flank profile used for evaluation

The process of evaluating tooth flanks from scanned data was developed by Urbas et al. [86]. The difference between actual and theoretical flank shape is calculated using expressions:

$$y_T = \frac{r_b^2 \cdot y_m + r_b \cdot x_m \cdot \sqrt{x_m^2 + y_m^2 - r_b^2}}{x_m^2 + y_m^2} \quad (37)$$

$$x_T = \frac{r_b^2 - y_m \cdot y_T}{x_m} \quad (38)$$

The points denoted with subscript T form a tangent to the base circle when connected to the points on the actual flank. From the values on the base circle, the angular position φ of each point can be calculated according to the expression (39). The points on theoretical involute can be calculated using expressions (40) and (41):

$$\varphi = \arccos \frac{x_T}{r_b} \quad (39)$$

$$x_A = r_b \cdot \cos \varphi + r_b \cdot \varphi \cdot \sin \varphi \quad (40)$$

$$y_A = r_b \cdot \sin \varphi - r_b \cdot \varphi \cdot \cos \varphi \quad (41)$$

The difference in the tangent between the actual and theoretical profile is the measured deviation. The process is presented in Figure 38.

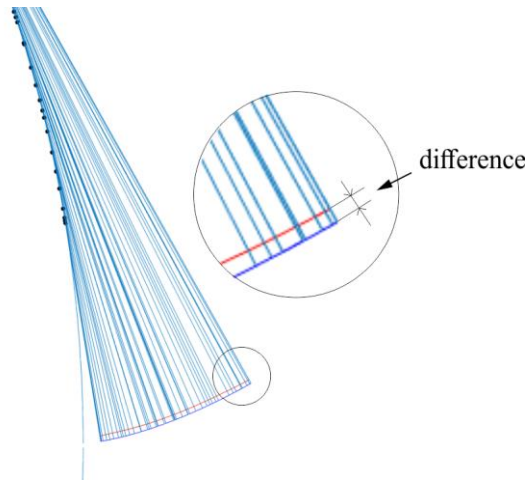


Figure 38. Tooth flank evaluation

Runout deviation F_r was measured by inserting a probing ball in each tooth gap. The diameter of the probing ball was 7 mm. The diameter of the circle passing through the probing ball center was 147.35 mm. Firstly, the center of the tooth gap is defined as half the distance between two neighboring flanks. Then, a sphere (ball) was constructed and projected on the scanned object with the condition of touching the object in two points, i.e., simultaneously touching both flanks. The theoretical probing ball position is represented in blue, while the actual probing ball position is represented in green (Figure 39). The difference between the measured distances from the worm wheel origin to each probing ball center is denoted as a runout deviation.

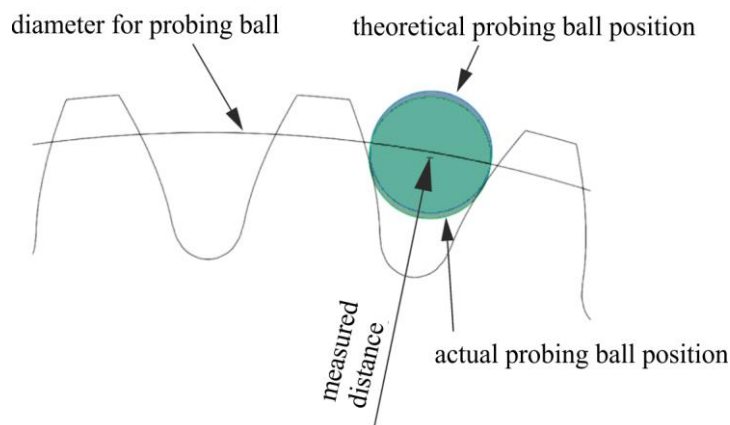


Figure 39. Runout deviation measurement on scanned data

Although this deviation is not considered through the standard [10,11], the axial runout was also measured on the worm wheel. Žeželj [25] noticed that axial runout greatly impacts contact patterns in worm wheels. Due to axial runout, the contact pattern can vary significantly among the teeth of the worm wheel. This can result in uneven load distribution and pitting formation. Axial runout is schematically represented in Figure 40. *Plane 3* is a symmetrical plane based on *Plane 1* and *Plane 2*, representing the worm wheel's sides. Thus, *Plane 3* is not necessarily

perpendicular to the worm wheel axis. *Mid-plane* is constructed as a perpendicular plane to the worm wheel axis and includes the intersection point of axis z and *Plane 3*. The axial runout is measured at the position of every worm wheel tooth as the distance between the *Plane 3* and *Mid-plane* in the direction of the worm wheel axis (Figure 35, axis z). A significant deviation between *Plane 3* and *Mid-plane* is shown for a better presentation.

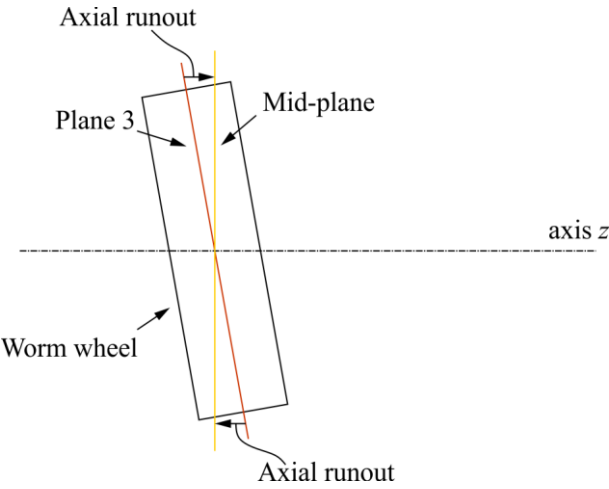


Figure 40. Axial runout

Lastly, the worm wheel wear was measured through tooth thickness reduction. Tooth thickness was measured on the reference circle in *Mid-plane* as an arc length between the left and right flank of the same tooth. The procedure was similar to pitch deviation measurement.

5

Surface texturing

Surface texturing is a topic of great interest today. It is primarily directed towards friction and wear reduction between contacting surfaces in various applications. Most research has been conducted on simple geometry tested in controlled environment. Applying surface texturing in machine elements (components) under actual working conditions is also available, albeit scarcer in literature. As a part of this thesis, the goal was to investigate available surface texturing methods and their applicability to worm pairs, either worm or worm wheel. This chapter will cover surface texturing methods, their application in gears, and the final selection of surface texturing method that will be applied and investigated in this research.

5.1 Surface texturing methods

In mechanical engineering, surface texturing is usually a modification in the surface topography of metal surfaces with the aim of friction and wear reduction. In literature, textured surfaces can also be referred to as “structured”, “patterned”, or “engineered.” The term “texture” is also used to define surface finish characterized by surface features: lay, roughness, and waviness [93]. Textured surfaces have been investigated in conformal or non-conformal contacts operating in dry or lubricated conditions. When discussing surface texture effects in lubricated conditions, the distinction is usually made between boundary, mixed, or hydrodynamic lubrication regimes, as each has fairly different characteristic. Surface textures are characterized by their shape, geometry (diameter and depth, Figure 41), aspect ratio (ratio

of the depth and the characteristic diameter of the surface feature), and texture density (ratio of the surface area covered by the texture and total area of a surface) [94]. The most common type of surface texture used in lubricated contacts are dimples of various shapes and surface density. Surface textures are created with a variety of methods, among which most used are laser surface texturing (LST) and etching. In contrast, among the other methods considered for surface texturing in this research, the focus can be placed on mechanical indentation, shot peening, and electropolishing [20,94–96].

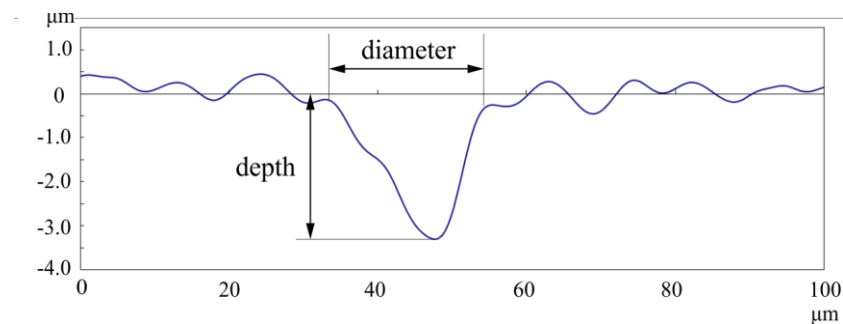


Figure 41. Dimple profile

Laser surface texturing (LST) is the most widely used method for surface texture creation. In LST, the laser beam melts and vaporizes the material from the surface, thus creating desirable shapes and sizes of microfeatures that can be as small as a few microns. High-frequency lasers (nanosecond and femtosecond laser) ensure high texturing speed and accuracy. Texture's depth and aspect ratio are controlled through laser pulse duration, wavelength, and power [97]. Due to the high energy present in LST, the thermal effects of LST affect nearby surface properties in terms of hardness reduction and creation of bulges/burrs around produced dimples which are often removed by a post-texturing process such as grinding or polishing [38] (Figure 42b). The most commonly used are CO₂ and Nd: YAG lasers, the latter being most suitable for creating textures on steel surfaces [96].

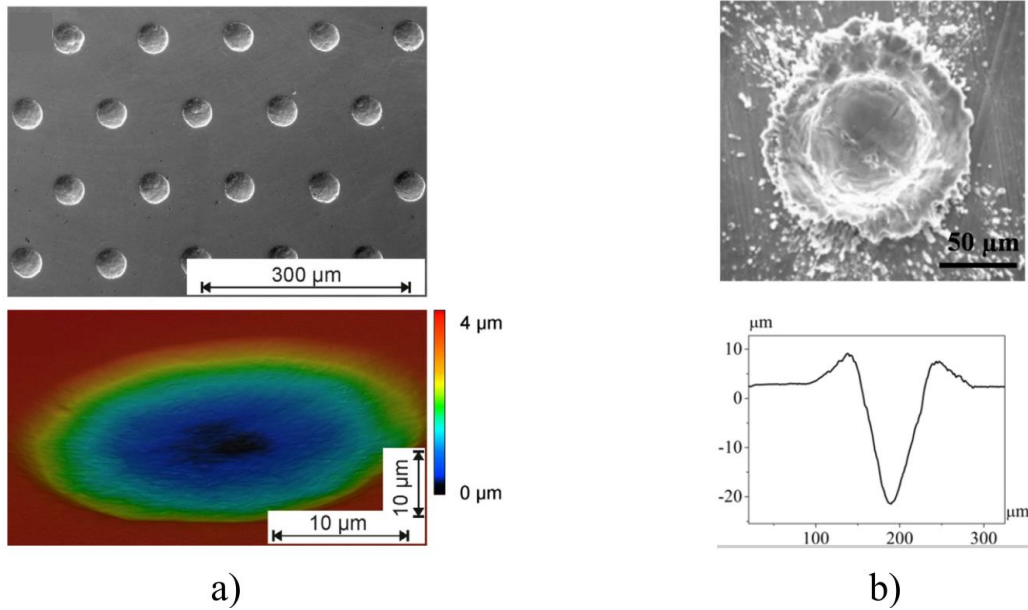


Figure 42. Laser surface textures: a) dimples of 40 μm in diameter (polished after LST) [98], b) dimple obtained with laser wavelength of 532 nm (non-polished after LST, visible bulges and debris) [99]

Etching is a material removal process due to a chemical reaction between exposed areas or patterns on base material with a chemical agent, usually acid or alkaline (wet etching) or plasma/reactive gases (dry etching). The method alters surface topography but does not alter the mechanical properties of the base material. Another advantage is that etching can be applied to complex geometry and irregular shapes which is not true with LST. A masking step defines the etching process regarding cost, texture pattern, and accuracy [95,97,100]. Some etching and masking methods include photolithography (the texturing technique is known as *photochemical texturing* [101]), ink-jet printing [102], and maskless electrochemical texturing (MECT) in which the pattern is present in cathode tool and avoids the need for masks to be applied to individual workpieces [103]. Examples of etched surfaces are presented in Figure 43.

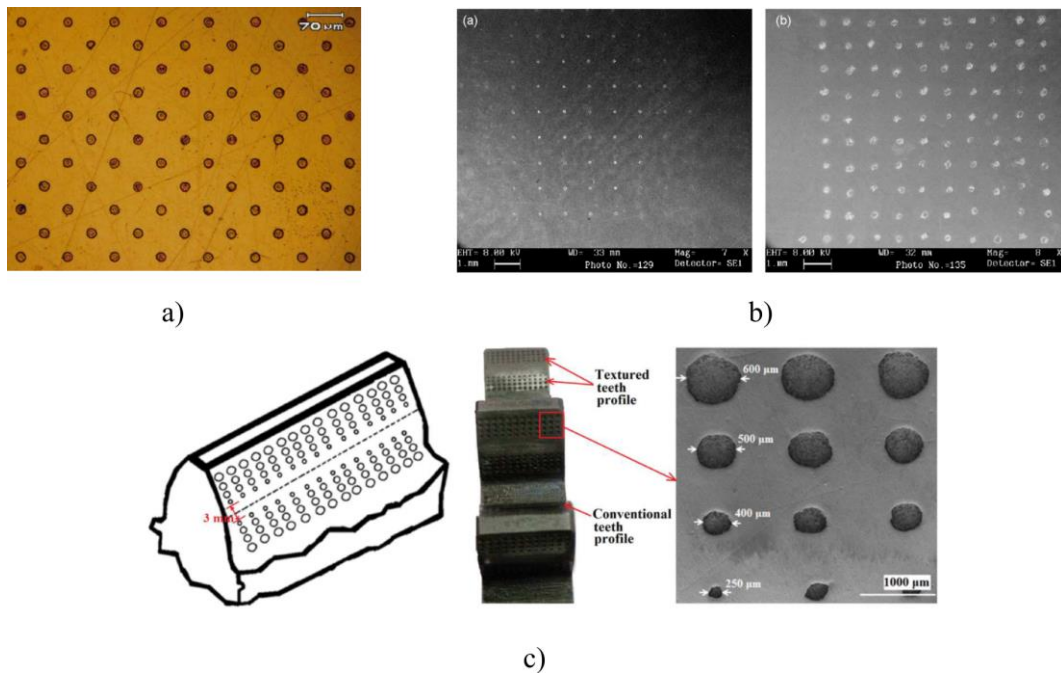


Figure 43. Etched surfaces: a) photolithography [104], b) MECT [103], c) chemically etched spur gear teeth [44]

Mechanical indentation is a method in which a single-shaped indenter, patterned roller, or patterned tool transfers its shape by being pressed into the surface (Figure 44). The indentation can also be done using Rockwell or Vickers indenters. However, the method can be very time-consuming if each dimple must be obtained one at a time [105].

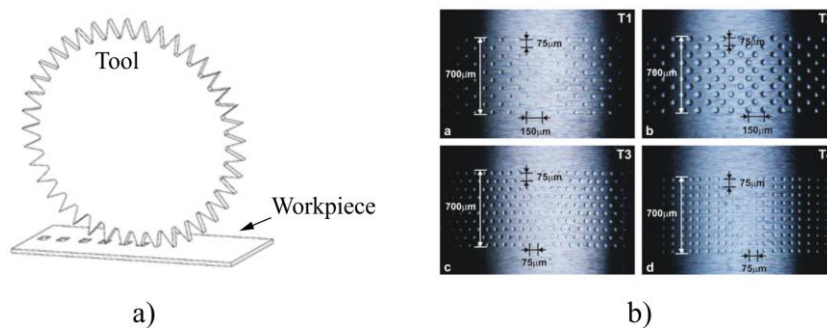


Figure 44. Surface textures created by mechanical indentation: a) micro-dimple rolling operation [106], b) roller surface indented using a Rockwell indenter [34]

Shot peening is a method widely used in industry to improve the fatigue strength of machine elements (e.g., gears, springs, shafts) subjected to fatigue loading. During the process, the surface is blasted with small beads of known diameter creating a residual compressive stress zone on the surface [107]. Additionally, a dimple-like surface texture is formed during the process as each impact creates a valley and peak. The beads are usually made of hardened steel or glass. The shot-peened surfaces are frequently polished afterward to smooth the peaks and reduce surface roughness, as seen in Figure 45 [108].

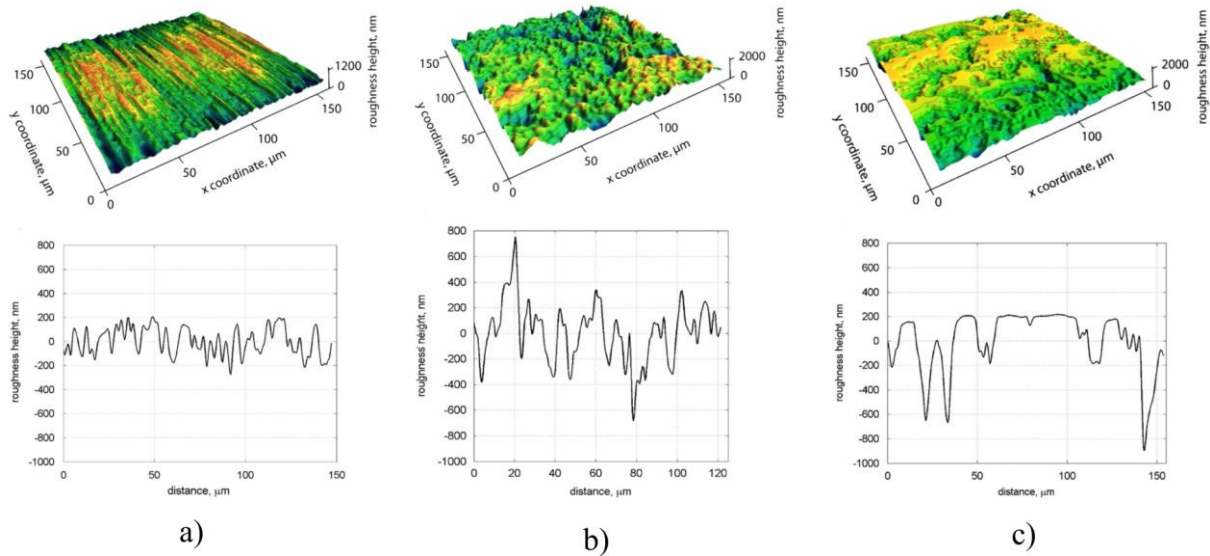


Figure 45. Shot peened surface: a) ground surface, b) shot peened surface, c) shot peened surface after polishing [108]

Electropolishing is an electrochemical process aimed to passivate, deburr, or improve the surface finish of the metal part by making it anodic in an appropriate solution [18]. Although almost any metal can be electropolished, the most common materials are stainless steel, aluminum, titanium, and copper. It is relatively simple, especially for complex geometry workpieces; it is used to sterilize equipment in the medical and food processing industry and to achieve mirror-like finishes in various products. However, when electropolishing is conducted at elevated potentials (higher current densities) the surface has many pores/pits and shallow dimples, therefore creating a surface texture. Examples of surfaces modified by electropolishing are presented in Figure 46.

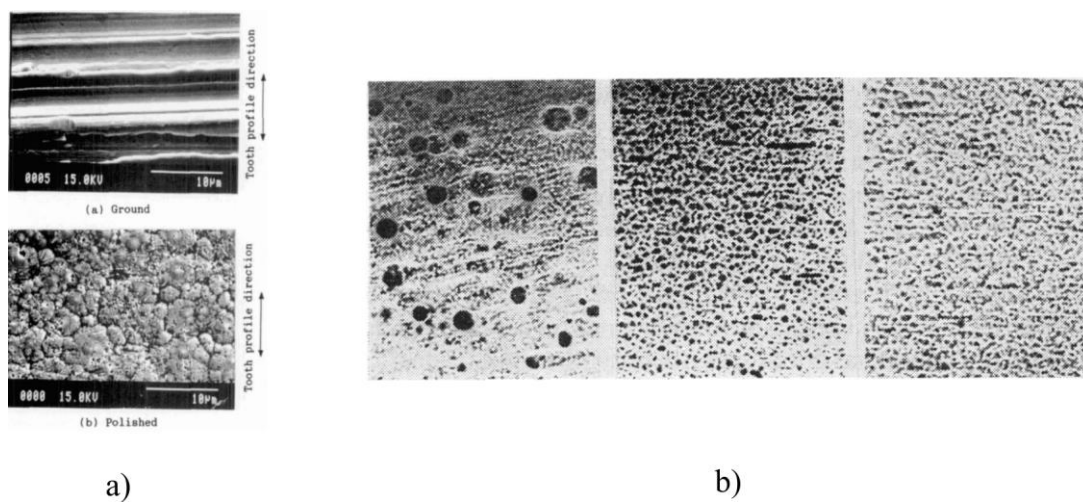


Figure 46. Electropolished surfaces: a) carbon gear steel ground vs. electropolished surface [109], b) stainless steel surfaces electropolished with various current densities and time duration [110]

5.2 Surface texturing in gears

Gears represent one of the most important means of motion and torque transmission. The tribological system in gear contact is characterized by non-conformal, highly loaded contact operating in boundary or mixed lubrication regimes. The oil film thickness in such contacts is often less than valley-to-peak height, thus leading to strong asperity interactions [42]. On the one hand, as gears are used in many industrial applications, they represent highly desirable machine elements for surface texture application. On the other hand, unfavorable contact and lubrication conditions suggest that surface textures would not withstand long in such conditions before degrading or losing their functional abilities. Moreover, complex gear geometry paired with tight tolerances poses another obstacle that must be overcome during surface texture application. Additionally, many gears are case-carburized. Therefore, the impact of a certain surface texturing method, such as the laser source, may severely reduce surface hardness [20]. Usually, gear lubrication conditions are improved by grinding or superfinishing. Britton et al. reported a decrease in friction by 30% in super-finished gears, presumably due to a significant reduction in asperity interaction [42]. However, successful effects of surface texturing in gears have been reported. Nakatsuji and Mori [40,41,43,109] investigated electropolished gear steel surfaces and electropolished gears. The produced surface had many micropores and shallow dimples that encouraged the creation of the oil film, consequently improving the pitting durability by 50%. Gupta et al. [44] chemically etched (Figure 43c) and laser textured [45] spur gear teeth flanks, producing a dimpled surface. Results showed reduced wear and a significant decrease in vibration amplitudes and temperature rise. The vertically placed ellipsoidal dimples yielded the best results regarding improved lubrication conditions. Li et al. [39] shot peened specimens made of gear steel using fine particles with an average diameter of less than 200 μm . A positive influence on the friction coefficient reduction in the boundary lubrication regime was attributed to the dimpled surface. Even better results were achieved using dual fine particle peening. Petare et al. [46,111] laser textured helical and straight bevel gears followed by an abrasive flow finishing process (AFF). The results showed friction reduction and higher wear resistance than untextured gears as AFF improved surface roughness and microhardness. Compared to available surface texturing research in literature, the application of surface texturing in gears is relatively scarce and has yet to be more thoroughly investigated.

5.3 Selection of surface texturing method

After a thorough literature review, by assessing potential surface texturing methods and considering their possible application in gears, a summary of the most influential factors evaluated for each surface texturing method is provided in Table 18.

Table 18. Summary of presented surface texturing methods

	LST	Etching	Indentation	Shot peening	Electropolishing
Easiness of use	-	-	+/-	-	+
Texturing speed	+	+	+/-	+	+
Texturing accuracy	+	+	+	+/-	-
Side effects on the base material	-	+	+	+	+/-
Application to complex geometry	-	+	+/-	+/-	+
Cost	-	+/-	+	+/-	+

Based on the evaluation criteria presented in Table 18, electropolishing was chosen as a promising surface texturing method that can successfully be applied in worm pairs. The method is simple and most easily applicable to complex geometry among all investigated surface texturing methods. The electropolishing duration is usually a few minutes long thus being relatively fast. The side effects on base material are non-existent or minimal if talking of surface hardness reduction when electropolishing with higher current densities [41]. Finally, the cost of the required equipment and the surface texturing process itself is low. However, the significant drawback of electropolishing is its inability to accurately control the surface texture geometry or surface density. Depending on the current density, the produced texture can have shallower or deeper pits/dimples and their surface density is only somewhat controlled by electropolishing duration. The exact position and arrangement of dimples cannot be achieved. Despite the apparent drawback, electropolishing is very economical process. On an industrial scale, electropolishing is usually employed on large batches meaning that surface texturing can simultaneously be applied to many workpieces.

In this research, electropolishing was applied to a worm made of case-carburized 16MnCr5 steel. Carburized steel, commonly used as a worm material, exhibits little to no wear due to its superior hardness compared to bronze, commonly used as the worm wheel material. The wear rate of the bronze wheel is the highest in the running-in period when the contact pattern is not

fully established. Therefore, any surface texture introduced on steel worm will last considerably longer and produce longer-lasting benefits introduced by surface texturing.

6

Tribological behavior of electropolished steel-bronze pair in mixed and boundary lubrication regimes

After the appropriate surface texturing method, in the form of electropolishing, was selected, it was investigated on a simple geometry. The block-on-disc experimental setup was employed, and the sliding tests were carried out. In this chapter, the electropolishing procedure will be explained and the effect of electropolishing parameters on the surface topography of case-carburized 16MnCr5 steel will be presented. Also, the results of the steel-bronze sliding tests will be presented in terms of coefficient of friction, wear, surface topography, and chemical composition modifications. The results presented in this chapter were published in an article *The Effect of Steel Electropolishing on the Tribological Behavior of a Steel–Bronze Pair in the Mixed and Boundary Lubrication Regimes* authored by Mašović, R.; Miler, D.; Čular, I.; Jakovljević, S.; Šercer, M.; Žeželj, D. [18].

6.1 Electropolishing process

Electropolishing (electrochemical polishing or electrolytic polishing) is an electrochemical process aimed to passivate, deburr, or improve the surface finish of the metal part by making it anodic in an appropriate solution. In other words, it is a finishing process that removes material from a metal based on an anodic dissolution process, in which the material is removed ion by ion from the workpiece surface. The workpiece is immersed in a temperature-

controlled bath comprised of an electrolytic solution and connected to the positive polarity of a power supply, thus serving as the anode. The negative polarity is connected to the cathode. As electric current passes from the anode to the cathode, the anodic dissolution occurs, removing surface impurities and irregularities. Reduction reaction occurs at the cathode, which normally produces hydrogen [112,113]. The result of electropolishing is a smooth and bright surface. Therefore, it is commonly employed to replace abrasive surface finishing methods such as grinding, polishing, or superfinishing, especially if surface finishing must be applied to complex geometries. The electrolytic solution or bath is normally a highly viscous and conductive media, such as concentrated phosphoric or sulfuric acid or acid mixtures [114–116]. According to electropolishing theory [117], a potential applied to an electropolishing cell (a system of anode, cathode, and electrolytic solution) results in the formation of viscous film (anodic film) on the surface of the anode that has greater electrical resistance and viscosity than the remainder of the electrolytic solution (Figure 47a). As surface peaks are covered with thinner viscous film, their electrical resistance is lower (A-B) than the valleys (C-D) and the rest of the surface. This allows the current to primarily affect surface irregularities, namely peaks, and thus reduce the surface roughness. The process continues until the peaks are reduced to the level of the surface [118]. The current density-voltage relationship plays a crucial role in the electropolishing process. As presented by Hahn and Marder [119], the curve has a few specific regions: A-B, etching (no anodic film); B-C, unstable etching (anodic film starts to form); C-D, stable plateau with polishing; and D-E, gas evolution with pitting (anodic film dissolves).

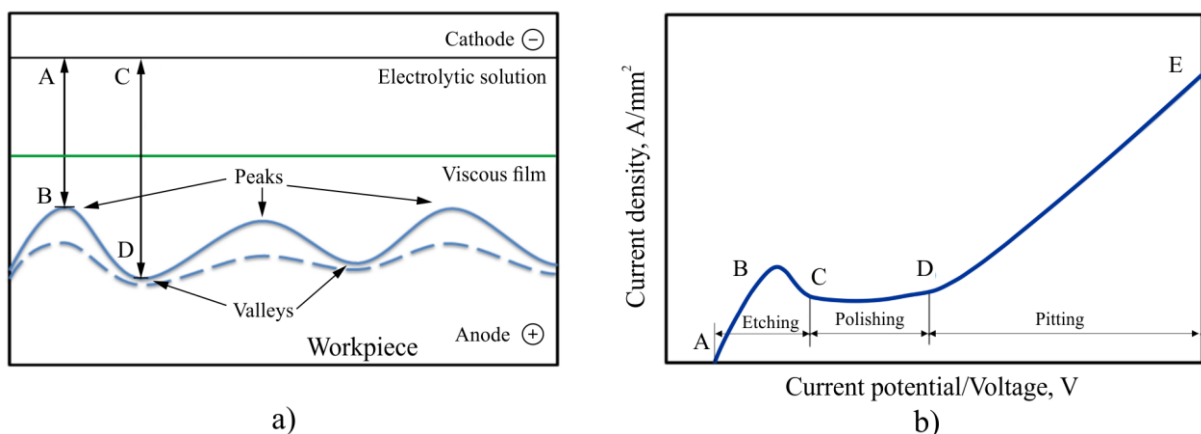


Figure 47. Fundamentals of electropolishing: a) electropolishing mechanism, b) electropolishing curve [119]

In terms of conventional electropolishing, i.e., aiming to achieve superior surface roughness and appearance, the goal is to conduct electropolishing in the C-D region (polishing plateau). However, if the goal is to induce pits/dimples and create a surface texture, one should aim

towards the D-E region where surface pitting appears due to gas evolution. Several potential explanations of pitting formation can be found in existing research. The formation mechanism of pitting is explained by the Broken Bubble Tunnelling Effect (BBTE) [118]. Under higher current densities, pitting occurs as oxygen bubbles evolve from the surface (i.e., gas evolution). A broken bubble represents a place with lower electrical resistance and, thus, higher current density. This leads to an increased dissolution rate, resulting in a pitting hole. Neufeld and Southall [110] reported that pitting occurs as oxygen evolves. Pits during electropolishing are internally polished and superimposed on the polishing process. In other words, pitting does not cause the breakdown of special surface conditions that support polishing. Apart from the gas evolution, Imboden and Sibley [120] argued that pits also occur near surface inclusions and can be significantly reduced by mild agitation of the solution. Lastly, Pendyala et al. [121] referred to a phenomenon known as streaking due to gas evolution which, contributing to uneven pit distribution. The authors also concluded that mechanically polished surfaces, due to the non-uniform nature of the oxide layer and sub-surface damage, resulted in pitting of the surface in the initial stages of electropolishing.

6.2 Electropolishing setup

Electropolishing of case-carburized 16MnCr5 is scarce in literature since carbon steels are not usually considered for finishing via electropolishing. The parameters for electropolishing plain carbon steel can be found in [120] while processing guidelines for carburized 20MnCr5 steel can be obtained from [122]. Moreover, some general information regarding the electropolishing parameters for various metals can be found in the ASTM-E1558 standard [123]. The employed electropolishing setup is shown in Figure 48.

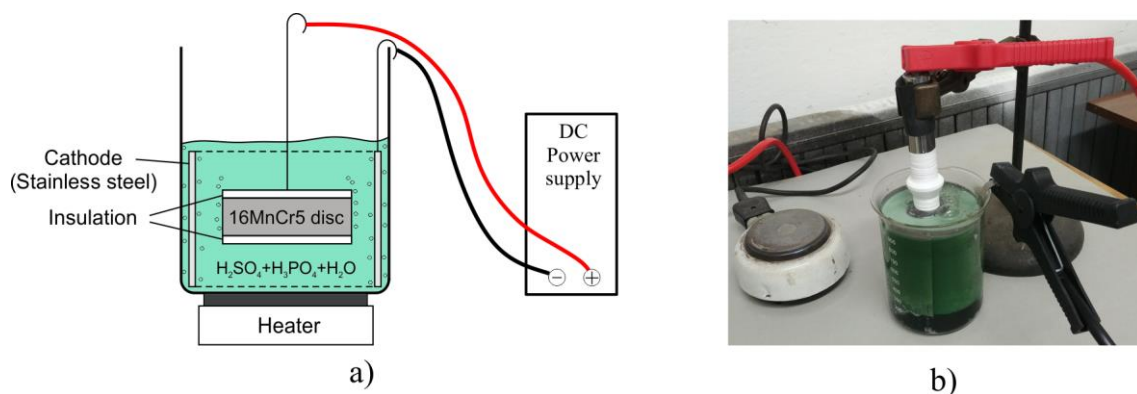


Figure 48. Electropolishing setup: a) schematic, b) electropolishing of steel worm

The employed electrolytic solution was a mixture of 34% sulfuric acid, 42% phosphoric acid, and 24% water, according to the recommendation from the ASTM-E1558 standard [123]. For electropolishing to be effective, the workpiece should be free of oils, grease, and other impurities. Before electropolishing, the steel discs were cleaned in an ultrasonic bath with ethanol (96%) for 10 minutes. Current density ranged from 15 to 50 A/dm², while electropolishing time was between 5 and 15 minutes. After electropolishing, the discs were rinsed and dried to remove the electropolishing solution completely. The solution was not agitated, and its temperature was kept at 50 ± 2°C. The cathode material was stainless steel AISI 304 in the form of circular hollow tube. In that way, the distance of approximately 3 cm between electropolished disc (or steel worm) and cathode was rather constant in every direction. The cathode surface was several times larger than the surface of the electropolished piece. The side surfaces of the steel disc were insulated using a polytetrafluoroethylene (PTFE) mask [18].

6.3 Experimental setup

Materials used were case-carburized 16MnCr5 steel discs and CuSn12 bronze specimens. The material combination was the same as the referent material combination used in worm pairs and the same as in worm pairs tested in this research (see Materials). Steel discs were ground or ground and then electropolished, while bronze specimens were either ground or milled. The surface hardness of steel discs was 800 HV whereas the surface hardness of bronze specimens was 110 HV. Steel discs and bronze specimens were tested under pure sliding initial line contact conditions. The lubrication oil was Castrol Alpha SP 150 mineral oil (see Lubricant selection).

The block-on-disc experimental rig is presented in Figure 49. A similar rig was used in the research of Miler et al. [124]. The rig comprises a housing, shaft, load cell, torque transducer, load application mechanism, and electric motor. The rig has a rotating axis and a vertical (static) axis. The rotating axis consists of an electric motor, a shaft, a torque transducer, bearings, and a steel disc. The vertical axis consists of a static bronze specimen placed in the specimen holder connected to the load cell. The load cell was loaded using a spindle piston, thus producing a normal load. The torque was provided by a 0.55 kW asynchronous electric motor. The rotational speed of the motor was controlled by a frequency regulator. The compressive load cell with a maximum capacity of 2 kN and an accuracy grade of 0.2 was used to measure normal force. The torque transducer with a maximum capacity of 20 Nm and an accuracy grade of 0.2 was used to measure the torque. A rotating steel disc with the outer diameter $d_{\text{disc}} = 60$ mm mounted

on a shaft and a static bronze specimen with the thickness $b = 5$ mm were used to produce initial line contact. The rotating speed of the steel disc was either 0.33 or 3 m/s, depending on establishing desirable lubrication regime and conditions. According to Figure 49, the coefficient of friction is calculated as a ratio of the frictional and the normal force:

$$\mu = \frac{F_{\text{friction}}}{F_N} = \frac{2 \cdot T_{\text{friction}}}{d_{\text{disc}} \cdot F_N} \quad (42)$$

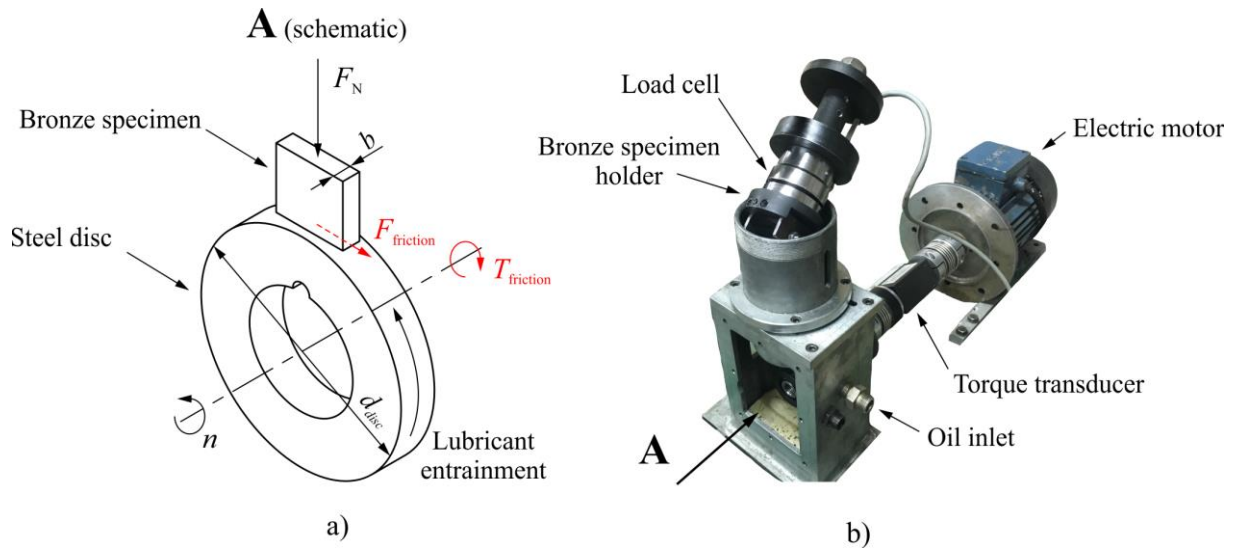


Figure 49. Block-on-disc experimental rig: a) schematic of contacting geometry, b) experimental rig, according to [18]

6.4 Surface characteristics of electropolished steel

6.4.1 Surface profile and hardness

In surface texturing, the aim should be to produce a surface with certain surface known to assist in reducing friction. When dealing with non-conformal highly loaded contact (as present in this experimental setup and worm pairs), the literature highlights kurtosis (R_{ku}) and skewness (R_{sk}) as surface parameters that tend to reduce friction. A symmetrical height distribution, i.e. with as many peaks as valleys, has zero skewness $R_{sk} = 0$, while predominant peaks and spikes on a surface result in positive skewness, $R_{sk} > 0$. In contrast, dimpled surfaces with deep valleys and peaks removed have negative skewness, $R_{sk} < 0$. The kurtosis coefficient describes the sharpness of the probability density of the profile. If $R_{ku} < 3$, the distribution curve is characterized by relatively few high peaks and low valleys. On the other hand, if $R_{ku} > 3$, the distribution curve is characterized by many high peaks and low valleys [125]. A schematic representation of kurtosis and skewness is given in Figure 50.

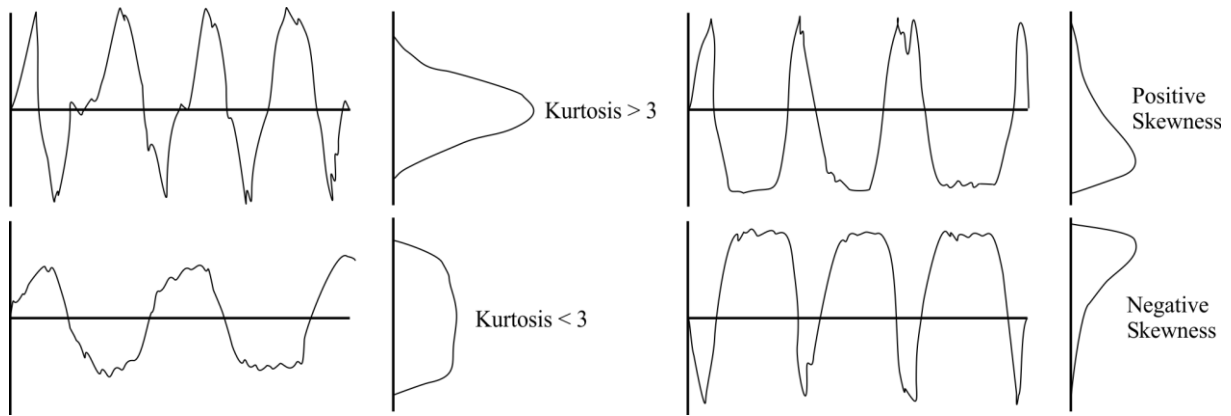


Figure 50. Kurtosis R_{ku} and skewness R_{sk} [18]

The effect of kurtosis and skewness was covered by many investigations in surface texturing. Akamatsu et al. [126] investigated rolling bearing fatigue life with several surface texture types under mixed and boundary lubrication regimes. Skewness ranged from -0.01 to -2.0. The results showed that bearings with more negative skewness had a longer life. Sedlaček et al. [127] investigated the tribological behavior of ground and polished hardened steel discs. Using different grades of grinding and polishing, the produced samples had significant differences in S_{sk} and S_{ku} parameters (S denotes areal parameters). The most dominant parameter in friction reduction was negative S_{sk} . The more negative it was, the lower friction could be expected, even at higher average surface roughness. Sedlaček et al. [128] also investigated surface textures produced by LST. They concluded that a combination of more negative skewness and high kurtosis results in a coefficient of friction reduction. Krupka et al. [36] observed that shallow pits work as lubricant micro reservoirs, while deep grooves can be detrimental in the form of lubrication film breakdown in non-conformal contacts under a mixed lubrication regime. Dzierwa [129] concluded that increased kurtosis and more negative skewness results in lower wear volume under dry sliding conditions in steel-steel contact. Podgornik et al. [130] investigated surface textures in terms of dimple size and density. In the case of textured surfaces, a reduction in dimple size and density resulted in higher kurtosis and more negative skewness, which led to lower friction under the boundary lubrication regime. The skewness was in the range from $R_{sk} = -0.5$ to $R_{sk} = -1.5$ while kurtosis varied from $R_{ku} = 1.8$ to $R_{ku} = 5.5$. Based on the literature overview, the conclusion arises that surface topography designated by high kurtosis and negative skewness positively contribute to friction and/or wear reduction in highly loaded non-conformal contacts.

The electropolished surface reported by Naktsuji and Mori [40] had values of $R_{sk} \approx -0.95$. This suggests that electropolishing can produce a desirable surface texture according to reports from

the literature. While producing a surface texture, it is important not to increase an average surface roughness R_a significantly, as rougher surfaces tend to have a higher coefficient of friction. The initial surface roughness of steel discs was $R_a = 0.2 \mu\text{m}$. In this research, two electropolishing parameters were varied: current density and electropolishing time. Generally, the higher current density and/or longer electropolishing time, the larger reduction in surface hardness and change in geometry can be expected. The results of produced electropolished surfaces are presented in Table 19.

Table 19. Surface parameters of electropolished steel surfaces [18]

Current density, A/dm ²	Time, min	Mass loss, g	R_a , μm	R_q , μm	R_{sk} , -	R_{ku} , -	R_k , μm	R_{pk} , μm	R_{vk} , μm
15	5	0.041	0.46	0.62	-0.08	3.3	1.38	0.48	0.62
25	15	0.37	0.27	0.41	-0.93	6.13	0.78	0.30	0.62
30	5	0.18	0.27	0.37	-1.15	7.13	0.93	0.34	0.98
30	10	0.35	0.31	0.44	-1.25	6.63	0.80	0.28	0.93
30	15	0.41	0.43	0.61	-1.39	6.61	1.05	0.34	0.86
40	15	0.47	0.34	0.44	-0.51	4.44	1.02	0.38	0.75
50	15	0.47	0.39	0.48	-0.79	4.83	1.11	0.36	0.77

The current density of 15 A/dm² produced an unacceptable surface with a higher R_a value and skewness $R_{sk} \approx 0$. Current densities of 25 A/dm² and 30 A/dm² yielded acceptable surfaces characterized by a small increase in surface roughness R_a and high R_{ku} and negative R_{sk} values. Higher values of current density (40 A/dm² and 50 A/dm²) produced surfaces with significantly higher R_a values. The current density of 30 A/dm² and electropolishing time of 5 minutes were adopted based on different combinations tested. The evaluating factors were produced surface topography and possible impact on surface hardness and geometry (significant mass loss can indicate a possible change in the outer diameter of the disc as it was the only surface being electropolished).

The hardness profile of steel discs is given in Figure 51. Surface hardness HV 0.2 for ground and electropolished steel discs corresponded to 810 HV and 661 HV, respectively, indicating an 18% reduced surface hardness of electropolished steel. Surface hardness reduction occurs due to the partial removal of a thin hardened layer and the formation of oxide and phosphoric film on the disc surface by electropolishing [43].

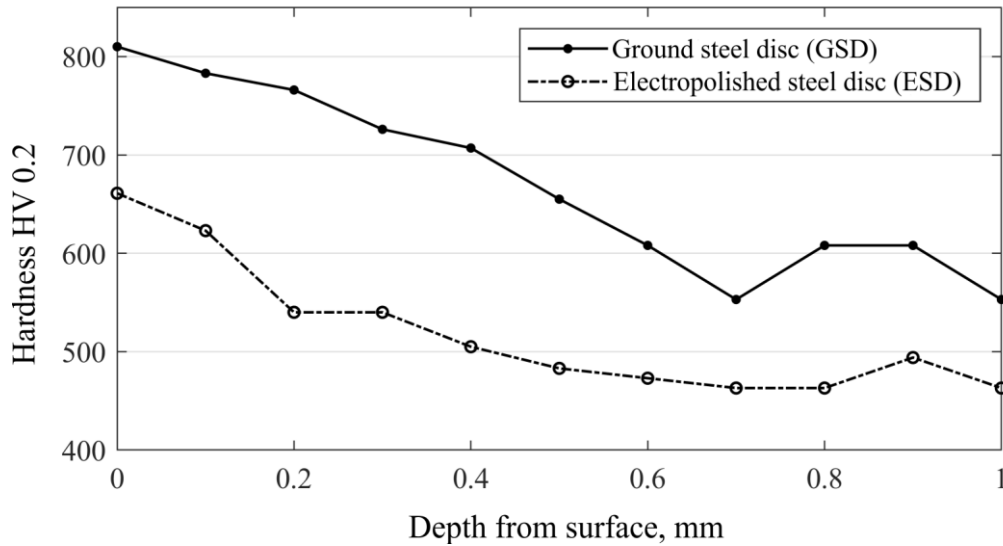


Figure 51. Hardness profile of steel discs [18]

The surface profile was acquired using a Mitutoyo SJ-500 measuring instrument according to the ISO 4287 standard [131]. A comparison of surface profiles of ground and electropolished steel discs is presented in Figure 52. The surface profile of ground steel exhibited a uniform shape with a $R_a = 0.169 \mu\text{m}$ and a $R_{sk} \approx 0$. On the other hand, the surface profile of the electropolished steel had stochastically distributed pits. Pit (dimple) diameter varies from approximately $10 \mu\text{m}$ to $20 \mu\text{m}$, with their depths ranging from $1 \mu\text{m}$ to $4 \mu\text{m}$. The surface pits on the electropolished steel disc increased the average surface roughness value to $R_a = 0.313 \mu\text{m}$ and changed skewness to $R_{sk} = -1.563$. It must be pointed out that a higher R_a value was primarily a consequence of produced pits. For example, the R_a of the electropolished surface profile measured between profile length from 0.4 mm to 0.6 mm (i.e., between two pits, Figure 52b) had $R_a = 0.194 \mu\text{m}$, similar to the value of $R_a = 0.169 \mu\text{m}$ measured on ground surface.

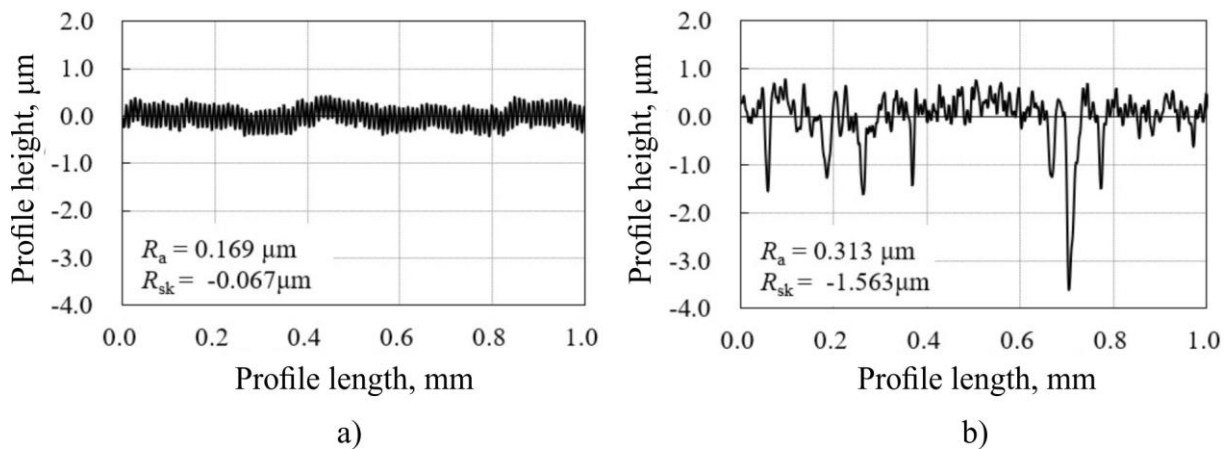


Figure 52. Surface roughness of a) ground steel disc, b) electropolished steel disc [18]

The summary of average surface profile values is provided in Table 20. Steel discs were ground or ground and additionally electropolished. Bronze specimens were milled or ground as these machining processes are commonly used for bronze worm wheel manufacturing.

Table 20. Average surface profile values of investigated steel discs and bronze specimens

Steel disc	R_a , μm	R_q , μm	R_{sk} , -	R_{ku} , -	R_k , μm	R_{pk} , μm	R_{vk} , μm
Ground	0.21	0.24	-0.07	1.88	0.67	0.10	0.14
Ground + Electropolished	0.27	0.37	-1.15	7.13	0.93	0.34	0.98

Bronze specimen	R_a , μm	R_q , μm	R_{sk} , -	R_{ku} , -	R_k , μm	R_{pk} , μm	R_{vk} , μm
Ground	0.13	0.16	0.13	2.73	0.33	0.25	0.09
Milled	0.69	0.86	0.37	2.76	2.09	0.98	0.63

6.4.2 Chemical composition and pit area density

The chemical composition of the ground and electropolished steel surfaces was obtained by Energy Dispersive Spectroscopy (EDS *Oxford Instruments*), presented in Figure 53. The comparison of results is presented in Table 21. The results of electropolished case-carburized 16MnCr5 steel draw a parallel with reported findings on medium carbon steel by Nakatsuji and Mori [43]. Electropolishing passivates the workpiece due to the formation of the oxide surface film and phosphoric compounds as a high percentage of oxygen and phosphorus was observed on the electropolished steel surface. The generation of the phosphate layer is a phenomenon also reported by Gabe [114] when mild steel electropolishing is conducted in phosphoric and sulfuric acid. The author stated that the layer has a role of secondary passivation. The darker appearance of electropolished steel discs can be attributed to changes in chemical composition and produced surface pits (Figure 54).

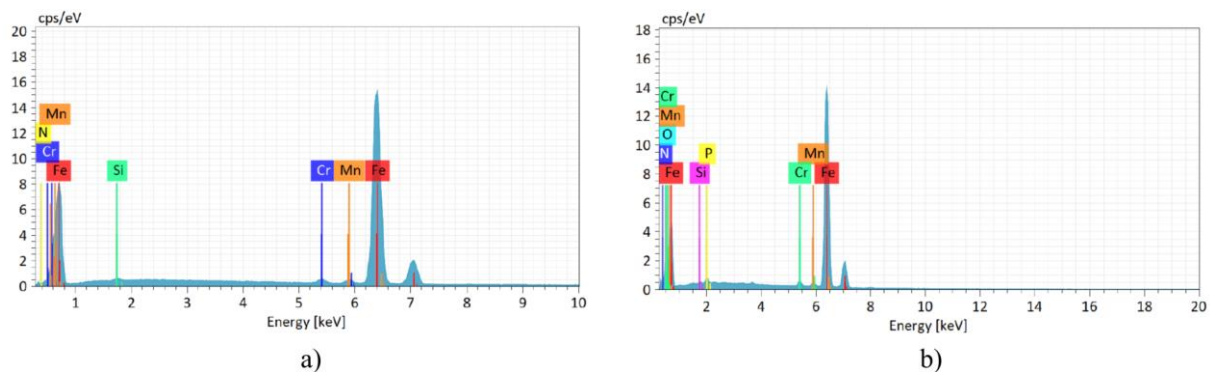


Figure 53. EDS spectrum of a) ground steel disc, b) electropolished steel disc [18]

Table 21. Comparison of surface chemical compositions, wt.% [18]

Element	Fe	O	P	N	Si	Cr	Mn
Ground steel	96.67	-	-	0.85	0.25	0.95	1.35
Electropolished steel	85.78	10.11	0.65	1.06	0.19	1.01	1.19

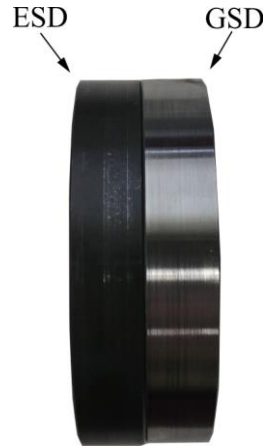


Figure 54. The appearance of electropolished steel disc (ESD) vs. ground steel disc (GSD)

Scanning electron microscope (SEM *Tescan Vega*) images of steel disc surfaces are presented in Figure 55. The ground steel surface was characterized by grinding marks. In contrast, pits of irregular shapes and various sizes characterized the electropolished surface. The distribution of the pits on the electropolished surface was uneven, meaning there were surface regions with sparser and denser pit distributions. This relates to the main drawback of the electropolishing process as surface features/textures cannot be precisely produced and evenly distributed. The pit area density was calculated using commercially available image processing software. In the regions with sparser pit distribution, the pit area density was 5% of the total area. In denser regions, that value increased to 12%. On average, the calculated pit area density was 10%. Area density in the 5–20% range was reported as beneficial in friction reduction in highly loaded non-conformal contacts [38,99,104,106,132].

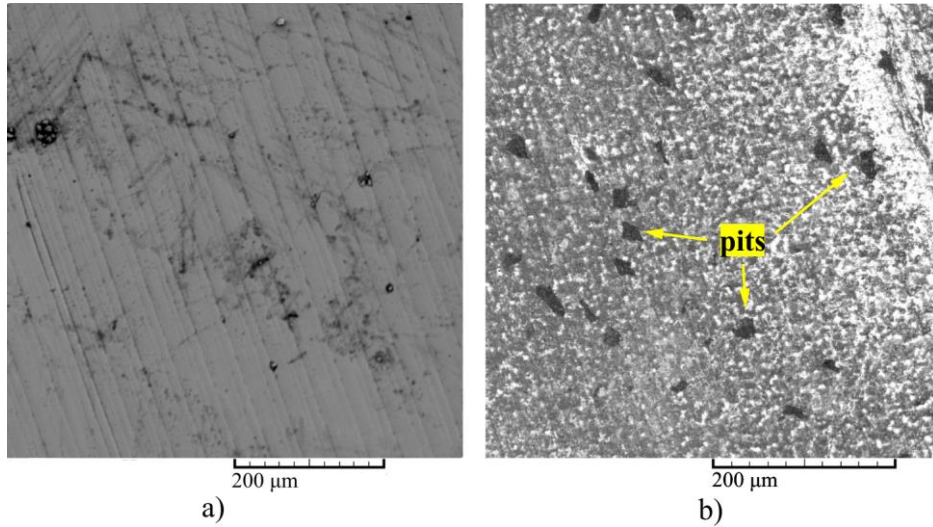


Figure 55. Sem image of a) ground steel surface, b) electropolished steel surface

6.5 Contact characteristics and variable selection

According to the presented experimental setup, the steel disc and the bronze specimen produce initial line contact. The normal load of 500 N was applied in all tests, resulting in the initial Hertzian pressure of 292 N/mm². The load was chosen as a possible design working point regarding the pitting resistance for CuSn12 at 425 N/mm² [3]. The goal was to replicate highly loaded non-conformal contact under mixed and boundary lubrication conditions, similar to those in worm pairs [2]. The film thickness parameter λ is often used to classify lubrication regimes. It is defined as the ratio of the minimum film thickness to the composite surface roughness [60]:

$$\lambda = \frac{h_{\min}}{\sqrt{R_{q1}^2 + R_{q2}^2}} \quad (43)$$

Values $\lambda < 1$ indicate boundary lubrication, $1 < \lambda < 3$ represents mixed lubrication, and $\lambda > 3$ designates hydrodynamic lubrication [62]. Minimum film thickness is represented as h_{\min} while R_{q1} and R_{q2} represent root mean square roughness of the contacting surfaces, in this case, the bronze specimen and the steel disc, respectively. In order to calculate h_{\min} , the corresponding dimensionless film thickness parameter for line contact, H_{\min} , was calculated according to Dowson [133]:

$$H_{\min} = \frac{2.65 \cdot U^{0.70} \cdot G^{0.54}}{W^{-0.13}} \quad (44)$$

A detailed description of the expression (44) can be found in [60,133,134]. Parameters used for calculating H_{\min} are given in Table 22 while the average surface profile values of steel discs and bronze specimens are provided in Table 20.

Table 22. Parameters used for the calculation of H_{\min}

R'	0.03 m	
E'	152 000 N/mm ²	
u_l	0.165 m/s	1.5 m/s
η'	5·10 ⁻³ Pas (at 60 °C)	
α	23·10 ⁻⁹ m ² /N	
U	1.81·10 ⁻¹²	1.65·10 ⁻¹¹
G	3445	
W	2.2·10 ⁻⁵	

The values of H_{\min} ranged from 5.2·10⁻⁶ in the boundary lubrication regime up to 2.5·10⁻⁵ in the mixed lubrication regime. The expression (45) is used to obtain the h_{\min} value:

$$h_{\min} = H_{\min} \cdot R' \quad (45)$$

After values of oil film thickness h_{\min} are known, it is possible to calculate λ values. The λ values in all setups presented in Table 23 ranged from 0.16 to 2.48, indicating a boundary or mixed lubrication regime. The variation in λ values was achieved by employing different sliding speeds (i.e., the rotational speed of a steel disc) and the initial surface roughness of steel discs and bronze specimens (Table 20). For example, sliding speed $v = 0.33$ m/s paired with milled bronze specimens is defined by very low λ values that indicate boundary lubrication regime conditions. In Table 23, “G”, “M”, and “E” stand for “ground”, “milled,” and “electropolished”, respectively, while “SD” and “BS” stand for “steel disc” and “bronze specimen”, respectively. Three test setup comparisons were performed according to the last column in Table 23: 1 vs. 2, 3 vs. 4, and 5 vs. 6. Each test was repeated three times to ensure the reproducibility of the results. The tests were conducted for six hours ($t = 21\ 600$ s) to investigate the duration of the running-in phase for different experimental setups and the coefficient of friction at the start of the test, during the running-in phase, and in a steady-state operation.

Table 23. Sliding test setups

No.	Steel disc	Bronze specimen	Sliding speed, m/s	λ	Lubrication regime	Abbreviation	Comparison
1	Ground	Ground	3	2.48	Mixed	GSD-GBS	1 vs. 2
2	Ground + Electropolished	Ground	3	1.86	Mixed	ESD-GBS	
3	Ground	Milled	3	0.83	Boundary	GSD-MBS	3 vs. 4
4	Ground + Electropolished	Milled	3	0.76	Boundary	ESD-MBS	
5	Ground	Milled	0.33	0.17	Boundary	GSD-MBS	5 vs. 6
6	Ground + Electropolished	Milled	0.33	0.16	Boundary	ESD-MBS	

6.6 Results and discussion

6.6.1 Friction and wear

The results of sliding tests are presented for two sliding times:

- a) In the first three minutes of the test ($t = 180$ s), initial non-conformal line contact can be assumed without a change in contact geometry. The assumption is that no significant bronze wear occurred during that period, and λ values from Table 23 are applicable. Results are presented in Figure 56.
- b) Total sliding time ($t = 21\ 600$ s) during which characteristic periods such as running-in and steady-state period can be observed with a corresponding coefficient of friction at the start of the test, during the running-in, and in a steady-state operation. Results are presented in Figure 58.

In the mixed lubrication regime defined by $\lambda = 2.48$ and $\lambda = 1.86$, and the boundary lubrication regime defined by $\lambda = 0.76$ and $\lambda = 0.83$, electropolished steel lowered the coefficient of friction significantly compared to ground steel (ESD-GBS vs. GSD-GBS pair, Figure 56a, and ESD-MBS vs. GSD-MBS pair, Figure 56b). However, in the boundary lubrication regime defined by $\lambda = 0.16$ and $\lambda = 0.17$, the electropolished steel increased the coefficient of friction in relation to ground steel (ESD-MBS vs. GSD-MBS pair, Figure 56c).

A coefficient of friction comparison for non-conformal line contact is provided in Figure 57. Electropolished steel surface reduced friction in the mixed lubrication regime and the upper range of the boundary lubrication regime ($\lambda = 0.76$ and $\lambda = 0.83$). ESD-GBS and ESD-MBS pairs had a 30% and 25% lower coefficient of friction compared to GSD pairs, respectively.

The electropolished surface had a higher R_q , contributing to lower λ values than the ground surface. Generally, rougher surfaces tend to increase friction, but induced surface pits provide a far greater friction reduction effect. This can be attributed to several factors:

- Surface pits act as lubricant reservoirs providing the functionality of micro-hydrodynamic bearings resulting in a local increase in the oil film thickness and a lower coefficient of friction [135,136].
- Dimples can entrap wear debris, especially in boundary lubrication regimes [94].
- Kovalchenko et al. [32,137] reported that the coefficient of friction is significantly reduced under a mixed lubrication regime as well as that surface texturing helps to expand the load- and speed-range for which mixed or hydrodynamic lubrication regime occurs.

However, the results were different in the lower range of the boundary lubrication regime ($\lambda = 0.16$ and $\lambda = 0.17$). The ESD-MBS pair had a 50% higher coefficient of friction compared to the GSD-MBS pair. The load in the boundary lubrication regime is completely supported by asperity-asperity interactions, meaning an increase in surface roughness plays a crucial role. Surface pits induced through electropolishing increase surface roughness, creating more asperity interactions (Table 20). Additionally, some reported findings expand the general understanding of surface texturing problems in highly loaded non-conformal contacts:

- For a given oil viscosity, a specific size of dimples is necessary for the maximum pressure buildup. Moreover, one set of texturing parameters cannot be optimal in all applications and for all operation points [98]. This suggests there is a possibility that produced surface pits are not optimal for operation in boundary lubrication regimes defined by low λ values.
- Under high load slow speed conditions, the edge stresses become the dominant factor affecting friction [138].
- If additional lubricant from pits cannot compensate for an increase in roughness and edge stresses, the coefficient of friction will increase [139].

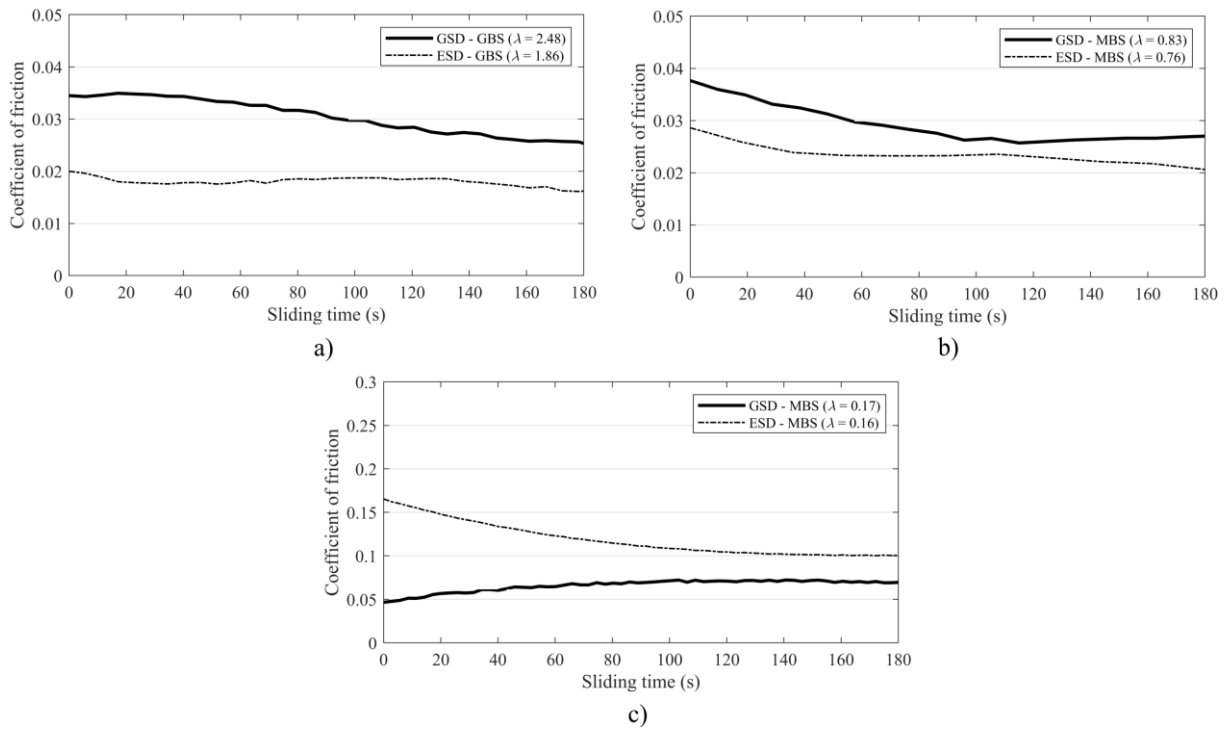


Figure 56. Results of sliding test ($t = 180$ s): a) the ground bronze specimen in the mixed lubrication regime, b) the milled bronze specimen in the boundary lubrication regime, c) the milled bronze specimen in the boundary lubrication regime [18]

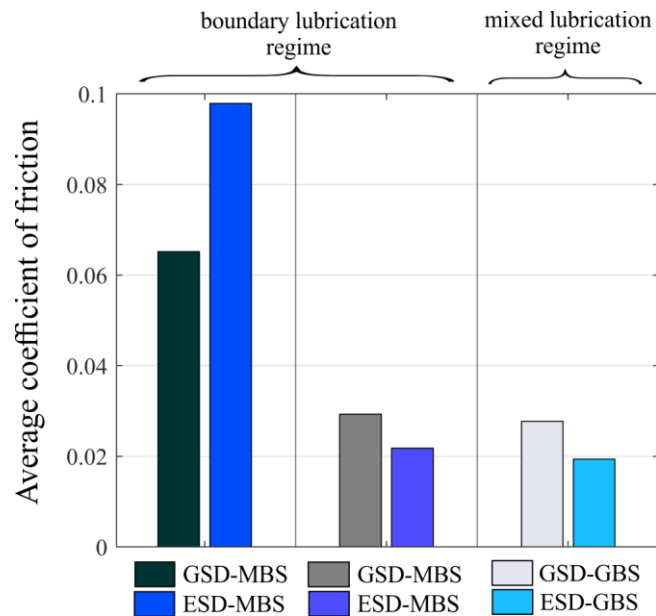


Figure 57. Comparison of coefficients of friction [18]

In sliding tests that lasted for a total sliding time of $t = 21\ 600$ s, electropolished steel performed with a lower coefficient of friction than ground steel for the tests that started in a mixed lubrication regime and boundary lubrication regime defined by $\lambda = 0.76$ and $\lambda = 0.83$ (Figure 58a and Figure 58b). Moreover, ESD pairs displayed a faster transition to steady-state friction

(shorter running-in period). The transition to steady-state friction is caused by bronze specimen wear, resulting in a contact geometry change. At the start of the test, steel discs and bronze specimens produce line contact that gradually changes to rectangular contact patch due to bronze wear (Figure 60). Specifically, contact geometry transforms from non-conformal line contact to more conformal cylinder-inner cylinder contact. A change in contact geometry resulted in a lubrication regime shift from boundary or mixed to hydrodynamic, which can also be observed by the lower coefficient of friction [18].

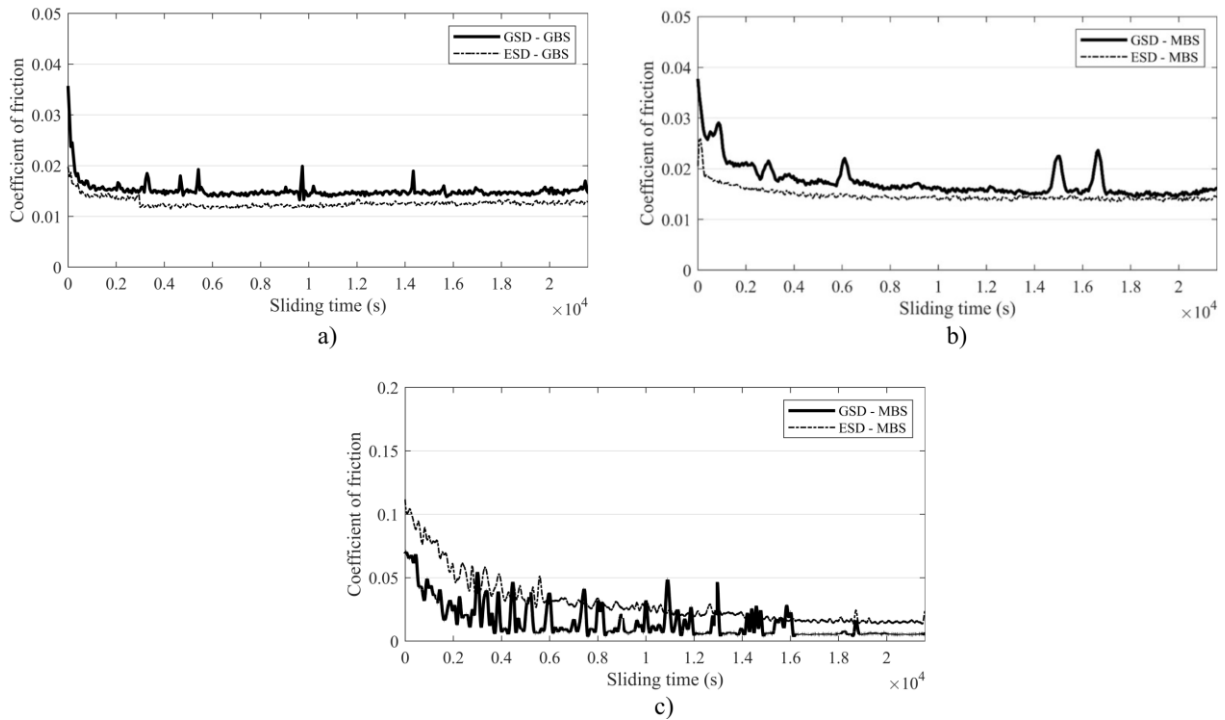


Figure 58. Results of the sliding test ($t = 21\ 600$ s): a) the ground bronze specimen in the mixed lubrication regime, b) the milled bronze specimen in the boundary lubrication regime, c) the milled bronze specimen in the boundary lubrication regime [18]

The bronze wear was assessed by measuring the contact patch area on bronze specimens after the test (Figure 59). Most of the wear occurred during initial line contact and transitioning to a more conformal rectangular patch contact. During this running-in period, the coefficient of friction gradually lowered until a steady-state friction was achieved. Low and unchanged coefficient of friction values indicate the onset of a hydrodynamic lubrication regime where the fluid film fully supports contacting surfaces and no further bronze wear occurs. A slightly larger contact patch area indicates that ESD produced more bronze wear. The difference in contact patch area can be attributed to a noticeable difference in starting λ values. As electropolished surfaces were characterized by higher R_a and R_q values, the λ value for the ESD-GBS pair ($\lambda = 1.86$) was considerably lower than the GSD-GBS pair ($\lambda = 2.48$). The difference in λ values indicated a more severe mixed lubrication regime for the ESD-GBS pair.

On the other hand, when the difference in starting λ values was smaller, i.e., GSD-MBS ($\lambda = 0.83$) and ESD-MBS ($\lambda = 0.76$), the difference in bronze wear was also smaller. Bronze wear was similar for ESD and GSD pairs that started from the boundary lubrication regime defined by $\lambda = 0.16\text{--}0.17$, as their λ values are essentially the same. The data shows that rougher electropolished steel discs (ESDs) produce additional wear. Similar findings for textured surfaces have been reported by Kovalchenko et al. [32] and Wos et al. [140].

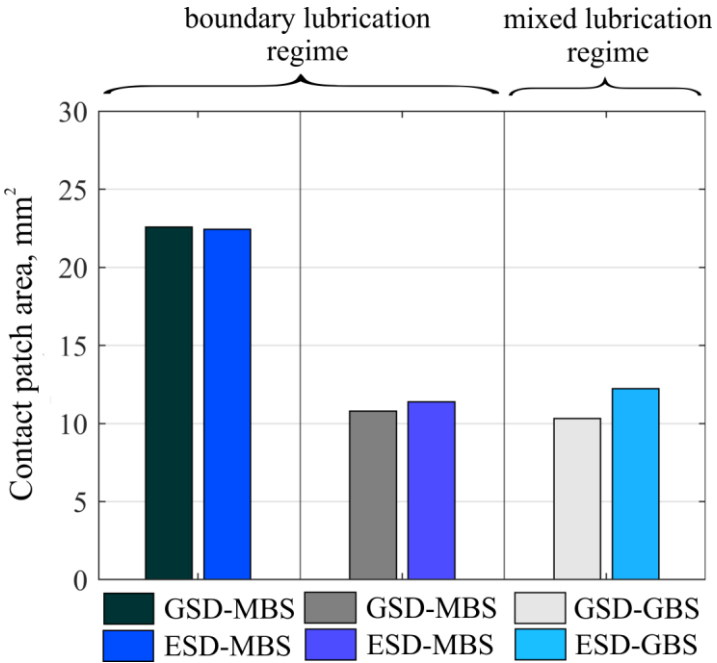


Figure 59. Comparison of bronze specimen wear [18]

Wear results suggest faster running-in for ESD, which was accompanied by somewhat higher wear. Ibatan et al. [94] and Gachot et al. [95] stated that surface texturing in highly loaded non-conformal contact tribological systems provides friction reduction through initial wear generation, allowing a transition of lubricated contact from the high friction boundary regime to the lower friction mixed regime. The mentioned effect could be beneficial if potential accelerated wear on the surface is acceptable. However, higher wear may be problematic for high-precision components. In practice, this finding could benefit components that heavily depend on proper and efficient running-in, such as gears and worm pairs. In contrast to gears where the contact is often established between two hardened steel surfaces, in worm pairs the contact is established between the hard (steel worm) and soft component (worm wheel). Accelerated bronze wear is inevitable in this case as the worm wheel slowly adjusts to a mating worm through wear. This effect could prove beneficial for hard-soft component systems as it promotes more efficient running-in.

6.6.2 State of surfaces after the tests

Surfaces were investigated by EDS and SEM after the sliding tests. The bronze surface can be seen in Figure 60, while the electropolished steel surface is presented in Figure 61. EDS analysis was conducted on two portions of the electropolished surface: base surface and wear track (Figure 61b). Also, wear track of the bronze specimen was inspected as well. The difference in chemical composition, mainly evident in the reduction of oxygen and phosphorus, indicates partial removal of the oxide and phosphate layer from the electropolished steel surface and partial transfer of oxide compounds on the bronze surface (Table 24).

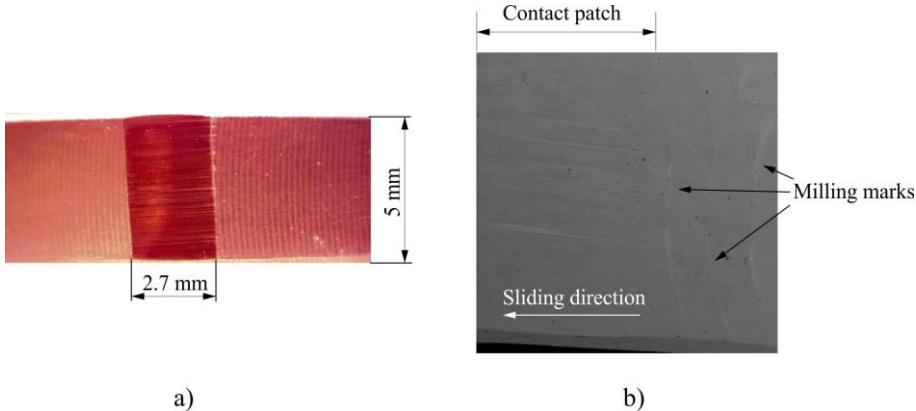


Figure 60. Bronze specimen after the test: a) rectangular contact patch [18], b) SEM image of the surface

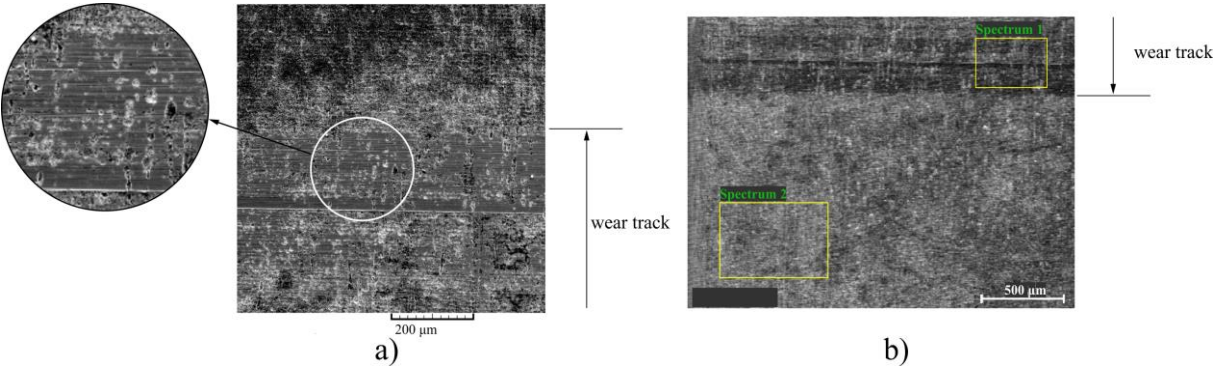


Figure 61. Electropolished steel surface after the test: a) visible pits on wear track, b) marked locations analyzed by EDS [18]

Table 24. EDS inspection of surfaces after the test, wt.%

Element	Fe	O	P	N	Si	Cr	Mn
Spectrum 1 (wear track)	94.31	2.38	0.21	0.55	0.26	1.02	1.27
Spectrum 2 (base surface)	85.78	10.11	0.65	1.06	0.19	1.01	1.19
Bronze (wear track)	0.35	4.94	0.03	-	0.12	-	-

Besides surface pits, the formation of an oxide surface layer due to the electropolishing process could be an additional contributing factor in friction reduction. Hager and Evans [141] showed that black oxide surfaces yield a similar or lower coefficient of friction than untreated surfaces and exhibit increased wear in low λ value conditions in oil-lubricated rolling/sliding contacts. Ueda et al. [142] investigated the influence of black oxide coatings on micropitting. The conclusion was that black oxide coating prevents micropitting on the mating surface through optimization of the running-in process. The findings in [141] and [142] correlate well with findings reported for electropolished steel surfaces presented in this research. Another chemical element in the surface layer of electropolished steel was phosphorus, indicating phosphates derived from phosphoric acid (H_3PO_4). Although its content is relatively small compared to oxygen (0.65 vs. 10.11 wt.%), phosphorus is commonly used in various friction reduction additives and coatings [143,144]. Its presence could also have contributed to the friction reduction observed in this research. As the results suggest, the oxide surface layer experienced significant wear during the running-in period and, as such, fulfilled the function of coating only for a shorter period, as opposed to conventional coatings, which are more durable [18].

Additionally, the surface profile of the electropolished steel wear track was inspected (Figure 62). According to the measured profile, no changes in R_a or R_{sk} values were detected and surface pits can still be distinguished (see Figure 61a). Based on the presented results, it can be concluded that no noticeable wear of the electropolished steel surface occurred despite the reduced surface hardness of electropolished steel.

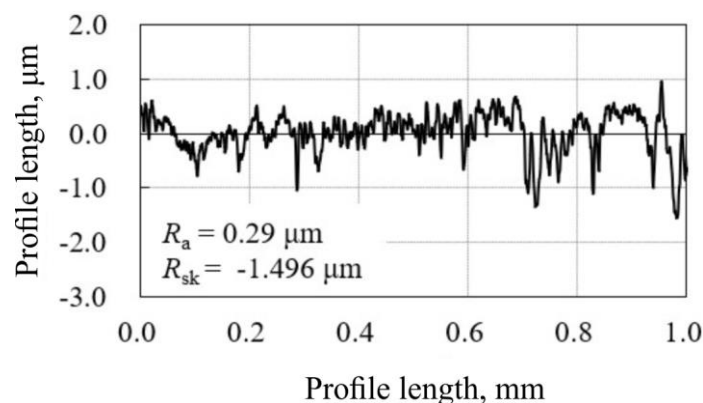


Figure 62. The surface profile of electropolished steel wear track [18]

The coefficient of friction results for non-conformal line contact (Figure 57) can also be visualized as an approximated Stribeck curve (Figure 63). The benefits of the electropolished surface first become evident in the boundary lubrication regime defined by $\lambda \approx 0.5$. As the λ value increases, and mixed lubrication regime is established ($1 < \lambda < 3$), the

coefficient of friction reduction becomes less significant. It is important to note that for the same sliding test conditions, electropolished steel discs (ESD) operated in lubrication regimes defined by lower λ ratios due to surface roughness changes. The employed electropolished surface lowered the λ ratio from 2.48 to 1.86 and 0.83 to 0.76. However, such lubrication regimes defined by lower λ ratios demonstrated significant friction reduction compared to ground steel discs (GSD). According to the presented Stribeck curve, positive effects should be expected for $\lambda > 0.5$, while for lower λ values, the coefficient of friction increases.

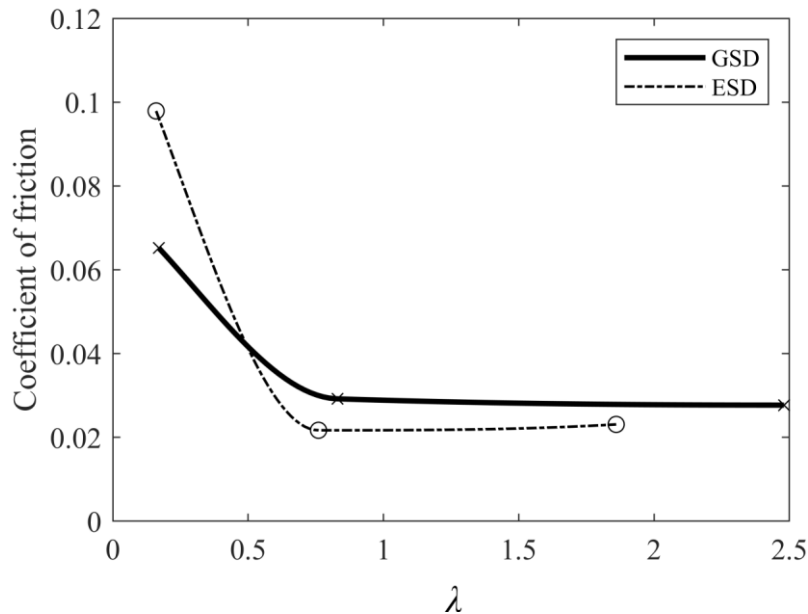


Figure 63. Stribeck curve for electropolished vs ground steel [18]

6.7 Summary

In this chapter, the tribological behavior of an electropolished steel-bronze pair was presented based on block-on-disc experimental sliding tests, surface topography evaluation, and surface chemical composition. The results were compared to the ground steel-bronze pair. The aim was to simulate tribological conditions found in worm pairs and evaluate the benefits of electropolished steel surfaces in such circumstances. The following conclusions can be drawn:

- Electropolished steel surface was modified in two ways: by creating surface texture in the form of surface pits and dimples and by generating a surface coating in the form of an oxide surface layer
- Compared to the ground steel-bronze pair, electropolished steel reduced friction by 25% and 30% in the boundary and mixed lubrication regimes defined by $\lambda = 0.76$ up to $\lambda = 2.48$. In a boundary lubrication regime defined by $\lambda < 0.5$, an increase in the coefficient of friction should be expected

- Electropolished steel surfaces resulted in slightly higher wear and faster running-in. This phenomenon was attributed to a higher average surface roughness R_a and formed oxide surface layer on the electropolished steel surface. Faster running-in could benefit machine components that depend on proper and efficient running-in, such as worm pairs.

Based upon the successful application and investigation of the electropolishing effect in steel-bronze pair, the continuation of the research will be aimed towards employing electropolishing on a hardened steel worm and investigating such worm pair behavior in working load conditions. The results will be compared to a conventional material pair: ground and hardened steel worm and bronze worm wheel. The expected improvement of lubrication conditions by employing electropolished worms should primarily be evident in higher overall efficiency (lower coefficient of friction) or lesser worm wheel tooth damage (pitting and wear).

7

Finite element model

This chapter presents the worm pair finite element method (FEM) model developed for evaluating load and stress distribution in worm pairs. The model is focused on real geometry worm pairs, meaning it is used to investigate worm pairs “as manufactured”, rather than ideal worm pair geometry. The goal of the FEM model is to gain a better understanding of how real geometry affects load and stress distribution in worm pairs. The FEM model is verified with ISO/TS 14521 standard. This FEM model, in its simplified form, was published in the article *Numerical Model for Worm Gear Pair Inspection Based on 3D Scanned Data* authored by Mašović, R.; Breški, T.; Čular, I.; Vučković, K.; Žeželj, D. [1]. The detailed results of FEM analyses are presented in chapter 9. *Results and discussion*.

7.1 Finite element method model

The finite element method (FEM) model was developed via commercially available software Abaqus-Standard [145] to obtain load and stress distribution in investigated worm pairs. The 3D optical scans of a worm and worm wheel resulted in a fine mesh primarily used for dimensional inspection in GOM Inspect software. In order to effectively employ scans as input geometry for the FEM model, the scans were carefully edited to remove redundant data such as hub, bolt, and shaft before further mesh processing. The edited mesh was then used to create closed-surface models based on the underlying mesh. Deviations from the underlying mesh of the worm wheel surface model are shown in Figure 64. Worm wheel surface flanks

were fitted with a deviation of less than 1 μm . Higher deviations, up to 5 μm , were present in edges and parts of the model that were not considered as contacting surfaces. Therefore, the surface accuracy in those regions was not of vital importance.

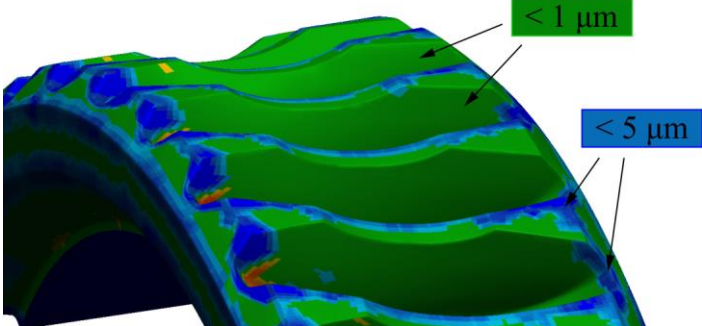


Figure 64. Surface model deviations

Created surface models were CAD models that represent the solid bodies of the worm and worm wheel. This process was needed as 3D scanned data is usually stored in STL format, which is unsuitable for easy manipulation or mesh editing in Abaqus-Standard. However, CAD models in their respective formats, e.g. SAT format, can be easily manipulated and edited in Abaqus-Standard. This enables easier optimization in terms of the type and number of finite elements used in the FEM model. The above-described process is illustrated in the worm wheel example in Figure 65. The same process was repeated for the worm CAD model.



Figure 65. Worm wheel model creation [1]

The modulus of elasticity and Poisson’s ratio for the worm made of 16MnCr5 steel were $E = 210\,000\text{ N/mm}^2$ and $\nu = 0.3$, respectively. The modulus of elasticity and Poisson’s ratio for bronze worm wheels made of CuSn12 were $E = 90\,000\text{ N/mm}^2$ and $\nu = 0.35$, respectively. The material was assumed to be homogeneous, isotropic, and linear-elastic. This FEM model was based upon the model presented in [15], where worm pair contact was modeled for a static

loading case. The model presented in this research additionally accounts for the worm pair’s rotation and worm shaft deflection. The model represents real contact patterns and load and stress distribution during a meshing cycle. A schematic representation of the finite element model is shown in Figure 66. Reference point RP_1 was constrained via *kinematic coupling* to the inner surface of the worm wheel. Reference points RP_2 and RP_3 were constrained via *kinematic coupling* to the outer surfaces of the worm shaft.

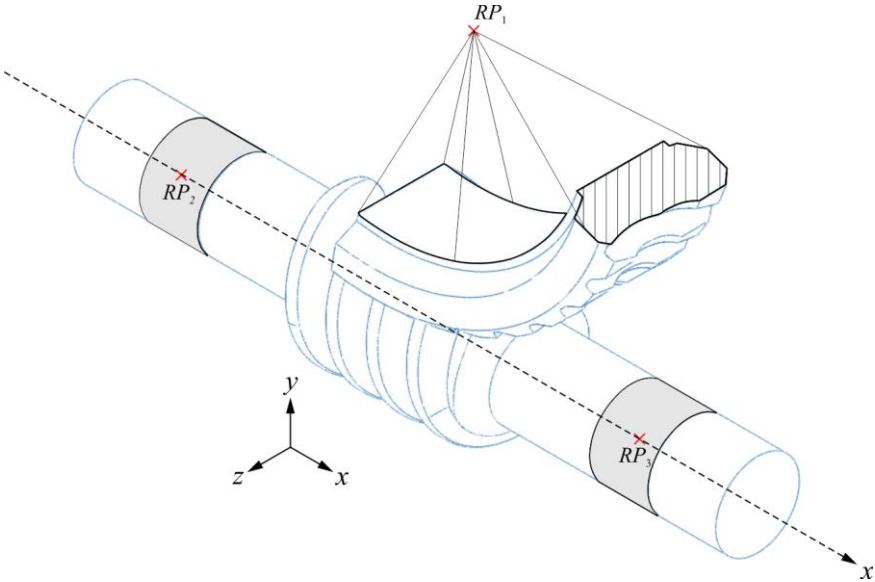


Figure 66. Schematic representation of finite element model

The model also accounts for the deviations obtained by inspecting 3D optical scan of the housing. The center distance and shaft angle deviation were considered in the model (Figure 67).

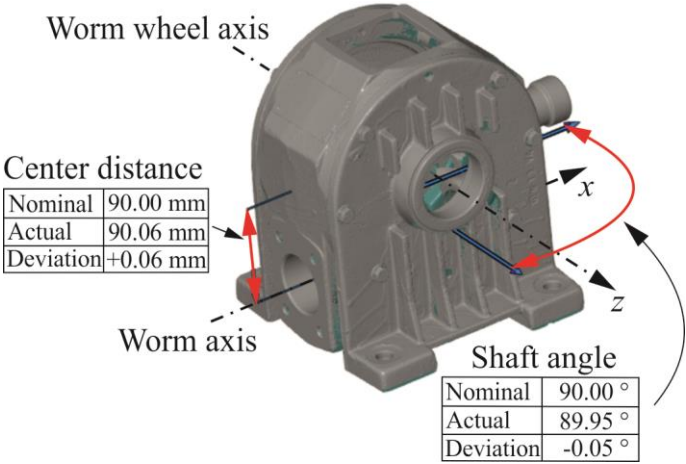


Figure 67. Housing deviations

7.1.1 Contact definition

Contact between the worm thread flanks and worm wheel flanks was established as *normal behavior*, with the softened *pressure-overclosure* relationship. Also, *tangential behavior* with *penalty* friction formulation was included with a coefficient of friction set at 0.04. Worm thread flanks were selected as *master* surfaces, while worm wheel flanks were selected as *slave* surfaces. Softened contact defined with a *pressure-overclosure* relationship was employed to mitigate problems with *hard contact* formulation in combination with tetrahedral elements. The default *hard contact* formulation may lead to local chattering and non-convergence of the solution, especially in tetrahedral elements such as C3D10 elements. In these cases, contact constraints associated with nodes at the corners of C3D10 elements are likely to chatter due to uneven force distributions for these elements. If the analysis does converge, the contact pressures are likely to be noisy even though the underlying element stresses are probably quite accurate. Also, convergence with slave surfaces based on C3D10 elements is improved if a softened *pressure-overclosure* contact is specified [146]. In this analysis, the *pressure-overclosure* relationship was defined by pressure at zero clearance $p_0 = 323 \text{ N/mm}^2$ (Hertzian contact pressure according to ISO/TS 14521, $\sigma_{Hm} = 323 \text{ N/mm}^2$, expression (5)) and clearance at zero pressure $c_0 = 0.005 \text{ mm}$ (Figure 68).

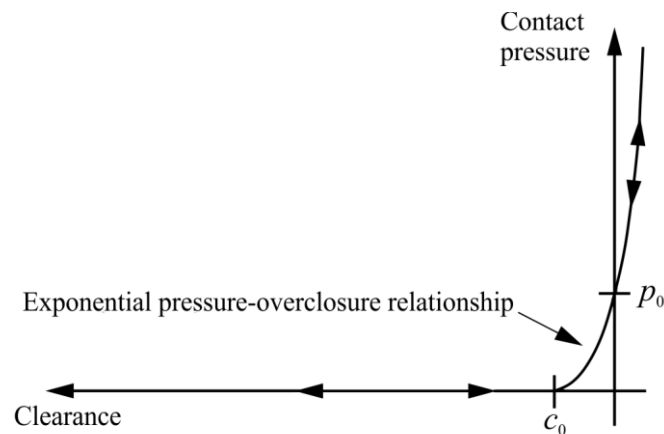


Figure 68. Pressure-overclosure relationship

7.1.2 Simulation steps and boundary conditions

The simulation was divided into two steps:

1. Application of torque T and establishing the contact
2. The input angle ϑ was assigned to the worm to enable rotation of the worm and worm wheel about their respective axes

In the first step, only rotational displacement about RP_1 was allowed. Translational degrees of freedom and a rotational degree of freedom about the worm axis were restricted in RP_2 , while translational degrees of freedom in the Y and Z directions were restricted in RP_3 . In the second step, boundary conditions were kept the same with a rotational degree of freedom about the worm axis allowed to enable worm rotation due to input angle ϑ . The non-linear geometry (NLGEOM) option is turned on within Abaqus-Standard to account for the effect of geometric nonlinearity due to large displacements induced by the incremental rotation of the worm and worm wheel. The second step was separated into ~ 200 time frames, with each frame representing a static loading case. Thus, a quasi-static simulation is achieved. In this way, a period defined by one worm wheel tooth entering and leaving the mesh was divided into 60 to 85 frames to ensure adequate resolution of the obtained results. The difference in the number of frames was because some analyses were conducted with worm pair geometry before running-in, and others were conducted with worm pair geometry at the end of the test. At the end of the test, the contact pattern was much larger than during running-in, and a higher contact ratio was achieved.

7.1.3 Element selection

The worm and worm wheel were meshed with second-order modified tetrahedral elements C3D10M. Tetrahedral elements were employed due to the worm and worm wheel's highly curved and complex surfaces. The difference between C3D10 and C3D10M is in additional mid-face nodes that generally solve contact problems much better, although with higher computational costs. This element is robust for large-deformation problems and contact problems using either the traditional node-to-surface or the surface-to-surface contact discretization and exhibits minimal shear and volumetric locking [145]. Also, C3D10M elements tend to underpredict maximum contact stress for highly localized stress concentration areas, whereas C3D10 elements may tend to overpredict maximum contact stress values [146]. The approximate mesh size on contacting surfaces was 2 mm on the worm thread flanks and 0.5 mm on the worm wheel flanks. Convergence analysis of worm pair contact problem was

conducted in [147]. The results showed that an approximate worm mesh size of 3 mm and worm wheel flank mesh size of 1 mm already provide acceptable results. The approximate total number of elements in the model was 50 000 for worm mesh and 80 000 for worm wheel mesh (Figure 69).

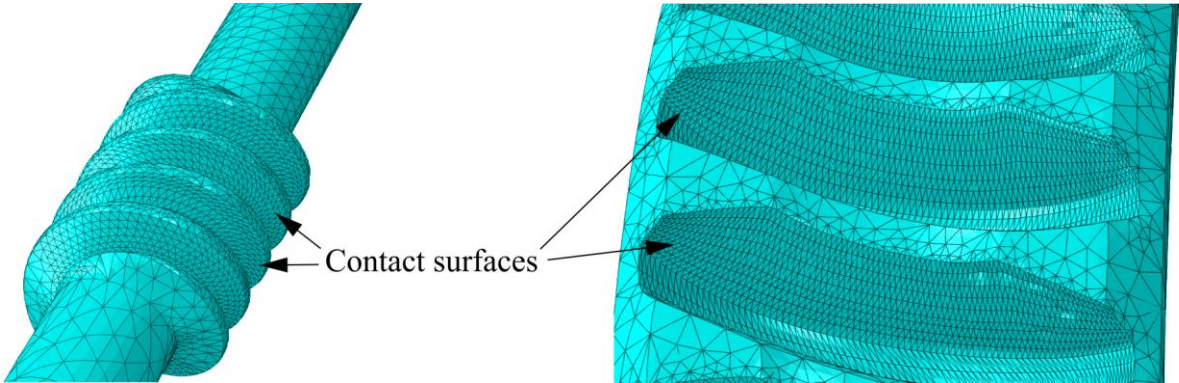


Figure 69. Worm pair mesh

7.2 Model verification

Model verification was conducted by comparing the value of worm shaft deflection obtained by the FEM model with the analytical value obtained through ISO/TS 14521 [3]. Important dimensions for shaft deflection calculation are bearing spacings, as shown in Figure 70. In this study, worm shaft geometry was characterized by bearing spacing values $l_1 = 140$ mm and $l_{11} = l_{12} = 70$ mm.

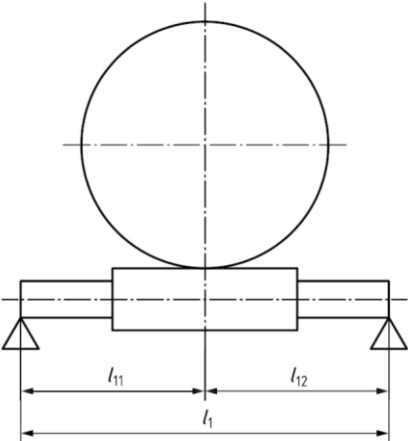


Figure 70. Bearing spacing according to ISO/TS 14521 [3]

According to ISO/TS 14521, for symmetrical bearing spacing ($l_{11} = l_{12}$), the resultant deflection can be estimated by the expression (46). The values used for calculation are given in Table 25.

$$\delta_m = 2 \cdot 10^{-6} \cdot l_1^3 \cdot F_{tm2} \cdot \frac{\sqrt{\tan^2(\gamma_{m1} + \arctan \mu_{zm}) + \tan^2 \alpha_0 / \cos^2 \gamma_{m1}}}{(1.1 \cdot d_{f1})^4} \quad (46)$$

Table 25. Values used for calculation of deflection of the worm

Variable	Value
l_1 , mm	140
F_{tm2} , N	4166
γ_{m1} , °	12.53
μ_{zm} , -	0.04
α_0 , °	20
d_{f1} , mm	26
δ_m , mm	0.016

The results of the deflection of the worm obtained by the developed FEM model are presented in Figure 71. The analysis was conducted with applied torque $T_2 = 300$ Nm ($F_{tm2} = 4166$ N). The presented results represent the change in the deflection during the worm's revolutions. The maximum deflection was 0.015 mm. The results of finite element analysis agree with the value $\delta_m = 0.016$ mm obtained by expression (46). Additionally, the contact pattern in Figure 72 was in accordance with the contact pattern obtained during the experimental testing of worm pairs.

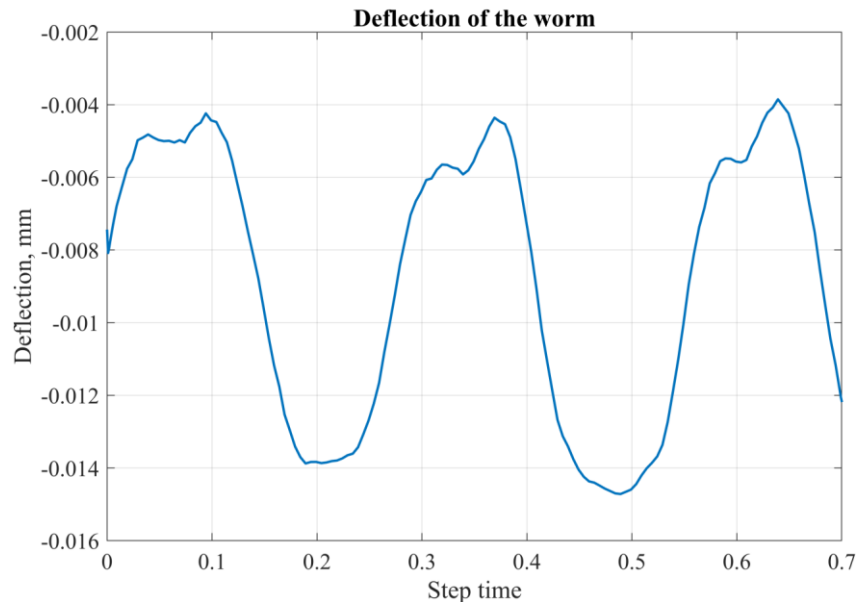


Figure 71. Worm deflection obtained by developed FEM model

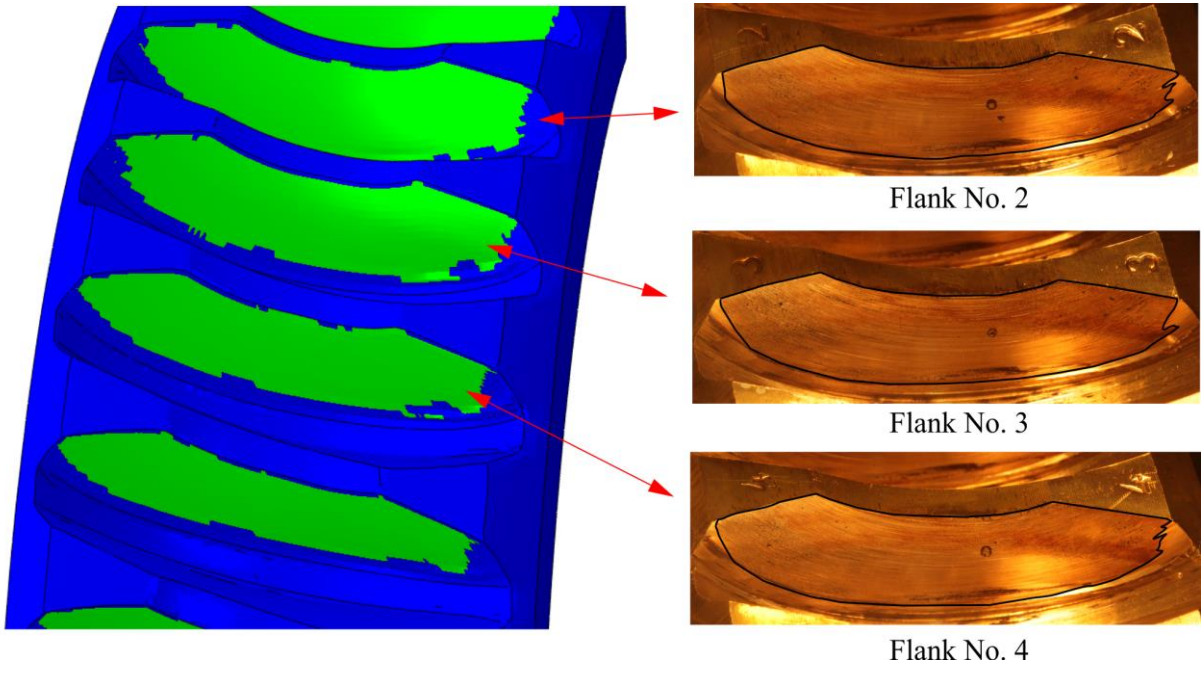


Figure 72. Comparison of contact patterns

8

Worm pair experimental setup

This chapter covers the experimental setup employed for worm pair testing. Also, the worm pair testing procedure, which included the running-in process, digital imaging of the worm wheel flank, and image post-processing, will be described. Worm pair experimental testing was performed in the Laboratory for Machine Elements at the Faculty of Mechanical Engineering and Naval Architecture, Zagreb.

8.1 Experimental setup

8.1.1 Gearbox and worm pair material combinations

The worm pair gearbox, presented in Figure 73, was a commercially available gearbox with specifically designed modifications for camera positioning and associated equipment for image acquisition of damaged worm wheel flanks. The same gearbox type was used in studies [25,53,54,148]. Roller bearings were used in both worm and wheel shaft. The bearings were replaced after every test run. Continuous lubrication was supplied through the top of the gearbox directly onto the worm wheel. The worm wheel carried the oil into the mesh with the worm positioned beneath.

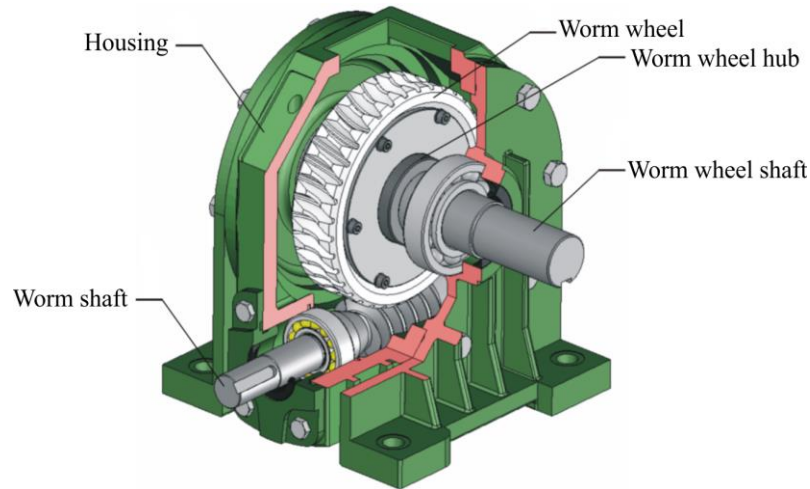


Figure 73. Gearbox CAD model [25]

The tested worm pair combinations are presented in Table 26. The focus was on 16MnCr5-CuSn12 worm pairs based on two motives. Firstly, it is a widely used worm pair material combination and is also considered a referent material combination by the current standard [3]. Secondly, based on favorable experimental results for the electropolished steel-bronze pair presented in Chapter 6, the comparison between worm pairs using electropolished worms and conventional worms was carried out to determine the effects of electropolishing in worm pairs during exploitation. For the remainder of this thesis, worm pairs operating with electropolished worm will be designated by abbreviation (*EP*). A worm pair employing CuAl10Fe5Ni5 bronze worm wheel was tested to compare its efficiency with CuSn12 worm pairs. However, as the abovementioned material is characterized by significantly higher pitting resistance contact stress $\sigma_{HlimT} = 660 \text{ N/mm}^2$, no pitting was observed at the experimental working load of $T_2 = 300 \text{ Nm}$. A worm wheel made of AlSn6 has already been investigated by Opalić [53], Rakamarić [54], and Žeželj [25]. However, as this material is not covered by standard [3] and there is no additional literature besides those mentioned above, this research provides an opportunity to explore AlSn6 as a worm wheel material further. The detailed worm pair geometry and oil specifications were already presented in Figure 10 and Table 7.

Table 26. Tested worm pair combinations

Worm material	Worm wheel material	Load T_2 , Nm	Designation
16MnCr5	CuSn12	300	Worm pair 1
16MnCr5, electropolished	CuSn12	300	Worm pair 2 (EP)
16MnCr5, electropolished	CuSn12	300	Worm pair 3 (EP)
16MnCr5	AlSn6	200	Worm pair 4
16MnCr5	CuAl10Fe5Ni5	300	Worm pair 5
16MnCr5	CuSn12	300	Worm pair 6*
Nominal worm speed	1480 rpm		
Oil inlet temperature	60 °C		
*scuffing occurred due to improper lubrication conditions			

8.1.2 Experimental stand

The experimental stand (Figure 74 and Figure 75) consisted of two main systems: an electro-mechanical system and a measurement system. The working principle of the stand was based on a DC motor/generator (GEN) working in a generator mode, thus providing load to the system. The rotational speed of the driving electric motor (EM) was regulated by frequency inverter (FI). The drive motor shaft was connected to the worm shaft using a shaft torque transducer (TT1) that measured input torque. The worm pair gearbox (WP-GB) output shaft, namely the worm wheel shaft, was connected by the shaft torque transducer (TT2) to the gearbox multiplier (MP). The output shaft torque transducer measured the worm wheel load. The gearbox multiplier (MP) increased the generator input shaft rotational speed. The load produced by the generator was regulated by controlling the excitation current (ECC) supplied to the generator windings. The generator load was the load set on the worm wheel (worm pair gearbox output torque, T_2). The generator produced electrical energy that was supplied to a heater. Oil circulation was carried out using two oil pumps (OP). The oil was constantly cooled by passing through the oil chiller (OC) and filtered through the oil filter (OF). The oil filter was replaced after every test run.

The measuring system consisted of a frequency inverter (FI), torque transducers (TT1 and TT2), temperature sensors (T1 and T2), and a measuring amplifier (MA) connected to a personal computer (PC). A frequency inverter (FI) was used to regulate the rotational speed of the electric motor (EM). The torque transducer (TT1) measured the input torque, while the torque transducer (TT2) measured the worm pair gearbox output torque (WP-GB). The relationship

between input torque T_1 and output torque T_2 , considering worm pair transmission ratio $i = 18$, can be expressed as gearbox efficiency:

$$\eta = \frac{T_2}{T_1 \cdot i} \tag{47}$$

The temperature sensor (T1) measured the inlet oil temperature. The temperature sensor (T2) was placed underneath the worm, and the outlet oil temperature was measured. All the abovementioned variables were measured periodically using a measurement amplifier and its software package. All acquired data was stored on a personal computer (PC) hard disk.

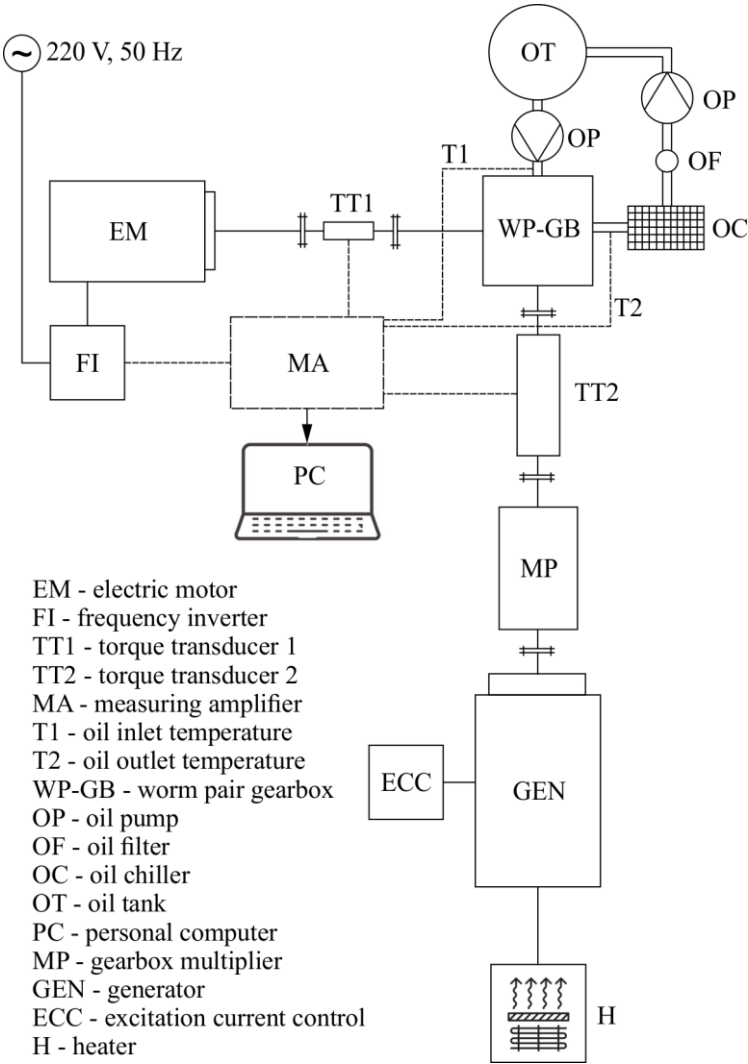


Figure 74. Experimental stand - scheme

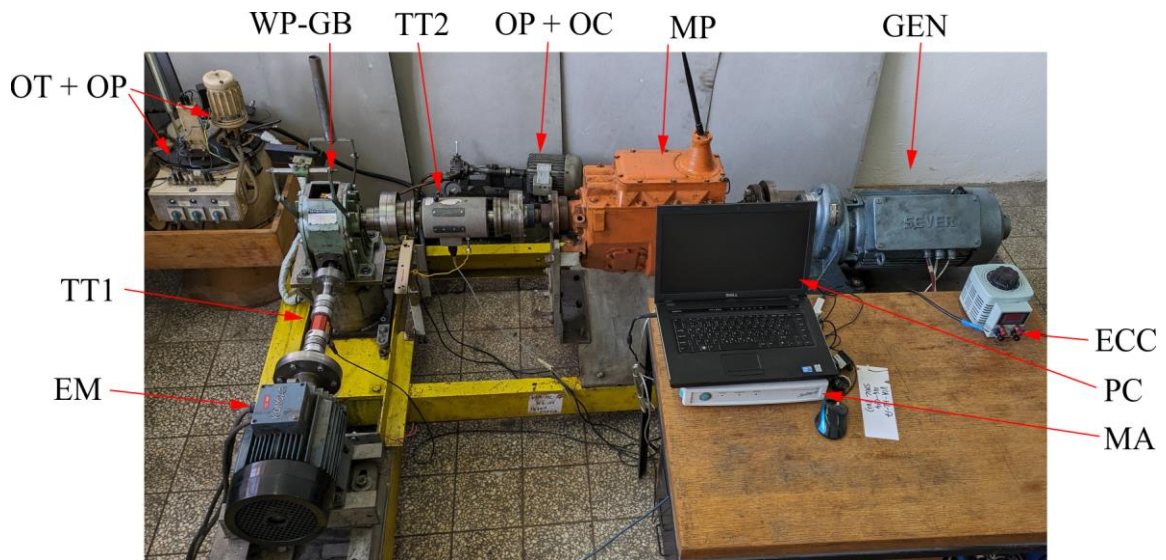


Figure 75. Experimental stand

8.1.3 Digital imaging equipment and requirements

The procedure for digital imaging and positioning was developed during the study [25] and was modified to meet the requirements of this research. The equipment consisted of camera, camera lighting, and auxiliary parts used for camera and worm wheel positioning. The requirements and conditions for worm wheel flank digital imaging were as follows:

- The worm pair gearbox was not disassembled during one experimental worm pair testing. The testing consisted of worm pair mounting and contact pattern adjusting, followed by a running-in procedure and test run. In this way, eventual assembling/disassembling errors were avoided. However, the worm wheel flank digital imaging had to be conducted while the worm wheel was inside the gearbox.
- The flank image had to include the whole flank area.
- The repeatability of imaging had to be assured. This was achieved by a camera positioning assembly and worm wheel positioning assembly mounted directly on the gearbox. The camera positioning assembly consisted of a rigid adjustable frame and 3D printed camera holder, specifically designed for the camera used in this research (Figure 76, parts 10-15). Such assembly ensured precise camera positioning and camera disassembling after images were taken and the test run was continued. The worm wheel positioning assembly (Figure 76, parts 1-6) was also mounted on the gearbox. The main part of the assembly was the pin designed to be inserted into each worm wheel tooth

gap, thus locking the worm wheel into position. This ensured exact flank positioning each time the image was taken.

- Worm wheel flanks were highly reflective surfaces due to the low surface roughness as a result of the worm pair running-in process. As such, the images of flank surfaces captured reflected light instead of the flank surface itself. Moreover, pitted areas on the flank had different surface texture and therefore different light reflection intensities than remainder of the flank. To overcome this problem, proper dimmed lighting conditions needed to be ensured. This was achieved by positioning the primary light source, in the form of two photo lamps, in the desired position. The light from photo lamps passed through the mask made from tracing paper. Tracing paper allowed the light to pass through. However, the passed light was significantly dimmed (Figure 77). This ensured suitable lighting conditions where flank images could be taken, i.e. the pitted areas on the images were easily distinguishable. Additionally, other light sources, such as daylight in the room, were kept to a minimum to ensure minimum interference with established lighting conditions for digital imaging.

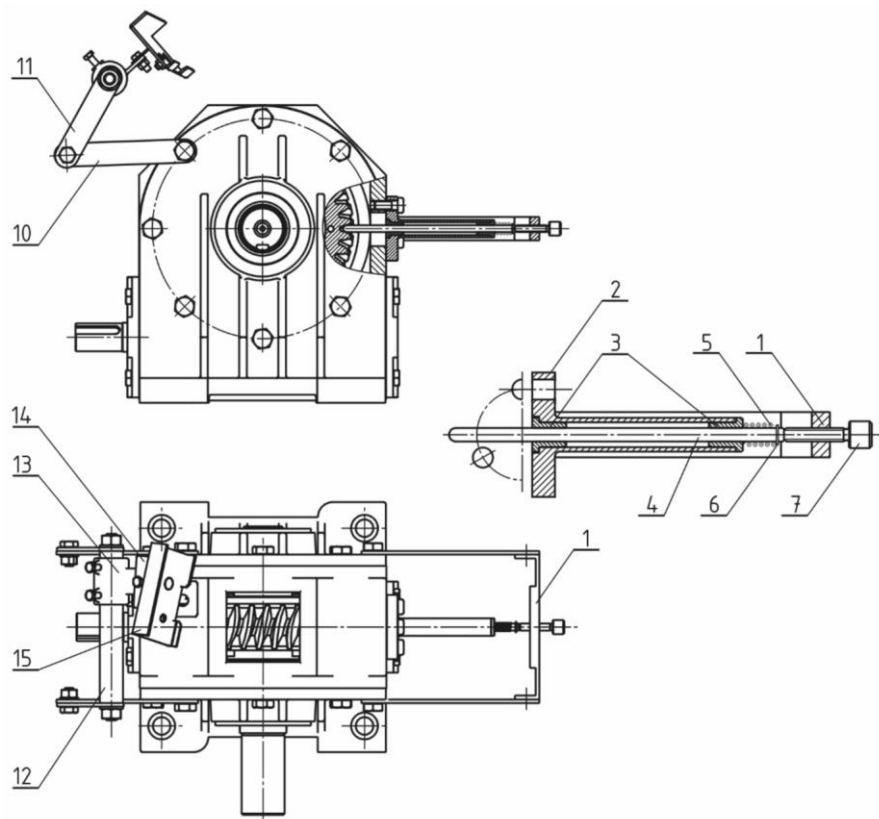


Figure 76. Camera and worm wheel positioning assemblies [25]

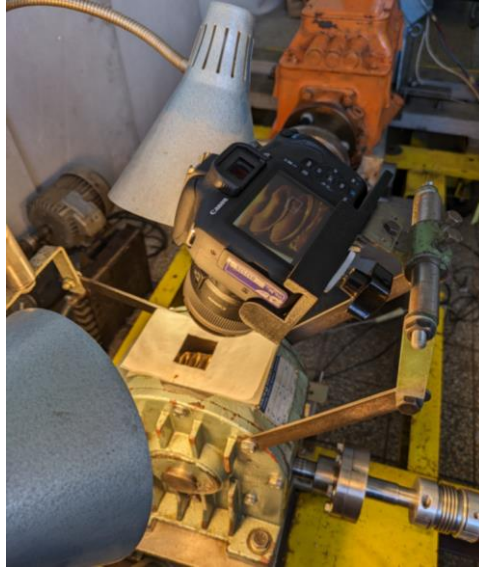


Figure 77. Photographing of worm wheel tooth flank

8.2 Testing procedure

There were two main aims of worm pair experimental testing. The first was to collect data regarding pitting formation and development by taking images of worm wheel tooth flanks in evenly spaced time intervals. The images were later post-processed to measure flank pitting percentage. The second aim was to continuously measure worm pair gearbox efficiency to investigate the effect of the electropolished worm on overall efficiency.

The goal of this research was to investigate pitting initial formation and development. There was no intent to investigate boundary cases of maximum possible pitting percentages. It is known that worm wheels can operate with up to 60% of the pitted flank area, which implies extremely long test runs if testing the worm wheel under acceptable working load conditions. According to [3,25,53], the calculated number of load cycles N_L for the expected pitting area $A_{P10,max}$ varies significantly. Therefore, the end of the test run based on $A_{P10,max}$ could not be unambiguously defined, and the decision on when to end the test was made by observing pitting development. As pitting initiation is defined by $A_{P10} = 2\%$, the tests were run until pitting developed reached a significantly higher value, e.g., $A_{P10,max} \approx 10\%$ or higher.

The overall testing procedure (including measurements conducted before and after the test run) was as follows:

1. 3D optical scanning of worm and worm wheel assembly

2. Surface roughness measurements of worm and worm wheel flank surfaces
3. Installation of worm wheel assembly (shaft, hub, and worm wheel) and worm in the worm pair gearbox
4. Assembling the worm pair gearbox with the experimental stand
5. Calibration of torque transducers
6. Adjustment of initial contact pattern by axial positioning of the worm wheel and contact pattern check by using indigo paste
7. Installation of supplementary equipment - camera positioning and worm wheel positioning assemblies
8. Running-in procedure
9. Continuous testing with nominal load
10. Digital imaging of all 36 teeth flanks
11. Post-processing of acquired images and evaluation of pitting areas (steps 9 to 11 were continuously carried out until the end of the test)
12. 3D optical scanning of worm and worm wheel assembly – after the test
13. Surface roughness measurements of worm and worm wheel flank surfaces – after the test

8.2.1 Contact pattern adjustment and running-in procedure

The initial contact pattern is usually established on the leaving side of the worm wheel tooth flank (Figure 78). The purpose of such a pattern is to provide an oil supply into the contact zone. Such initial contact pattern is achieved by manufacturing the worm wheel using an oversized tool (either hob or fly cutter) and by inclining the tool for a small angle (as discussed in *Geometry and manufacturing of ZN worm pairs*). If the initial contact occurred on the entering side of the flank, the oil would not be supplied towards the center and leaving side of the flank where contact conditions and pressures are more severe.

Due to the right-hand worm, the axial force acts toward the worm wheel shaft output. The bolts were installed through the gearbox housing to act upon the outer bearing ring. The bearing is axially adjusted by bolt tightening, positioning the worm wheel in the desired position inside the gearbox. This way, the contact pattern was adjusted through the running-in procedure until at least 50% of the contact pattern was achieved on the worm wheel tooth flank surface.

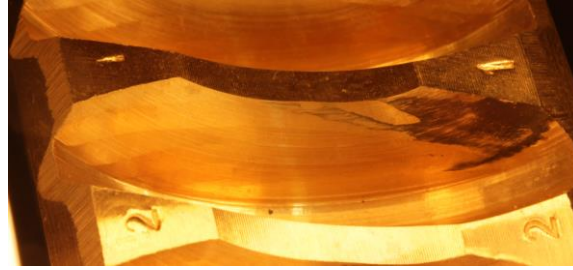


Figure 78. Initial “no load” contact pattern on worm wheel 3

The running-in process is of vital importance for the proper operation of worm pairs. Running-in aims to achieve an adequate worm wheel tooth contact pattern. An appropriate contact pattern ensures better and more uniform load and stress distribution and provides oil supply into the contact zone. After running-in, the contacting surfaces will be smoothed, resulting in a lower coefficient of friction. During running-in, a relatively small portion of the worm wheel tooth flank is in contact, implying that relatively high contact stresses can occur. This is also the reason why high wear rate characterizes running-in. The goal is to conduct running-in in a short period and gradually increase the load as the contact pattern develops to avoid premature fatigue failure of the worm wheel material.

Since there are no standardized guidelines for running-in procedures in worm pairs, the procedure relies mainly on empirical knowledge and known practice. In this research, the running-in guidelines from [25] and [53] were adopted. Running-in was carried out in three steps:

1. Nominal worm speed (1480 rpm) and load $0.4 \cdot T_2$ for 1 h,
2. Nominal worm speed (1480 rpm) and load $0.7 \cdot T_2$ Nm for 1 h,
3. Nominal worm speed (1480 rpm) and load T_2 Nm for 1 h,

The contact pattern was evaluated after each step. If necessary, the worm wheel was axially adjusted. An appropriate contact pattern was established after the third step in each investigated worm wheel. An example of contact pattern development during the running-in process is shown in Figure 79. The contact pattern is highlighted by a black border. The majority of the contact pattern developed through steps 1 and 2.

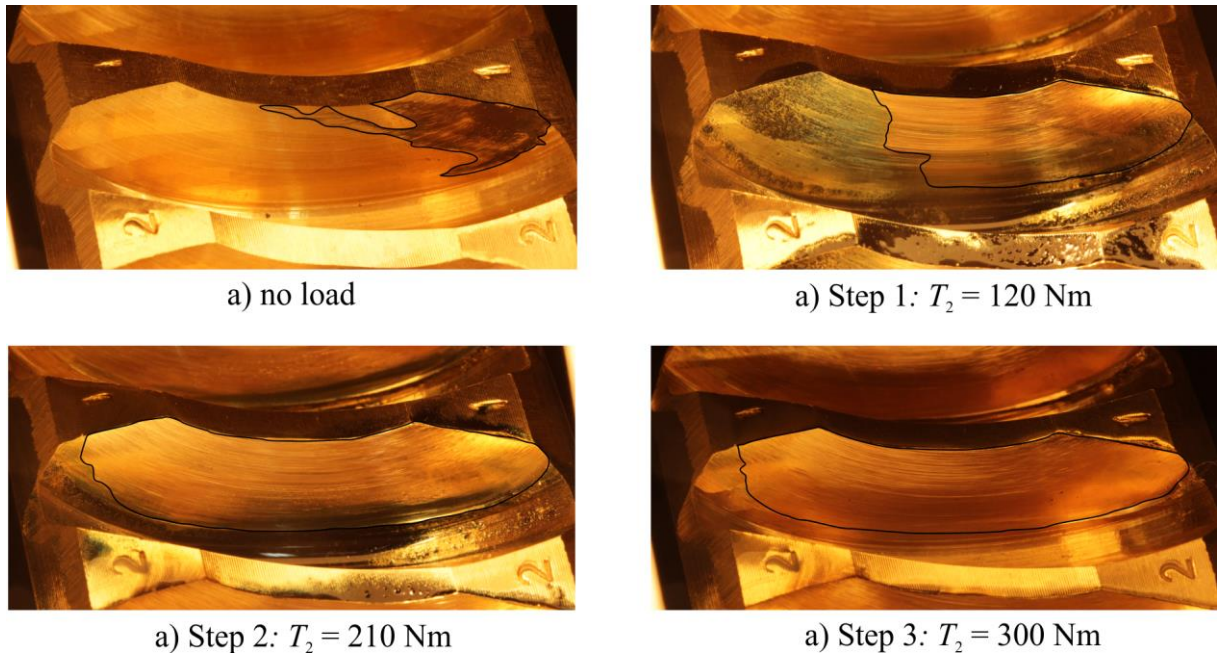


Figure 79. Contact pattern development during running-in

8.2.2 Digital image acquisition and post-processing

Digital imaging of worm wheel tooth flanks was conducted periodically, approximately after every $N_L = 2 \cdot 10^6$. If, by visual inspection, a large increase in pitting was observed, the flanks were photographed before the abovementioned period. For every worm pair, the image scale had to be defined. After the camera was mounted and positioned, graph paper was placed in the middle of the flank (Figure 80). Therefore, a referent square was drawn in the middle of the paper in the middle of the flank. It is assumed that minimum distortion and flank curvature effect were present in the middle of the flank if camera placement is considered. Based on image resolution, the error of inscribing the referent square in the image was 3 pixels. Converted to the actual flank surface, this represents an error of 2.26%.

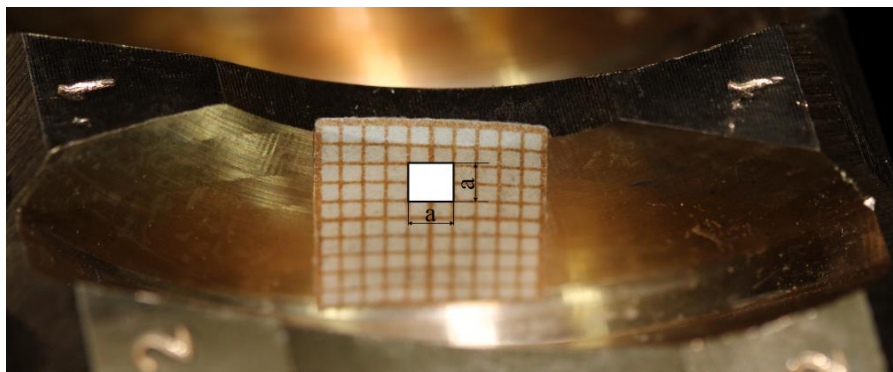


Figure 80. Defining the image scale

After the image scale was established, it was possible to measure the flank area in the image. Due to flank curvature, the measured flank area in the image was smaller than the actual flank area. The actual flank area was measured on the 3D scanned data of the worm wheel. On average, the flank's actual surface was $303 \pm 2 \text{ mm}^2$. The measured flank surface in the image was 4.6% to 6.1% smaller than the actual surface, depending on the image scale. The variation in image scale was due to the camera mounting position. The camera position could not be exactly repeated for every worm wheel due to gearbox disassembling after each test run.

The digital imaging procedure was as follows:

1. Pausing the test run, which included turning off all equipment (electric motor, pumps, generator, measurement equipment) and allowing the gearbox to cool down
2. Visual inspection of the worm wheel
3. Camera installation
4. Surface cleaning of worm wheel tooth flanks
5. Adjustment of lighting conditions, which includes positioning of photo lamps and tracing paper mask
6. Ensuring the position of the flank by inserting the positioning pin
7. Digital imaging of the flank (steps 4 to 6 were repeated until images of all 36 flanks were taken)
8. Dismounting of camera, photo lamps, and tracing paper mask
9. Inspecting the acquired measurement data for possible irregularities during the observed portion of the test run.
10. Heating the oil until an inlet temperature of $60 \text{ }^\circ\text{C}$ was reached.
11. Turning on all equipment and continuing the test run

The acquired images were taken in 24-megapixel resolution. Post-processing was carried out through a developed MATLAB script. Every step of the procedure resulted in an image output used as an input for the next step. The post-processing procedure was as follows:

- The image mask was applied to the original image. The mask removed all portions of the image except the portions of the flank where pitting was present.
- The image, originally RGB, was converted to a grayscale image.
- Adaptive contrast was applied to the image to highlight the pitting. As pitting holes produced significantly less light reflection, those parts of the image were considerably darker than the surrounding areas.

- Based on the applied contrast, the contrast threshold was employed to isolate only the pitting areas on the flank. The threshold value selection was based on image lighting conditions and could differ from one set of images to another. The eventual error based on threshold selection was up to 1% of the total pitting area.
- Any additional pitting areas not highlighted through applied contrast were manually defined and added.
- Automatic calculation of the total pitting area based on a sum of all individual pitting areas was carried out. The calculated total pitting area was expressed in flank surface percentage based on a predefined image scale.
- Visual inspection of the image with detected pitting.
- Contour plotting around detected pitting areas and saving the image.

The list of possible errors that could occur during image post-processing is presented in Table 27. The total error of $\pm 3.86\%$ represents a possible variation in the pitting percentage detected in the image. As pitting is reported in percentage as well, to avoid confusion, the example of total error is presented: if the detected pitting area is $A_P = 10\%$, the possible boundary values of detected pitting are $A_P = 9.614\%$ and $A_P = 10.386\%$.

Table 27. Image post-processing errors

Image post-processing errors	
Referent square error	2.26%
Actual flank surface variation	0.66%
Contrast threshold error	1%
Total error	3.86%

9

Results and discussion

In this chapter, the results of worm pair experimental tests are presented and compared to existing literature. The results include worm pair efficiency, pitting percentage, and worm wheel tooth flank wear. Also, the influence of dimensional accuracy on worm wheel pitting formation and development is presented by analyzing worm pair deviations obtained through 3D optical scanning. Lastly, the results obtained through the developed FEM model are used to investigate load and stress distribution in worm pairs.

9.1 Influence of surface texturing

9.1.1 Overall efficiency and running-in effect

The comparison of the efficiency of worm pairs with CuSn12 worm wheels is presented in Figure 81. The average efficiencies of worm pairs 1, 2 (EP), and 3 (EP) were 84.9%, 85.8%, and 90.1%, respectively. Both worm pairs with electropolished worms performed better in terms of efficiency than conventional worm pair. This can be attributed to the surface texture produced on a worm surface through electropolishing. The surface had many pits and pores that served as micro-oil reservoirs, thus providing secondary lubrication and increasing oil film thickness. In turn, this effect causes friction reduction which leads to higher overall efficiency. An additional property of electropolished steel surfaces paired with bronze was higher initial wear and faster running-in observed in worm pair 3 (EP). This phenomenon was also observed

in the results of block-on-disc sliding tests. By observing efficiency plots in Figure 81, both worm pairs 1 and 3 had a period of decreasing efficiency at the start of the tests, up to $N_L = 0.25 \cdot 10^6$. This may indicate that the running-in process was prolonged until the steady-state performance was achieved at around $N_L = 0.4 \cdot 10^6$. Worm wheels were 3D optically scanned before and after the tests to measure tooth thickness reduction that occurred as a consequence of sliding wear.

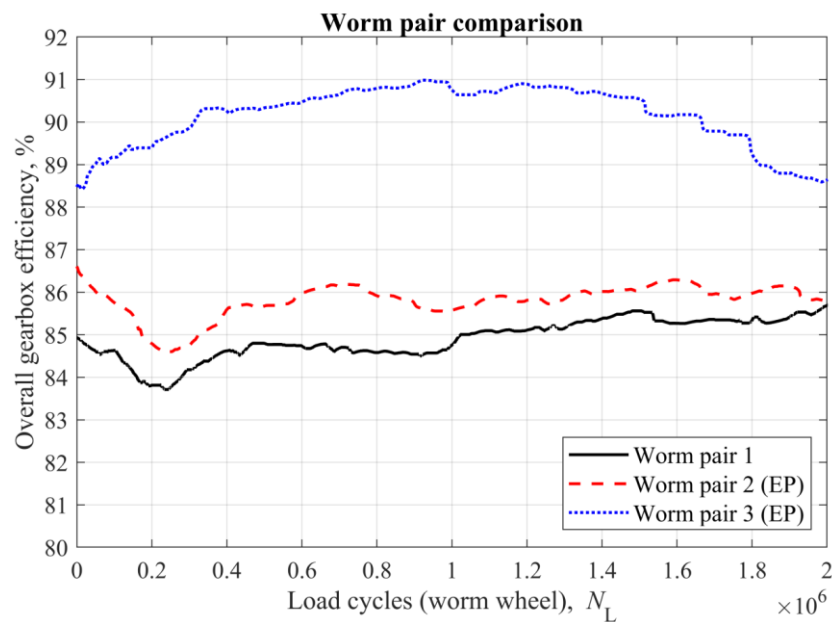


Figure 81. Worm pair efficiency comparison

To visually present the worm wheel wear, the comparison based on images of tooth No. 1 for all three worm pairs after running-in and at the end of the tests is presented in Figure 82. The amount of wear that occurred can be easily noticed by inspecting the lower right part of the worm wheel tooth. The ridge on the images of worm pair 3 (EP) is considerably larger and deeper, suggesting that the amount of wear that occurred was larger than the other two worm pairs. Moreover, the difference in wear between *after running-in* images and *end of test* images is relatively minor. This implies that the majority of wear occurred during the running-in period, which was expected considering the nature of wear in sliding contacts (see Figure 22). Average values of worm wheel tooth thickness are given in Table 28.

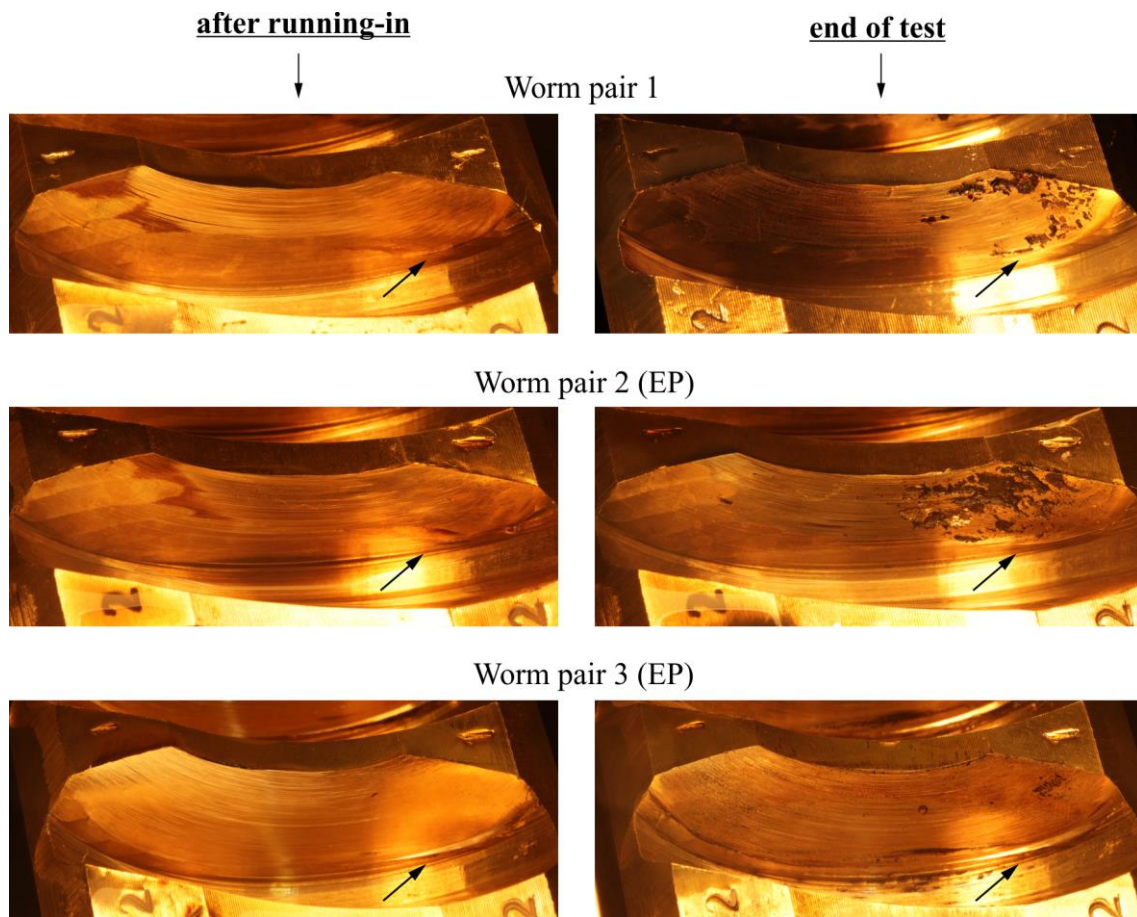


Figure 82. Visual comparison of worm wheel wear

Table 28. Average worm wheel tooth thickness “as manufactured” vs. “end of test”

Tooth thickness s_{m2}	As manufactured, mm	End of the test, mm	Difference, mm
Worm wheel 1	6.150	6.099	0.051
Worm wheel 2 (EP)	6.174	6.107	0.067
Worm wheel 3 (EP)	6.086	5.832	0.254

According to the difference in tooth thickness, worm wheel 3 experienced the most wear, which aligns with the images presented. Larger wear during the running-in phase of worm wheel 3 also resulted in a larger initial contact pattern compared to worm wheel 1 and 2. It can be said that worm wheel 3 had a full contact pattern. Moreover, worm pair 1 had a larger initial contact pattern than worm pair 2 (EP) (Figure 82, column: *after running-in*). Larger contact patterns result in more uniform stress distribution, directly affecting lubrication conditions, primarily in the form of more uniform and/or thicker oil film. According to the Stribeck curve (see Figure 12), thicker oil films promote hydrodynamic lubrication that is characterized by higher λ values. However, higher λ values do not assure a lower coefficient of friction that should benefit overall

efficiency. In the case of 16MnCr5-CuSn12 worm pairs, Huber [57] showed that neither larger contact patterns nor loads or pitting have an unambiguous effect on efficiency rating (Table 29).

Table 29. Results of 16MnCr5-CuSn12 worm pair tests by Huber [57]

Load, Nm	Pitting, %	Contact pattern, %	Overall gearbox efficiency, %
400	5.5	65	90
500	15.3	98	86
720	30.3	100	87
860	7.0	100	86

The full contact pattern established in worm wheel 3 can be considered the closest to the contact pattern in worm pairs with theoretically ideal geometry. In general, a full contact pattern limits the oil from entering the contact zone, promoting scuffing and worm pair failure. However, although the full contact pattern was established, no problems with scuffing occurred. The highest efficiency and lowest pitting were recorded for worm pair 3. However, it should be noted that the decrease in efficiency for worm pair 3 started around $N_L = 1.4 \cdot 10^6$. At that same time, micropitting started developing on the entering side of the flank (see Figure 89). This indicates that contact pressure started to build up on the entering side of the flank, decreasing the amount of oil supplying the contact zone. The consequence of such contact conditions was reflected in lower worm pair efficiency.

An additional test run was performed to investigate the behavior of conventional worm pair (ground steel worm and bronze worm wheel) under full contact pattern. The results of worm pair 6 are presented in Figure 83. The test ended prematurely due to two periods of scuffing. The first scuffing period was already at $N_L = 2 \cdot 10^5$, while the second was at $N_L = 11 \cdot 10^5$. Between two scuffing periods, worm pair 6 was running with relatively high efficiency but such running was accompanied by high sliding wear. High sliding wear prevented pitting formation as the material was constantly removed from the flank. Also, wear resulted in worn-out worm wheel teeth that eventually led to a second period of scuffing causing worm pair failure. The teeth of the worm wheel after the test are shown in Figure 84. Scuffing periods were characterized by low efficiency and a high rise in outlet oil temperature. In worm pairs 1 to 3, the common oil outlet temperature was 72 to 76 °C, whereas in worm pair 6 the temperature rose to 81 °C during the first scuffing period and was above 120 °C before the test was aborted. These results show that the operation of conventional worm pairs under a full contact pattern is

not sustainable because improper lubrication led to breakdown of lubrication and scuffing. On the other hand, worm pair 3 (EP) results presented earlier suggest that surface texturing can modify the worm surface to provide improved or additional lubrication that reliably supports full contact pattern in worm pairs.

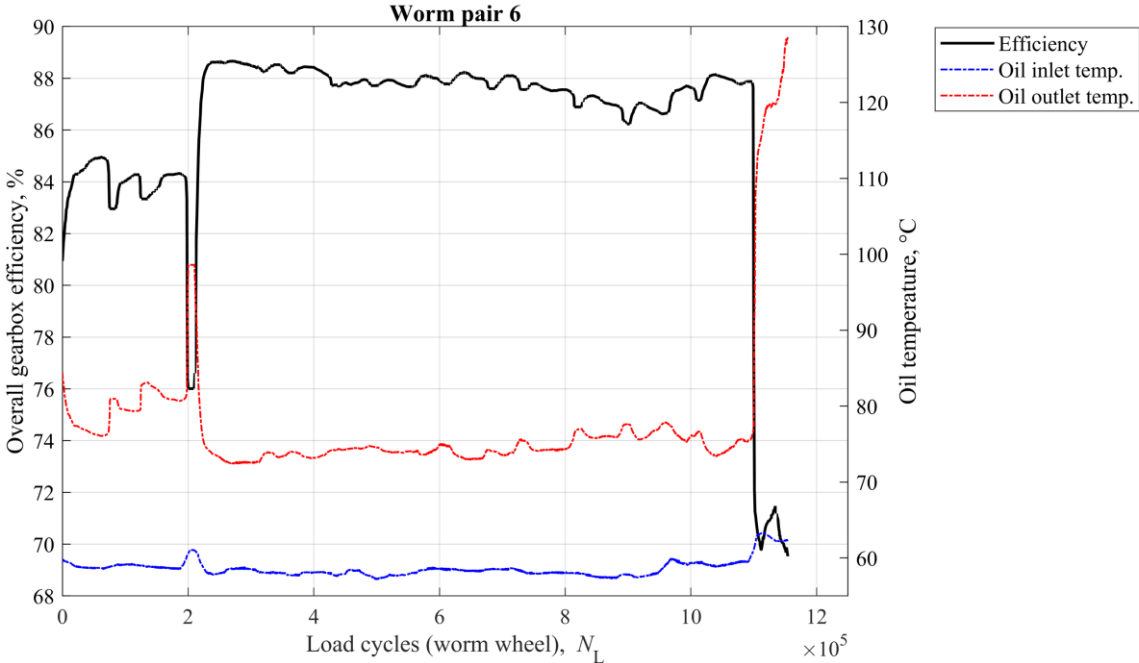


Figure 83. Worm pair 6 – efficiency and scuffing

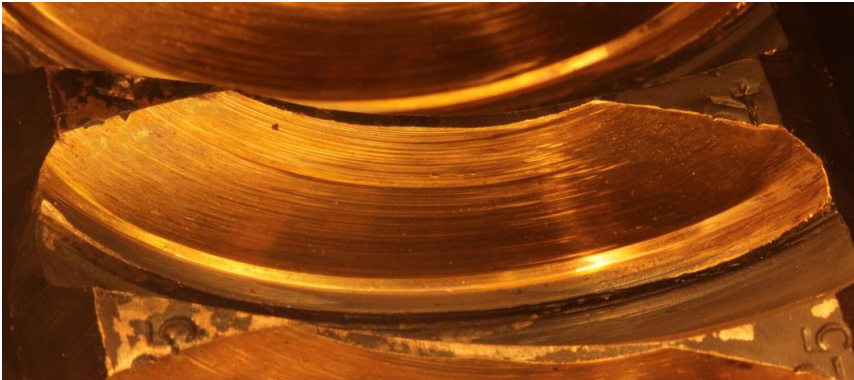


Figure 84. Worm wheel 6 - worn out and pointed teeth due to scuffing

9.1.2 Surface topography

Another explanation for higher efficiencies in worm pairs with electropolished worms could be found by examining corresponding worm surface profiles in Figure 85. Worm 2 and worm 3 were electropolished, and their surface was characterized by many pits. While worm 2

had deeper (2-5 μm) and smaller in diameter (20-50 μm) pits, worm 3 had shallower (1-2 μm) and larger in diameter (50-100 μm) pits. This can be attributed to slightly different electropolishing conditions (Table 30). The current density of 20 A/dm^2 produced deeper pits on the surface of worm 2, while the lower current density of 15 A/dm^2 produced shallower pits on the surface of worm 3. In addition, lower current density enlarged already existing valleys on the worm ground surface that were about 1 μm deep, which explains the difference in pit diameter between worm 2 and worm 3.

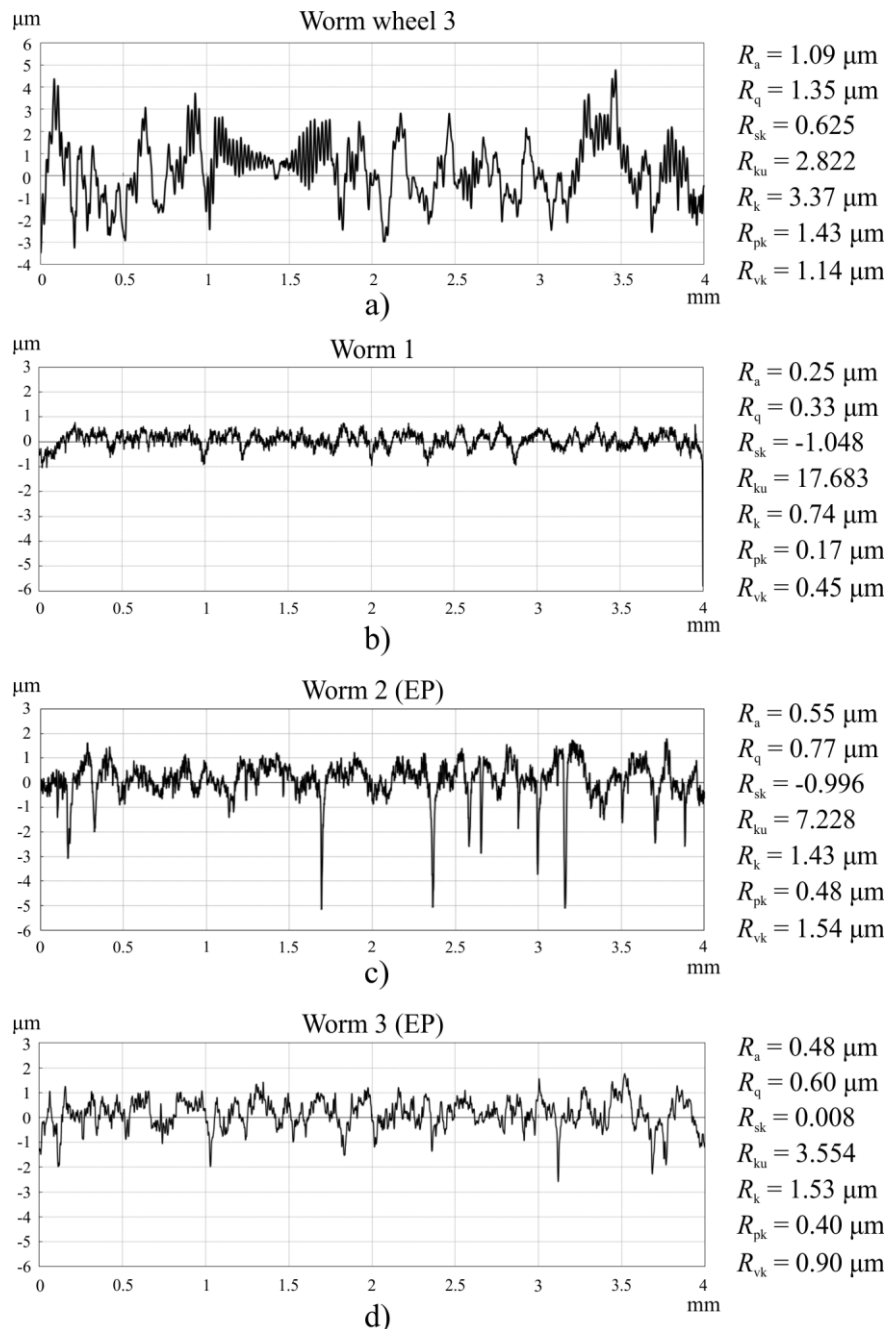


Figure 85. Surface profiles: a) worm wheel 3, b) worm 1, c) worm 2 (EP), d) worm 3 (EP)

Table 30. Electropolishing parameters of worm 2 and worm 3

	Solution temperature, °C	Potential, V	Current density, A/dm ²	Time, min
Worm 2	50	6.1	20	5
Worm 3	50	4.7	15	5

Higher wear evident on both worm wheels paired with electropolished worms can be attributed to increased surface roughness [32,140]. The present results suggest that an electropolished surface may be beneficial in terms of friction reduction if increased wear of the worm wheel is acceptable. As most of wear occurred during running-in, more efficient running-in benefits machine components that heavily depend on proper running-in process, such as worm pairs. From that perspective, the increased worm wheel wear should not be considered a disadvantageous attribute. Wear of 0.254 mm on worm wheel 3 was considerably higher than 0.051 mm and 0.067 mm measured on worm wheels 1 and 2, respectively (Table 28). Worm wheel wear as a product of the running-in process is a function of surface roughness/topography, worm pair geometry, worm wheel axial adjustment, and material homogeneity. Due to many simultaneously acting factors, it is hard to point out only one factor that can explain increased wear on worm wheel 3. One possible explanation can be laid out based on surface profiles in Figure 85. Worm 2's profile had easily distinguishable deep pits. In contrast, worm 3's profile was characterized by many larger and shallower pits that almost overlapped. Therefore, it can be stated that pit density was larger on the surface of worm 3. Wos et al. [140] found that higher dimple density surfaces produce more initial abrasive wear as the contact geometry changes from non-conformal to more conformal. At this moment, this is only a speculative explanation for higher initial wear found on worm wheel 3. More testing with different surface textures should clarify such phenomenon with more certainty.

Although both electropolished surfaces exhibited improved worm pair efficiency compared to conventional worm pair 1, worm 3 surface characterized by shallower and larger pits resulted in the highest overall efficiency among observed worm pairs with CuSn12 worm wheels. Several effects of dimple geometry (depth and size) on oil film thickness can be found in the literature. Deeper micro-cavities influence the flow of lubricant in the contact zone, resulting in an oil film thickness reduction that is caused by a notable side leakage of the entraining fluid as well as a fall of hydrodynamic pressure while the micro-cavity is entering the contact. Mourier et al. [149] found that in the case of deep dimples, the lubricant undergoes a sharp

decrease in pressure, which leads to a drop in viscosity that prevents the lubricant from completely separating the contacting surfaces. Due to the reasons mentioned above, deep pits can significantly reduce the fatigue life of the component [35]. Presented surface textures on worms 2 and 3 have dimple/pit depths considered shallow by the literature. However, the results suggest that the shallower and larger the dimple, the better lubrication conditions should be expected, at least in the presented case of rolling-sliding contact in worm pairs.

The inspection of surface profile parameters leads to several interesting remarks. The average surface roughness of the ground surface of worm 1 was $R_a = 0.25 \mu\text{m}$ compared to approximately $R_a = 0.5 \mu\text{m}$ in electropolished worms. While this significant difference in R_a would usually manifest in higher friction and lower efficiency in untextured surface contacts, this is not true with modified surface topography of electropolished worm. The higher R_a value of the electropolished surface was primarily a consequence of induced pits, not a result of a “rougher” surface in terms of additional peaks. Concerning other surface profile parameters, the ground surface of worm 1 already exhibited favorable negative R_{sk} and high R_{ku} parameters, as previously discussed in section 6.4.1 *Surface profile and hardness*. The surface profile of worm 2 exhibited similar R_{sk} and R_{ku} parameters whereas the surface profile of worm 3 had $R_{sk} \approx 0$ and a considerably smaller value of the R_{ku} parameter. Despite the similarities and differences in R_{sk} and R_{ku} parameters, which are often used in the design of surface textures in lubricated contacts [18,126,128,150,151], the results presented in this research suggest that the focus should primarily be placed on the geometry of the dimple/pits (depth and size). Then, the dimple geometry should be complemented by the mentioned surface profile parameters as a potential guide toward producing surface textures with beneficial properties in lubricated non-conformal contacts.

After the test, worm pair 3 (EP) surface profiles are presented in Figure 86. The values of R_a , R_{sk} , and R_{ku} of the electropolished worm surface were similar to those presented in Figure 85. Furthermore, the pits produced by electropolishing remained on the surface. By comparing surface profiles and topography of the electropolished worm, it can be concluded that minimal to no wear occurred on the worm surface as its parameters remained unchanged. In contrast to conventional gear material pairs (usually steel-steel), the steel-bronze material pair prolongs the durability of surface modifications produced on steel worm as most wear occurs on a softer component, namely the bronze wheel.

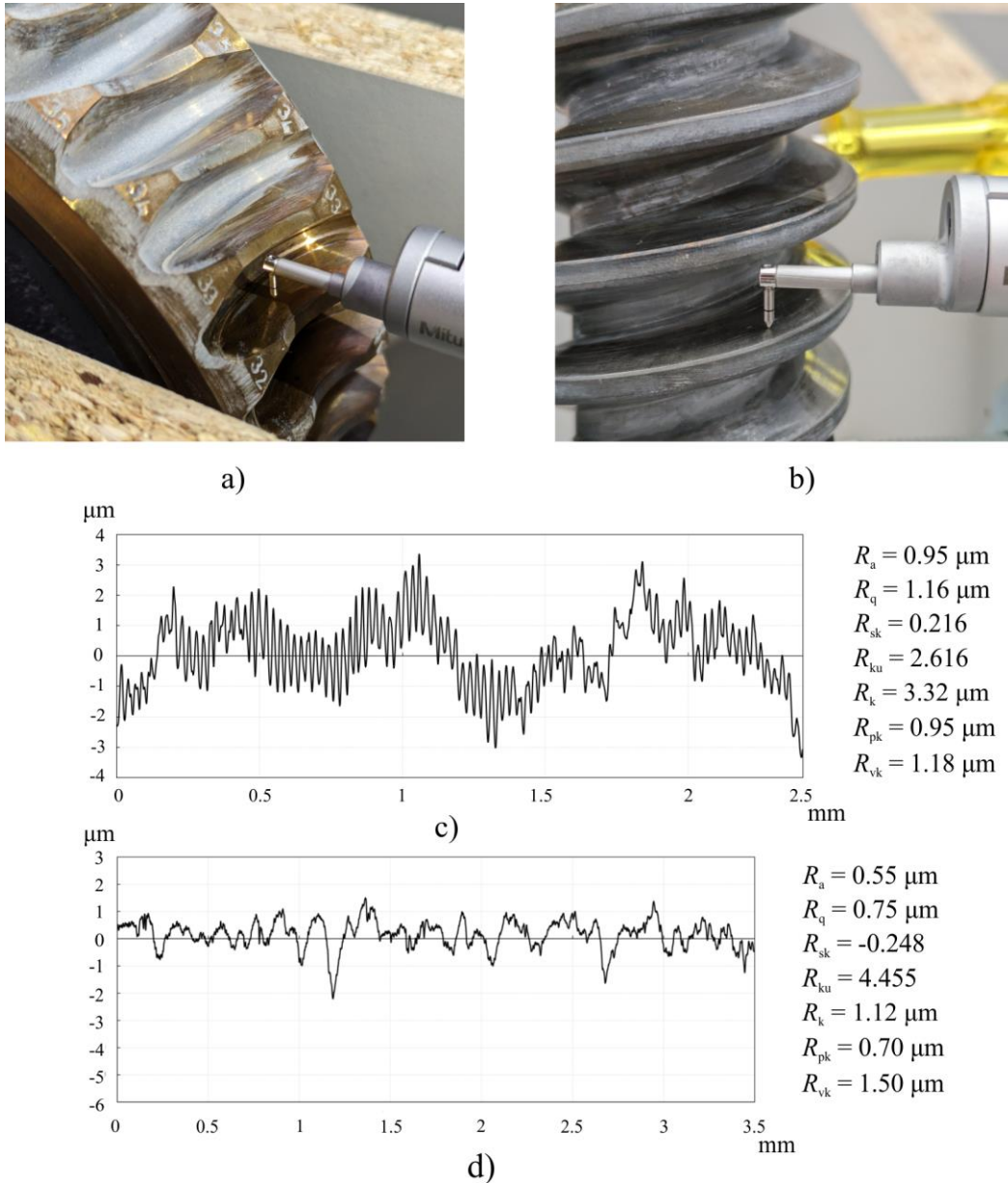


Figure 86. Surface profile measurement after the test: a) worm wheel 3, b) worm 3 (EP), c) worm wheel 3 surface profile, d) worm 3 (EP) surface profile

9.2 Pitting

The results of efficiency, average pitting percentage $A_{P,avg}$ and average pitting percentage of the 10 % most damaged teeth A_{P10} for worm pair 1, worm pair 2 (EP), worm pair 3 (EP), and worm pair 4 are given in Figure 87, Figure 88, Figure 89 and Figure 90, respectively. According to the results, there is no evident correlation between the increase in pitting and efficiency. In worm pair 1 and worm pair 2 (EP), with the increase in pitting the efficiency was unchanged. Relatively unchanged efficiency, despite the increase in pitting, was also reported by several other studies [6,8,25]. This phenomenon can be explained by pits acting as oil reservoirs thus

providing secondary lubrication in the contact zone. In worm pair 3 (EP), as pitting starts to develop, a slight decrease in efficiency can be observed. In worm pair 4, pitting development was accompanied by a decrease in efficiency during the first half of the test, while in the second half of the test, although the pitting was increasing, the efficiency remained constant. For comparison purposes, the efficiency of worm pair 5 (CuAl10Fe5Ni5 worm wheel) is presented in Figure 91.

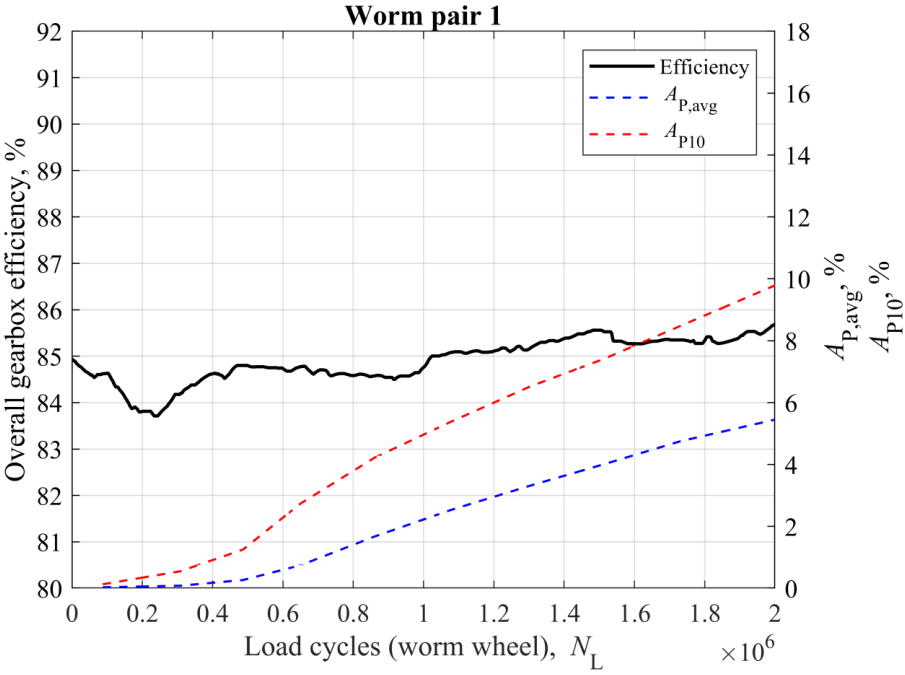


Figure 87. Worm pair 1 - efficiency and pitting percentage

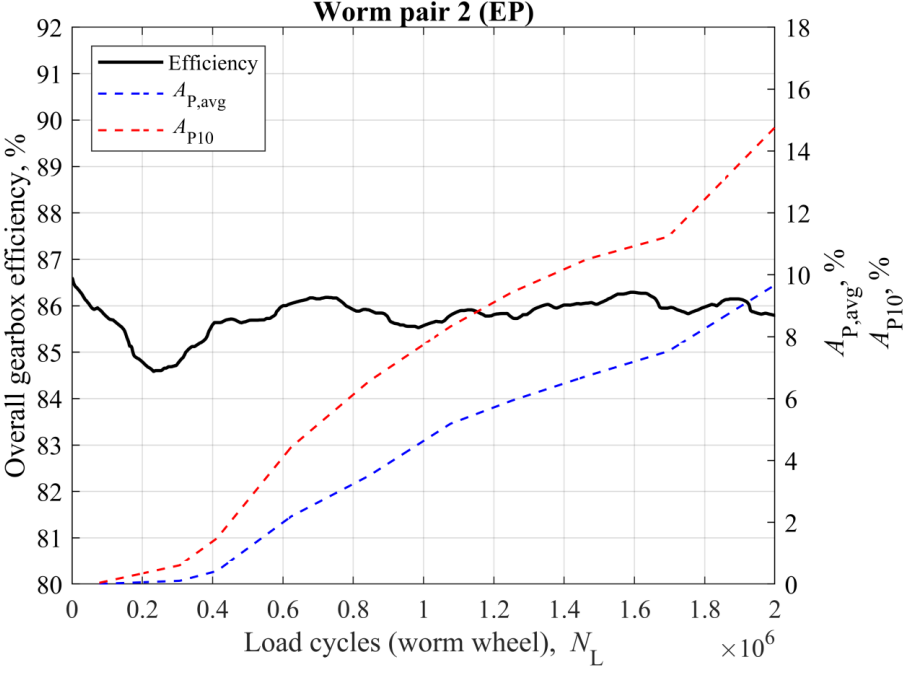


Figure 88. Worm pair 2 (EP) - efficiency and pitting percentage

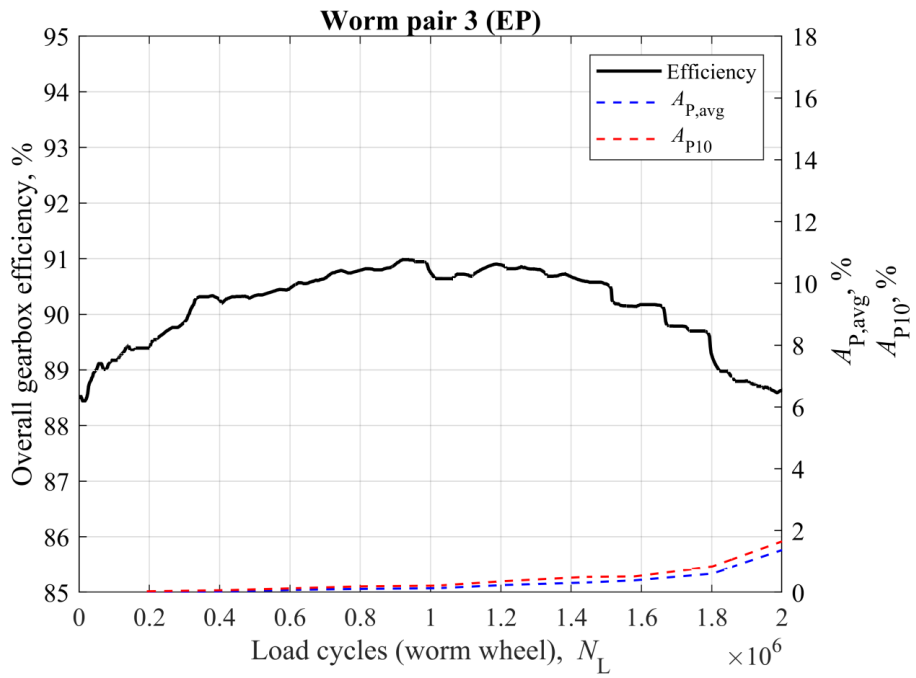


Figure 89. Worm pair 3 (EP) - efficiency and pitting percentage

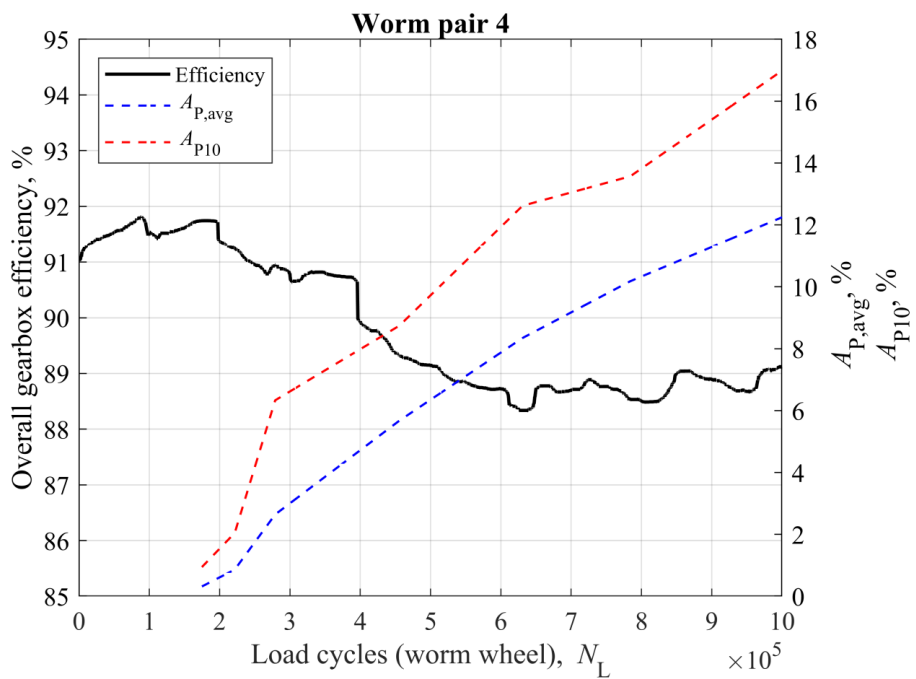


Figure 90. Worm pair 4 - efficiency and pitting percentage

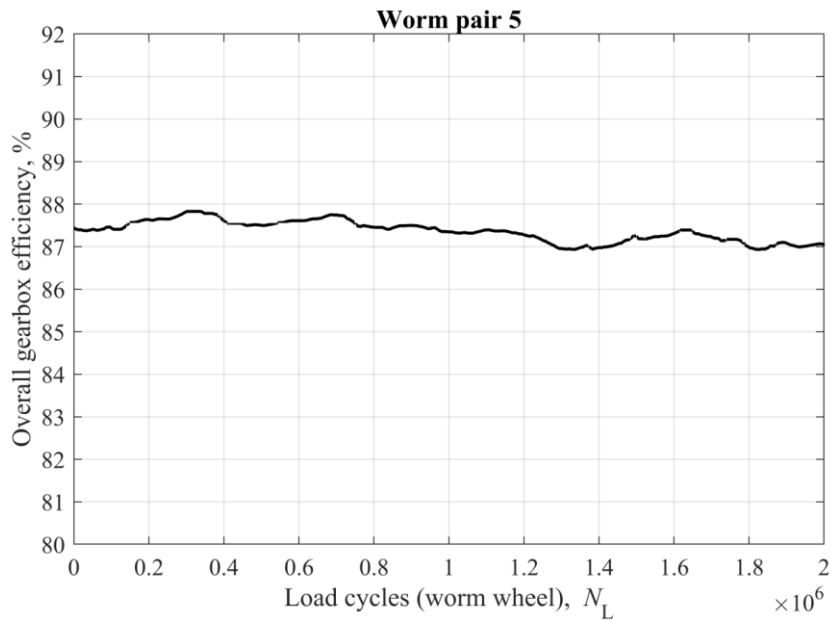


Figure 91. Worm pair 5 - efficiency

The comparison of the pitting results with ISO/TS 14521 standard [3], Žeželj [25], and Opalić [53] is provided in Figure 92 (CuSn12 worm wheels) and Figure 93 (AlSn6 worm wheel). Generally, presented pitting results, and results obtained by Žeželj [25], have a parabolic form. As reported by Huber [57], this nature of pitting formation is characteristic in worm pairs lubricated by mineral oils.

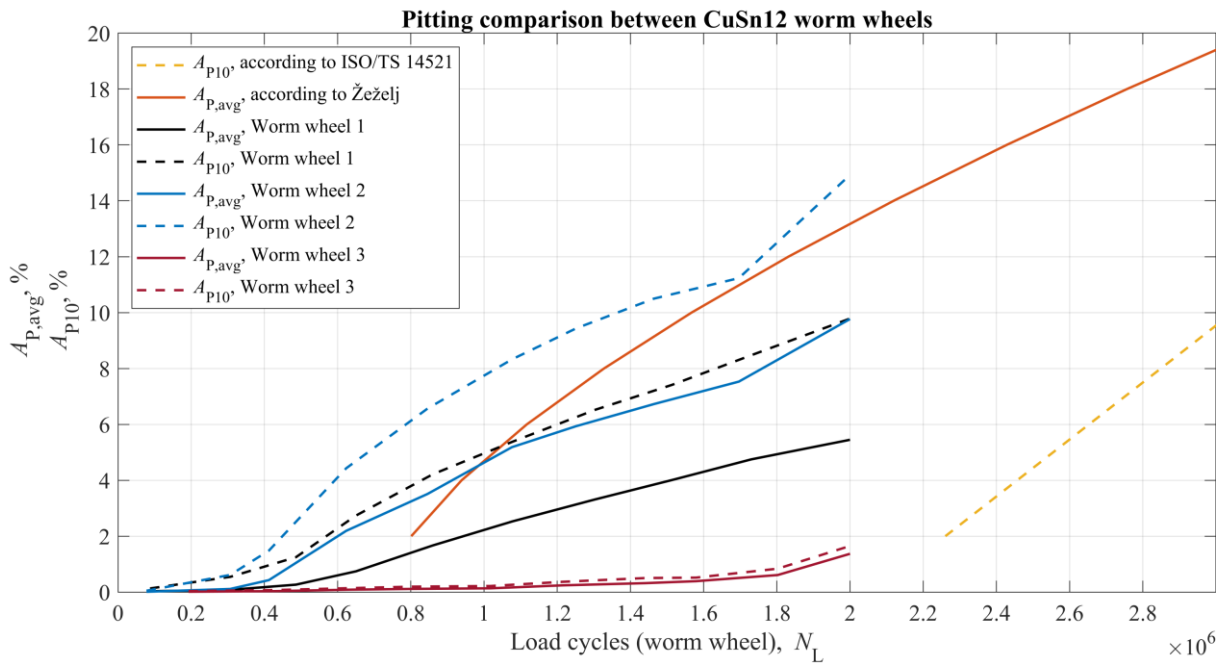


Figure 92. Pitting comparison - CuSn12 worm wheels

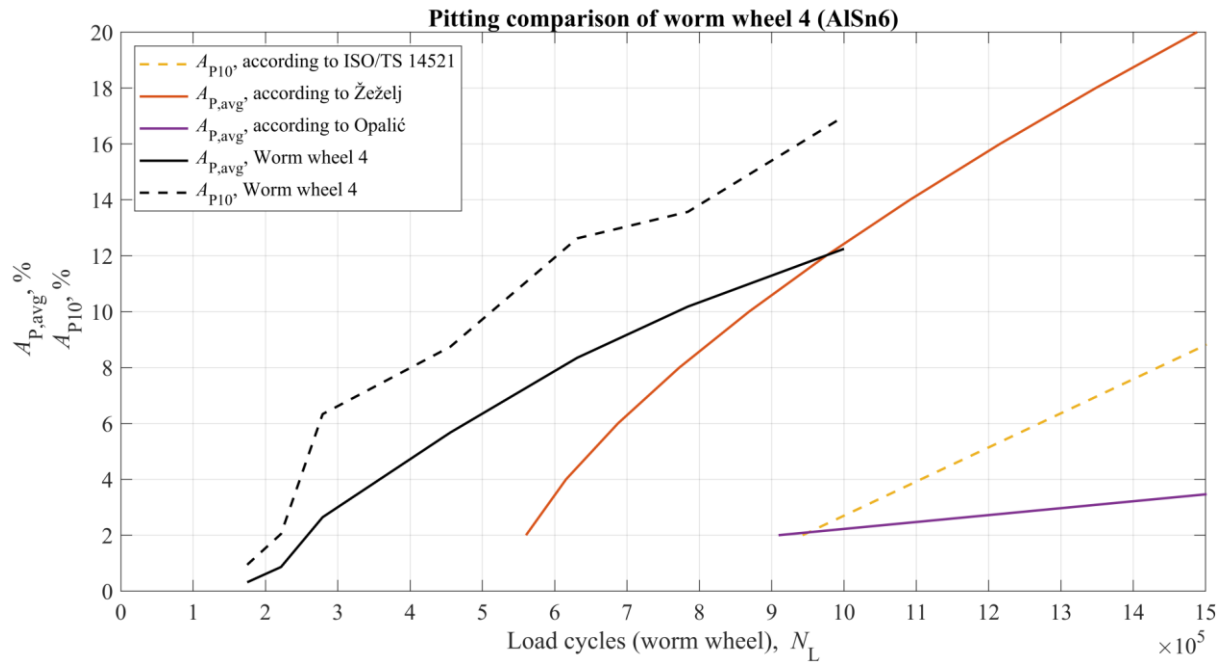


Figure 93. Pitting comparison of AlSn6 worm wheel

Both pitting comparison point out that pitting percentages, obtained through this research and studies of Žeželj [25] and Opalić [53], as well as predicted by ISO/TS 14521 standard [3], are relatively scattered. Worm wheels 1 and 2 were in fair agreement with the results, according to Žeželj [25], while worm wheel 3 differed significantly. Worm wheel 3 tends to agree with the pitting predicted by standard [3]. Pitting on worm wheel 4 was larger than predicted by Žeželj [25], although in an acceptable deviation range. Pitting calculated for AlSn6 by the standard [3] and Opalić [53] is considerably lower than the presented worm wheel 4 results. There are a couple of explanations for such discrepancy in results. The pitting calculation procedure in standard [3] is defined by boundary conditions (Table 9), many of which do not apply to this research. Also, the standard does not outline the method for obtaining values of pitted areas [3] and therefore cannot be appropriately compared to the method used in this research. Also, AlSn6 as a worm wheel material has only been covered by a few studies to this date [25,53,54]. Different geometries, loads, sliding speeds, and lubricant oils should be experimentally tested for a better understanding of pitting formation on AlSn6 worm wheels.

Nevertheless, pitting percentages varied significantly among tested worm wheels. This was to some degree expected and one of the main motivations for this research. In order to better explain such variation, further analysis focused on the dimensional accuracy of worm pairs was conducted to improve the understanding of the process of pitting formation on worm wheels.

9.2.1 Worm pair 1

9.2.1.1 Pitting

The first noticeable pitting was recorded after $N_L = 0.31 \cdot 10^6$ with average pitting $A_{P,avg} = 0.08\%$ and $A_{P10} = 0.55\%$. The first pitting occurred in the middle and on the leaving side of the worm wheel teeth flank. The middle of the worm wheel tooth flank is known to be insufficiently lubricated due to the oil-thinning effect promoted by high contact temperatures (see Figure 14). The contact on the leaving side of the worm wheel tooth flank is characterized by the smallest equivalent radii of curvature and the highest Hertzian contact pressures [26].

Pitting results for worm wheel 1 are reported in Figure 94. The results are reported for all flanks, odd, and even flanks. This is because worm pairs in this research had worm wheels with $z_2 = 36$ teeth, and worms with $z_1 = 2$ teeth (threads) corresponding to transmission ratio $i = 18$. Such a combination causes odd flanks to mesh with the same worm thread. In this case, worm thread “1” and all even flanks meshed with the worm thread “2”. Additionally, there was a characteristic difference between odd and even flanks in terms of deviations that will be discussed later in this section. At the end of the test, the average pitting on odd flanks was 4.77% higher than on even flanks. The difference between the most damaged tooth flank, No.11, and the least damaged tooth flank, No. 30, was 10.24%. The results for flank No. 22 were reported because it was the flank with the most initial damage. For $N_L = 0.31 \cdot 10^6$, flank No. 22 had $A_P = 1.72\%$. The second flank with the highest pitting for $N_L = 0.31 \cdot 10^6$ was flank No. 11 with $A_P = 0.25\%$. However, throughout the testing, the increase in pitting damage on flank No. 22 was relatively small compared to the increase in average pitting values or pitting increase on flank No.11. Moreover, the initial pitting location on flank No. 22 was on the entering side of the flank (Figure 95). Such behavior suggests that pitting can form suddenly and that its initial formation or location may not imply continuous pitting growth. In other words, the most pitting on the flank at the start of the test cannot be used as a certain predictor for the most damaged flank at the end.

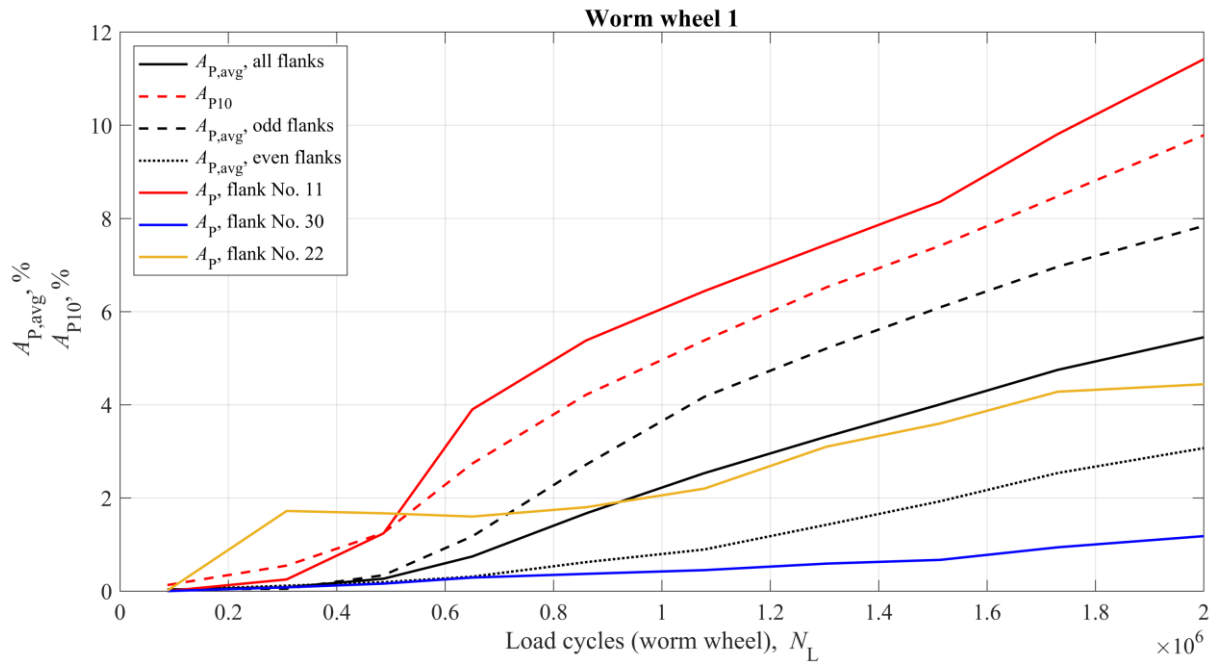


Figure 94. Pitting percentages for worm wheel 1

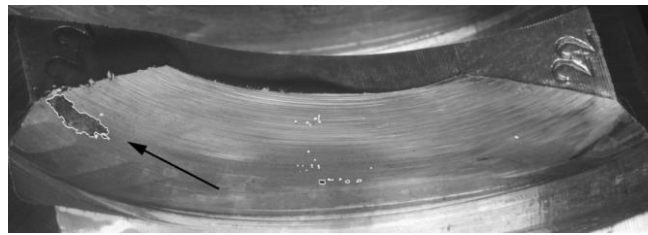


Figure 95. Flank No. 22 – initial pitting location

Pitting formation and development on flank No. 11 are presented in Figure 96. Pitting formed at the top of the leaving side of the flank and propagated towards the bottom. The nature of pitting damage was characterized by uneven increases, although the measurement intervals were relatively similar ($N_L \approx 0.2 \cdot 10^6$). For example, between $N_L = 0.48 \cdot 10^6$ and $N_L = 0.65 \cdot 10^6$ pitting increased by 2.66%, while between $N_L = 1.3 \cdot 10^6$ and $N_L = 1.51 \cdot 10^6$ pitting increased by only 0.92%. However, the flank surface was already severely damaged. This uneven and often abrupt increase in pitted area is a characteristic behavior in worm wheels as flank material removed due to pitting is in the form of larger pieces of material [25]. Pitting development, in terms of pitting location overlap, is depicted in Figure 97.

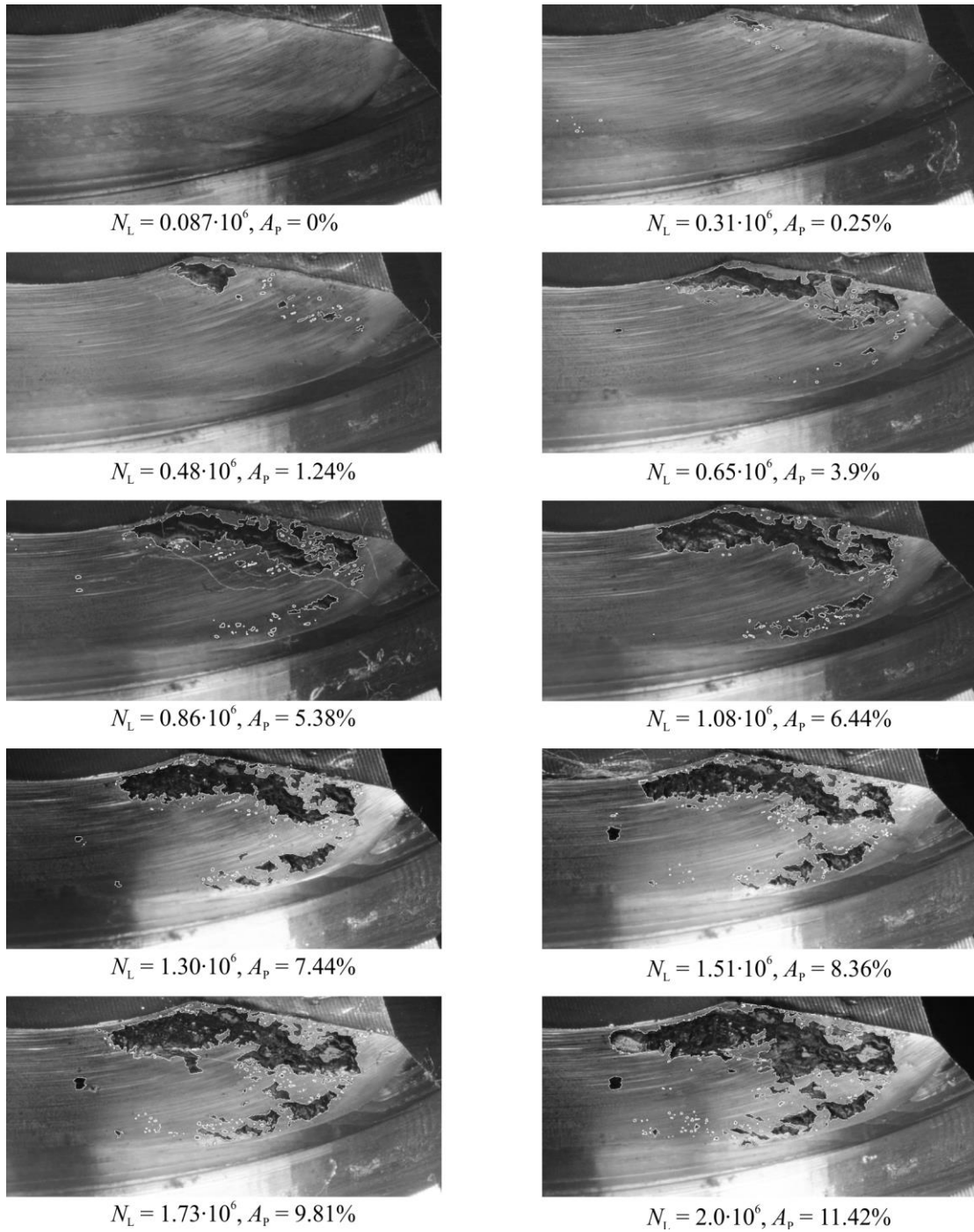


Figure 96. Pitting development on flank No. 11

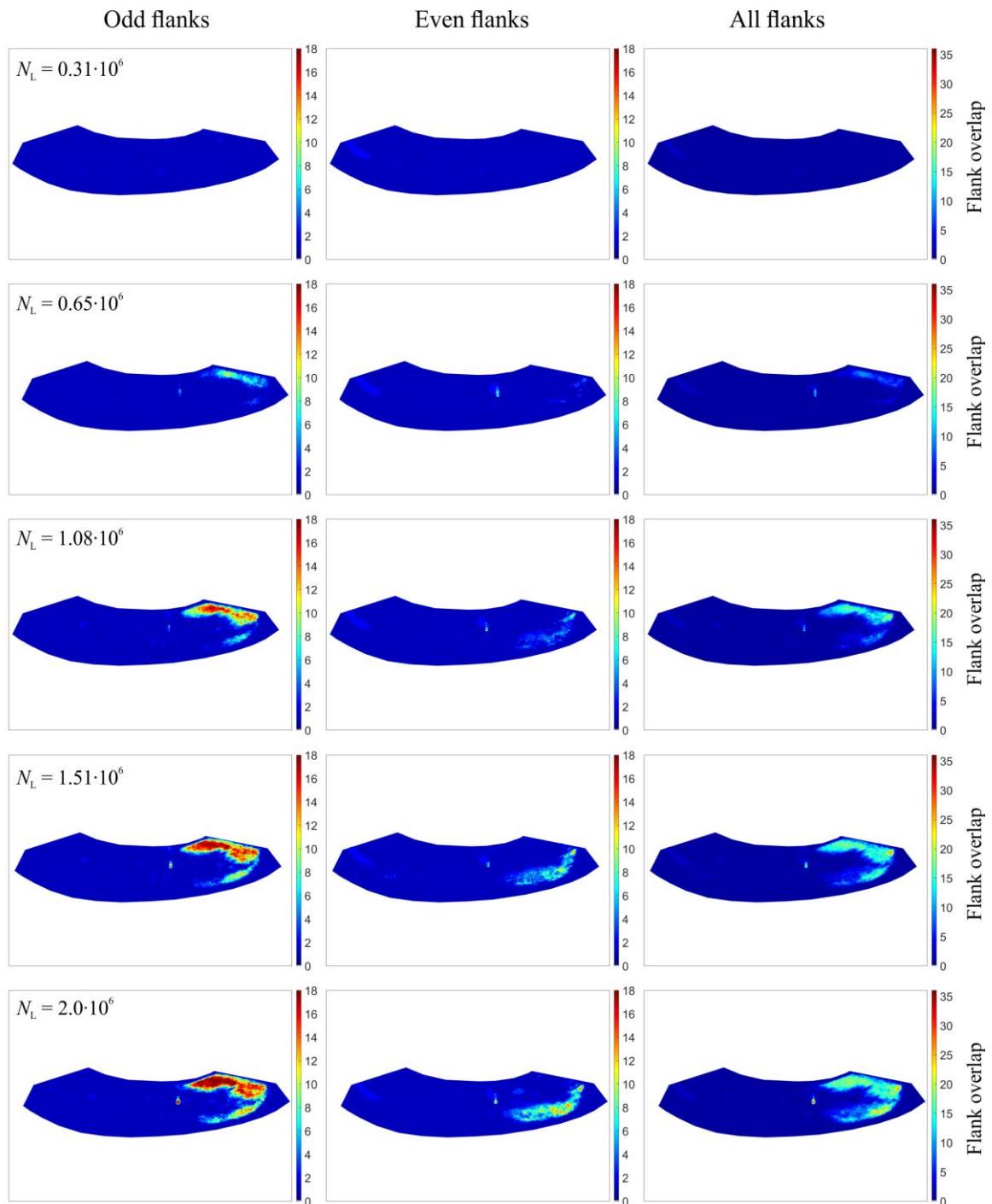


Figure 97. Pitting location (overlapped) on flanks of worm wheel 1

After $N_L = 1.08 \cdot 10^6$, the majority of odd flanks had noticeable pitting in the top of the leaving side of the flank, while less than half of even flanks started to show pitting in the bottom of the leaving side of the flank. By the end of the test, $N_L = 2.0 \cdot 10^6$, pitting location in odd flanks propagated towards the bottom part of the flank. In contrast, pitting remained in the bottom of the flank in even flanks, although in larger percentages. All flanks had a small pitted area towards the middle of the flank in common. As already mentioned, the middle of the worm

wheel tooth flank has relatively poor film generation and oil entrainment, resulting in very thin oil film and much more severe lubrication conditions. The mentioned pitted area in the middle of the flank is shifted towards the leaving side of the flank. The contact shift towards the leaving side usually ensures better oil entrainment into the contact zone [5]. A relatively high positive correlation ($r = 0.64$) was observed between pitting at $N_L = 6.5 \cdot 10^5$ and pitting at the end of the test.

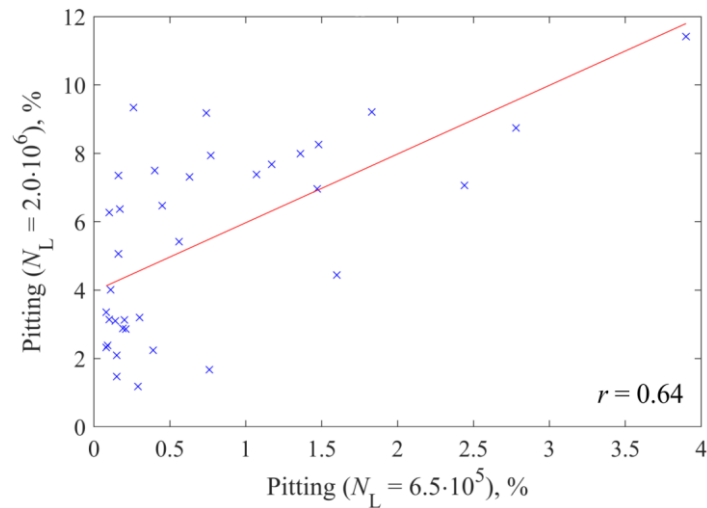


Figure 98. Pitting correlation for worm wheel 1

9.2.1.2 Deviations, wear, and pitting model

The reason for uneven pitting distribution, besides material defects, system vibrations, or worm wheel wear, could be found by examining worm pair deviations and their possible effect on such phenomenon. The worm wheel deviations are given in Figure 99. Single pitch deviations f_{p2} had a characteristic distribution. Odd-numbered pitches had a negative deviation, while even-numbered pitches had a positive deviation. The same single pitch deviation distribution was found in all investigated CuSn12 worm wheels, as all wheels were produced in the same batch. The periodic nature of single pitch deviation suggests a specific inaccuracy during the worm wheel manufacturing process. One possible explanation could be inaccurate worm wheel hob cutter geometry. The worm wheel hob cutter must have the same geometry as the mating worm. In this case, the hob has two starts (two threads). When worm wheel teeth number z_2 is a multiple of worm thread number z_1 (e.g., $z_2 = 36$ and $z_1 = 2$), the same thread is constantly in mesh with either even or odd worm wheel teeth. The same applies to the worm wheel hob. This means that one hob start/thread will cut odd worm wheel teeth while another

hob start/thread will cut even worm wheel teeth. There is a strong indication that one of the cutting hob threads had inaccurate geometry due to improper sharpening (grinding), producing single pitch deviation in such a characteristic manner. A similar deviation distribution can be found in total profile deviation F_{a2} . Radial runout, F_{r2} , was expressed in negative values as the distance between the actual probing ball position and worm wheel axis was smaller than the distance from the ideal ball position and worm wheel axis. In other words, the more negative the individual radial runout deviation, the closer the probing ball is to the worm wheel axis. This can also be interpreted in the form of wider tooth gap.

The worm deviations, namely single pitch and runout deviations were measured at six points along the active part of the worm thread length, and the average deviations are reported in Table 31. Regarding deviation F_{r1} , the provided values of 0.875 mm and 0.870 mm were distances between the theoretical probing ball and the actual probing ball in GOM Inspect software. The runout deviation is always provided as the largest difference among measured teeth (threads). Hence, the focus should be placed on their mutual difference, which is 5 μm . Worm pair 1 quality grades for all measured deviations are given in Table 32.

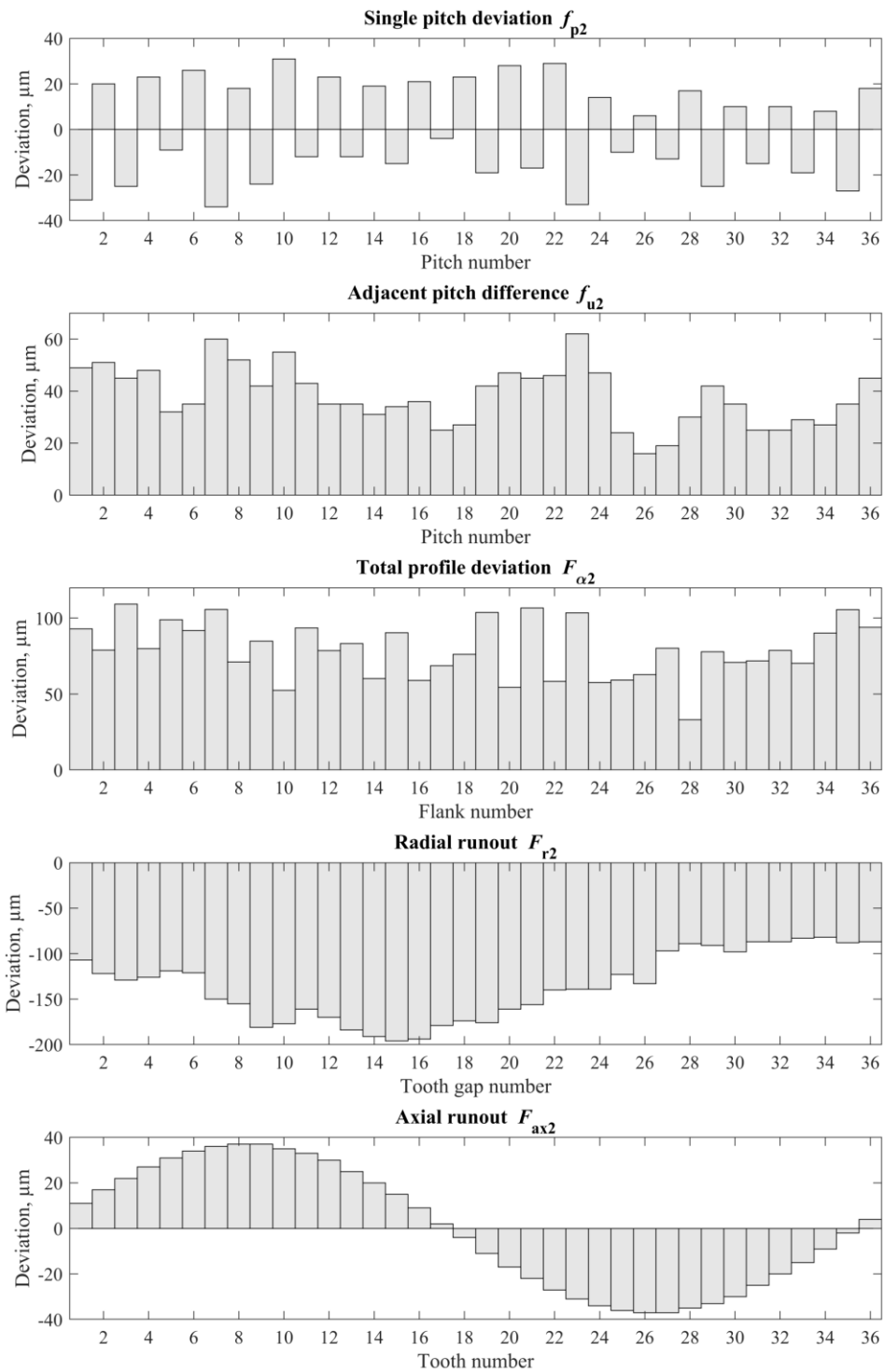


Figure 99. Worm wheel 1 – deviations

Table 31. Worm 1 - deviations

	f_{px} , mm	F_{r1} , mm
Thread 1	-0.020	0.875
Thread 2	-0.012	0.870

Table 32. Worm pair 1 – quality grades (Q)

Deviation	Worm		Wheel	
Single pitch deviation (axial)	f_{px}	Q9	-	-
Single pitch deviation	-	-	f_{p2}	Q10
Adjacent pitch difference	f_{ux}	Q6	f_{u2}	Q11
Total pitch deviation	F_{pz}	Q11	-	-
Total cumulative pitch deviation	-	-	F_{p2}	Q9
Total profile deviation	$F_{\alpha 1}$	Q11	$F_{\alpha 2}$	Q12
Runout	F_{r1}	Q3	F_{r2}	Q11

Single pitch deviations (f_{px} in worm, f_{p2} in wheel) influence load sharing among gear teeth which is directly related to bending stress in the tooth root or contact stress on the tooth flank. In gears, the most unfavorable single pitch deviation distribution is when one gear tooth has positive deviation ($+f_p$) and is meshed with another gear tooth having negative deviation ($-f_p$), or vice versa [152–154]. The example of gear teeth position in double contact in which maximum increase of contact stresses occur is shown in Figure 100.

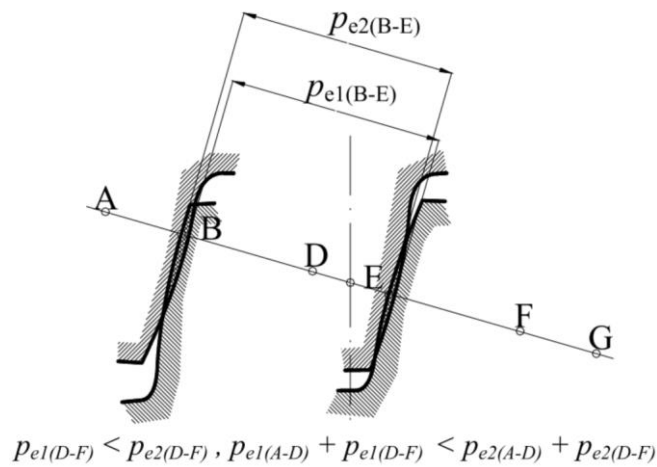


Figure 100. Pitch error in double contact [152]

In the case of worm pair 1, the driving worm with both threads having “ $-f_{px}$ ” was meshed with the driven wheel having odd teeth with “ $+f_{p2}$ ” and even teeth with “ $-f_{p2}$ ”. The worm pair was assembled to achieve the mesh between *thread 1/odd-numbered teeth* having $-f_{px} / -f_{p2}$ and *thread 2/even-numbered teeth* having $-f_{px} / +f_{p2}$. In the presented case, the most of load should be distributed among the *thread 2/even-numbered teeth* contact due to an unfavorable combination of $-f_{px} / +f_{p2}$. Therefore, most pitting should also be present on even worm wheel flanks. However, based on the pitting results presented in Figure 97, most pitting occurred on

odd flanks. As this phenomenon was unexpected, further investigation was conducted to find a cause for such pitting distribution.

The axial profile curvature of worm threads is presented in Figure 101. The presented results are averages of four axial profiles of each thread. The ideal ZN worm axial profile is slightly concave in the axial section [51]. However, the curvature of worm threads was convex, with *thread 1* being noticeably more convex than *thread 2*. The difference between the axial profiles was up to 24 μm . This difference was larger than most of the worm wheel single pitch deviations f_{p2} presented in Figure 99. The reason behind such a difference in curvature from the ideal profile was presumably incorrect geometry of the grinding wheel or wrong positioning of the grinding wheel during the grinding process.

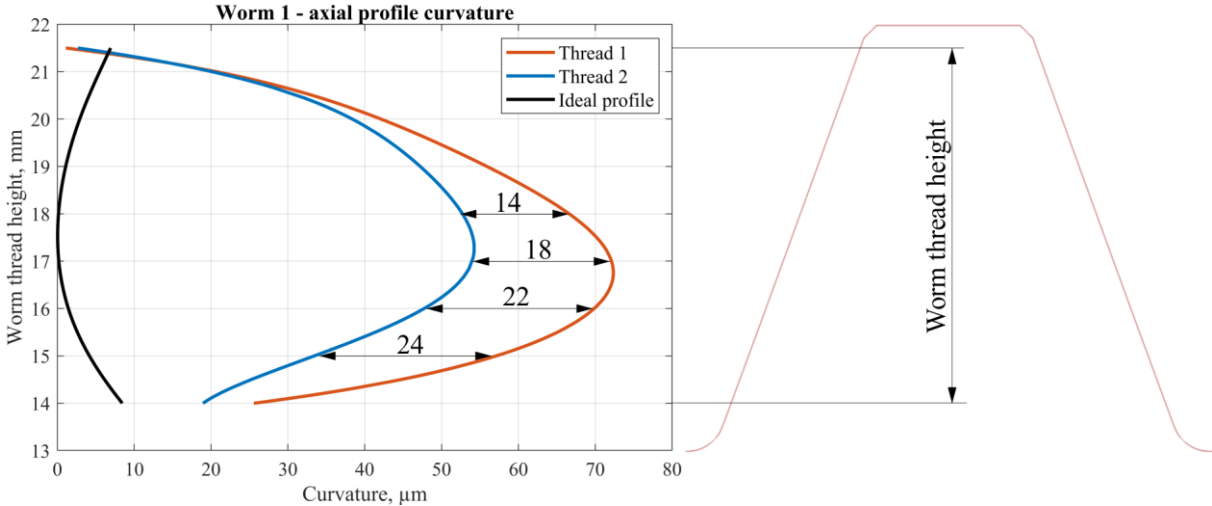


Figure 101. Worm 1 – axial profile curvature

The greater part of the profile convex curvature was present in the lower part of the worm thread, below the worm reference diameter $d_{m1} = 36 \text{ mm}$ (corresponds to a worm thread height of 18 mm). This is also the portion of the worm thread where worm pair contact starts, as depicted in Figure 102. As pitting results showed, most pitting developed in the upper part of the odd flanks paired with *thread 1* and later propagated toward the bottom part of the flank. Both worm threads influenced the contact in a way that it was shifted towards the top part of the worm wheel flank. This can be observed by the established contact pattern after the running-in period, as shown in Figure 82.

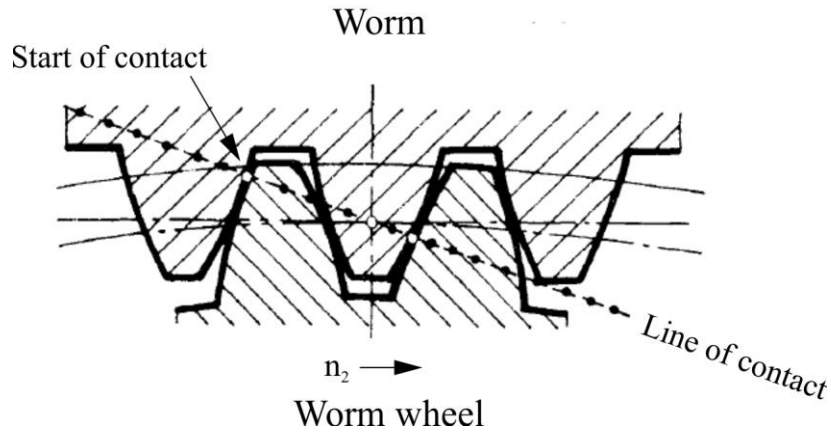



Figure 102. Worm pair contact

Another factor distinguishing worm pairs from other gear types is a running-in process characterized by a substantial worm wheel material removal. In presented worm pairs, the tooth thickness reduction due to wear was 50 to 250 μm , when measured in the middle of the tooth on the reference circle. This amount of material removal alters the contact conditions far from ideal geometry. It implies that each worm pair will adapt differently, hence the importance of proper running-in. The adaptation will primarily be based on worm geometry as it is a harder material that has negligible wear in comparison to bronze worm wheel. Also, as each worm pair adapts differently, it is difficult to consider the amount and intensity of wear when predicting the final contact pattern. To illustrate the different amounts of wear, the tooth thickness was additionally measured on the leaving side of the flank where the majority of the contact takes place (marked as location 2). The results are presented in Table 33. The value of Δs_{m2} represents wear on the worm wheel reference circle while Δs_2 represents wear on the leaving side of the flank.

Table 33. Worm wheel 1 - tooth thickness difference after the test

	Δs_{m2} (1), μm	Δs_2 (2), μm	
	Odd teeth	50	143
	Even teeth	51	126
	All teeth	51	135

The difference between the tooth thickness (wear) measured in the middle (1) and on the leaving side (2) of the flank was 84 μm . Moreover, on average, odd teeth experienced 17 μm more wear than even teeth. The measured difference in wear was similar to the difference in *thread 1* and

thread 2 curvature (Figure 101). Uneven wear distribution along the wheel flank was expected as the contact pattern was directed towards the leaving side of the flank to favor lubrication conditions. Besides, the contact pressures are the highest on the leaving side of the flank due to low equivalent radii of curvature [26].

The correlation between wear in the middle (Wear (1)), wear on the leaving side of the flank (Wear (2)) and pitting or deviations is presented in Figure 103. While wear in the middle of the flank shows no correlation with the pitting ($r = -0.07$), wear on the leaving side of the flank shows moderate correlation with the pitting ($r = 0.57$). Radial runout F_{r2} was highly correlated with the wear in the middle of the flank ($r = 0.70$). As tooth gaps were wider (more negative F_{r2}), less wear occurred in the middle of the flank. There was no correlation between Wear (2) and F_{r2} ($r = -0.09$). Axial runout F_{ax2} showed a mutually inverse correlation between Wear (1) and Wear (2).

These findings indicate that in some worm wheels, larger pitting can be expected in the locations of increased wear. Moreover, radial and axial runouts should be considered when predicting or modeling worm wheel wear behavior. Also, these results suggest that correlating wear measured in the middle of the flank and pitting can be deceiving in some cases, especially if the majority of contact pattern is established on the leaving side of the worm wheel flank.

Linear regression was employed to develop a model that describes pitting formation and development on worm wheel 1 flanks in relation to load cycles, inspected worm wheel deviations, and worm thread deviation (Figure 101). Worm thread profile deviation is designated as F_{worm} in the models. It was set as a categorical variable with coding (0,1). Linear models were developed based on criterion of 10% of the most damaged teeth, A_{P10} . A_{P10} was divided into two stages as presented in the ISO/TS 14521 standard. The first stage is the beginning of pitting defined by $A_{P10} \leq 2\%$. The second stage is the pitting growth stage which can be defined by $A_{P10,max} \leq 2...60\%$. In this research, the tests were carried out for $N_L = 2.0 \cdot 10^6$ and different values of $A_{P10,max}$ were achieved. In the case of worm pair 1, the value of $A_{P10,max} = 10\%$ was achieved by the end of the test. The results of linear regression models are presented in Table 34.

The presented models were developed for three cases: “Overall pitting”, “Beginning of pitting” and “Pitting growth stage”. “Overall pitting” is a model that predicts pitting for all load cycles, N_L . “Beginning of pitting” considers the load cycles needed for first pitting, defined by ISO/TS 14521 standard as $A_{P10} = 2\%$. Number of load cycles for $A_{P10} = 2\%$ was $N_L = 5.7 \cdot 10^5$.

“Pitting growth stage” models the growth of pitting between $A_{P10} = 2\%$ and $A_{P10,max} = 10\%$. The relevant range of load cycles for the pitting growth stage was $5.7 \cdot 10^5 < N_L \leq 2.0 \cdot 10^6$. Complete data used for developing pitting linear models is provided in the Appendix.

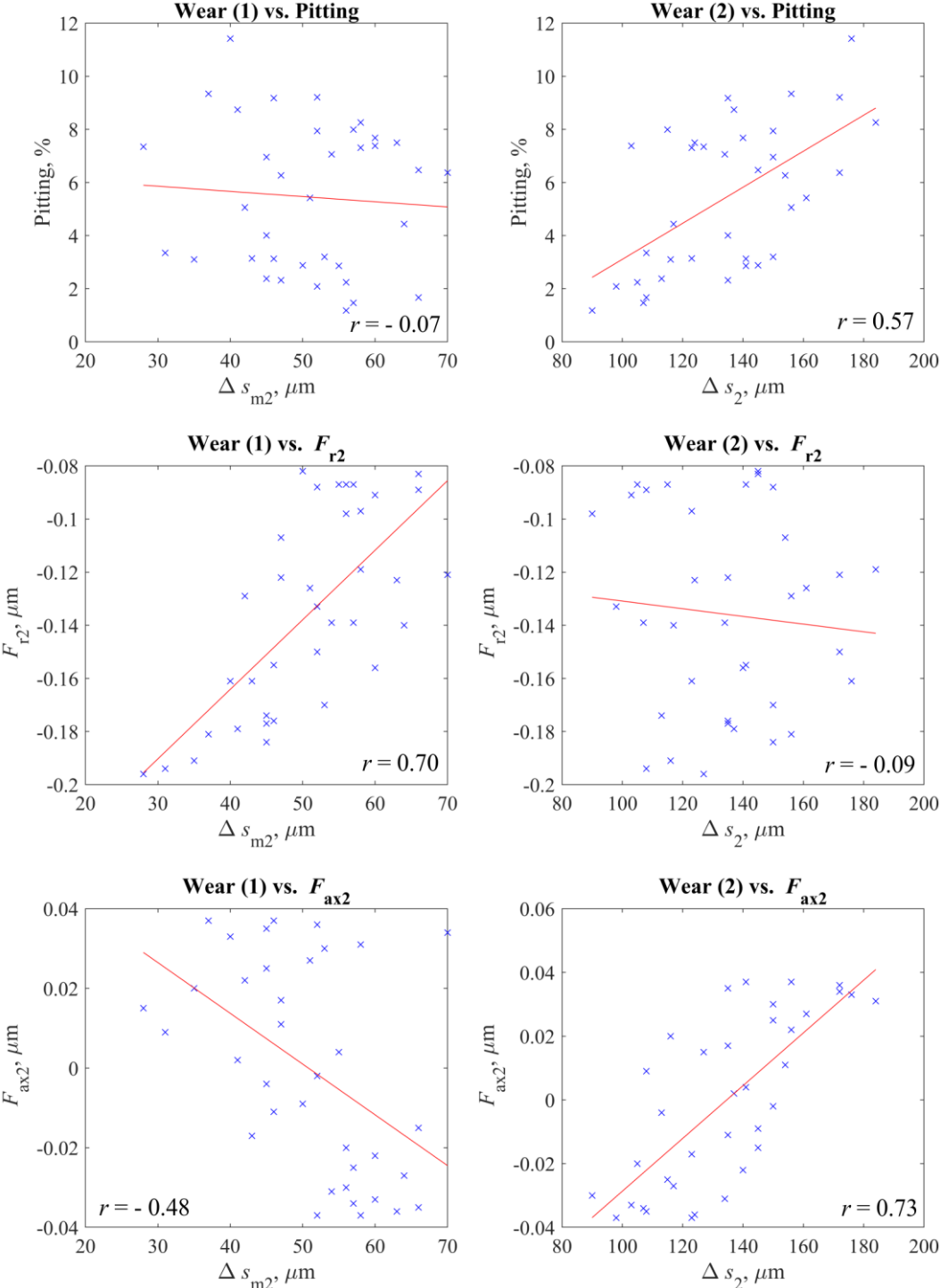


Figure 103. Worm wheel 1 - Correlation between wear, pitting, and deviations

Table 34. Pitting linear models for worm wheel 1

	Predictors	Linear model	R²
Overall pitting	$N_L \leq 2.0 \cdot 10^6$	$A_P(\%) = -0.884 + 0.000003 \cdot N_L$	53.81%
Overall pitting	$N_L \leq 2.0 \cdot 10^6$	$A_P(\%) = -2.058 + 0.000003 \cdot N_L$ $+ 2.348 \cdot F_{\text{worm}} + 8.34 \cdot F_{\text{ax2}}$	75.03%
	Worm wheel deviations + worm deviation		
Beginning of pitting ($A_{P10} = 2\%$)	$N_L \leq 5.7 \cdot 10^5$	$A_P(\%) = -0.1084 + 0.000001 \cdot N_L$	15.73%
Beginning of pitting ($A_{P10} = 2\%$)	$N_L \leq 5.7 \cdot 10^5$	$A_P(\%) = -0.1842 + 0.000001 \cdot N_L$ $+ 0.1514 \cdot F_{\text{worm}}$	18.92%
	Worm wheel deviations + worm deviation		
Pitting growth stage ($A_{P10,\text{max}} = 10\%$)	$5.7 \cdot 10^5 < N_L \leq 2.0 \cdot 10^6$	$A_P(\%) = -1.345 + 0.000003 \cdot N_L$	35.93%
Pitting growth stage ($A_{P10,\text{max}} = 10\%$)	$5.7 \cdot 10^5 < N_L \leq 2.0 \cdot 10^6$	$A_P(\%) = -3.015 + 0.000003 \cdot N_L$ $+ 3.341 \cdot F_{\text{worm}} + 12.28$ $\cdot F_{\text{ax2}}$	79.05%

The number of load cycles N_L was a dominant predictor in all presented models. This was anticipated as pitting is a form of material fatigue damage expected to be proportional to the number of load cycles. The predictors in the form of worm pair deviations increased the R^2 value in models for “Overall pitting” and “Pitting growth stage”. The increase was 21.22% and 43.12%, respectively. However, none of the worm wheel deviations were statistically relevant for the “Beginning of pitting” model. This was largely due to the nature of measured pitting percentages in that test period. Except for the few damaged flanks, other flanks had relatively similar pitting that could not be distinguished by the model. The problem with the $A_{P10} = 2\%$ criterion is that it considers only the average pitting of the four most damaged flanks. The

criterion is adequate when considering the beginning of pitting on worm wheel flanks in general. However, this criterion is not practical for defining the beginning of pitting when considering pitting percentages on each flank individually, as is the case in this research. An alternative criterion $A_{P,avg} = 2\%$ is proposed (Table 35). This criterion becomes applicable when average pitting measured on all flanks amounts to at least 2%. For $A_{P,avg} = 2\%$, the A_{P10} criterion takes on values much higher than 2%. In the example of worm wheel 1, when $A_{P,avg} = 2\%$ was met, the A_{P10} was 5.38%. The proposed alternative criterion also helps distinguish between the most and least damaged flanks more easily.

Table 35. Pitting linear model for worm wheel 1 - alternative beginning of pitting criterion

Beginning of pitting* ($A_{P,avg} = 2\%$)	$N_L \leq 1.1 \cdot 10^6$	$A_P(\%) = -0.633 + 0.000003 \cdot N_L$	39.56%
Beginning of pitting* ($A_{P,avg} = 2\%$)	$N_L \leq 1.1 \cdot 10^6$	$A_P(\%) = -1.161 + 0.000003 \cdot N_L$ $+ 1.056 \cdot F_{worm}$	54.12%

In order to understand how certain deviations impact the occurrence of first pitting and pitting at the end of the test, radar plots for the four most damaged and four least damaged flanks are given in Figure 104. The deviations were normalized in the range of -1 to 1. The largest radial runout is the closest probing ball position to the wheel axis and is normalized as 1. The bigger the tooth gap between two consecutive wheel teeth the larger the radial runout was measured (the probing ball was closer to the wheel axis). The largest differences between the most and least damaged flanks for $A_{P10} = 2\%$ criterion can be seen in f_{p2} and $F_{\alpha 2}$ deviations. It must be noted that the f_{p2} deviation presented here is primarily influenced by worm deviation F_{worm} and, therefore, should not be considered on its own. For the $A_{P10} = 10\%$ criterion in most damaged flanks, deviations F_{ax2} , F_{r2} , and $F_{\alpha 2}$ were positioned towards the maximum range, meaning the flanks with the largest of these deviations experienced the most pitting. On the contrary, when observing the least damaged flanks, those deviations were heavily inclined toward the other end of the deviation range. This was most noticeable for axial runout F_{ax2} where the positive range corresponds to axial runout measured in the positive axis-z direction (Figure 105). Plots for $A_{P,avg} = 2.54\%$ have a more similar deviation distribution than those at the end of the test ($A_{P10} = 9.78\%$). Also, radar plots of most damaged flanks are more alike than plots of least damaged flanks. Lastly, the position of the flanks on the wheel, defined by their numbers, was

more consistent in the most damaged flanks. Flanks No. 7 and No. 11 were the most damaged in all cases.

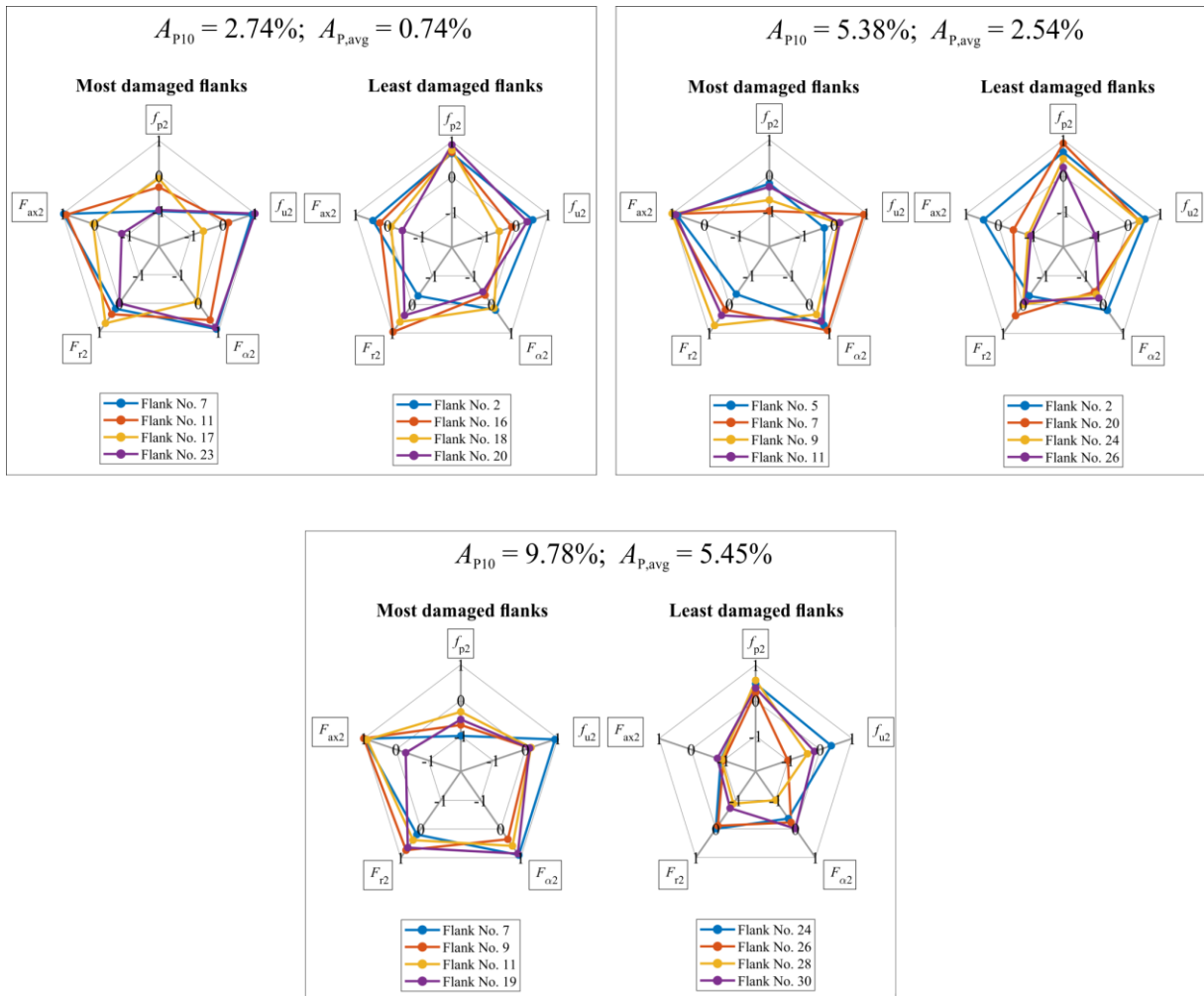


Figure 104. Worm wheel 1 - deviation distribution among the least and the most damaged flanks

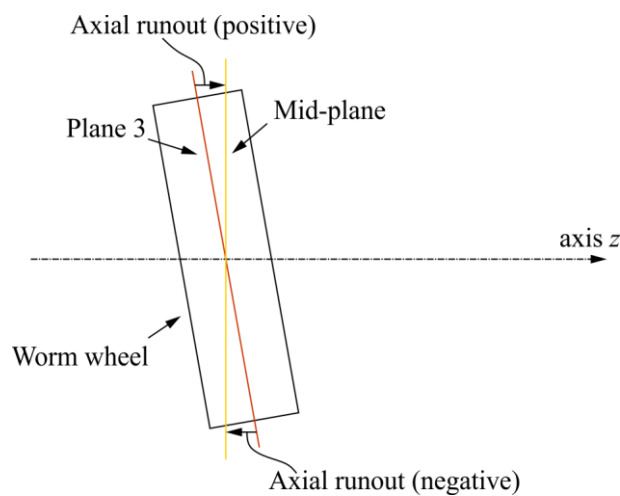


Figure 105. Axial runout – definition of positive and negative axial runout

9.2.2 Worm pair 2 (EP)

9.2.2.1 Pitting

Similar to worm pair 1, the first noticeable pitting was recorded after $N_L \approx 0.31 \cdot 10^6$ with average pitting being $A_{P,avg} = 0.11\%$ and $A_{P10} = 0.62\%$. Pitting formed on the top of the leaving side of the flank. According to Figure 106, the average pitting was $A_P = 9.77\%$ at the end of the test, while the average pitting on odd and even flanks was $A_P = 11.46\%$ and $A_P = 8.08\%$, respectively. The difference between the most and the least pitted flank, flank No. 35 and flank No. 10, was 12.5%. Interesting pitting development behavior was recorded for flank No. 12. After initial pitting development, up to $N_L \approx 1 \cdot 10^6$, for the remainder of the test, the increase in pitting was negligible compared to the average pitting increase on all flanks. This example suggests that it is possible to have worm wheel flanks with very little pitting development after the initial pitting is formed.

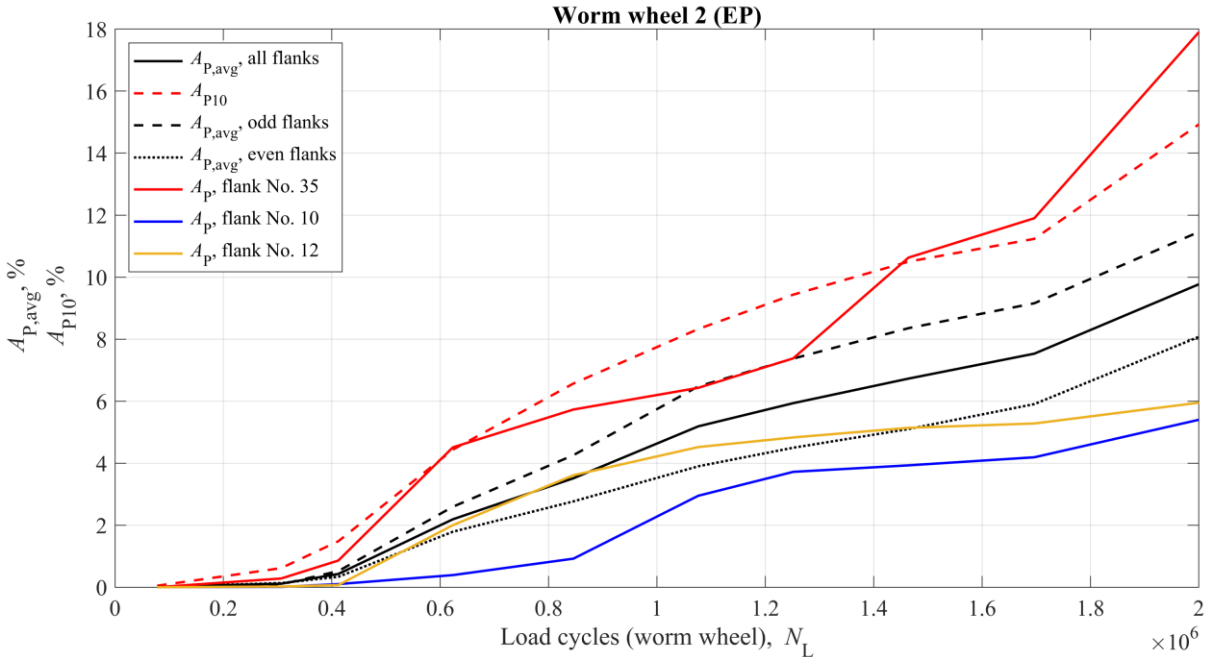


Figure 106. Pitting percentages for worm wheel 2

Pitting formation and development on flank No. 35 are presented in Figure 107. Pitting formed on the top of the leaving side of the flank and gradually developed across the top of the flank towards the middle of the tooth. According to Figure 108, a moderate correlation between the first pitting and pitting at the end of the test was also found in worm wheel 2 ($r = 0.59$), similar to worm wheel 1 ($r = 0.64$).

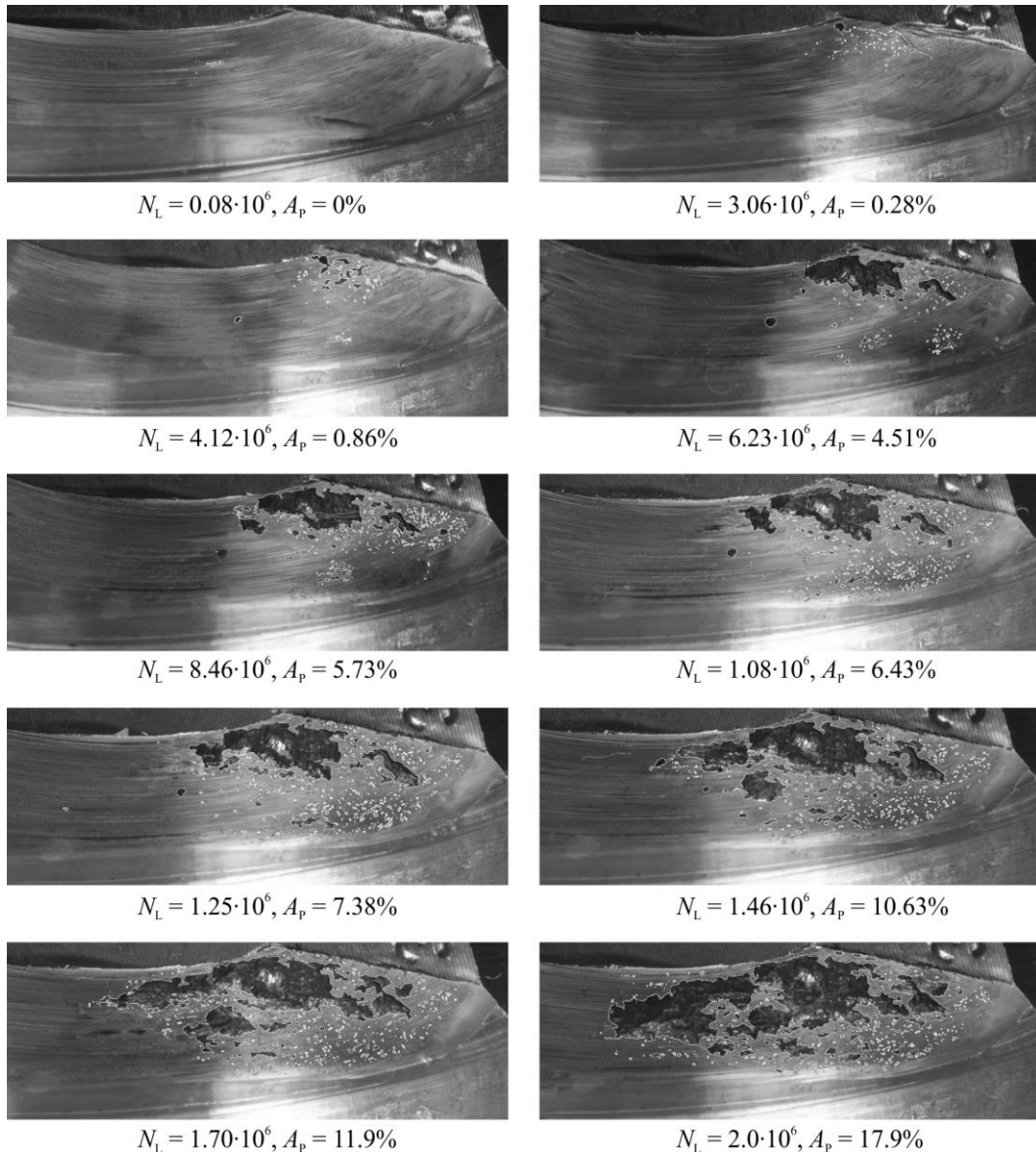


Figure 107. Pitting formation and development on flank No. 35

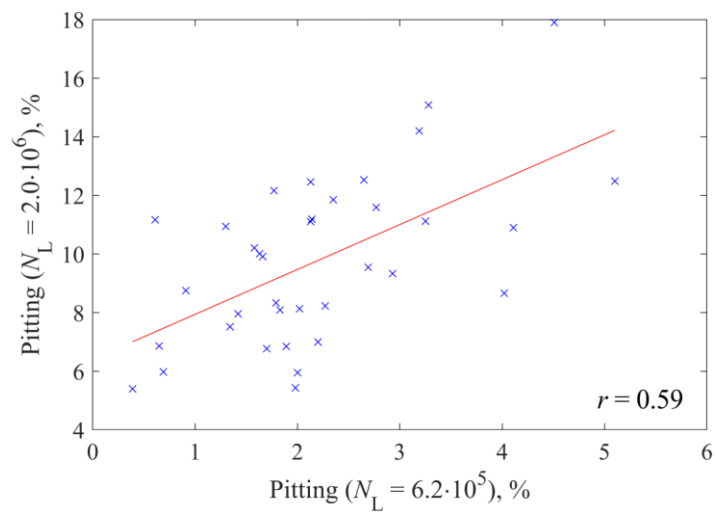


Figure 108. Pitting correlation for worm wheel 2

Pitting locations on tooth flanks are provided in Figure 109. Unlike pitting development in worm wheel 1 where odd flanks had pitting in the top while even flanks had in the bottom of the flank, here first pitting formed on both odd and even flanks on top of the leaving side of the flank and then gradually spread towards the bottom of the flank. Also, odd flanks were more damaged. The average pitting at the end of the test was $A_P = 11.46\%$ on odd flanks compared to $A_P = 8.08\%$ on even flanks.

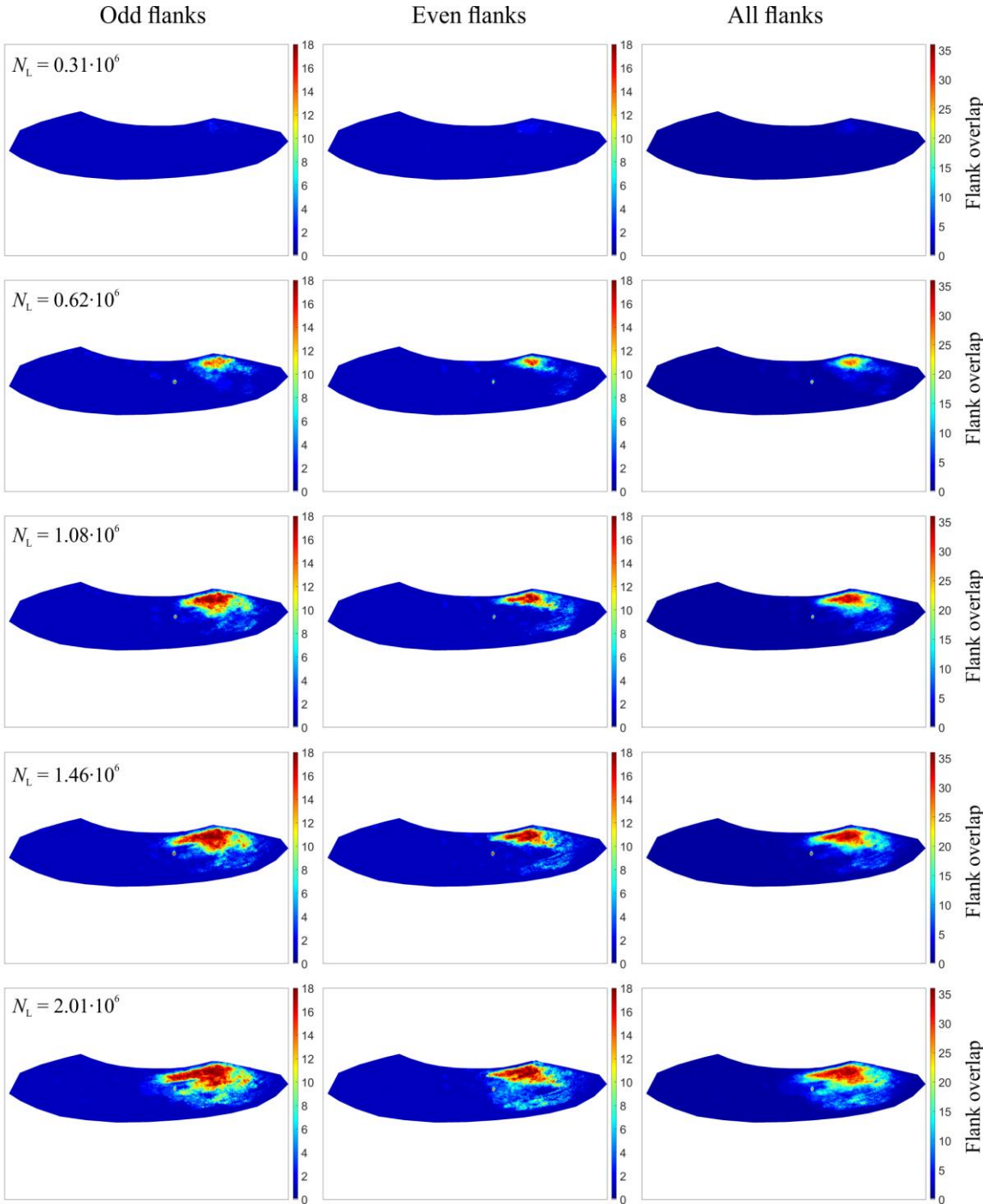


Figure 109. Pitting formation and development on worm wheel 2 flanks

Pitting depth analysis was conducted by analyzing computed tomography scans of tooth/flank No. 35 (CT, measuring device *exaCT 130S*). At the end of the test, flank No. 35 had a pitting area of $A_P = 17.9\%$. The maximum measured pitting depth was 0.55 mm (Figure 110). The location of the deepest pit was in the middle of the tooth where the tooth is the thinnest. Paired with the amount of wear of 0.06 mm measured at that location, the total material loss was 0.61 mm. The tooth thickness reduction criterion is only considered for wear load capacity calculation. According to the presented results, the largest tooth thickness reduction results from pitting and not wear.

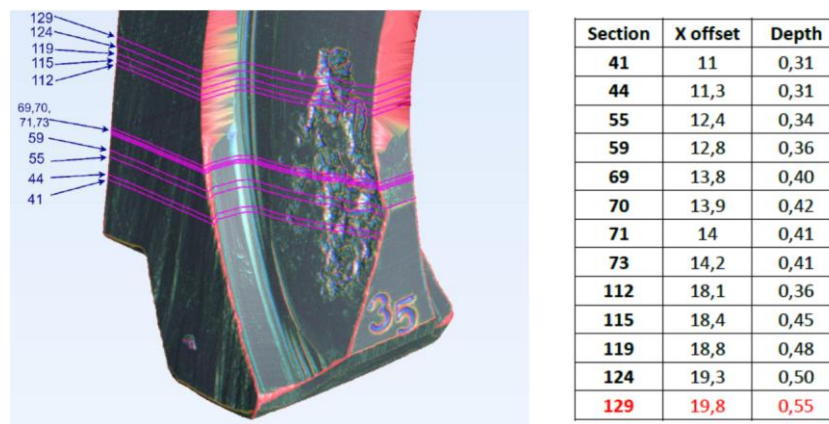


Figure 110. Pitting depth analysis of flank No. 35

9.2.2.2 Deviations, wear, and pitting model

The worm wheel deviations are given in Figure 111, while worm 2 average single pitch and runout deviations, measured at six points along the active part of worm thread length, are provided in Table 36. Worm pair 2 (EP) quality grades are given in Table 32.

Worm 2 single pitch deviations f_{px} were identical, while runout deviation F_{r1} was 3 μm . Also, the differences between axial profiles of worm threads were minimal (Figure 112). As worm 2 deviations could not point out meaningful differences between two worm threads, the only deviations that can be considered to explain the variance in pitting were worm wheel 2 deviations. As in worm wheel 1, the distribution of worm wheel single pitch deviation f_{p2} was unchanged. One positive pitch deviation was followed by one negative pitch deviation. By comparing Table 32 and Table 37, it can be noticed that worm 2 was characterized by lower quality grades compared to worm 1 (lower quality grade means lower deviations, thus better dimensional accuracy). On the other hand, worm wheel 2 had larger deviations than worm wheel 1 (worm wheel 2 had higher quality grades). Additionally, axial runout in worm wheel 1 was $F_{ax2} = \pm 37 \mu\text{m}$ compared to worm wheel 2 axial runout of $F_{ax2} = \pm 14 \mu\text{m}$. Radial runout

was larger in worm wheel 2 as well. However, the individual tooth gap values were also less negative compared to worm wheel 1. This can also be interpreted as the tooth gaps being narrower; therefore, the teeth were thicker in the worm wheel 2.

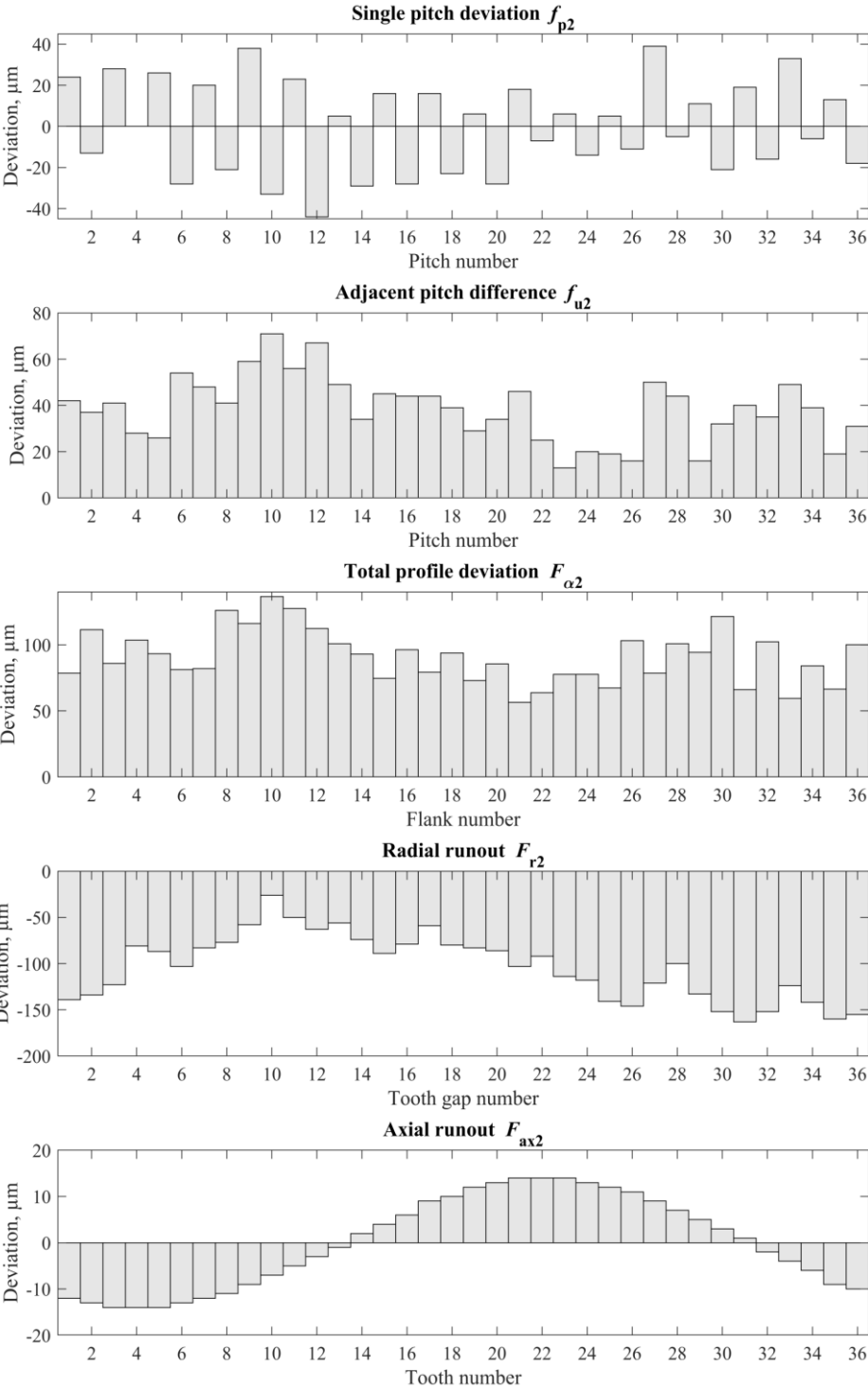


Figure 111. Worm wheel 2 - deviations

Table 36. Worm 2 - deviations

	f_{px} , mm	F_{r1} , mm
Thread 1	-0.020	0.830
Thread 2	-0.020	0.827

Table 37. Worm pair 2 (EP) – quality grades (Q)

Deviation	Worm		Wheel	
Single pitch deviation (axial)	f_{px}	Q9	-	-
Single pitch deviation	-	-	f_{p2}	Q11
Adjacent pitch difference	f_{ux}	Q1	f_{u2}	Q11
Total pitch deviation	F_{pz}	Q9	-	-
Total cumulative pitch deviation	-	-	F_{p2}	Q9
Total profile deviation	$F_{\alpha 1}$	Q10	$F_{\alpha 2}$	Q12
Runout	F_{r1}	Q1	F_{r2}	Q12

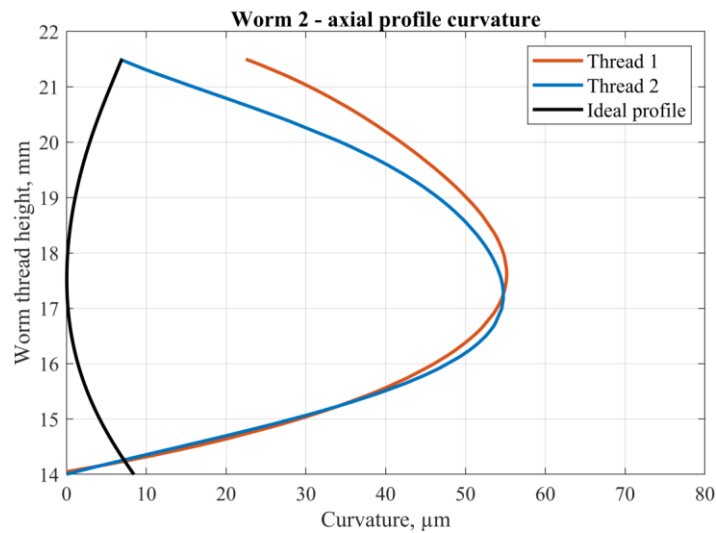
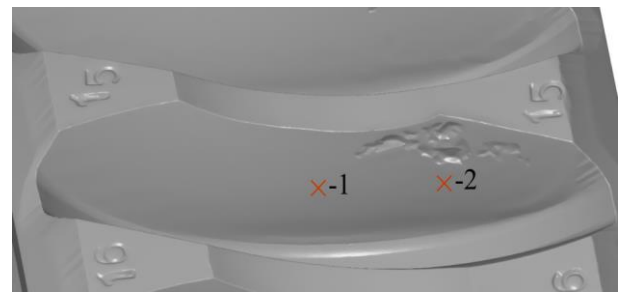


Figure 112. Worm 2 – axial profile curvature

Wear analysis was conducted similarly as in worm wheel 1. Wear was evaluated in the middle (Wear (1)) and on the leaving side of the flank (Wear (2)) by measuring tooth thickness before and after the test. The difference in tooth thickness Δs_{m2} represents wear on the worm wheel reference circle, while Δs_2 represents wear on the leaving side of the flank (Table 38). In contrast to worm wheel 1, the difference in wear between odd and even flanks was minimal or negligible, according to Δs_{m2} and Δs_2 values. As worm 2 thread profile curvatures were similar, this focuses on the significant difference in profile curvature in worm 1. Presumably, the large differences in worm 1 thread profiles were the main cause for dissimilar wear values among odd and even flanks present in worm wheel 1. Also, the wear did not correlate with the pitting in worm wheel 2 (Figure 113). In contrast, the positive moderate correlation between wear on the leaving side of the flank and pitting was present in worm wheel 1 (Figure 103). Compared to a high correlation of $r = 0.7$ between Wear (1) and radial runout in worm wheel 1, worm wheel 2 showed a moderate correlation of $r = 0.57$ between Wear (1) and radial runout. A high correlation was observed between Wear (1) and tooth thickness.

Table 38. Worm wheel 2 - tooth thickness difference after the test

		Δs_{m2} (1), μm	Δs_2 (2), μm
Odd teeth		71	120
Even teeth		64	118
All teeth		67	119

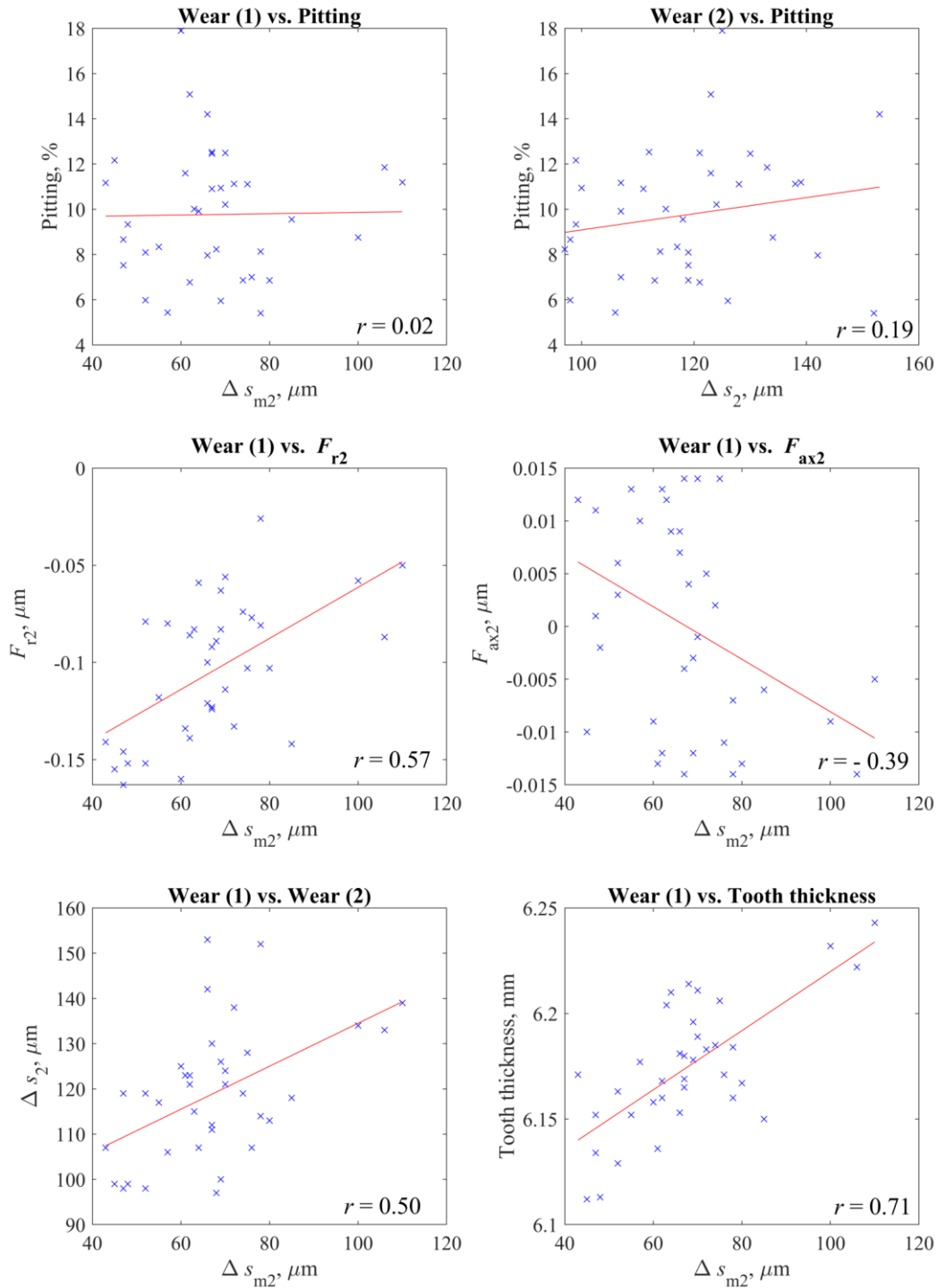


Figure 113. Worm wheel 2 - Correlation between wear, pitting, and deviations

Pitting linear models for “Overall pitting”, “Beginning of pitting,” defined by $A_{P10} = 2\%$, and “Pitting growth stage,” defined by $A_{P10,max} = 15\%$ at the end of the test, are presented in Table 39. Additionally, the linear model for alternative “Beginning of pitting” criterion $A_{P10} = 2\%$ is presented in Table 40. Significant increases in explained variance R^2 occurred when predicting the “Beginning of pitting” and “Pitting growth stage” with the inclusion of worm wheel deviations. The explained variance was higher by 11.50% and 19.68%,

respectively. The f_{p2} and F_{r2} were statistically relevant in all models. The axial runout F_{ax2} was not statistically significant in pitting linear models on worm wheel 2. The value of axial runout value was considerably smaller than in worm wheel 1 ($\pm 14 \mu\text{m}$ vs. $\pm 37 \mu\text{m}$). Thus, its effect on pitting was not found to be significant by the presented models.

Table 39. Pitting linear models for worm wheel 2

	Predictors	Linear model	R²
Overall pitting	$N_L \leq 2.0 \cdot 10^6$	$A_P(\%) = -1.176 + 0.000005 \cdot N_L$	79.96%
Overall pitting	$N_L \leq 2.0 \cdot 10^6$	$A_P(\%) = -2.21 + 0.000005 \cdot N_L + 36.32$ $\cdot f_{p2} - 9.93 \cdot F_{r2}$	86.54%
	Worm wheel deviations		
Beginning of pitting ($A_{P10} = 2\%$)	$N_L \leq 5.1 \cdot 10^5$	$A_P(\%) = -0.3416 + 0.000002 \cdot N_L$	34.99%
Beginning of pitting ($A_{P10} = 2\%$)	$N_L \leq 5.1 \cdot 10^5$	$A_P(\%) = -0.876 + 0.000002 \cdot N_L + 4.41$ $\cdot f_{p2} - 5.13 \cdot F_{r2}$	46.49%
	Worm wheel deviations		
Pitting growth stage ($A_{P10,max} = 15\%$)	$5.1 \cdot 10^5 < N_L \leq 2.0 \cdot 10^6$	$A_P(\%) = -0.797 + 0.000005 \cdot N_L$	59.47%
Pitting growth stage ($A_{P10,max} = 15\%$)	$5.1 \cdot 10^5 < N_L \leq 2.0 \cdot 10^6$	$A_P(\%) = -2.117 + 0.000005 \cdot N_L + 54.56$ $\cdot f_{p2} - 12.67 \cdot F_{r2}$	79.15%
	Worm wheel deviations		

Table 40. Pitting linear model for worm wheel 2 - alternative “Beginning of pitting” criterion

Beginning of pitting* ($A_{P,avg} = 2\%$)	$N_L \leq 6.2 \cdot 10^5$	$A_P(\%) = -0.690 + 0.000004 \cdot N_L$	47.65%
Beginning of pitting* ($A_{P,avg} = 2\%$)	$N_L \leq 1.1 \cdot 10^6$	$A_P(\%) = -1.426 + 0.000003 \cdot N_L + 6.83$ $\cdot f_{p2} - 7.07 \cdot F_{r2}$	56.63%

The most and the least damaged worm wheel flanks characterized by their deviations are presented in Figure 115. The first pitting developed on flanks with large positive single pitch deviation f_{p2} and large runout deviation F_{r2} (Figure 115a). As worm 2 threads had no difference in single pitch deviation (both threads had $f_{px} = -0.020$ mm), the worst pitch combination in terms of load distribution is expected when worm wheel flanks will have positive f_{p2} (-/+ combination of single pitch deviations). This was evident in all presented plots in Figure 115. On the other hand, the least damaged flanks were characterized by negative f_{p2} and smaller runout deviation F_{r2} (between 0 and -1). Tooth profile deviation $F_{\alpha 2}$ was in the negative range in most damaged flanks (between 0 and -1) and in the positive range in the least damaged flanks. The most damaged flanks were distributed between flank No. 23 and No.1, while the least damaged flanks were positioned from flank No. 10 to No. 18, if excluding flank No. 25. This flank distribution indicates that there can be sectors with higher and lower pitting damage on worm wheel, primarily influenced by F_{r2} deviation. Pitting measured after $N_L = 0.62 \cdot 10^6$ for nine consecutive flanks with large F_r (flank No. 30 to flank No. 2) and small F_r (flank No. 6 to flank No. 14) is displayed in Figure 114. The worm wheel sector with large F_r had $A_{P,avg} = 3.10\%$ compared to $A_{P,avg} = 1.38\%$ found in the sector with low F_r . In the case of worm wheel 2, the most damaged flanks were not the same for $A_{P10} = 2.54\%$ and $A_{P10} = 14.92\%$, although relatively close by their position on the worm wheel. The same holds for least damaged flanks. This observation further supports the earlier statement regarding worm wheel sectors with more or less pitting.

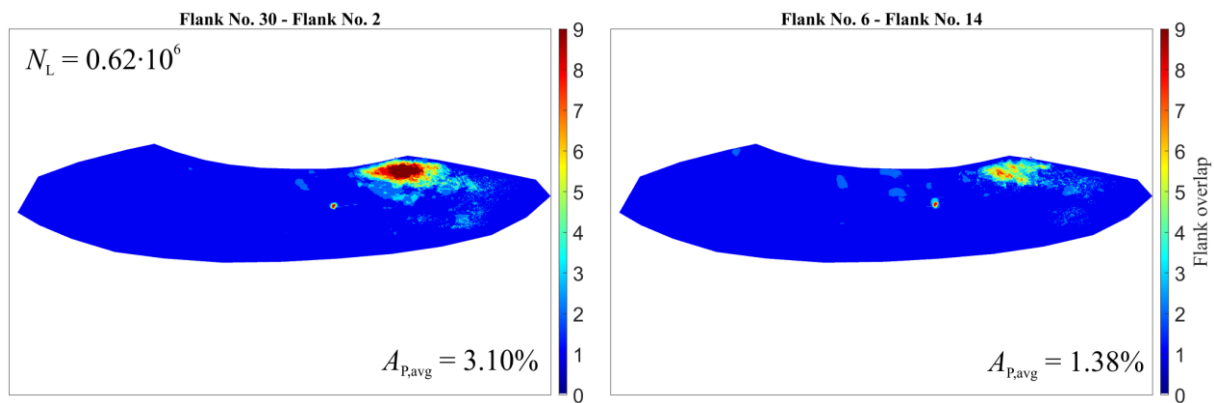


Figure 114. Overlap of nine consecutive flanks: a) large F_r , b) small F_r

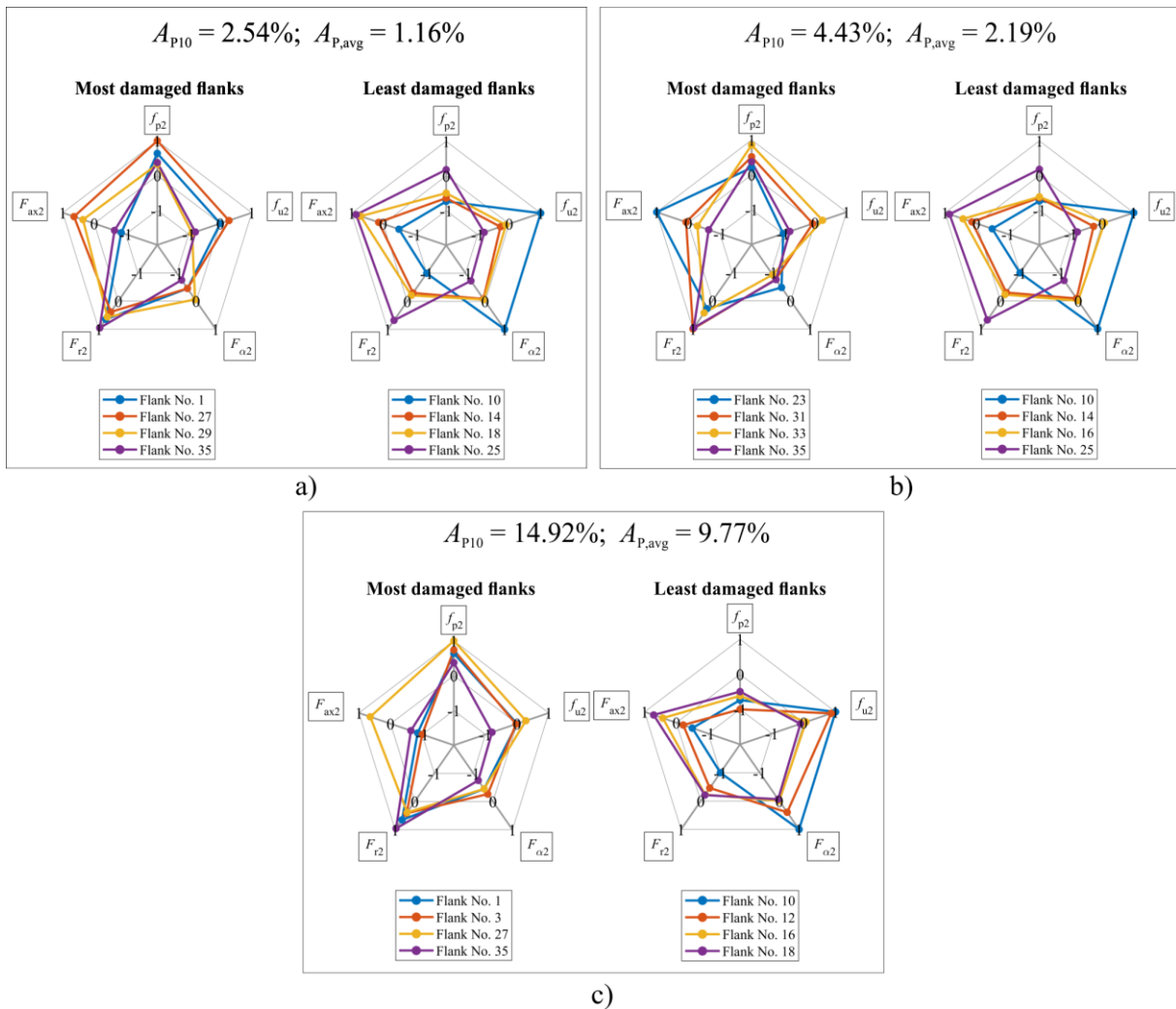


Figure 115. Worm wheel 2 - deviation of most damaged and least damaged flanks

9.2.3 Worm pair 3 (EP)

9.2.3.1 Pitting and wear

Worm wheel 3 was paired with electropolished worm 3. The pair was characterized by the largest contact pattern due to higher initial wear and faster and better running-in. In part, this can be attributed to the electropolished worm surface as a similar phenomenon was observed during the block-on-disc experiment presented in this research, and the literature [32,142]. Also, worm wheel 3 had substantially lower pitting than the other two pairs. Pitting percentages are presented in Figure 116. The pitting location at the end of the test, overlapped for odd, even, and all flanks, is shown in Figure 117.

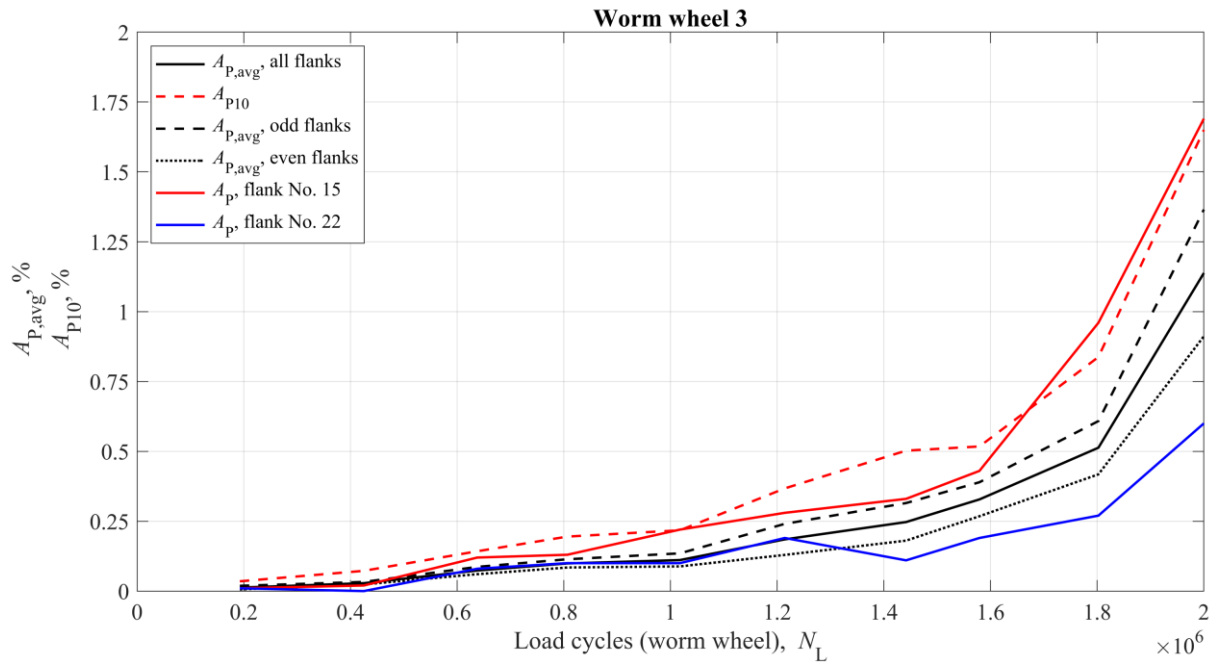


Figure 116. Pitting on worm wheel 3

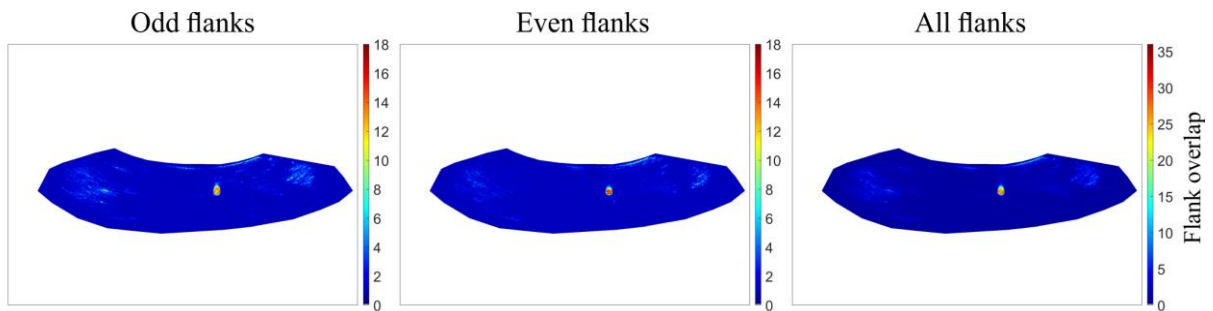


Figure 117. Pitting location (overlapped) on flanks of worm wheel 3

Due to the established full contact pattern, the pitting developed on the leaving side of the flank, while micropitting developed on the entering side of the flank (Figure 118). Generally, pitting or micropitting development on the entering side of the flank indicates that the contact pattern is not adequate. Micropitting occurring on the entering side usually indicates a significant contact pressure build-up which can limit the oil entering the contact zone. This can create unfavorable lubrication conditions. Most of the pitting overlap occurred in the middle of the flanks. In the middle of the flank, the oil film thinning effect is intensified due to significant convection of temperature from the worm wheel into the oil and unfavorable contact geometry [30]. However, as already explained in section 9.1 *Influence of surface texturing*, the effects of electropolished worm surface, primarily enhanced running-in and improved lubrication, play a vital role in the efficiency and pitting behavior of worm wheel 3. Furthermore, the improved

lubrication conditions enable worm pair 3 to work with a full contact pattern without harmful effects. In worm pairs with ground-only worms, the full contact pattern promotes the onset of scuffing due to insufficient lubrication (e.g., worm pair 6).

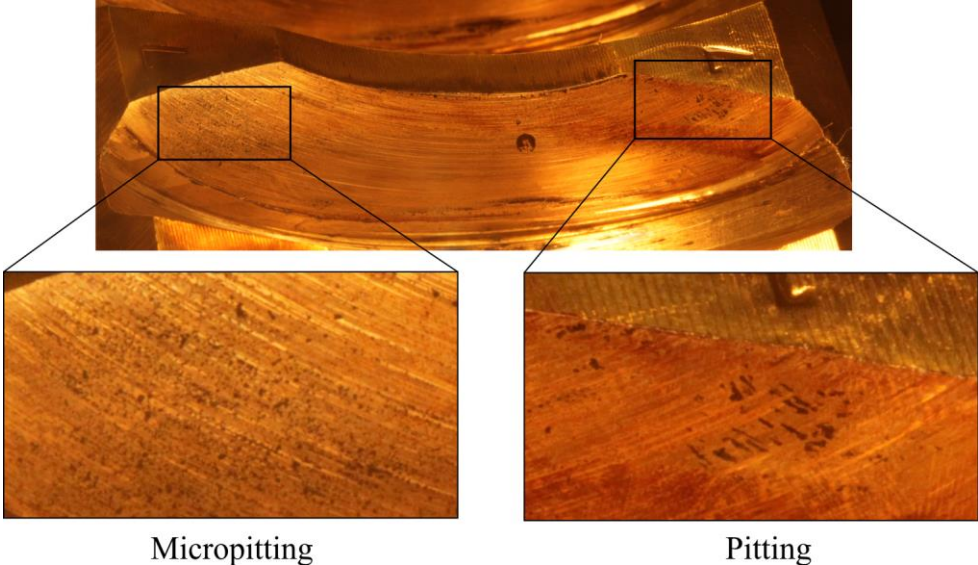


Figure 118. An example of micropitting and pitting

Wear was measured through tooth thickness reduction in the middle and on the leaving side of the flank (Table 41). Obtained values in worm wheel 3 were a lot higher compared to $\Delta s_{m2} = 51 \mu\text{m}$ and $\Delta s_2 = 135 \mu\text{m}$ in worm pair 1, and $\Delta s_{m2} = 67 \mu\text{m}$ and $\Delta s_2 = 119 \mu\text{m}$ in worm pair 2 (EP).

Table 41. Worm wheel 3 - tooth thickness difference after the test

		$\Delta s_{m2} (1), \mu\text{m}$	$\Delta s_2 (2), \mu\text{m}$
	Odd teeth	264	407
	Even teeth	244	420
	All teeth	254	414

The increased wear is not desirable, if observed as an isolated phenomenon. The interconnected system of contact pattern, sliding wear, and pitting is a complex topic in worm pairs. Sliding wear is necessary to achieve an adequate contact pattern. Also, the amount of wear can vary depending on worm pair geometry, as seen from the presented results. For worm pairs in this research, the measured amount of wear at the end of the test run can be roughly approximated as the amount of wear that occurred as a byproduct of running-in. This is because most wear

occurs during running-in or at the end of a lifetime when severe wear precedes component failure. In conducted test runs, the number of load cycles was $N_L = 2 \cdot 10^6$, which is far lower than N_L estimated through wear load capacity calculation. Therefore, the eventual wear that precedes the end of a lifetime for the worm wheel can be ignored.

On the other hand, if a high wear rate continues throughout the worm pair operation, e.g., after the running-in process, it will cause worm wheel teeth to thin and tooth tip to break. A high enough wear rate might mitigate the onset and development of pitting as the material is constantly removed from the flank [25,29]. Another possibility is that when the load is uniformly distributed and accompanied by favorable lubrication conditions, the wear after the running-in period will be minimal, and pitting development will slowly take place. This is the most likely scenario that was observed in worm wheel 3. However, the high wear rate will occur during stage III of pitting development, appropriately named the “Wear stage” by the ISO/TS 14521 standard. As a large portion of the worm wheel tooth surface is damaged, its load-carrying ability is significantly reduced, resulting in increased wear on the remainder of the flank surface. This behavior usually indicates the end of the lifetime of a worm wheel.

9.2.3.2 Deviations

The worm wheel deviations are given in Figure 119. Single pitch deviation had the same distribution as in previous worm wheels. Worm wheel 3 had the smallest tooth thickness among observed worm wheels. This is the reason for larger negative individual runout deviations than worm wheels 1 and 2. The overall runout deviation was $F_{r2} = 137 \mu\text{m}$, expressed as the difference between the smallest and the largest individual runout deviation. The axial runout was $F_{ax2} = \pm 42 \mu\text{m}$.

Worm 3 average single pitch and runout deviations, measured at six points along the active part of worm thread length, are provided in Table 42. The comparison of profile curvatures is presented in Figure 120. Once again, the measured deviations did not point to significant differences among worm threads. Worm pair 3 (EP) quality grades are given in Table 43. The total profile deviation measured on worm wheel 3 was larger than the Q12. Therefore, no appropriate quality grade could be assigned according to the DIN 3974 standard [11].

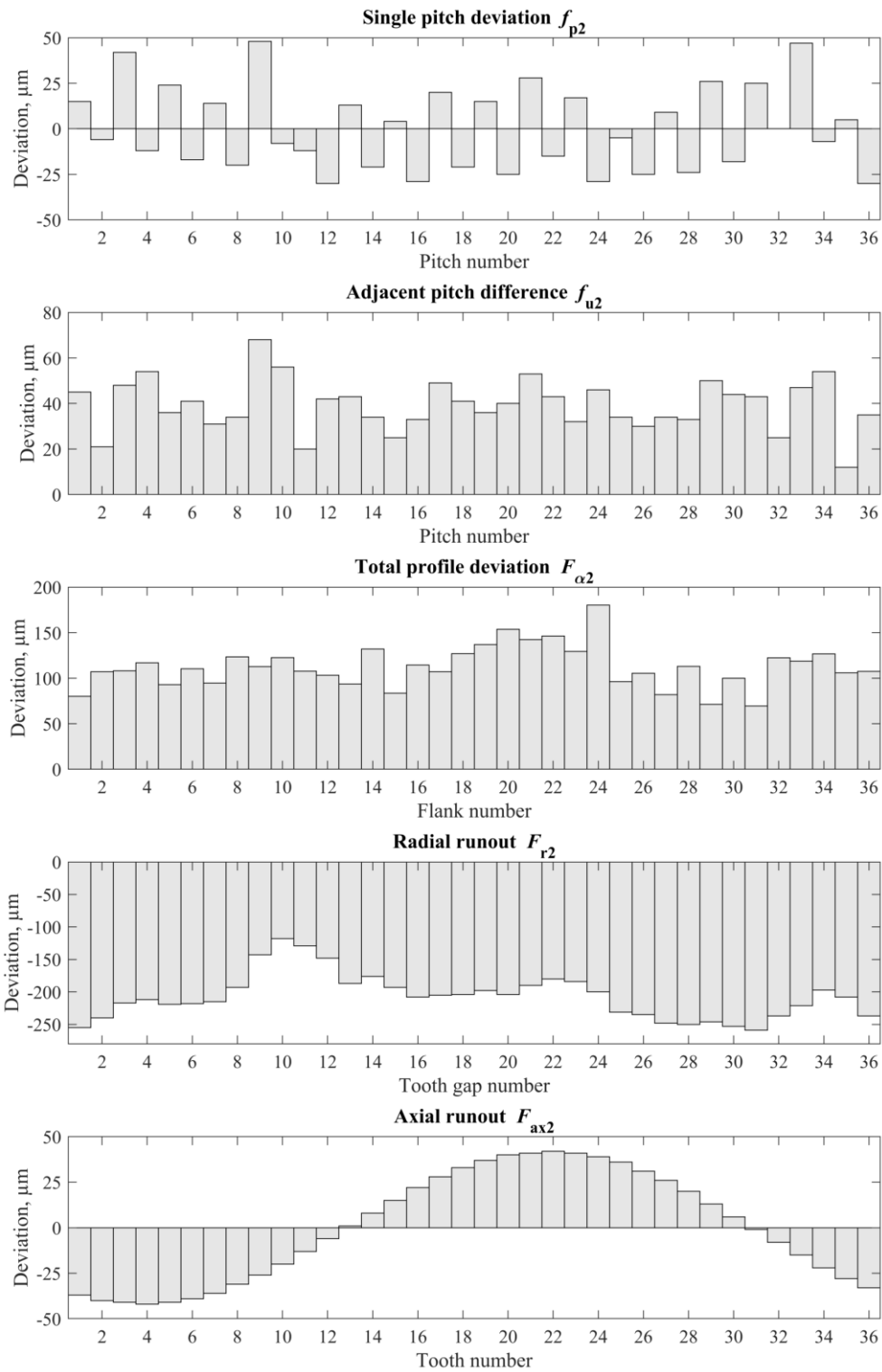


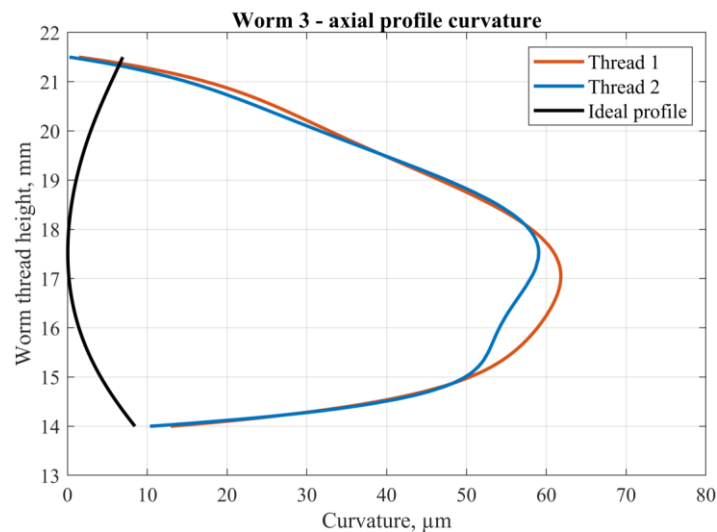
Figure 119. Worm wheel 3 – deviations

Table 42. Worm 3 - deviations

	f_{px} , mm	F_{r1} , mm
Thread 1	-0.015	0.890
Thread 2	-0.018	0.890

Table 43. Worm pair 3 (EP) – quality grades (Q)

Deviation	Worm		Wheel	
Single pitch deviation (axial)	f_{px}	Q9	-	-
Single pitch deviation	-	-	f_{p2}	Q11
Adjacent pitch difference	f_{ux}	Q3	f_{u2}	Q11
Total pitch deviation	F_{pz}	Q9	-	-
Total cumulative pitch deviation	-	-	F_{p2}	Q9
Total profile deviation	$F_{\alpha 1}$	Q11	$F_{\alpha 2}$	N/A
Runout	F_{r1}	Q1	F_{r2}	Q12

**Figure 120.** Worm 3 – axial profile curvature

In the case of worm wheel 3, an appropriate pitting linear model could not be adequately formulated as pitting was relatively low. The maximum pitting measured on the four most damaged teeth was $A_{P10} = 1.65\%$. This was below the $A_{P10} = 2\%$ criterion that is usually considered for the beginning of pitting. An additional problem with low pitting percentages is that it is hard to objectively distinguish which flanks should be considered the most damaged (or the least damaged) due to the small pitting differences among flanks. Moreover, when a lot of micropitting is present on the flank, it becomes problematic to accurately capture all relevant micro pits during image post-processing. Thus, there is a tendency towards higher image post-processing errors. Pitting at the end of the test is presented in Figure 121. The most damaged flanks are highlighted in red and the least damaged flanks are highlighted in blue. Pitting formation occurred on flanks characterized by positive f_{p2} due to an unfavorable pitch combination with negative f_{px} on mating worm threads. Compared to axial runout in worm

wheel 2 ($F_{ax2} = \pm 14 \mu\text{m}$), when axial runout is larger (worm wheel 1, $F_{ax2} = \pm 37 \mu\text{m}$; worm wheel 3, $F_{ax2} = \pm 42 \mu\text{m}$), it becomes an influential factor in pitting formation.

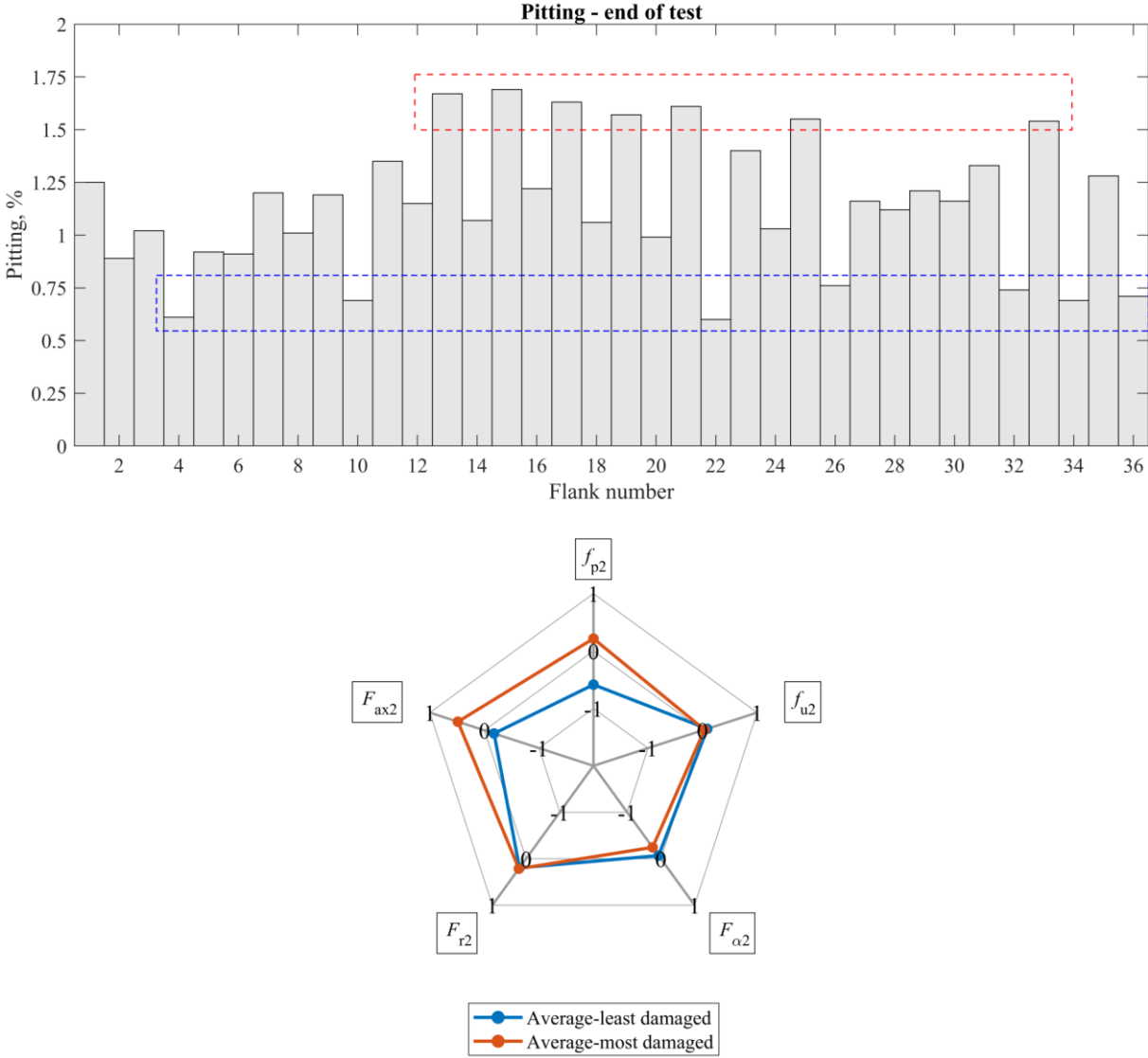


Figure 121. Worm wheel 3 – pitting at the end of the test

9.2.4 Worm pair 4 (AlSn6 worm wheel)

9.2.4.1 Pitting

Besides test runs with CuSn12 worm wheels, an additional test run with AlSn6 worm wheel was conducted. Due to the lower mechanical properties of worm wheel material, the applied load was $T_2 = 200$ Nm. Pitting development on worm wheel flanks is presented in Figure 122. Both odd and even flanks were characterized by the same pitting percentage, unlike in CuSn12 wheels, where a major difference was observed between odd and even flanks. By analyzing CuSn12 wheels, it was found that the characteristic nature of single pitch deviation (one positive deviation followed by one negative deviation) was the main reason for the uneven pitting distribution. Deviations on worm wheel 4 had no such characteristic nature, yet the distribution was more stochastic without any observable pattern. A more detailed analysis of deviations will be presented later in this section. The difference between the most pitted flank, No. 14, and the least pitted flank, No.30, was $A_P = 13\%$, or in percentage difference, 88%. The first pitting occurred across the flanks; no exact location could be specified. However, as the test run continued, pitting continued to develop only on the leaving side of the flanks. The comparison of pitting development on flanks No. 14 and No. 30 is shown in Figure 123.

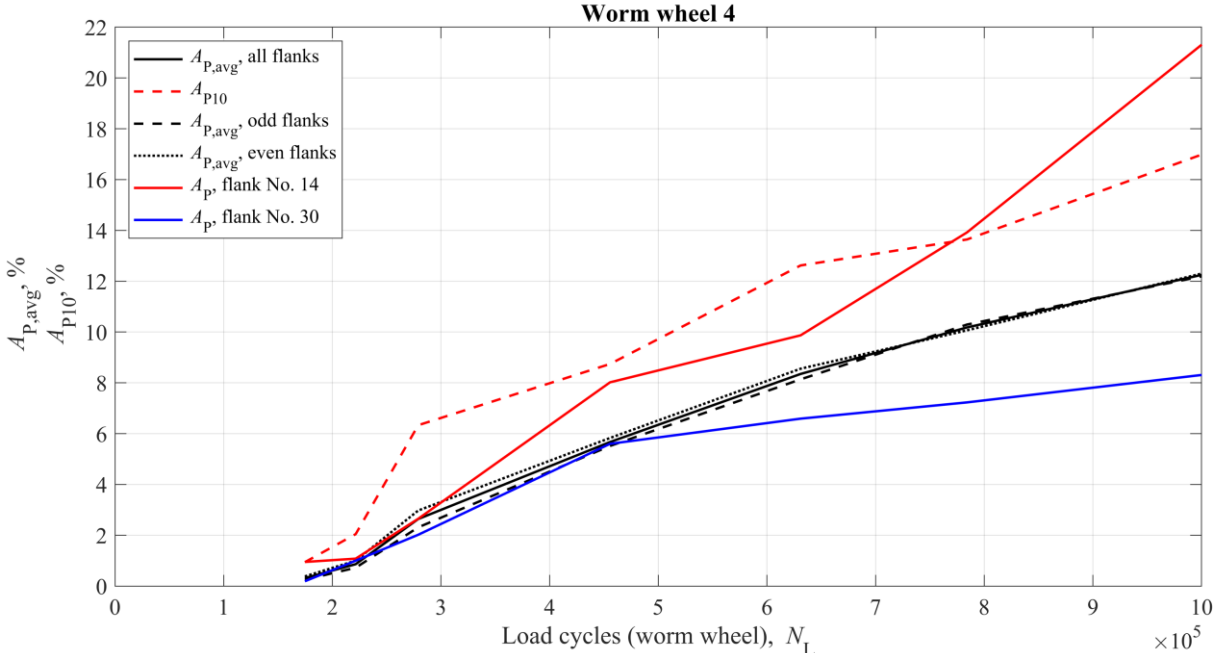


Figure 122. Pitting on worm wheel 4

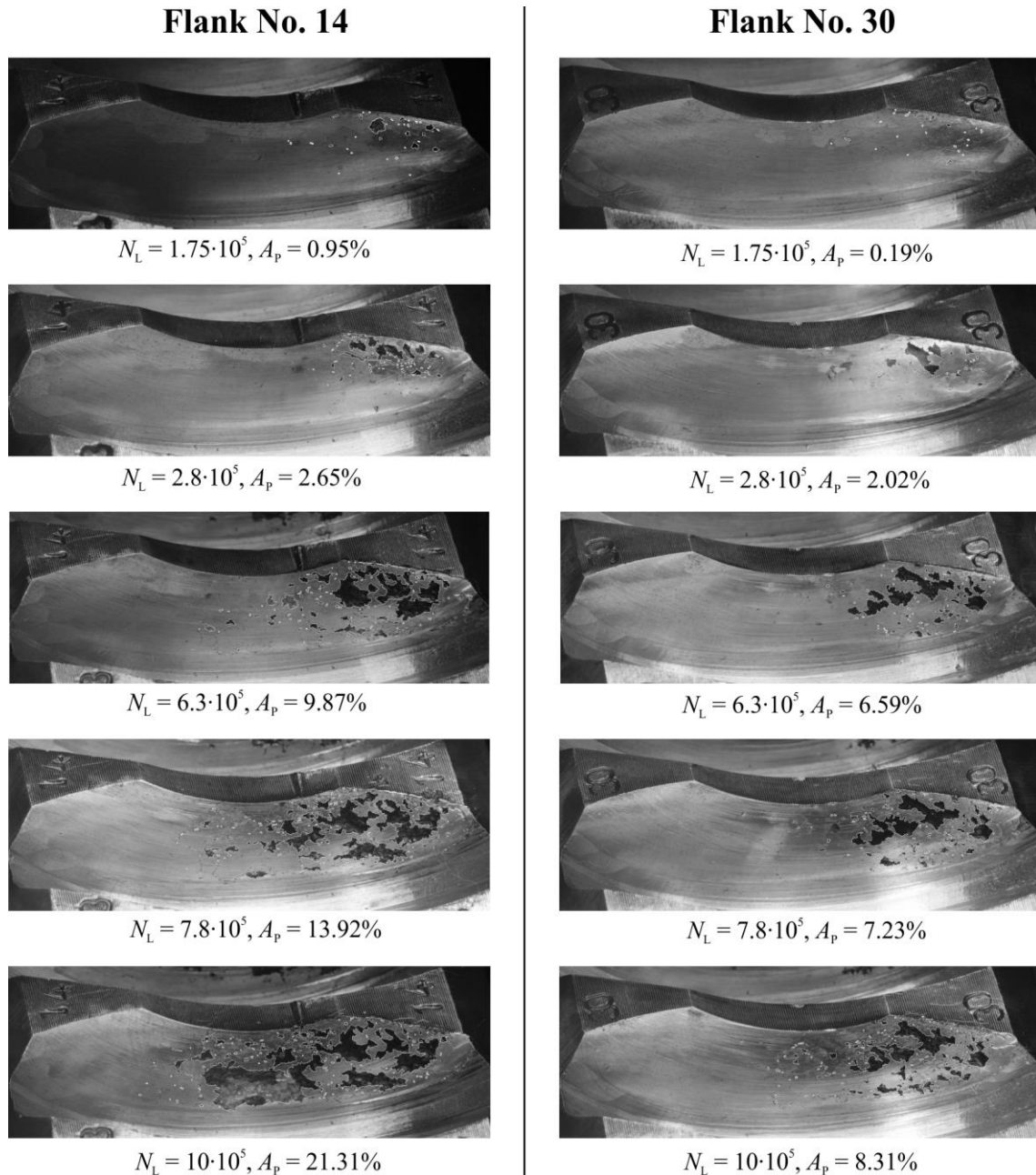


Figure 123. Pitting formation and development on AlSn6 worm wheel flanks

Generally, the AlSn6 wheel had much more pitting compared to the results reported by other authors (see Figure 93). The uneven and abrupt increase in pitted area was more evident in the AlSn6 worm wheel than in CuSn12 wheels. Besides the material's microstructure, the reason behind this could be the amount of porosity found in AlSn6 material. Computed tomography (CT, measuring device *exaCT 130S*) was employed to investigate the quality of cast material. The results are presented in Figure 124. A considerable amount of shrinkage volume/porosity defects had been found. Porosity defects in the material can act as stress concentrators from where the crack initiates and propagates toward the surface. If the crack propagates through several near-surface porosity defects, it can result in the removal of a large piece of material.

The measured pit depth varied from 0.18 to 0.3 mm (Figure 125). These pits were considerably shallower compared to the pit depth of 0.31 to 0.55 mm found in worm wheel 2.

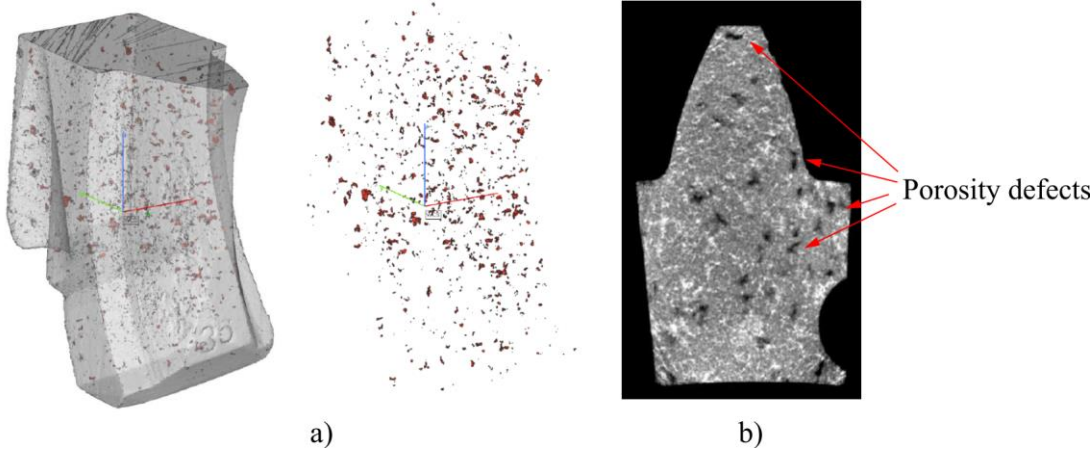


Figure 124. CT scan of AlSn6 worm wheel: a) detected shrinkage volume, b) porosity defects

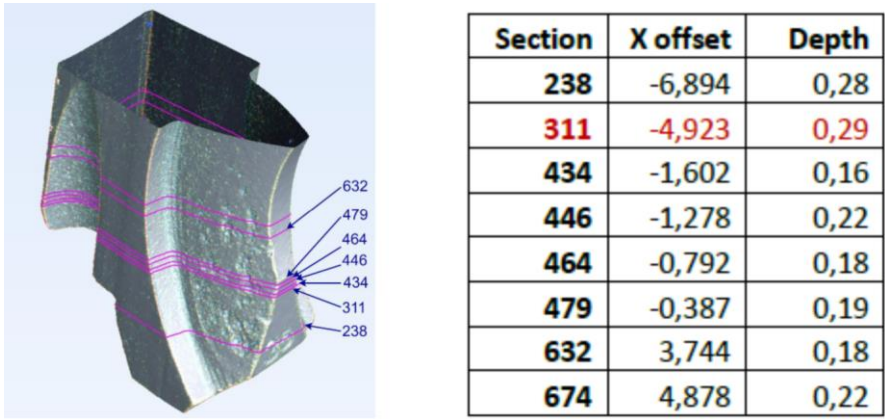


Figure 125. Pit depth across different axial sections

9.2.4.2 Deviations and pitting model

Worm wheel deviations are given in Figure 126, and worm deviations are provided in Table 44. Single pitch deviation f_{p2} and total profile deviation $F_{\alpha 2}$ had stochastic distribution. Unlike in CuSn12 worm wheels, no characteristic or specific pattern was observed. The distribution of radial and axial runout had typical distributions. Radial runout usually has regions or sectors with more pronounced deviations as it is a consequence of inaccuracies that occur during machining. This refers to inaccurate clamping/fixation of the part being manufactured or radial runouts of rotary tables, indexing machines. Axial runout had expected sinusoidal distribution based on the employed measuring principle for its measurement (see

Figure 40). The overall runout deviation was $F_{r2} = 146 \mu\text{m}$, while the axial runout was $F_{ax2} = \pm 45 \mu\text{m}$. Worm profile curvatures are presented in Figure 127. The dimensional accuracy of worm pair 4 is presented in Table 45. According to quality grades, worm pair 4 had the lowest deviations among all investigated worm pairs.

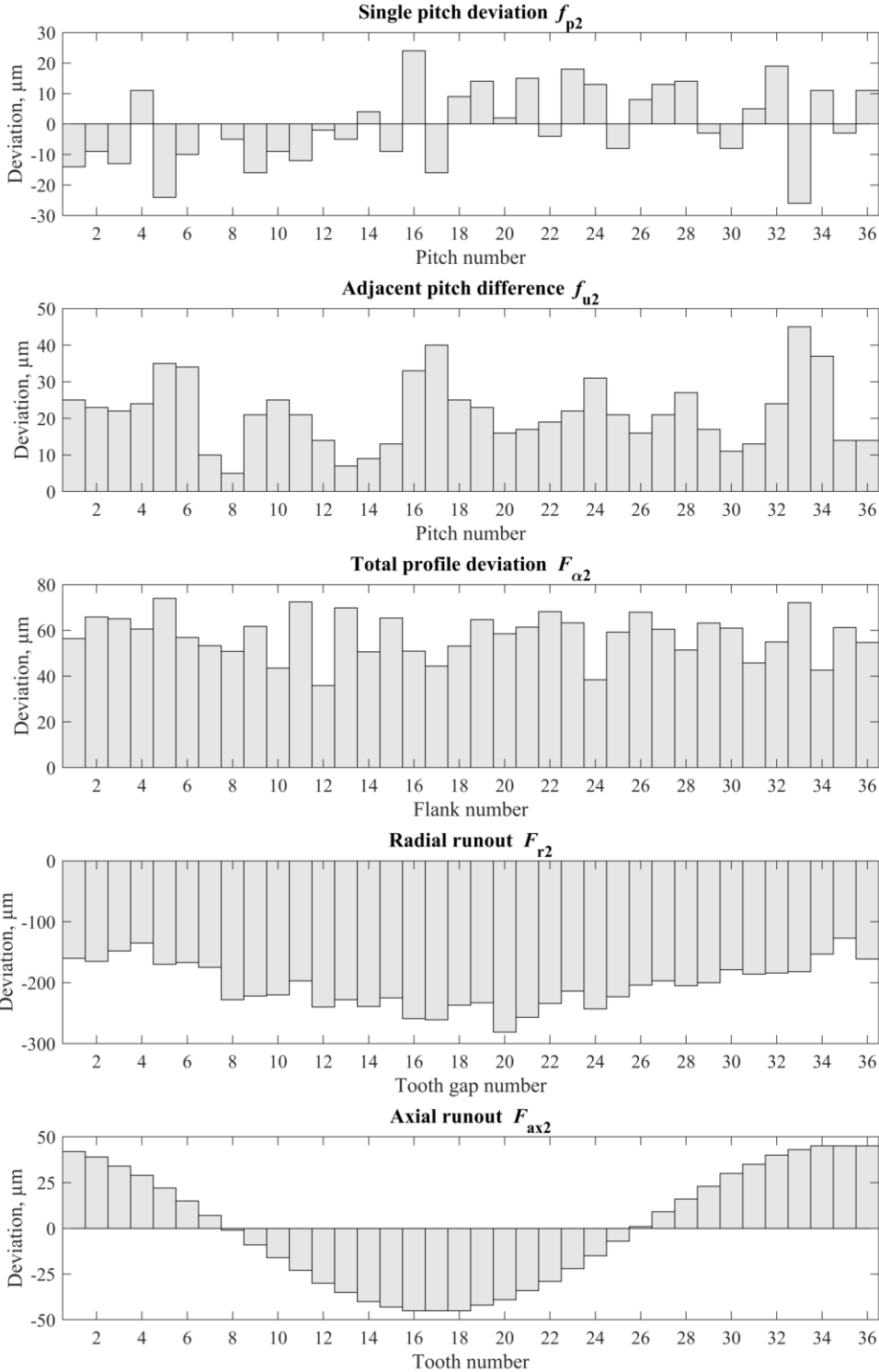


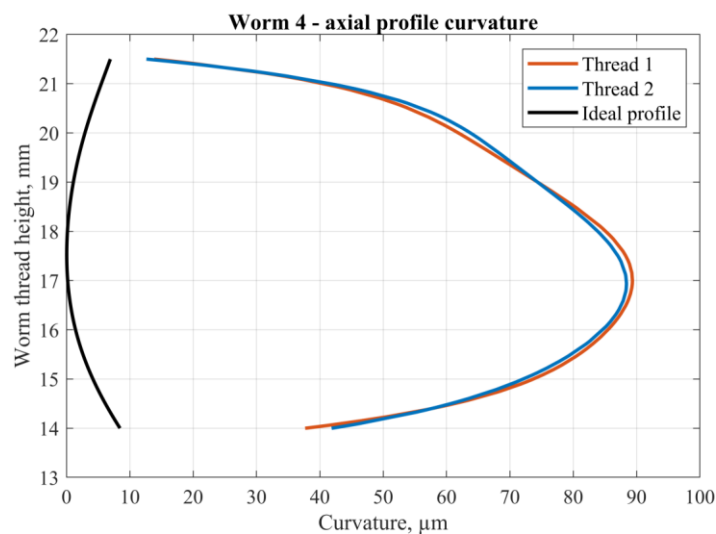
Figure 126. Worm wheel 4 – deviations

Table 44. Worm 4 - deviations

	f_{px} , mm	F_{r1} , mm
Thread 1	0.007	0.890
Thread 2	0.008	0.895

Table 45. Worm pair 4 – quality grades (Q)

Deviation	Worm		Wheel	
Single pitch deviation (axial)	f_{px}	Q6	-	-
Single pitch deviation	-	-	f_{p2}	Q10
Adjacent pitch difference	f_{ux}	Q1	f_{u2}	Q10
Total pitch deviation	F_{pz}	Q7	-	-
Total cumulative pitch deviation	-	-	F_{p2}	Q10
Total profile deviation	$F_{\alpha 1}$	Q11	$F_{\alpha 2}$	Q11
Runout	F_{r1}	Q3	F_{r2}	Q12

**Figure 127.** Worm 4 – axial profile curvature

Linear pitting models were developed for “Overall pitting”, “Beginning of pitting” defined by $A_{P10} = 2\%$, and “Pitting growth stage,” defined by $A_{P10,max} = 17\%$ at the end of the test (Table 46). In contrast to linear models developed for CuSn12 worm wheels, worm wheel deviations have little impact on improving the explained variance R^2 in “Overall pitting” and “Pitting growth stage” models. A more significant increase in R^2 occurred when predicting “Beginning of pitting” and “Beginning of pitting” with the alternative criterion of at least

$A_{P,avg} = 2\%$ (Table 47). Due to the stochastic nature of f_{p2} distribution and its lower values, the primary predictor, the number of load cycles N_L , becomes predominant in predicting “Overall pitting” and “Pitting growth stage”. None of the models recognized the f_{p2} deviation as statistically significant in predicting AlSn6 worm wheel pitting. The conclusion arises that as single pitch deviation f_{p2} becomes smaller, and, more importantly, stochastically distributed, the less of an impact it will have on pitting development.

In the example of worm wheel 4, the argument for $A_{P,avg} = 2\%$ criterion, can again be seen when predicting pitting in each flank. In the case of $A_{P10} = 2\%$, except for the few damaged flanks (flank Nos. 8, 13, 15, and 26), other flanks had relatively similar pitting that could not be distinguished by the model (Figure 128). Using the alternative criterion, linear pitting models resulted in a larger explained variance.

Table 46. Pitting linear models for worm wheel 4

	Predictors	Linear model	R²
Overall pitting	$N_L \leq 1.0 \cdot 10^6$	$A_P(\%) = -2.36 + 0.000015 \cdot N_L$	83.34%
Overall pitting	$N_L \leq 1.0 \cdot 10^6$	$A_P(\%) = -1.082 + 0.000015 \cdot N_L - 23.37$ $\cdot F_{ax2} - 26 \cdot f_{u2}$	86.27%
	Worm wheel deviations		
Beginning of pitting ($A_{P10} = 2\%$)	$N_L \leq 2.2 \cdot 10^5$	$A_P(\%) = -1.728 + 0.000012 \cdot N_L$	28.04%
Beginning of pitting ($A_{P10} = 2\%$)	$N_L \leq 2.2 \cdot 10^5$	$A_P(\%) = -1.471 + 0.000012 \cdot N_L - 4.74$ $\cdot F_{ax2} - 11.98 \cdot f_{u2}$	43.09%
	Worm wheel deviations		
Pitting growth stage ($A_{P10,max} = 17\%$)	$2.2 \cdot 10^5 < N_L \leq 1.0 \cdot 10^6$	$A_P(\%) = -2.252 + 0.0000015 \cdot N_L$	72.94%
Pitting growth stage ($A_{P10,max} = 17\%$)	$2.2 \cdot 10^5 < N_L \leq 1.0 \cdot 10^6$	$A_P(\%) = -2.252 + 0.000015 \cdot N_L - 32.09$ $\cdot F_{ax2}$	78.39%
	Worm wheel deviations		

Table 47. Pitting linear model for worm wheel 4 - alternative “Beginning of pitting” criterion

Beginning of pitting* ($A_{P,avg} = 2\%$)	$N_L \leq 2.8 \cdot 10^5$	$A_P(\%) = -3.824 + 0.000023 \cdot N_L$	43.93%
Beginning of pitting* ($A_{P,avg} = 2\%$)	$N_L \leq 2.8 \cdot 10^5$	$A_P(\%) = -3.824 + 0.000023 \cdot N_L$ $- 12.99 \cdot F_{ax2}$	52.13%

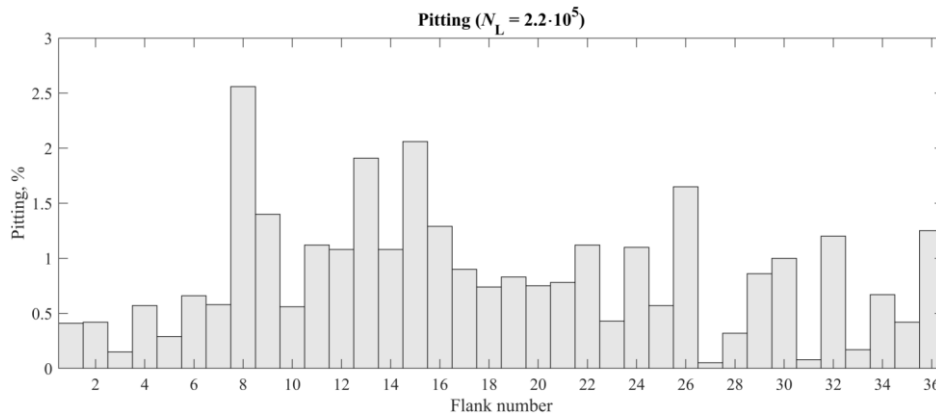


Figure 128. Pitting corresponding to criterion $A_{P10} = 2\%$

Normalized deviations from -1 to 1 were used to describe the most and least damaged flanks (Figure 130). When pitting formation reached $A_{P10} = 2.05\%$, the differences among flank deviations were less evident than when pitting reached $A_{P,avg} = 2.64\%$. Most damaged flanks were characterized by negative F_{ax2} and large F_{r2} . The opposite was true for the least damaged flanks. Both most and least damaged flanks were close by their respective flank number, meaning there were sectors of the worm wheel with more or less pitting. Similar pitting distribution was already seen in worm wheels 1 and 2. Based on these observations, pitting distribution is largely governed by radial and axial runout of the worm wheel. The correlation between pitting at the start and end of the test found on worm wheel 4 was non-existent (Figure 129, $r = 0.26$). This is somewhat contrary to positive correlations found in worm wheel 1 ($r = 0.64$) and worm wheel 2 ($r = 0.59$). This lack of correlation can also be explained by deviation distribution. In worm wheels 1 and 2, either a dominant deviation was found in worm thread profiles (worm 1) or a characteristic single pitch deviation was found on worm wheels (one positive f_{p2} followed by one negative f_{p2}). These deviations induced first pitting that continued to develop on these same flanks. In the case of worm wheel 4, there were no such distinguishing deviations; instead, the f_{p2} distribution was mainly stochastic, causing pitting to be more uniformly distributed.

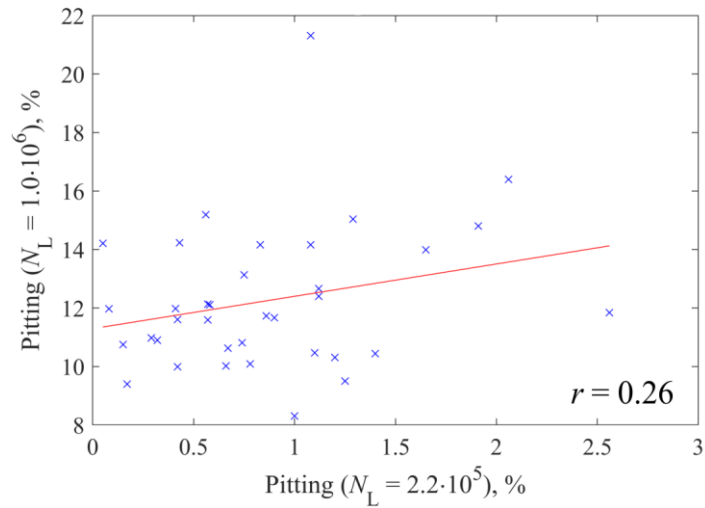


Figure 129. Pitting correlation for worm wheel 4

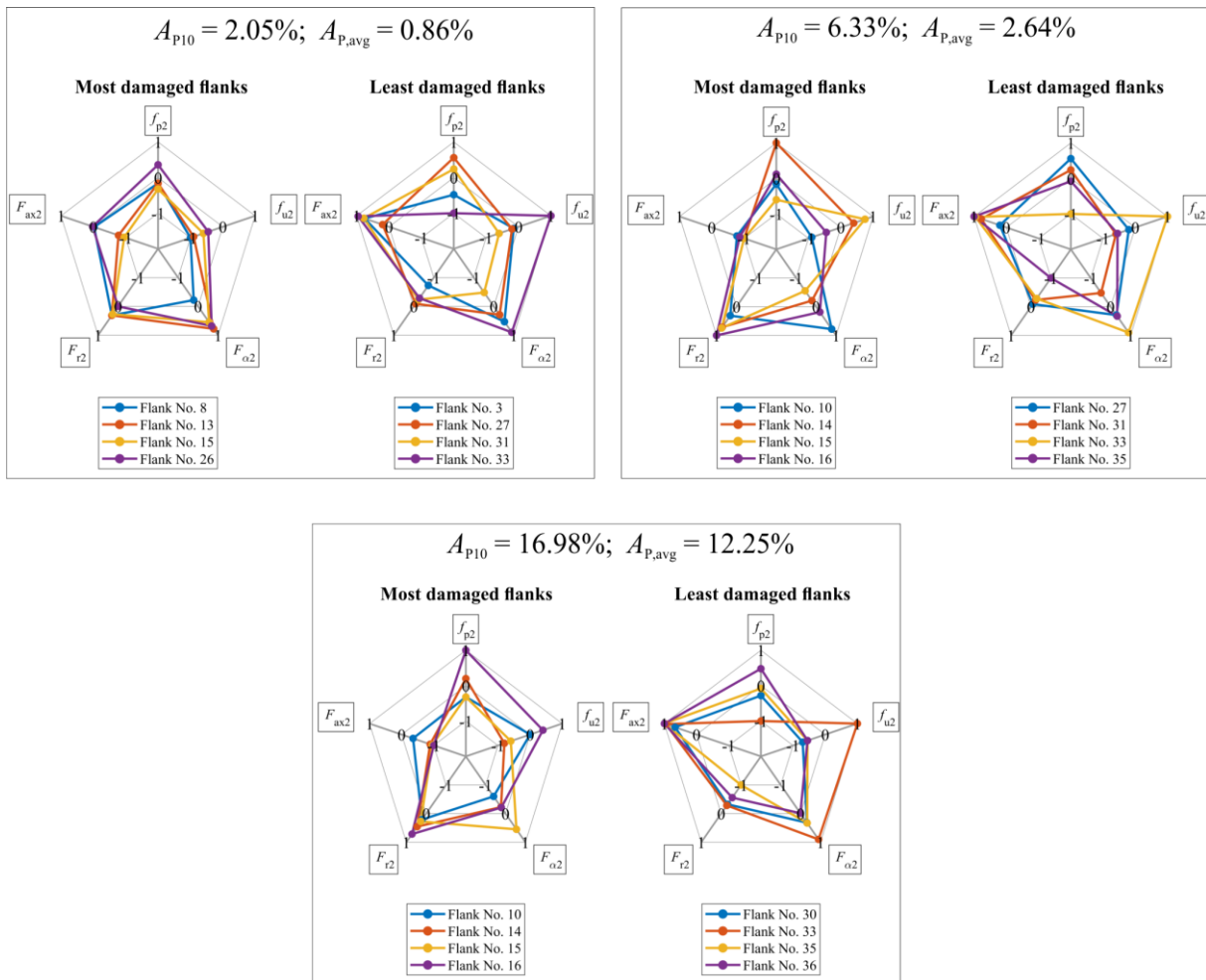


Figure 130. Worm wheel 4 - deviation distribution among the least and the most damaged flanks

9.3 Finite element analysis results

The results presented in this section are obtained by the FEM model described earlier in section 7. *Finite element model*. Before results analysis, the general purpose of the model, as well as its limitations, should be considered:

- The purpose of the model was to represent the contact pattern, load, and stress distribution in worm pairs represented by real geometry as closely as possible. Literature usually considers ideal geometry that does not account for geometry deviations or changes of geometry that take place after the running-in process.
- The worm pair geometry was acquired through 3D optical scanning before and at the end of experimental test runs. Therefore, there are two distinct geometries considered in this research. The limitation of this approach was that there was no worm pair scanning after the running-in process during which a majority of geometry changes took place due to extensive worm wheel wear. Worm pair geometry was not scanned after the running-in as this would imply disassembling of a worm pair gearbox. As the worm wheel was axially adjusted during running-in to establish a proper contact pattern, the disassembling of the gearbox would result in disrupting the established worm pair position. However, this would induce a new running-in process, changing the contacting geometry of the worm pair again.
- Due to scanning inaccuracies and deviations present in surface fitting, the worm and worm wheel CAD models deviate from the real parts. Also, as softened contact with a pressure-overclosure relationship was employed, the obtained values of contact stresses cannot be considered exact. Therefore, contact stresses should be considered as a good approximation of real contact stresses. The model verification showed good agreement with analytical calculation and established contact patterns.

For the remainder of this section, initial load conditions imply a load of $T_2 = 50$ Nm before running-in. The geometry used in these analyses was “as manufactured,” obtained by 3D optical scanning before test runs.

End-of-test conditions assume a load of $T_2 = 300$ Nm and an established contact pattern. The geometry used in these analyses was obtained by 3D optical scanning after the test runs.

9.3.1 Initial load distribution and contact pattern

Initial worm pair contact was analyzed with the torque of $T_2 = 50$ Nm, corresponding to inertia loads present in the worm pair experimental stand. Normal load distribution acting on worm wheel 1 tooth flanks is presented in Figure 131. Similar initial contact results were also obtained for other CuSn12 worm wheels.

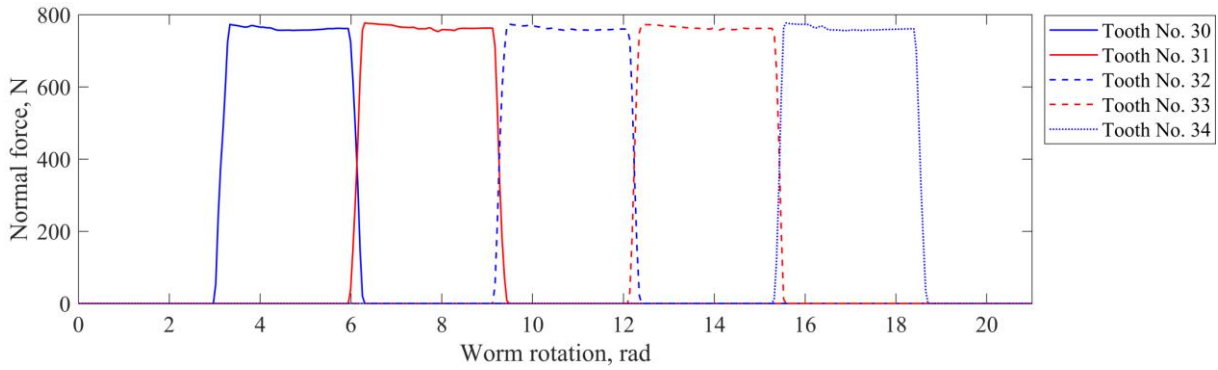


Figure 131. Initial load distribution on worm wheel 1

The overlap between blue and red lines represents a period when two tooth pairs were in simultaneous contact during mesh. Load distribution among tooth pairs is usually expressed by contact ratio. Contact ratio is the average number of teeth in contact with one another as the gears operate. In a worm pair, the contact ratio is obtained by the ratio of the distance between the two positions of the worm defined when the first line of contact is tangent to the zone of contact and the last line of contact is tangent to the zone of contact, divided by the axial pitch [51]. A theoretical contact ratio for worm pairs [47] can be approximated by the expression:

$$\varepsilon_m \approx \frac{\sqrt{r_{a2}^2 - (r_{m2} \cdot \cos \alpha_0)^2} - \sqrt{r_{m2}^2 - (r_{m2} \cdot \cos \alpha_0)^2} + \frac{h_{a1}}{\sin \alpha_0}}{\cos \alpha_0 \cdot \cos^2 \gamma_m \cdot p_{x1}} \quad (48)$$

The contact ratio of worm pairs investigated in this research was $\varepsilon_m \approx 1.93$. The contact ratio can also be extracted from the load distribution plot. In the presented FEM model, the increment size was set to a fixed value of 0.005 throughout the second step (rotation step) of the analysis. In quasi-static analysis, each increment represents one analysis frame. As every frame had the same increment size, it was possible to define the worm rotation angle per frame. If the worm rotation angle per frame is multiplied by the number of frames during which one tooth flank is in contact, and then multiplied by the worm lead, the result is a linear path during which the worm was in contact with the same worm wheel flank. The contact ratio is obtained if that path

is divided by the axial pitch p_{x1} . By employing this approach, the contact ratio for worm wheel 1 under initial load conditions was $\epsilon_m \approx 1.05$ ($T_2 = 50$ Nm).

Under initial load conditions, the contact was achieved on the top of the leaving side of the worm wheel flank (Figure 132a). Such initial contact was expected as worm wheels were produced using an oversized hob that promotes contact on the leaving side of the flank.

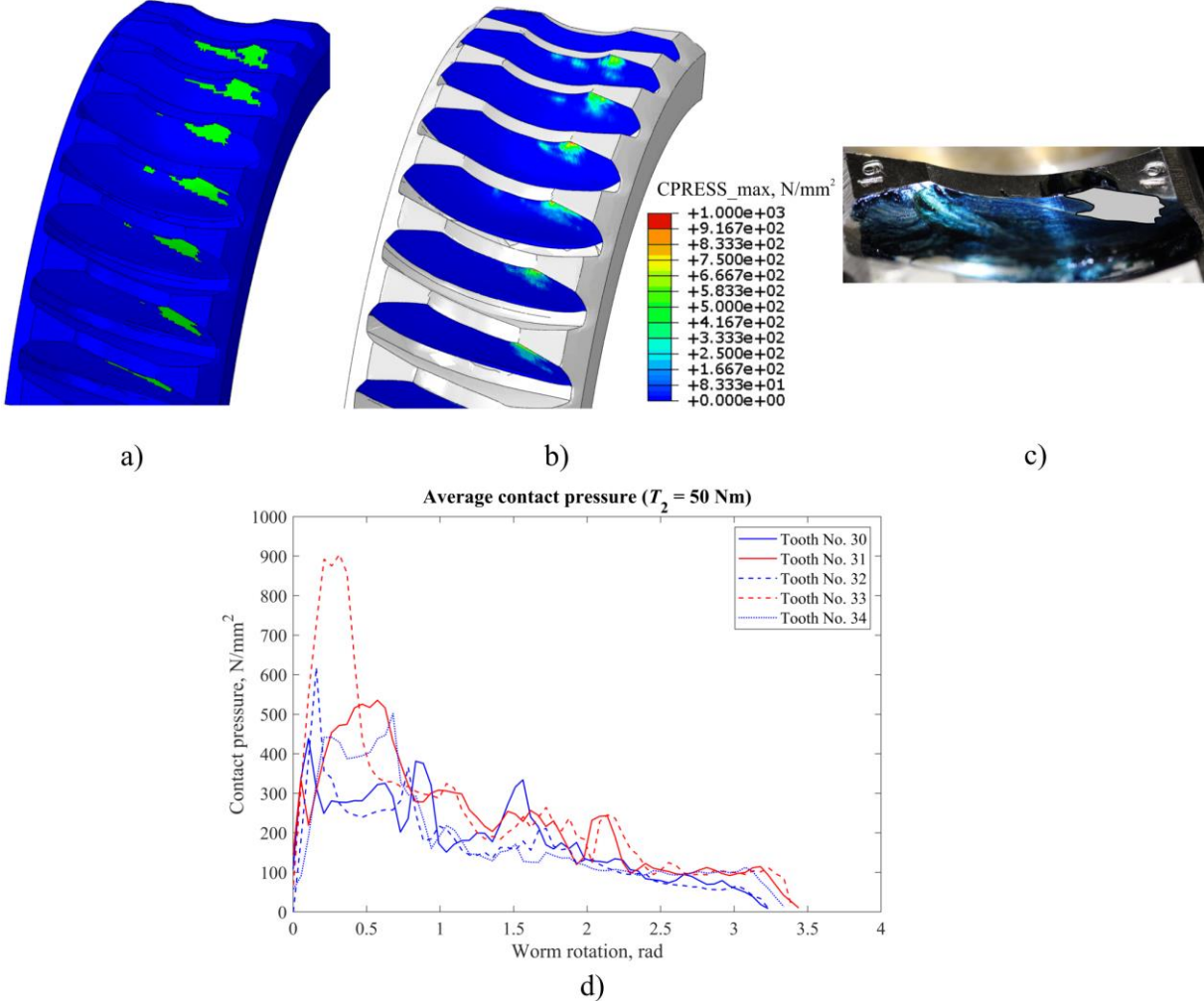


Figure 132. Initial contact of worm wheel 1: a) contact pattern defined by variable *CSTATUS*, b) contact pressure, c) initial contact pattern on worm wheel 1, d) average contact pressure

Contact pressures (Abaqus variable *CPRESS*) were high and well above mean contact stress $\sigma_{Hm} = 323$ N/mm² obtained through ISO/TS 14521 standard (Figure 132b). High contact pressures occur due to a small contacting surface, although the applied torque of $T_2 = 50$ Nm was relatively minor. These results highlight the importance of a proper running-in process to establish adequate contact pattern and distribute the load more uniformly. The difference in average contact pressures between odd and even flanks was most evident at the beginning of the contact. As contact was first established at the top of the leaving side of the flanks, these

results coincide with the pitting locations on worm wheel flanks. As such high contact pressures can occur even under light loads, there is evidence that contact conditions during the running-in process may play a significant role in pitting initiation. For reference, a pitting areas in flanks No. 31 and No. 33 were $A_P = 7.99\%$ and $A_P = 6.47\%$, respectively, compared to $A_P = 1.18\%$, $A_P = 2.24\%$ and $A_P = 2.88\%$ in flanks No. 30, No. 32, No. 34, respectively. In Figure 132c, the highlighted grey area represents the initial contact pattern before the test run. Odd flanks had negative single pitch deviation and were in contact with worm thread 1 which had higher worm profile deviation (was more convex). This combination of errors produced more concentrated contact spread over the lower surface area. Therefore, average contact pressure was higher in odd worm wheel flanks when compared to even flanks (Figure 132d). Odd flanks were also the more pitted flanks at the end of the test.

In order to investigate the theoretical contact conditions under full working load, an additional analysis was conducted with the applied torque of $T_2 = 300 \text{ Nm}$. It is important to note that this will not be the case in the actual worm pair application as running-in is usually conducted in several steps with gradually increasing load. Nonetheless, these observations serve as a good indication of what would happen if the full working load was applied before running-in. The results are presented in Figure 133. A larger load would result in a higher contact ratio, $\varepsilon_m \approx 1.36$, and a more spread contact pattern due to elastic deformation of the teeth. Nevertheless, the contact pattern would be unfavorable and located only on top of the flanks. Contacting stresses would be high, well above 1000 N/mm^2 , with peaks reaching up to 2000 N/mm^2 in certain locations on the flank as the load is not uniformly distributed due to an inadequate contact pattern. For reference, the pitting resistance for the CuSn12 worm wheel is $\sigma_{HlimT} = 425 \text{ N/mm}^2$.

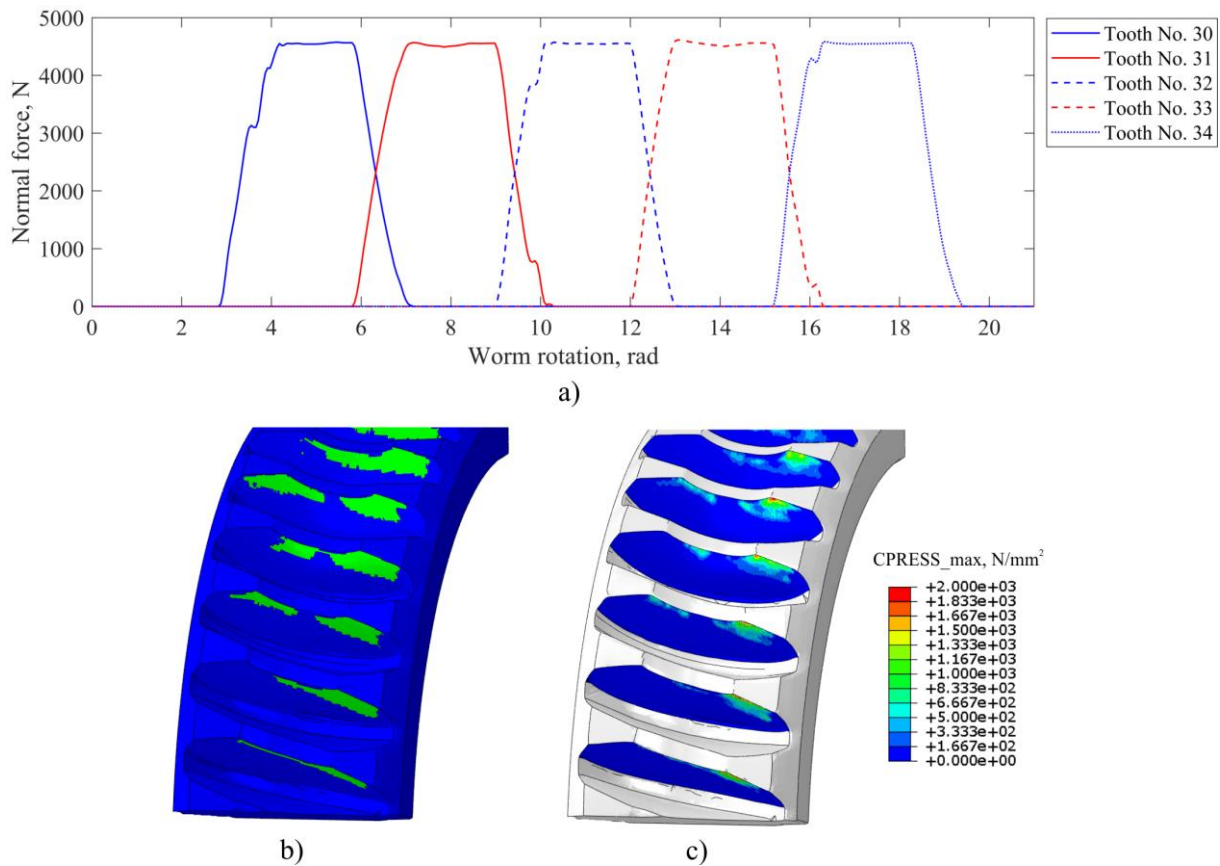


Figure 133. Theoretical worm wheel contact ($T_2 = 300 \text{ Nm}$): a) load distribution, b) contact pattern, c) contact pressure

This type of analysis can also be indicative in terms of predicting initial pitting locations. An analysis of theoretical contact pressures was conducted for worm wheel 2. Worm wheel 2 was characterized by positive single pitch deviation on odd flanks and negative single pitch deviations on even flanks. Both worm 2 threads had negative single pitch deviation. A combination of negative worm deviation and positive wheel deviation should yield the most unfavorable contact conditions in terms of load and stress sharing. The example of average contact pressures on worm wheel 2 flanks is presented in Figure 134. Odd flanks would experience noticeably higher contact pressures at the start of the contact. As contact is usually adjusted on the leaving side of the flank, these results would coincide with the pitting locations found on the flanks of worm wheel 2. Presented results can be considered in good agreement with measured pitting at the end of the test: flank No.25; $A_P = 11.17\%$, flank No.26; $A_P = 7.52\%$, flank No.27; $A_P = 14.2\%$, flank No.28; $A_P = 7.96\%$, flank No.29; $A_P = 11.12\%$.

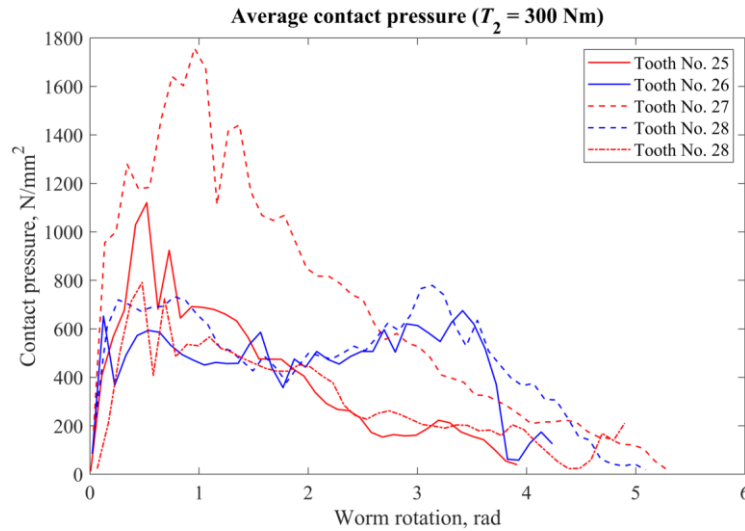


Figure 134. Theoretical average contact pressures on worm wheel 2

Flanks of worm wheel 2 characterized by large radial runout F_r exhibited more pitting, as already presented in Figure 114. An analysis was conducted to determine the contact pressure of a few consecutive flanks characterized by large F_r and a few consecutive flanks with smaller F_r . The results of average contact pressure for Flanks No. 9 to No. 12 (average $F_r = -0.049$ mm) and flanks No. 25 to No. 29 (average $F_r = -0.128$ mm) are given in Figure 135. The average contact pressure at the beginning of the contact can be higher by 50% on flanks with large radial runout F_r . These results would coincide with the pitting locations in Figure 114 and can serve as a good predictor for potential pitting formation.

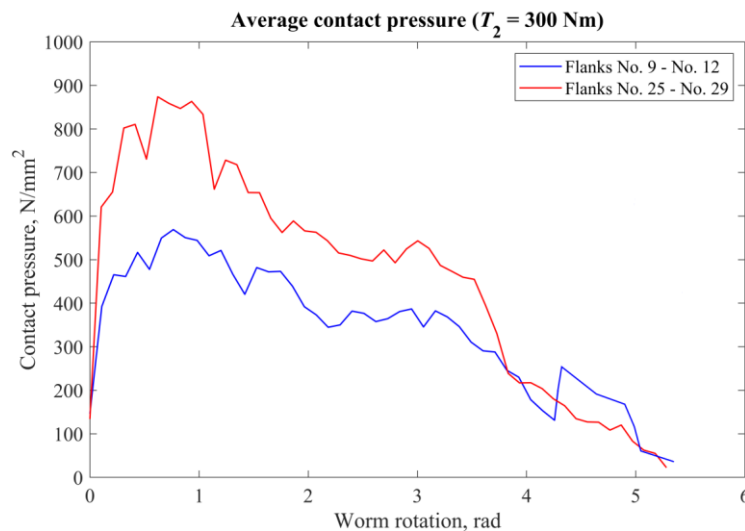


Figure 135. Average contact pressure among flanks with large F_r and small F_r

9.3.2 Contact pattern, stress, and load distribution at the end of the test

By the end of the test, worm wheels experienced several processes that contributed to changes in their geometry. Firstly, running-in resulted in a considerable amount of bronze wear. Secondly, continuous bronze wear, although at lower rates, occurred throughout the testing period. The steel worm also experienced wear, although negligible compared to bronze worm wheel. Lastly, as the test run progressed, pitting formation and development altered contact conditions by reducing worm wheel flank surface area and shifting the contact pattern due to flank material loss. Cumulatively, these processes were evident on scanned geometry after the test and had direct effects on contact conditions in presented FEM results. Contact patterns at the end of test runs obtained by the FEM model are presented in Figure 136.

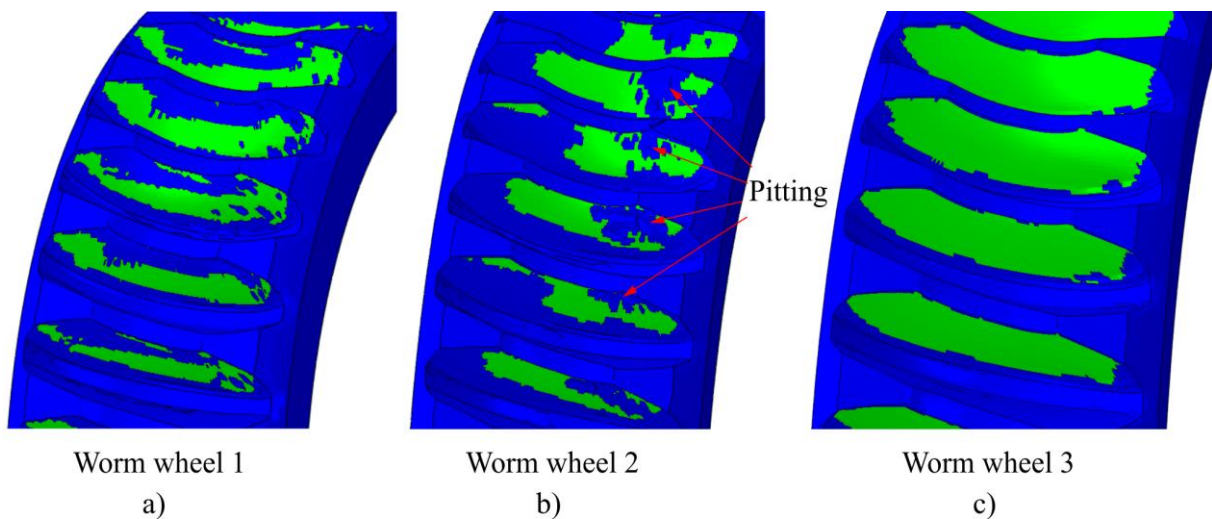


Figure 136. Contact patterns at the end of test runs (variable *CSTATUS*): a) worm wheel 1, b) worm wheel 2, c) worm wheel 3

Worm wheel 1 contact pattern was spread across the wheel width and more focused in the lower half of the flank. During the test run, the pitting slowly shifted towards the bottom of the flank, as already shown in Figure 97. This indicates that the contact pattern also shifted from the top to the bottom of the flank as pitting and wear progressed. The upper part of the flank was heavily pitted and worn out. These findings suggest that contact can transfer across the worm wheel flank due to changes in contact surface and geometry primarily induced by wear and pitting.

Worm wheel 2's contact pattern was smaller and distinct differences between odd and even flanks can be observed. Odd flanks had more uniform contact spread from the entering to the leaving side. On the other hand, even flanks had a slightly split contact pattern, with a little contact on the entering side followed by a lack of contact, and then the majority of the contact

pattern was located from the middle towards the leaving side of the flanks. Odd flanks were the ones characterized by negative single pitch deviations. On both worm wheels 1 and 2, the lack of contact pattern enclosed by the green surface was locations of pitting where the contacting surface was nonexistent. Therefore, no contact could be established.

Worm wheel 3 exhibited a full contact pattern. As no significant pitting had occurred on worm wheel 3 ($A_{P10} < 2\%$), no enclosed areas with a lack of contact could be found. Worm wheel 3 had higher bronze wear and faster running-in. This was correlated to electropolished worm surfaces and was more pronounced in worm wheel 3 compared to worm wheel 2, both of which were paired with electropolished worms. Full contact pattern also contributed to more even load distribution and delayed onset of pitting.

The distribution of contact pressures is shown in Figure 137. To highlight the regions with the highest contact pressures, the upper limit for contact pressure representation was set to 500 N/mm². This means that the red color depicts contact pressures of 500 N/mm² or above (the highest localized contact pressures were 1500 N/mm²). The set threshold value was selected based on pitting resistance for CuSn12 worm wheels, $\sigma_{HlimT} = 425$ N/mm².

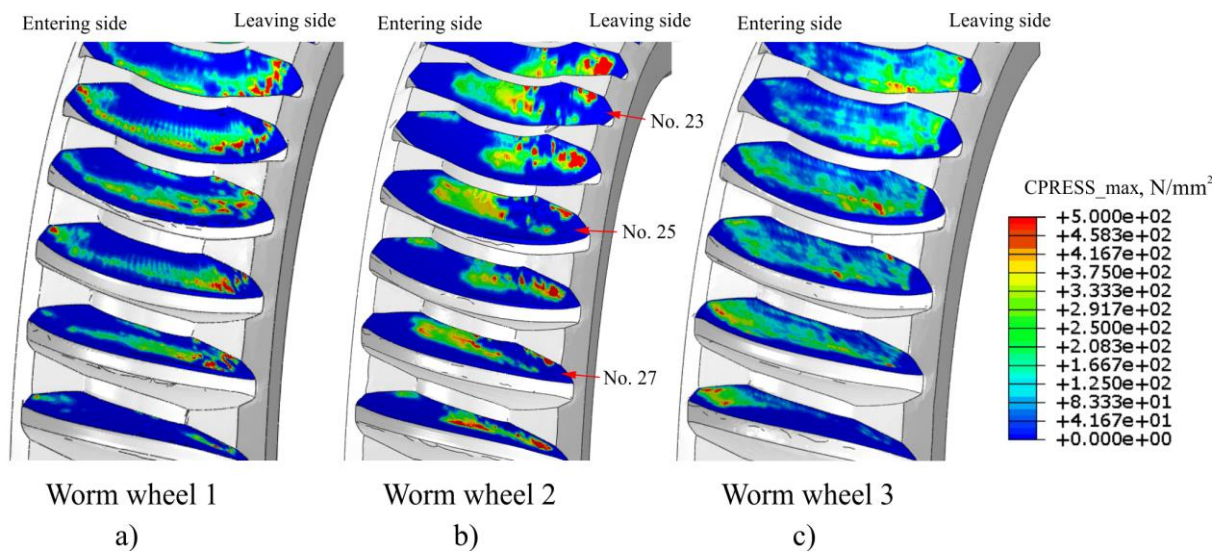


Figure 137. Contact pressures at the end of test runs (variable *CPRESS*): a) worm wheel 1, b) worm wheel 2, c) worm wheel 3

In worm wheel 1, the highest contact pressures were present in the bottom on the leaving side of the flanks. This was the same location where pitting started to develop at the end of the test, especially on even flanks. Worm wheel 2 was characterized by high pressures on the leaving side of the flanks, where the majority of the pitting had developed. It must be noted that due to local geometrical irregularities and lack of supporting surface due to pitting, the stress concentrations are expected to be near the locations of existing pitting. In some degree, higher

contact pressures were detected in the middle of the odd flanks. As the contacting surface was severely damaged by pitting on the leaving side of the flanks, pitting usually tends to progress towards the middle and entering side of the flank where sufficient contacting surface is still present [25]. Worm wheel 3 had uniformly distributed contact pressure, with few stress concentrations above the set threshold. Also, the contact pressure value was relatively similar on both the entering and leaving sides of the flank. This was in line with the detected pitting on both sides of the flank, as presented in Figure 117 and Figure 118. The locations of high contact pressures acquired by the FEM model can serve as a good indication of where the continuation of pitting development could take place. Moreover, these results suggest that pressure distribution in worm pairs is far more complex and inconsistent compared to theoretical pressure distribution.

The average contact pressures for worm wheel 2 and worm wheel 3 are presented in Figure 138. As contact starts on top of the leaving side of the flank, it coincides with locations of existing pitting where the contacting surface is reduced, thus resulting in high contact pressures. Although odd and even flanks had pitting, albeit odd flanks in larger percentages, the difference in average contact pressures is significant. This indicates that pitting will tend to develop on already highly pitted flanks as long as the flank surface is large enough to support the load. Also, this is in line with a positive correlation between pitting at the start of the test vs. at the end of the test, found in worm wheels 1 and 2. In other words, a highly pitted flank at the start of the test will continue to develop more pitting faster than a flank with low initial pitting. This claim can also be supported by the results of pitting development found during the test runs.

On the other hand, the results of contact pressures for worm wheel 3 show a more uniform distribution with lower peak values. Although worm wheel 3 also had characteristic single pitch deviation, establishing a full contact pattern reduced the influence of the mentioned deviation. The differences in pitting between odd and even flanks were present but to a lesser extent. Moreover, the influence of deviations on describing the most and least damaged flanks was not as clear as in worm wheels 1 and 2 (see Figure 121). Based on already mentioned findings and coupled with the results of FEM analysis, it cannot be stated with certainty that pitting will continue to develop on already more damaged flanks (odd flanks), as is the case with worm wheel 2. It can be argued that a full contact pattern reduces the impact of worm wheel deviations on pitting formation due to more uniform load and stress distribution.

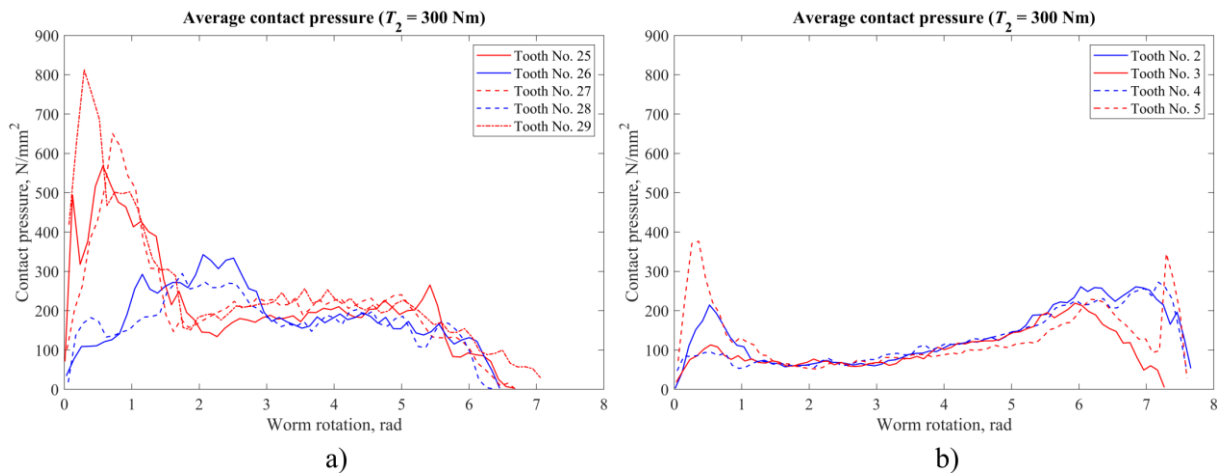


Figure 138. Average contact pressures at the end of the test: a) worm wheel 2, b) worm wheel 3

Load distribution in worm wheels is provided in Figure 139. The presented results illustrate a distribution of total normal contact force on five consecutive flanks during worm pair rotation. The contact ratio was calculated based on load distribution plots: worm wheel 1, $\varepsilon_m \approx 2.38$; worm wheel 2, $\varepsilon_m \approx 2.06$; worm wheel 3, $\varepsilon_m \approx 2.41$. Contact ratios obtained via the FEM model were larger compared to the theoretical contact ratio, $\varepsilon_m \approx 1.93$. These FEM results reveal multiple differences between worm wheels 1 and 3 compared to worm wheel 2 and can be used for explaining higher pitting percentages in worm wheel 2. In worm wheels 1 and 3, the contact pattern was distributed across the entire worm wheel width, thus ensuring a more uniform load distribution. On average, the peak value of total normal contact force in worm wheel 2 was 4134 N compared to 3668 N and 3235 N in worm wheels 1 and 3, respectively. Moreover, values of contact ratios and periods of three tooth pairs in contact (hatched area) were more prominent in worm wheels 1 and 3. As in other gears, the theoretical contact ratio in worm pairs is defined through geometry (see expression (48)). Also, the contact ratio will increase with an increase in load due to elastic deformations of tooth pairs.

Furthermore, the contact ratio heavily depends on established contact patterns in worm pairs. In worm wheels 1 and 3, the contact pattern was spread across the entire worm wheel width thus covering both the entering and leaving sides of the flank. The entering side of worm wheel 1 was partially in contact, while worm wheel 3 had a full contact pattern. In practice, contact patterns are usually established in the middle and towards the leaving side of the flank (contact pattern in worm wheel 2) to enable better oil entrainment into the contact zone. A full contact pattern in conventional worm pairs (ground steel-bronze material pairs) tends to induce scuffing, as was the case with worm pair 6 in this research. However, as observed in worm pair 3, the electropolished steel-bronze pair had no problems with full contact pattern. Partial contact

patterns in worm wheels 1 and 2 mitigate the problem of insufficient lubrication but also worsen contact conditions in terms of higher contact pressures and earlier pitting formation (Figure 140).

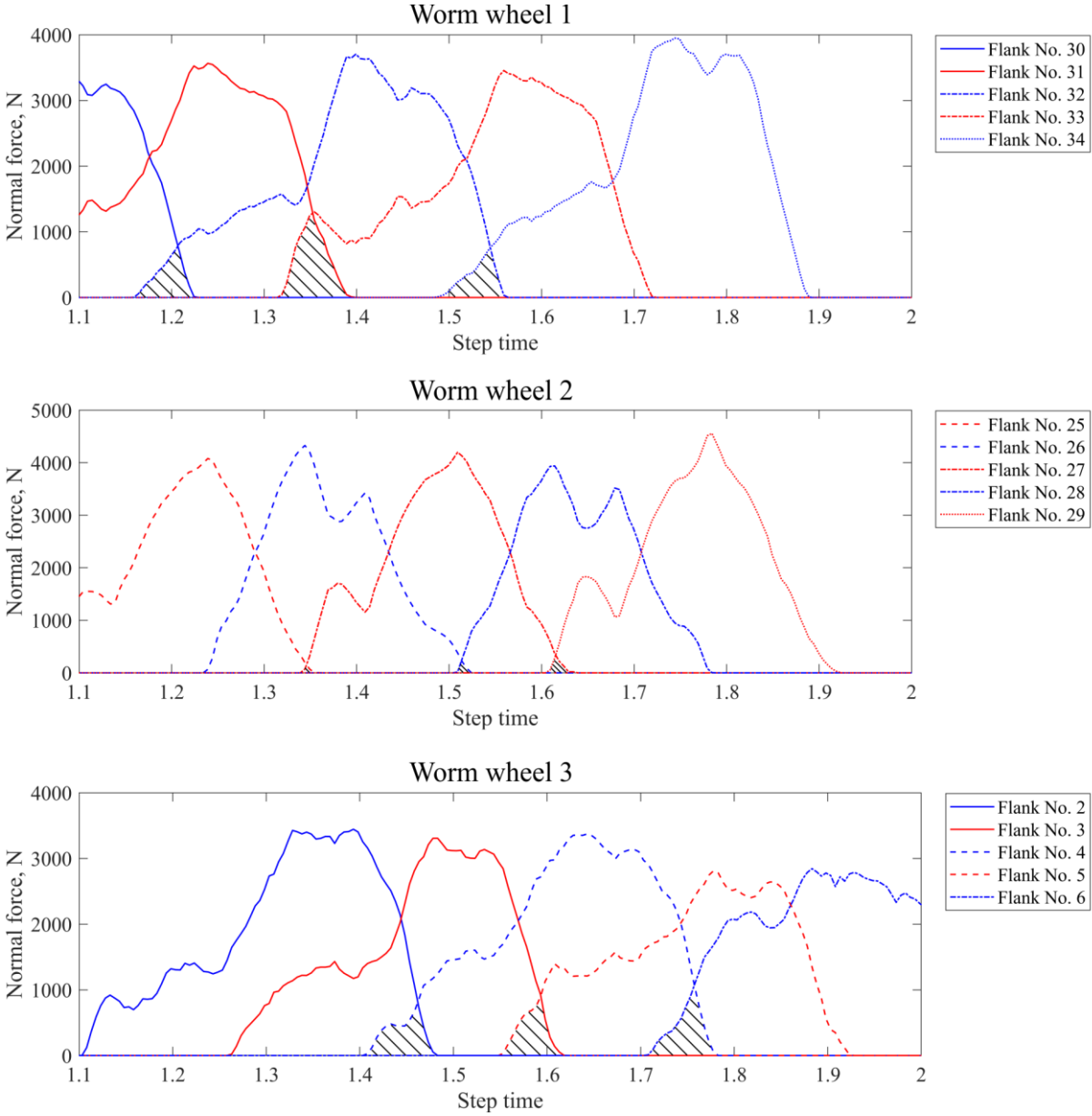


Figure 139. Load distribution in worm wheels

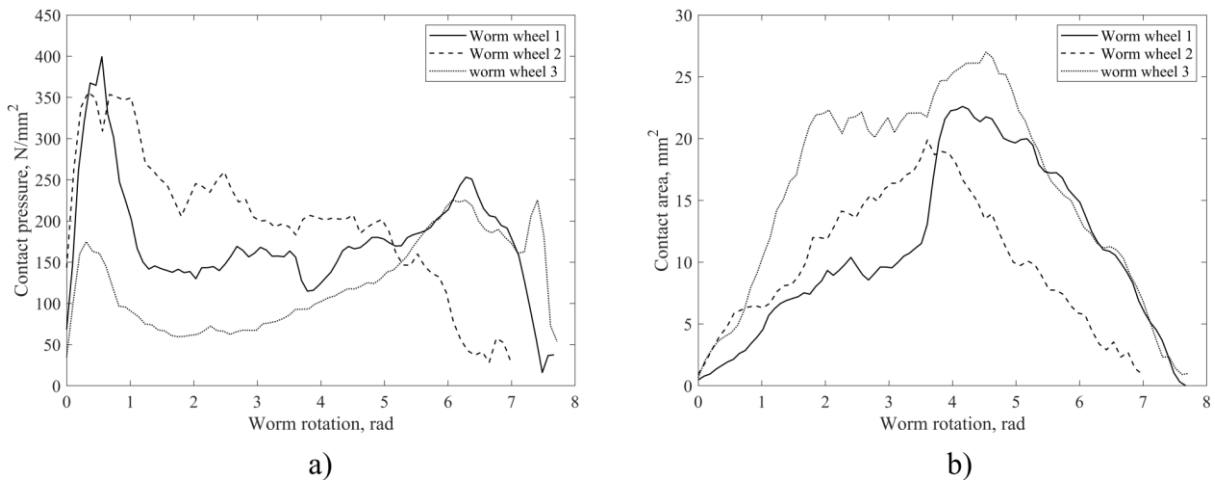


Figure 140. FEM results: a) average contact pressure, b) contact area

The detected differences in investigated worm pairs can lead to rather contradictory conclusions. One can argue it is better to have a full contact pattern, therefore better load distribution and delayed wear and pitting damage. However, there is a serious possibility of scuffing due to bad lubrication conditions. Others can claim that partial contact patterns certainly ensure good lubrication conditions. On the one hand, this lowers the danger associated with sudden scuffing at the expense of worse load distribution and earlier onset of damage, primarily pitting. The latter argument makes more sense from a practical standpoint, as worm wheels can operate with up to 60% of pitted flanks. More importantly, pitting develops slowly over time compared to scuffing. Scuffing occurs in a rather short period of time and can result in a quick failure of the worm pair, thus making it certainly a more dangerous damage mechanism. However, this also opens possibilities for further research as optimal, or at least narrowly defined solution for the presented problem has not yet been found. A possible step in that direction can be focusing on surface modifications that benefit overall efficiency and improved lubrication in worm pairs with full contact pattern.

Based on the presented FEM results, it can be concluded that different contact conditions largely influenced the difference in pitting among bronze wheels in this research. On the other hand, contact conditions are a product of many factors that act simultaneously: worm pair geometry, running-in, established contact pattern, the topography of contacting surfaces, or lubrication conditions. Individual worm pair deviations showed a meaningful role in describing overall pitting on worm wheels. However, their mutual interaction and combinations form the overall worm pair geometry. The FEM results showed that contact conditions can to a large degree be unlike theoretical ones. One of the main goals of this FEM model was to investigate and describe contact conditions derived from real worm pair geometry and application. By

utilizing actual geometry obtained through 3D optical scanning, the presented approach enables the investigation of gears and other machine components in a more realistic manner.

10

Conclusions

In this doctoral thesis, the influence of worm pair dimensional accuracy on pitting formation and development on worm wheels made of CuSn12 and AlSn6 was investigated. Moreover, electropolishing was used as a non-conventional surface texturing method to alter steel worm surface topography and improve lubrication conditions in worm pairs. Furthermore, a finite element method (FEM) model based on 3D optical scans of worm pairs was developed to gain further insight into the real working conditions of worm pairs.

Analysis of pitting formation and development proved to be a challenging task due to several factors. Firstly, the running-in process used for establishing acceptable contact pattern in worm pairs results in a complete alternation of contacting geometry. The change in geometry, due to initial bronze wear, is by an order of magnitude larger than measured deviations. The legitimate question arises as to whether it is possible to correlate worm pair deviations with real working contact conditions and pitting damage. Contact patterns were achieved by axial adjustment of the worm wheel. When an acceptable contact pattern was established, the worm pair was considered ready for the test run under full load. As every worm pair required individual contact pattern adjustment, it was not possible to establish the same contact pattern in all investigated worm pairs. Also, establishing a full contact pattern proved to be catastrophic in conventional worm pairs (scuffing on worm wheel 6). Established contact patterns were all adequate, although different from one another, thus implementing another variable into the problem that had to be considered. Moreover, it was shown that contact patterns can change as a result of

uneven flank wear, all due to geometry deviations present in manufactured worm pairs (worm wheel 1). Lastly, pitting tends to occur suddenly, removing large pieces of material. This creates a spike in the measured pitted area and presents a problem with defining pitting criteria and developing pitting models.

A total of six worm pairs were tested, four of which were considered for analysis of pitting formation and development (three CuSn12 worm wheels and one AlSn6 worm wheel). Two of the three CuSn12 worm wheels were paired with electropolished worms to investigate the influence of surface modification on lubrication conditions. Due to different worm wheel materials, the specific nature of deviation distribution, and worm wheel pairing with conventional or electropolished worms, the overall general pitting model could not be reliably developed. Rather, multiple pitting models for each inspected worm wheels were developed. Each of the worm pairs was thoroughly analyzed based on deviation distribution, established contact pattern, and supplemented with the results of load and stress distribution through FEM analyses. The following conclusions can be drawn:

- If a specific deviation distribution is present, it will govern the pitting formation and development on worm wheel flanks. In the example of worm pair 2, one positive worm wheel pitch deviation was followed by one negative pitch deviation. As worm threads had similar deviations, most pitting occurred on worm wheel flanks characterized by positive single pitch deviation. However, if worm threads have distinct differences, as observed in worm pair 1, the unfavorable deviation present in one of the worm threads will induce the majority of pitting on worm wheel flanks, despite its single pitch deviation distribution.
- If there is no specific distribution of deviations, the locations of pitting can be explained by radial and axial runout. The locations of the most and least damaged flanks are distributed in sectors (a few consecutive flanks in a row) closely related to the position of maximum/minimum runout deviations.
- In the case of no specific deviation distribution, the variance in pitting is dominantly explained by the number of load cycles, as seen in worm wheel 4. The increase in explained variance by including worm wheel deviations was 2.93% for the “Overall pitting” model and up to 15.05% for the “Beginning of pitting” model. On the other hand, when there is a specific deviation distribution present, the deviations have a much larger impact on explaining variance in pitting, up to 43.12%, as presented by pitting models for worm wheel 1.

- Pitting formation occurs at the top of the leaving side of the flank in all investigated worm wheels. This coincides with the initial contact position prior to the running-in process. As pitting develops, it spreads towards the bottom and middle of the flank.
- The maximum measured pitting depth was 0.55 mm. Paired with the amount of wear of 0.06 mm, total material loss was 0.61 mm. Based on these findings, the largest tooth thickness reduction is a product of pitting damage, not wear. Tooth thickness reduction due to pitting is not considered in wear and pitting load capacity calculations according to standard [3].
- Besides deviations, pitting was largely influenced by the established contact pattern. Generally, the larger the contact pattern, the less pitting damage was observed.
- Larger contact patterns resulted in a more even load and stress distribution and higher contact ratio. Also, measured contact ratios were higher by approximately 20% from a theoretical one.
- Based on FEM results, contact conditions in terms of stress and load distribution differ significantly from theoretical ones. This implies that each worm pair establishes its equilibrium state during the running-in process and that contact conditions tend to change during the operation, primarily due to worm wheel wear (worm wheel 1).
- The effects of single pitch deviation and radial runout used to describe pitting on worm wheels were in good agreement with obtained contact pressures by the FEM model. The results obtained by the model can serve as good predictors for pitting formation.
- Worm wheel wear was uneven across the flank. Wear on the leaving side of the flank was 63% up to 170% higher than the wear in the middle of the flank. This finding contradicts the assumption of even worm wheel wear assumed by the standard [3]. Regarding deviations, radial runout showed a positive correlation with increased wear. No reliable correlation could be found between wear and pitting, thus the mutual influence of these two damage mechanisms remains to be explored.

Based on the results and conclusions presented, it can be concluded that the first hypothesis is confirmed.

Hypothesis 1:

By analyzing worm wheel dimensional accuracy and its influence on load and stress distribution, it is possible to define worm wheel tooth flank pitting initial location and pitting formation more accurately.

Besides investigating the influence of dimensional accuracy on pitting formation and development, the other aim of this thesis was to improve lubrication conditions in worm pairs. Firstly, model testing was carried out to validate electropolishing as a viable surface texturing method. Then, electropolishing was applied in worm pairs by electropolishing steel worms. According to the obtained results of model testing and worm pair test runs, the impact of electropolished surface can be summarized by the following conclusions:

- Surface texture through electropolishing at elevated potentials (higher current densities) can successfully be applied on case-carburized 16MnCr5 steel.
- Electropolished steel surface was modified in two ways: by creating surface texture in the form of surface pits and dimples and by generating a surface coating in the form of an oxide surface layer
- In comparison to conventional ground steel-bronze pair, electropolished steel reduced friction by 25% and 30% in the boundary and mixed lubrication regimes defined by $\lambda = 0.76$ up to $\lambda = 2.48$. In the boundary lubrication regime defined by $\lambda < 0.5$ an increase in the coefficient of friction should be expected.
- The application of electropolished worms improved overall efficiency in worm pairs. Worm pairs 2 (EP) and 3 (EP) had an average efficiency of 85.8% and 90.1% compared to 84.9% in worm pair 1.
- Surface topography of the electropolished worm characterized by larger and shallower pits resulted in the highest overall efficiency. Also, it resulted in faster and improved running-in that led to the establishment of a full contact pattern in worm pair 3.
- Surface texturing can modify the worm surface to provide improved or additional lubrication that reliably supports full contact pattern in worm pairs. On the other hand, the operation of conventional worm pairs under full contact pattern was unsustainable due to inadequate lubrication conditions that lead to lubrication breakdown and scuffing in worm pair 6.
- Minimal to no wear occurred on the electropolished worm surface as surface parameters remained relatively unchanged before and after the test. This can be attributed to the steel-bronze material pair that prolongs the durability of surface modifications produced on steel worm as most wear occurs on a bronze wheel.

Based on the presented results of improved efficiency and running-in, it can be concluded that surface texturing presents a reliable path toward improving lubrication conditions in worm pairs. Therefore, the second hypothesis is confirmed.

Hypothesis 2:

By employing surface texturing on a worm or worm wheel tooth flank, it is possible to improve worm pair lubrication conditions.

10.1 Research limitations

The research limitations can be summarized into four points. Firstly, due to the smaller sample size of investigated worm pairs, the generalized pitting model for predicting pitting could not be developed. This was mainly due to specific differences in deviations, their distribution, and different worm wheel materials employed. With a larger dataset, this limitation could be easily addressed.

Secondly, the developed FEM model can be used as a good approximation of real working conditions. However, it has certain drawbacks. The geometry of the worm pair is partially altered due to the anti-reflection coating applied by spraying to make the scanned part opaque. Also, the process of converting the scans into CAD models resulted in slight deviations of underlying geometry. Furthermore, the mesh in the contact zone should be denser to obtain more accurate results. In this thesis, a compromise had to be made between a number of finite elements and needed computational resources due to the size and complexity of the model.

Thirdly, this research deals with worm pair geometry “as manufactured” and geometry obtained at the end of test runs. In between these two distinct cases, there is a running-in process that largely alters worm wheel geometry. As 3D optical scanning of worm pairs was not conducted after running-in due to possible reassembly errors (mainly in the form of worm wheel axial positioning), the important geometry information of worm pairs is lacking. By including worm pair geometry after running-in, it would be possible to associate deviations with the running-in process and better understand wear behavior and load distribution in worm pairs. Also, it would help interpret pitting formation as contact pressures can be remarkably high during running-in, and there is reasonable doubt that some pitting subsurface cracks are initiated as early as in the running-in process.

Lastly, although worm pair geometry was analyzed through 3D optical scans, the underlying causes of some deviations and their distribution can only be obtained by knowing manufacturing process parameters. Information like hob oversize, hob cutting angle, or grinding wheel geometry would contribute to a better understanding of worm pair deviations. These parameters should be considered in future research.

10.2 Scientific contributions

Scientific contributions of the research conducted in the scope of this thesis:

- Pitting models were developed to predict pitting percentage on worm wheel tooth flanks. The models consider the number of load cycles and dimensional accuracy of the worm pair.
- Certain deviations that have greater effects on pitting formation are highlighted. Therefore, these deviations should be more carefully inspected or considered during the manufacturing of worm pairs.
- The coefficient of friction in the steel-bronze material pair was reduced by creating surface texture on case-carburized 16MnCr5 steel. The texture was produced via electropolishing at higher current densities. By applying electropolishing on 16MnCr5 steel worms, higher efficiency was achieved in 16MnCr5-CuSn12 worm pairs.
- FEM model was developed based on real worm pair geometry acquired through 3D optical scanning. The model accounts for worm pair rotation, deflection of the worm, and housing deviations. It enables the representation of real contact patterns and load and stress distribution in worm pairs.

10.3 Outlook and future work

While future work should address the research limitations outlined in the previous section, there are also some prominent directions for future research on pitting formation and the application of electropolishing as a surface texturing method.

This research again outlined the complex nature of the running-in process in worm pairs. As mentioned earlier in this thesis, by scanning the worm pair after the running-in process (before the test run), the obtained scans could provide valuable information on how each worm wheel flanks adapts and how change in geometry after running-in can be associated with pitting formation. However, the prerequisite for such an approach is to develop a method for ensuring an established worm pair's exact position in the gearbox at the end of the running-in process. A minor change in the axial position of the worm wheel (e.g. 50 μm) drastically changes the contact pattern and promotes a new partial running-in process.

The presented pitting models can be used for predicting pitting on each individual worm wheel flank. As the models were developed for each of the investigated worm wheels, the natural

continuation of the research should be directed towards conducting more worm pair test runs to develop a general model for the presented worm pair geometry and steel-bronze material pair.

As there is still a portion of unexplained variance in pitting models, it would be interesting to investigate additional research areas to explain uneven pitting formation. One such area should be the quality of cast material, with a primary focus on the near-surface microporosity of each flank. Another direction could be studying vibrations in the system and how the system response changes with the development of pitting.

The presented research can be considered preliminary research of surface texturing case-carburized 16MnCr5 steel by electropolishing. The potential of electropolishing has not been fully explored, nor has the process been optimized. Different surface textures could be obtained and studied by varying electropolishing parameters, mainly current density and time, to lower friction or reduce wear.

References

1. Masovic, R.; Breski, T.; Cular, I.; Vuckovic, K.; Zezelj, D. Numerical Model for Worm Gear Pair Inspection Based on 3D Scanned Data. *Int. J. Simul. Model.* **2021**, *20*, 637–648, doi:10.2507/IJSIMM20-4-573.
2. Fontanari, V.; Benedetti, M.; Straffelini, G.; Girardi, C.; Giordanino, L. Tribological Behavior of the Bronze-Steel Pair for Worm Gearing. *Wear* **2013**, *302*, 1520–1527, doi:10.1016/j.wear.2013.01.058.
3. International Organization for Standardization *ISO/TS 14521 Gear - Calculation of Load Capacity of Worm Gears*; Geneva, 2020;
4. Deutsches Institut für Normung *DIN 3996 - Tragfähigkeitsberechnung von Zylinder-Schneckengetrieben Mit Sich Rechtwinklig Kreuzenden Achsen*; Frankfurt, 2005;
5. Janninck, W. Contact Surface Topology of Worm Gear Teeth. *Gear Technol.* **1988**, 31–47.
6. Mautner, E.M.; Sigmund, W.; Stemplinger, J.P.; Stahl, K. Efficiency of Worm Gearboxes. *Proc. Inst. Mech. Eng. Part C J. Mech. Eng. Sci.* **2016**, *230*, 2952–2956, doi:10.1177/0954406215602286.
7. Opalić, M.; Žeželj, D.; Vučković, K. A New Method for Description of the Pitting Process on Worm Wheels Propagation. *Wear* **2015**, *332–333*, 1145–1150, doi:10.1016/j.wear.2015.01.053.
8. Sievers, B.; Gerke, L.; Predki, W.; Pohl, M. Verschleiß- Und Grübchen- Tragfähigkeit von Bronze- Schneckenrädern. *Giesserei* **2011**, 36–45.
9. Simon, V. V. Influence of Tooth Errors and Shaft Misalignments on Loaded Tooth Contact in Cylindrical Worm Gears. *Mech. Mach. Theory* **2006**, *41*, 707–724, doi:10.1016/j.mechmachtheory.2005.09.004.
10. Deutsches Institut für Normung *DIN 3974-1 Toleranzen Für Schneckengetriebe-Verzahnungen - Teil 1: Grundlagen* 1995.
11. Deutsches Institut für Normung *DIN 3974-2 Toleranzen Für Schneckengetriebe-Verzahnungen - Teil 2: Toleranzen Für Abweichungen Einzelner Bestimmungsgrößen* 1995.
12. Sharif, K.J.; Kong, S.; Evans, H.P.; Snidle, R.W. Contact and Elastohydrodynamic Analysis of Worm Gears Part 1: Theoretical Formulation. *Proc. Inst. Mech. Eng. Part C J. Mech. Eng. Sci.* **2001**, *215*, 817–830, doi:10.1243/0954406011524171.
13. Fontanari, V.; Benedetti, M.; Girardi, C.; Giordanino, L. Investigation of the Lubricated Wear Behavior of Ductile Cast Iron and Quenched and Tempered Alloy Steel for Possible Use in Worm Gearing. *Wear* **2016**, *350–351*, 68–73, doi:10.1016/j.wear.2016.01.006.
14. Benedetti, M.; Fontanari, V.; Torresani, E.; Girardi, C.; Giordanino, L. Investigation of Lubricated Rolling Sliding Behaviour of WC/C, WC/C-CrN, DLC Based Coatings and Plasma Nitriding of Steel for Possible Use in Worm Gearing. *Wear* **2017**, *378–379*, 106–113, doi:10.1016/j.wear.2017.02.029.

15. Litvin, F.L.; Gonzalez-Perez, I.; Yukishima, K.; Fuentes, A.; Hayasaka, K. Design, Simulation of Meshing, and Contact Stresses for an Improved Worm Gear Drive. *Mech. Mach. Theory* **2007**, *42*, 940–959, doi:10.1016/j.mechmachtheory.2006.08.005.
16. Sohn, J.; Park, N. Modified Worm Gear Hobbing for Symmetric Longitudinal Crowning in High Lead Cylindrical Worm Gear Drives. *Mech. Mach. Theory* **2017**, *117*, 133–147, doi:10.1016/j.mechmachtheory.2017.07.004.
17. Simon, V. V. Characteristics of a New Type of Cylindrical Worm-Gear Drive. *J. Mech. Des.* **1998**, *120*, 139–146, doi:10.1115/1.2826666.
18. Mašović, R.; Miler, D.; Čular, I.; Jakovljević, S.; Šercer, M.; Žeželj, D. The Effect of Steel Electropolishing on the Tribological Behavior of a Steel–Bronze Pair in the Mixed and Boundary Lubrication Regimes. *Lubricants* **2023**, *11*, 325, doi:10.3390/lubricants11080325.
19. Pacholke, P.J.; Marshek, K.M. Improved Worm Gear Performance with Colloidal Molybdenum Disulfide Containing Lubricants. *Gear Technol.* **1988**, *5*, 10–16.
20. Rosenkranz, A.; Grützmacher, P.G.; Gachot, C.; Costa, H.L. Surface Texturing in Machine Elements – A Critical Discussion for Rolling and Sliding Contacts. *Adv. Eng. Mater.* **2019**, *21*, 1900194, doi:10.1002/adem.201900194.
21. Simon, V. Load Distribution in Cylindrical Worm Gears. *J. Mech. Des.* **2003**, *125*, 356–364, doi:10.1115/1.1561043.
22. Simon, V. The Influence of Gear Hobbing on Worm Gear Characteristics. *J. Manuf. Sci. Eng.* **2007**, *129*, 919–925, doi:10.1115/1.2752524.
23. Simon, V. Computer Aided Loaded Tooth Contact Analysis in Cylindrical Worm Gears. *J. Mech. Des.* **2005**, *127*, 973–981, doi:10.1115/1.1904050.
24. Falah, A.H.; Alfares, M.A.; Elkholy, A.H. Localised Tooth Contact Analysis of Single Envelope Worm Gears with Assembly Errors. *Int. J. Adv. Manuf. Technol.* **2013**, *68*, 2057–2070, doi:10.1007/s00170-013-4821-4.
25. Žeželj, D. Istraživanje Nosivosti Prijenosa s Pužnim Parovima, University of Zagreb, Faculty of Mechanical Engineering and Naval Architecture, 2007.
26. Stahl, D.-I.K.; B-R Höhn, D.-I.; Hermes, D.-I.J.; Monz, D.-I.A. Pitting Resistance of Worm Gears: Advanced Model for Contact Pattern of Any Size, Position, Flank Type. *Gear Technol.* **2012**, 44–49.
27. Jbily, D.; Guingand, M.; De Vaujany, J.P. A Wear Model for Worm Gear. *Proc. Inst. Mech. Eng. Part C J. Mech. Eng. Sci.* **2015**, *230*, 1290–1302, doi:10.1177/0954406215606747.
28. Sharif, K.J.; Evans, H.P.; Snidle, R.W.; Barnett, D.; Egorov, I.M. Effect of Elastohydrodynamic Film Thickness on a Wear Model for Worm Gears. *Proc. Inst. Mech. Eng. Part J J. Eng. Tribol.* **2006**, *220*, 295–306, doi:10.1243/13506501JET122.
29. Octrue, M. Relationship Between Wear and Pitting Phenomena in Worm Gears.; 1997; pp. 30–36.
30. Sharif, K.J.; Kong, S.; Evans, H.P.; Snidle, R.W. Contact and Elastohydrodynamic Analysis of Worm Gears Part 2: Results. *Proc. Inst. Mech. Eng. Part C J. Mech. Eng. Sci.* **2001**, *215*, 831–846, doi:10.1243/0954406011524180.

31. Kong, S.; Sharif, K.; Evans, H.P.; Snidle, R.W. Elastohydrodynamics of a Worm Gear Contact. *J. Tribol.* **2001**, *123*, 268–275, doi:10.1115/1.1308003.
32. Kovalchenko, A.; Ajayi, O.; Erdemir, A.; Fenske, G. Friction and Wear Behavior of Laser Textured Surface under Lubricated Initial Point Contact. *Wear* **2011**, *271*, 1719–1725, doi:10.1016/j.wear.2010.12.049.
33. Schneider, J.; Braun, D.; Greiner, C. Laser Textured Surfaces for Mixed Lubrication: Influence of Aspect Ratio, Textured Area and Dimple Arrangement. *Lubricants* **2017**, *5*, 32, doi:10.3390/lubricants5030032.
34. Vrbka, M.; Šamánek, O.; Šperka, P.; Návrát, T.; Křupka, I.; Hartl, M. Effect of Surface Texturing on Rolling Contact Fatigue within Mixed Lubricated Non-Conformal Rolling/Sliding Contacts. *Tribol. Int.* **2010**, *43*, 1457–1465, doi:10.1016/j.triboint.2010.02.002.
35. Vrbka, M.; Křupka, I.; Šamánek, O.; Svoboda, P.; Vaverka, M.; Hartl, M. Effect of Surface Texturing on Lubrication Film Formation and Rolling Contact Fatigue within Mixed Lubricated Non-Conformal Contacts. *Meccanica* **2011**, *46*, 491–498, doi:10.1007/s11012-010-9288-x.
36. Křupka, I.; Koutný, D.; Hartl, M. Behavior of Real Roughness Features within Mixed Lubricated Non-Conformal Contacts. *Tribol. Int.* **2008**, *41*, 1153–1160, doi:10.1016/j.triboint.2008.02.005.
37. Ali, S.; Kurniawan, R.; Moran, X.; Ahmed, F.; Danish, M.; Aslantas, K. Effect of Micro-Dimple Geometry on the Tribological Characteristics of Textured Surfaces. *Lubricants* **2022**, *10*, 328, doi:10.3390/lubricants10120328.
38. Galda, L.; Pawlus, P.; Sep, J. Dimples Shape and Distribution Effect on Characteristics of Stribeck Curve. *Tribol. Int.* **2009**, *42*, 1505–1512, doi:10.1016/j.triboint.2009.06.001.
39. Li, W.; Lu, L.; Zeng, D. The Contribution of Topography Formed by Fine Particle Peening Process in Reducing Friction Coefficient of Gear Steel. *Tribol. Trans.* **2020**, *63*, 9–19, doi:10.1080/10402004.2019.1648913.
40. Nakatsuji, T.; Mori, A. The Tribological Effect of Electrolytically Produced Micro-Pools and Phosphoric Compounds on Medium Carbon Steel Surfaces in Rolling - Sliding Contact. *Tribol. Trans.* **2001**, *44*, 173–178, doi:10.1080/10402000108982444.
41. Nakatsuji, T.; Mori, A. Tribological Properties of Electrolytically Polished Surfaces of Carbon Steel. *Tribol. Trans.* **1998**, *41*, 179–188, doi:10.1080/10402009808983737.
42. Britton, R.D.; Elcoate, C.D.; Alanou, M.P.; Evans, H.P.; Snidle, R.W. Effect of Surface Finish on Gear Tooth Friction. *J. Tribol.* **2000**, *122*, 354–360, doi:10.1115/1.555367.
43. Nakatsuji, T.; Mori, A. Pitting Durability of Electrolytically Polished Medium Carbon Steel Gears - Succeeding Report. *Tribol. Trans.* **1999**, *42*, 393–400, doi:10.1080/10402009908982233.
44. Gupta, N.; Tandon, N.; Pandey, R.K. An Exploration of the Performance Behaviors of Lubricated Textured and Conventional Spur Gearsets. *Tribol. Int.* **2018**, *128*, 376–385, doi:10.1016/j.triboint.2018.07.044.
45. Gupta, N.; Tandon, N.; Pandey, R.K.; Vidyasagar, K.E.C.; Kalyanasundaram, D. Tribological and Vibration Studies of Textured Spur Gear Pairs under Fully Flooded and

- Starved Lubrication Conditions. *Tribol. Trans.* **2020**, *63*, 1103–1120, doi:10.1080/10402004.2020.1794093.
46. Petare, A.; Deshwal, G.; Palani, I.A.; Jain, N.K. Laser Texturing of Helical and Straight Bevel Gears to Enhance Finishing Performance of AFF Process. *Int. J. Adv. Manuf. Technol.* **2020**, *110*, 2221–2238, doi:10.1007/s00170-020-06007-0.
 47. Oberšmit, E. *Ozubljenja i Zupčanici*; SNL: Zagreb, 1982;
 48. Crosher, W.P. *Design and Application of the Worm Gear*; ASME Press: New York, 2002; ISBN 0-7918-0178-0.
 49. Litvin, F.L.; Fuentes, A. *Gear Geometry and Applied Theory*; Second Edi.; Cambridge University Press: New York, 2004; ISBN 978-0-511-23000-4.
 50. Razdevich, S.P. *Dudley's Handbook of Practical Gear Design and Manufacture*; Third Edit.; CRC Press, 2016; ISBN 9781498753104.
 51. International Organization for Standardization *ISO/TR 10828:2015 Worm Gears-Worm Profiles and Gear Mesh Geometry*; Geneva, 2015;
 52. Jelaska, D. *Gear and Gear Drives*; First Edit.; John Wiley & Sons Ltd., 2012;
 53. Opalić, M. Prilog Istraživanju Opteretivosti Bokova Pužnih Kola Pužnih Prijenosnika, University of Zagreb, 1984.
 54. Rakamarić, P. Utjecaj Maziva Na Trošenje Materijala Pužnih Kola, Univeristy of Zagreb, 1995.
 55. Panić, N. Wear of Worm Wheels Tooth Face, Univeristy of Zagreb, 2013.
 56. Rabinowicz, E. The Determination of the Compatibility of Metals through Static Friction Tests. *A S L E Trans.* **1971**, *14*, 198–205, doi:10.1080/05698197108983243.
 57. Huber, G. Untersuchungen Über Flankentragfähigkeit Und Wirkungsgrad von Zylinderschneckengetrieben (Evolventenschnecken), TU München, 1978.
 58. Magyar, B.; Sauer, B.; Horák, P. Tribological Investigation of K Type Worm Gear Drives. *Acta Polytech. Hungarica* **2012**, *9*, 233–252.
 59. Sabiniak, H.G. Testing Worm Gears with Cooperating Elements Made of Different Materials. *Proc. Inst. Mech. Eng. Part J J. Eng. Tribol.* **2017**, *231*, 341–346, doi:10.1177/1350650116656982.
 60. Gwidon W. Stachowiak; Batchelor, A.W. *Engineering Tribology*; Elsevier, 2014; ISBN 9780123970473.
 61. Hamrock, B.J.; Schmid, S.R.; Jacobson, B.O. *Fundamentals of Fluid Film Lubrication*; Marcel Dekker, 2004;
 62. Hutchings, I.; Shipway, P. *Tribology - Friction and Wear of Engineering Materials*; Second Edi.; Elsevier, 2017; ISBN 978-0-08-100910-9.
 63. Grilec, K.; Jakovljević, S.; Marić, G. *Tribologija u Strojstvu*; first.; Fakultet strojarstva i brodogradnje, 2017; ISBN 978-953-7738-42-6.
 64. Höhn, B.-R.; Michaelis, K. Influence of Oil Temperature on Gear Failures. *Tribol. Int.* **2004**, *37*, 103–109, doi:10.1016/S0301-679X(03)00047-1.

65. Muminović, A.; Repčić, N.; Žeželj, D. The Efficiency of Worm Gears Lubricated with Oils of Mineral and Synthetic Bases. *Trans. Famena* **2013**, *37*, 65–72.
66. Ding, Y.; Rieger, N.F. Spalling Formation Mechanism for Gears. *Wear* **2003**, *254*, 1307–1317, doi:10.1016/S0043-1648(03)00126-1.
67. Olver, A. V. The Mechanism of Rolling Contact Fatigue: An Update. *Proc. Inst. Mech. Eng. Part J J. Eng. Tribol.* **2005**, *219*, 313–330, doi:10.1243/135065005X9808.
68. Fernandes, P.J.L.; McDuling, C. Surface Contact Fatigue Failures in Gears. *Eng. Fail. Anal.* **1997**, *4*, 99–107, doi:10.1016/S1350-6307(97)00006-X.
69. Keer, L.M.; Bryant, M.D. A Pitting Model for Rolling Contact Fatigue. *J. Lubr. Technol.* **1983**, *105*, 198–205, doi:10.1115/1.3254565.
70. Way, S. Pitting Due to Rolling Contact. *J. Appl. Mech.* **1935**, *2*, A49–A58.
71. Dawson, P.H. Effect of Metallic Contact on the Pitting of Lubricated Rolling Surfaces. *J. Mech. Eng. Sci.* **1962**, *4*, 16–21, doi:10.1243/JMES_JOUR_1962_004_005_02.
72. Jeng, Y.-R.; Lin, Z.-W.; Shyu, S.-H. Changes of Surface Topography During Running-In Process. *J. Tribol.* **2004**, *126*, 620–625, doi:10.1115/1.1759344.
73. Mallipeddi, D.; Norell, M.; Sosa, M.; Nyborg, L. Influence of Running-in on Surface Characteristics of Efficiency Tested Ground Gears. *Tribol. Int.* **2017**, *115*, 45–58, doi:10.1016/j.triboint.2017.05.018.
74. Khonsari, M.M.; Ghatrehsamani, S.; Akbarzadeh, S. On the Running-in Nature of Metallic Tribo-Components: A Review. *Wear* **2021**, *474–475*, 203871, doi:10.1016/j.wear.2021.203871.
75. Gupta, K.; Jain, N.K.; Laubscher, R. Measurement of Gear Accuracy. In *Advanced Gear Manufacturing and Finishing*; Elsevier, 2017; pp. 197–218 ISBN 9780128044605.
76. Deutsches Institut für Normung DIN 21772:2007 Gears – Cylindrical Involute Gears and Gear Pairs – Definition of Deviations 2007.
77. International Organization for Standardization ISO 1328-1 Cylindrical Gears - ISO System of Flank Tolerance Classification 2013.
78. Goch, G. Gear Metrology. *CIRP Ann.* **2003**, *52*, 659–695, doi:10.1016/S0007-8506(07)60209-1.
79. Lu, X.; Zhao, X.; Hu, B.; Zhou, Y.; Cao, Z.; Tang, J. A Measurement Solution of Face Gears with 3D Optical Scanning. *Materials (Basel)*. **2022**, *15*, 6069, doi:10.3390/ma15176069.
80. Gear Measuring Instrument Available online: <https://www.accretech.com/en/product/measuring/software/for3dsoftware/gearpro.html> (accessed on 19 December 2023).
81. Zuo, C.; Feng, S.; Huang, L.; Tao, T.; Yin, W.; Chen, Q. Phase Shifting Algorithms for Fringe Projection Profilometry: A Review. *Opt. Lasers Eng.* **2018**, *109*, 23–59, doi:10.1016/j.optlaseng.2018.04.019.
82. Feng, S.; Zuo, C.; Zhang, L.; Tao, T.; Hu, Y.; Yin, W.; Qian, J.; Chen, Q. Calibration of Fringe Projection Profilometry: A Comparative Review. *Opt. Lasers Eng.* **2021**, *143*,

- 106622, doi:10.1016/j.optlaseng.2021.106622.
83. Matache, G.; Dragan, V.; Puscasu, C.; Vilag, V.; Paraschiv, A. A Comparison between 3D Scanning and CMM Dimensional Inspection of Small Size Gas Turbine. *Adv. Mater. Res.* **2015**, *1128*, 347–352, doi:10.4028/www.scientific.net/AMR.1128.347.
 84. Gapinski, B.; Wieczorowski, M.; Marciniak-Podsadna, L.; Dybala, B.; Ziolkowski, G. Comparison of Different Method of Measurement Geometry Using CMM, Optical Scanner and Computed Tomography 3D. *Procedia Eng.* **2014**, *69*, 255–262, doi:10.1016/j.proeng.2014.02.230.
 85. Barbero, B.R.; Ureta, E.S. Comparative Study of Different Digitization Techniques and Their Accuracy. *Comput. Des.* **2011**, *43*, 188–206, doi:10.1016/j.cad.2010.11.005.
 86. Urbas, U.; Zorko, D.; Černe, B.; Tavčar, J.; Vukašinović, N. A Method for Enhanced Polymer Spur Gear Inspection Based on 3D Optical Metrology. *Measurement* **2021**, *169*, 108584, doi:10.1016/j.measurement.2020.108584.
 87. Ghandali, P.; Khameneifar, F.; Mayer, J.R.R. A Pseudo-3D Ball Lattice Artifact and Method for Evaluating the Metrological Performance of Structured-Light 3D Scanners. *Opt. Lasers Eng.* **2019**, *121*, 87–95, doi:10.1016/j.optlaseng.2019.03.005.
 88. Mendricky, R. DETERMINATION OF MEASUREMENT ACCURACY OF OPTICAL 3D SCANNERS. *MM Sci. J.* **2016**, *2016*, 1565–1572, doi:10.17973/MMSJ.2016_12_2016183.
 89. Urbas, U.; Zorko, D.; Vukašinović, N.; Černe, B. Comprehensive Areal Geometric Quality Characterisation of Injection Moulded Thermoplastic Gears. *Polymers (Basel)*. **2022**, *14*, doi:10.3390/polym14040705.
 90. Urbas, U.; Hrga, T.; Povh, J.; Vukašinović, N. Novel Alignment Method for Optical 3D Gear Metrology of Spur Gears with a Plain Borehole. *Meas. J. Int. Meas. Confed.* **2022**, *192*, 110839, doi:10.1016/j.measurement.2022.110839.
 91. GOM Inspect Suite 2020.
 92. Thurman, D. Calculating SAP and TIF. *Gear Technol.* **1999**, *September*, 65–68.
 93. Evans, C.J.; Bryan, J.B. “Structured”, “Textured” or “Engineered” Surfaces. *CIRP Ann.* **1999**, *48*, 541–556, doi:10.1016/S0007-8506(07)63233-8.
 94. Ibatan, T.; Uddin, M.S.; Chowdhury, M.A.K. Recent Development on Surface Texturing in Enhancing Tribological Performance of Bearing Sliders. *Surf. Coatings Technol.* **2015**, *272*, 102–120, doi:10.1016/j.surfcoat.2015.04.017.
 95. Gachot, C.; Rosenkranz, A.; Hsu, S.M.; Costa, H.L. A Critical Assessment of Surface Texturing for Friction and Wear Improvement. *Wear* **2017**, *372–373*, 21–41, doi:10.1016/j.wear.2016.11.020.
 96. Sudeep, U.; Tandon, N.; Pandey, R.K. Performance of Lubricated Rolling/Sliding Concentrated Contacts With Surface Textures: A Review. *J. Tribol.* **2015**, *137*, 031501, doi:10.1115/1.4029770.
 97. Coblas, D.G.; Fatu, A.; Maoui, A.; Hajjam, M. Manufacturing Textured Surfaces: State of Art and Recent Developments. *Proc. Inst. Mech. Eng. Part J J. Eng. Tribol.* **2015**, *229*, 3–29, doi:10.1177/1350650114542242.

98. Braun, D.; Greiner, C.; Schneider, J.; Gumbsch, P. Efficiency of Laser Surface Texturing in the Reduction of Friction under Mixed Lubrication. *Tribol. Int.* **2014**, *77*, 142–147, doi:10.1016/j.triboint.2014.04.012.
99. Ezhilmaran, V.; Vasa, N.J.; Vijayaraghavan, L. Investigation on Generation of Laser Assisted Dimples on Piston Ring Surface and Influence of Dimple Parameters on Friction. *Surf. Coatings Technol.* **2018**, *335*, 314–326, doi:10.1016/j.surfcoat.2017.12.052.
100. Costa, H.L.; Hutchings, I.M. Some Innovative Surface Texturing Techniques for Tribological Purposes. *Proc. Inst. Mech. Eng. Part J J. Eng. Tribol.* **2015**, *229*, 429–448, doi:10.1177/1350650114539936.
101. Zhang, J.; Meng, Y. A Study of Surface Texturing of Carbon Steel by Photochemical Machining. *J. Mater. Process. Technol.* **2012**, *212*, 2133–2140, doi:10.1016/j.jmatprotec.2012.05.018.
102. Muhl, J.; Alder, G.M. Direct Printing of Etch Masks under Computer Control. *Int. J. Mach. Tools Manuf.* **1995**, *35*, 333–337, doi:10.1016/0890-6955(94)P2391-R.
103. Costa, H.L.; Hutchings, I.M. Development of a Maskless Electrochemical Texturing Method. *J. Mater. Process. Technol.* **2009**, *209*, 3869–3878, doi:10.1016/j.jmatprotec.2008.09.004.
104. Wang, X.; Liu, W.; Zhou, F.; Zhu, D. Preliminary Investigation of the Effect of Dimple Size on Friction in Line Contacts. *Tribol. Int.* **2009**, *42*, 1118–1123, doi:10.1016/j.triboint.2009.03.012.
105. Křupka, I.; Vrbka, M.; Hartl, M. Effect of Surface Texturing on Mixed Lubricated Non-Conformal Contacts. *Tribol. Int.* **2008**, *41*, 1063–1073, doi:10.1016/j.triboint.2007.11.016.
106. Ghaei, A.; Khosravi, M.; Badrossamay, M.; Ghadbeigi, H. Micro-Dimple Rolling Operation of Metallic Surfaces. *Int. J. Adv. Manuf. Technol.* **2017**, *93*, 3749–3758, doi:10.1007/s00170-017-0790-3.
107. Mitrovic, S.; Adamovic, D.; Zivic, F.; Dzunic, D.; Pantic, M. Friction and Wear Behavior of Shot Peened Surfaces of 36CrNiMo4 and 36NiCrMo16 Alloyed Steels under Dry and Lubricated Contact Conditions. *Appl. Surf. Sci.* **2014**, *290*, 223–232, doi:10.1016/j.apsusc.2013.11.050.
108. Vrbka, M.; Křupka, I.; Svoboda, P.; Šperka, P.; Návrát, T.; Hartl, M.; Nohava, J. Effect of Shot Peening on Rolling Contact Fatigue and Lubricant Film Thickness within Mixed Lubricated Non-Conformal Rolling/Sliding Contacts. *Tribol. Int.* **2011**, *44*, 1726–1735, doi:10.1016/j.triboint.2011.06.019.
109. Nakatsuji, T.; Mori, A.; Shimotsuma, Y. Pitting Durability of Electrolytically Polished Medium Carbon Steel Gears. *Tribol. Trans.* **1995**, *38*, 223–232, doi:10.1080/10402009508983399.
110. Neufeld, P.; Southall, D. Gas Evolution and Pitting in Electropolishing. *Trans. IMF* **1976**, *54*, 40–44, doi:10.1080/00202967.1976.11870370.
111. Petare, A.C.; Mishra, A.; Palani, I.A.; Jain, N.K. Study of Laser Texturing Assisted Abrasive Flow Finishing for Enhancing Surface Quality and Microgeometry of Spur Gears. *Int. J. Adv. Manuf. Technol.* **2019**, *101*, 785–799, doi:10.1007/s00170-018-2944-

- 3.
112. Han, W.; Fang, F. Fundamental Aspects and Recent Developments in Electropolishing. *Int. J. Mach. Tools Manuf.* **2019**, *139*, 1–23, doi:10.1016/j.ijmactools.2019.01.001.
 113. Yang, G.; Wang, B.; Tawfiq, K.; Wei, H.; Zhou, S.; Chen, G. Electropolishing of Surfaces: Theory and Applications. *Surf. Eng.* **2017**, *33*, 149–166, doi:10.1080/02670844.2016.1198452.
 114. Gabe, D.R. Electropolishing of Mild Steel in Phosphoric and Perchloric Acid Containing Electrolytes. *Corros. Sci.* **1973**, *13*, 175–185, doi:10.1016/0010-938X(73)90013-9.
 115. Feliu, S.; Gonzalez, J.A. D.C. and A.C. in the Dissolution and Electropolishing of Steel in Organic H₃PO₄ Baths. *Corros. Sci.* **1971**, *11*, 307–318, doi:10.1016/S0010-938X(71)80064-1.
 116. Łyczkowska-Widłak, E.; Lochyński, P.; Nawrat, G. Electrochemical Polishing of Austenitic Stainless Steels. *Materials (Basel)*. **2020**, *13*, 2557, doi:10.3390/ma13112557.
 117. Landolt, D. Fundamental Aspects of Electropolishing. *Electrochim. Acta* **1987**, *32*, 1–11, doi:10.1016/0013-4686(87)87001-9.
 118. Lee, S.J.; Chen, Y.H.; Hung, J.C. The Investigation of Surface Morphology Forming Mechanisms in Electropolishing Process. *Int. J. Electrochem. Sci.* **2012**, *7*, 12495–12506.
 119. Hahn, T.S.; Marder, A.R. Effect of Electropolishing Variables on the Current Density-Voltage Relationship. *Metallography* **1988**, *21*, 365–375, doi:10.1016/0026-0800(88)90001-8.
 120. Imboden, R.L.; Sibley, R.S. Anodic Polishing of Plain Carbon Steels. *Trans. Electrochem. Soc.* **1942**, *82*, 227, doi:10.1149/1.3071410.
 121. Pendyala, P.; Bobji, M.S.; Madras, G. Evolution of Surface Roughness During Electropolishing. *Tribol. Lett.* **2014**, *55*, 93–101, doi:10.1007/s11249-014-0336-x.
 122. Rangaswamy, P.; Scherer, C.P.; Bourke, M.A.M. Experimental Measurements and Numerical Simulation of Stress and Microstructure in Carburized 5120 Steel Disks. *Mater. Sci. Eng. A* **2001**, *298*, 158–165, doi:10.1016/S0921-5093(00)01292-2.
 123. *ASTM-E1558 Standard Guide for Electrolytic Polishing of Metallographic Specimens*; 1999;
 124. Miler, D.; Hoić, M.; Domitran, Z.; Žeželj, D. Prediction of Friction Coefficient in Dry-Lubricated Polyoxymethylene Spur Gear Pairs. *Mech. Mach. Theory* **2019**, *138*, 205–222, doi:10.1016/j.mechmachtheory.2019.03.040.
 125. Gadelmawla, E.S.; Koura, M.M.; Maksoud, T.M.A.; Elewa, I.M.; Soliman, H.H. Roughness Parameters. *J. Mater. Process. Technol.* **2002**, *123*, 133–145, doi:10.1016/S0924-0136(02)00060-2.
 126. Akamatsu, Y.; Tsushima, N.; Goto, T.; Hibi, K. Influence of Surface Roughness Skewness on Rolling Contact Fatigue Life. *Tribol. Trans.* **1992**, *35*, 745–750, doi:10.1080/10402009208982180.
 127. Sedlaček, M.; Podgornik, B.; Vižintin, J. Correlation between Standard Roughness Parameters Skewness and Kurtosis and Tribological Behaviour of Contact Surfaces.

- Tribol. Int.* **2012**, *48*, 102–112, doi:10.1016/j.triboint.2011.11.008.
128. Sedlaček, M.; Gregorčič, P.; Podgornik, B. Use of the Roughness Parameters S_{sk} and S_{ku} to Control Friction—A Method for Designing Surface Texturing. *Tribol. Trans.* **2017**, *60*, 260–266, doi:10.1080/10402004.2016.1159358.
 129. Dzierwa, A.; Pawlus, P. Wear of a Rough Disc in Dry Sliding Contact with a Smooth Ball: Experiment and Modeling. *Arch. Civ. Mech. Eng.* **2021**, *21*, 1–20, doi:10.1007/s43452-021-00240-4.
 130. Podgornik, B.; Vilhena, L.M.; Sedlaček, M.; Rek, Z.; Žun, I. Effectiveness and Design of Surface Texturing for Different Lubrication Regimes. *Meccanica* **2012**, *47*, 1613–1622, doi:10.1007/s11012-012-9540-7.
 131. International Organization for Standardization *ISO 4287:1997 Geometrical Product Specifications (GPS) — Surface Texture: Profile Method — Terms, Definitions and Surface Texture Parameters*; International Organization for Standardization, 1997;
 132. Ronen, A.; Etsion, I.; Kligerman, Y. Friction-Reducing Surface-Texturing in Reciprocating Automotive Components. *Tribol. Trans.* **2001**, *44*, 359–366, doi:10.1080/10402000108982468.
 133. Dowson, D. Paper 10: Elastohydrodynamics. *Proc. Inst. Mech. Eng. Conf. Proc.* **1967**, *182*, 151–167, doi:10.1243/PIME_CONF_1967_182_014_02.
 134. Dowson, D.; Higginson, G.R. *Elasto-Hydrodynamic Lubrication*; Second Edi.; Pergamon Press, 1977; ISBN 0-08-021303-0.
 135. Ren, N.; Nanbu, T.; Yasuda, Y.; Zhu, D.; Wang, Q. Micro Textures in Concentrated-Conformal-Contact Lubrication: Effect of Distribution Patterns. *Tribol. Lett.* **2007**, *28*, 275–285, doi:10.1007/s11249-007-9271-4.
 136. Yan-qing, W.; Gao-feng, W.; Qing-gong, H.; Liang, F.; Shi-rong, G. Tribological Properties of Surface Dimple-Textured by Pellet-Pressing. *Procedia Earth Planet. Sci.* **2009**, *1*, 1513–1518, doi:10.1016/j.proeps.2009.09.233.
 137. Kovalchenko, A.; Ajayi, O.; Erdemir, A.; Fenske, G.; Etsion, I. The Effect of Laser Texturing of Steel Surfaces and Speed-Load Parameters on the Transition of Lubrication Regime from Boundary to Hydrodynamic. *Tribol. Trans.* **2004**, *47*, 299–307, doi:10.1080/05698190490440902.
 138. Hsu, S.M.; Jing, Y.; Hua, D.; Zhang, H. Friction Reduction Using Discrete Surface Textures: Principle and Design. *J. Phys. D. Appl. Phys.* **2014**, *47*, 335307, doi:10.1088/0022-3727/47/33/335307.
 139. Costa, H.L.; Hutchings, I.M. Effects of Die Surface Patterning on Lubrication in Strip Drawing. *J. Mater. Process. Technol.* **2009**, *209*, 1175–1180, doi:10.1016/j.jmatprotec.2008.03.026.
 140. Wos, S.; Koszela, W.; Pawlus, P. Tribological Behaviours of Textured Surfaces under Conformal and Non-Conformal Starved Lubricated Contact Conditions. *Proc. Inst. Mech. Eng. Part J J. Eng. Tribol.* **2015**, *229*, 398–409, doi:10.1177/1350650114535759.
 141. Hager, C.H.; Evans, R.D. Friction and Wear Properties of Black Oxide Surfaces in Rolling/Sliding Contacts. *Wear* **2015**, *338–339*, 221–231, doi:10.1016/j.wear.2015.06.013.

142. Ueda, M.; Spikes, H.; Kadiric, A. Influence of Black Oxide Coating on Micropitting and ZDDP Tribofilm Formation. *Tribol. Trans.* **2022**, *65*, 242–259, doi:10.1080/10402004.2021.1940407.
143. Zhu, L.; Wu, X.; Zhao, G.; Wang, X. Tribological Characteristics of Bisphenol AF Bis(Diphenyl Phosphate) as an Antiwear Additive in Polyalkylene Glycol and Polyurea Grease for Significantly Improved Lubrication. *Appl. Surf. Sci.* **2016**, *363*, 145–153, doi:10.1016/j.apsusc.2015.12.008.
144. Liu, C.; Chen, L.; Zhou, J.; Zhou, H.; Chen, J. Tribological Properties of Adaptive Phosphate Composite Coatings with Addition of Silver and Molybdenum Disulfide. *Appl. Surf. Sci.* **2014**, *300*, 111–116, doi:10.1016/j.apsusc.2014.02.015.
145. Dassault Systems ABAQUS 6.13 2013.
146. Boubes, R.J. *Troubleshooting Finite-Element Modeling with Abaqus*; Springer International Publishing: Cham, 2020; ISBN 978-3-030-26739-1.
147. Masovic, R.; Cular, I.; Vuckovic, K.; Zezelj, D.; Breski, T. Gear Geometry Inspection Based on 3D Optical Scanning: Worm Wheel Case Study. In Proceedings of the 2021 12th International Conference on Mechanical and Aerospace Engineering (ICMAE); IEEE, July 16 2021; pp. 262–268.
148. Panić, N. Trošenje Bokova Kola Pužnih Prijenosnika, University of Zagreb, Faculty of Mechanical Engineering and Naval Architecture, 2013.
149. Mourier, L.; Mazuyer, D.; Ninove, F.-P.; Lubrecht, A.A. Lubrication Mechanisms with Laser-Surface-Textured Surfaces in Elastohydrodynamic Regime. *Proc. Inst. Mech. Eng. Part J J. Eng. Tribol.* **2010**, *224*, 697–711, doi:10.1243/13506501JET771.
150. Sedlaček, M.; Podgornik, B.; Vižintin, J. Planning Surface Texturing for Reduced Friction in Lubricated Sliding Using Surface Roughness Parameters Skewness and Kurtosis. *Proc. Inst. Mech. Eng. Part J J. Eng. Tribol.* **2012**, *226*, 661–667, doi:10.1177/1350650112439809.
151. Wang, W.; Chen, H.; Hu, Y.; Wang, H. Effect of Surface Roughness Parameters on Mixed Lubrication Characteristics. *Tribol. Int.* **2006**, *39*, 522–527, doi:10.1016/j.triboint.2005.03.018.
152. Franulović, M.; Basan, R.; Križan, B. Kritični Položaj Zuba HCR Zupčanika s Obzirom Na Odstupanja Koraka Na Zahvatnoj Crti (Critical Position of Hcr Gear Teeth With Regard To Pitch Error). **2008**, *2*, 1–10.
153. Franulovic, M.; Markovic, K.; Vrcan, Z.; Soban, M. Experimental and Analytical Investigation of the Influence of Pitch Deviations on the Loading Capacity of HCR Spur Gears. *Mech. Mach. Theory* **2017**, *117*, 96–113, doi:10.1016/j.mechmachtheory.2017.07.006.
154. Wei, J.; Sun, W.; Wang, L. Effects of Flank Deviation on Load Distributions for Helical Gear. *J. Mech. Sci. Technol.* **2011**, *25*, 1781–1789, doi:10.1007/s12206-011-0416-x.

Curriculum Vitae

Robert Mašović was born on May 18th, 1994, in Zagreb, Croatia. He attended elementary school in Zagreb and in 2012 graduated from the 1st Gymnasium in Zagreb, Croatia. He acquired his bachelor's degree from the University of Zagreb, Faculty of Mechanical Engineering and Naval Architecture in 2016. During master studies, he was an exchange student through Erasmus+ program at Chalmers University of Technology, Goteborg, Sweden. He obtained his master's degree from the University of Zagreb, Faculty of Mechanical Engineering and Naval Architecture in 2018, specializing in Design and Product Development. Since then, he has been employed as a research assistant and Ph.D. candidate at the aforementioned Faculty, Department of Design. His main research areas are tribology, worm pairs, machine elements, and numerical simulations. He is a member of the Croatian Society for Mechanics and an author of 12 papers, four of which were published in scientific journals indexed in the Web of Science.

Journal papers indexed in Web of Science

1. Mašović, Robert; Miler, Daniel; Čular, Ivan; Jakovljević, Suzana; Šercer, Mario; Žeželj, Dragan. The Effect of Steel Electropolishing on the Tribological Behavior of a Steel–Bronze Pair in the Mixed and Boundary Lubrication Regimes // *Lubricants*, 2023 (2023), 1-18. doi: 10.3390/lubricants11080325
2. Masovic, R. ; Breski, T. ; Cular, I. ; Vuckovic, K. ; Zezelj, D. Numerical Model for Worm Gear Pair Inspection Based on 3D Scanned Data // *International journal of simulation modelling*, 20 (2021), 4; 637-648. doi: 10.2507/ijstimm20-4-573
3. Domitran, Zoran ; Mašović, Robert ; Serdar, Jure ; Jelić, Mislav. The conceptual design of a smart wrist orthosis and functional performance - project overview // *Tehnički glasnik*, 15 (2021), 3; 387-391. doi: 10.31803/tg-20210710123243
4. Vučković, Krešimir ; Čular, Ivan ; Mašović, Robert ; Galić, Ivica ; Žeželj, Dragan. Numerical model for bending fatigue life estimation of carburized spur gears with consideration of the adjacent tooth effect // *International journal of fatigue*, 153 (2021) (2021), 106515, 13. doi: 10.1016/j.ijfatigue.2021.106515

Journal and conference papers

1. Vlašićek, Dorian; Miler, Daniel; Mašović, Robert; Žeželj, Dragan. Approaches to reducing gear mass and their effects on gearing stresses and deformations // Proceedings of the Design Society, Volume 4: DESIGN 2024. Online: Cambridge University Press, 2024. str. 3033-3040 doi: 10.1017/pds.2024.307
2. Martinec, Tomislav; Valjak, Filip; Horvat, Nikola; Goudswaard, Mark; Nygård Ege, Daniel; Ballantyne, Robert; Berg, Martin Francis; Glaser, Tobias; Grosse, Cornelius; Lipšinić, Zvonimir et al. Virtual design hackathons: a data collection framework // Proceedings of the Design Society, Volume 4: DESIGN. Online: Cambridge University Press, 2024. str. 45-54 doi: 10.1017/pds.2024.7
3. Čular, Ivan ; Vučković, Krešimir ; Mašović, Robert ; Žeželj, Dragan ; Galić, Ivica. The effect of the adjacent tooth and rim elasticity on fatigue behavior in thin-rimmed spur gears // Proceedings to the 1516th International Conference on Recent Innovations in Engineering and Technology. 2023. str. 1-5
4. Mašović, Robert ; Čular, Ivan ; Vučković, Krešimir ; Žeželj, Dragan ; Breški, Tomislav. Gear Geometry Inspection Based on 3D Optical Scanning: Worm Wheel Case Study // 12th International Conference on Mechanical and Aerospace Engineering (ICMAE) / Agarwal, Ramesh K. (ur.). Institute of Electrical and Electronics Engineers (IEEE), 2021. str. 262-268 doi: 10.1109/ICMAE52228.2021.9522366
5. Mašović, Robert ; Čular, Ivan ; Miler, Daniel ; Žeželj, Dragan. Prilagodba teksture površine cementiranog čelika elektropoliranjem // Zbornik radova Desetog susreta Hrvatskog društva za mehaniku / Damjanović, Darko ; Kozak, Dražen ; Konjatić, Pejo et al. (ur.). Slavonski Brod, 2020. str. 157-162
6. Vukić, Mislav ; Čular, Ivan ; Mašović, Robert ; Vučković, Krešimir. Effect of friction on nominal stress results in a single tooth bending fatigue test // IOP conference series. Materials science and engineering / Marjanović, Nenad (ur.). 2019. doi: 10.1088/1757-899x/659/1/012004

7. Mašović, Robert ; Jagarčec, Valentina ; Miler, Daniel ; Domitran, Zoran ; Bojčetić, Nenad ; Žeželj, Dragan. Analysis of printing direction impact on dimensional accuracy of spur gears // *Advances in Mechanism and Machine Science* / Tadeusz, Uhl (ur.). Cham: Springer, 2019. str. 1111-1120 doi: 10.1007/978-3-030-20131-9_110

8. Miler, Daniel ; Perišić, Marija Majda ; Mašović, Robert ; Žeželj, Dragan. Predicting student academic performance in Machine elements course // *Advances in Mechanism and Machine Science* / Tadeusz, Uhl (ur.). Cham: Springer, 2019. str. 825-834 doi: 10.1007/978-3-030-20131-9_82

Appendix

Appendix table 1. Pitting (%) on flanks of worm wheel 1

Flank No.	Load cycles $N_L \cdot 10^6$									
	0.087	0.31	0.48	0.65	0.86	1.08	1.30	1.51	1.73	2.0
1	0.02	0	0.06	0.1	0.53	1.18	3.26	4.4	5.02	6.27
2	0.04	0.01	0.03	0.08	0.17	0.27	0.44	0.88	1.93	2.32
3	0.02	0.01	0.03	0.16	0.66	2.73	3.24	3.55	3.94	5.06
4	0.02	0.01	0.25	0.56	1.97	2.06	2.79	4.51	4.82	5.42
5	0	0.01	0.6	1.48	3.48	4.71	6.12	6.79	7.85	8.26
6	0	0	0.02	0.17	0.3	0.74	2.61	3.97	5.07	6.37
7	0.04	0.1	0.25	1.83	3.43	5.28	5.89	6.79	7.66	9.21
8	0.01	0	0.21	0.2	0.5	1.32	1.73	1.98	2.6	3.13
9	0	0.02	0.06	0.26	3	5.1	6.53	7.08	8.43	9.34
10	0	0.01	0.06	0.11	0.95	1.62	2.75	3.11	3.59	4.01
11	0	0.25	1.24	3.9	5.38	6.44	7.44	8.36	9.81	11.42
12	0	0.06	0.25	0.3	0.53	0.7	1.16	1.79	2.43	3.2
13	0.04	0.03	0.99	1.47	3.36	4.67	5.01	5.64	5.95	6.96
14	0	0	0.07	0.14	0.74	1.21	1.72	2.2	2.64	3.1
15	0	0.01	0.06	0.16	1.9	4.36	5.52	5.89	7.03	7.35
16	0	0	0.03	0.08	1	1	1.27	1.91	2.43	3.35
17	0	0.04	0.53	2.78	3.92	4.6	5.89	6.24	7.38	8.74
18	0	0.01	0.06	0.09	0.36	0.7	0.87	1.13	1.97	2.38
19	0	0	0	0.74	2.78	4.03	5.48	6.55	7.81	9.18
20	0.03	0	0.02	0.1	0.17	0.39	1.29	1.53	2.63	3.14
21	0	0.05	0.06	1.17	2.96	3.69	4.28	5.31	6.98	7.68
22	0.01	1.72	1.67	1.6	1.8	2.2	3.1	3.6	4.28	4.44
23	0.1	0.08	1.1	2.44	4.08	4.65	5.33	5.82	6.46	7.06
24	0	0	0.15	0.15	0.19	0.33	0.44	0.76	1.19	1.47
25	0.07	0.06	0.37	0.4	0.9	3.7	4.72	5.3	6.68	7.5
26	0.09	0.07	0.07	0.15	0.2	0.41	0.5	0.92	2.06	2.09
27	0.02	0.09	0.1	0.63	2.57	4.57	6	7.17	7.02	7.31
28	0.02	0.01	0	0.76	0.84	0.82	0.99	1.24	1.4	1.67
29	0.01	0	0	1.07	3.02	4.25	4.56	5.67	6.24	7.38
30	0	0.08	0.16	0.29	0.37	0.45	0.59	0.67	0.94	1.18
31	0.04	0.01	0.39	1.36	1.56	3.23	4.86	6.82	7.5	7.99
32	0.09	0.06	0.14	0.39	0.54	0.66	0.8	1.35	1.67	2.24
33	0.22	0.12	0.17	0.45	2.8	4.55	4.97	5.25	5.94	6.47
34	0.16	0.04	0.08	0.19	0.25	0.56	1.43	1.76	2.23	2.88
35	0.07	0.02	0.13	0.77	2.55	3.67	4.66	7.05	7.65	7.94
36	0.01	0	0.17	0.21	0.31	0.63	1.14	1.41	1.74	2.86

Appendix table 2. Worm wheel 1 - deviations

Flank No.	Deviation, mm				
	f_{p2}	f_{u2}	F_{u2}	F_{r2}	F_{ax2}
1	-0.031	0.049	0.093	-0.107	0.011
2	0.02	0.051	0.0789	-0.122	0.017
3	-0.025	0.045	0.1093	-0.129	0.022
4	0.023	0.048	0.0799	-0.126	0.027
5	-0.009	0.032	0.0989	-0.119	0.031
6	0.026	0.035	0.0918	-0.121	0.034
7	-0.034	0.06	0.1057	-0.15	0.036
8	0.018	0.052	0.0711	-0.155	0.037
9	-0.024	0.042	0.0848	-0.181	0.037
10	0.031	0.055	0.0525	-0.177	0.035
11	-0.012	0.043	0.0936	-0.161	0.033
12	0.023	0.035	0.0786	-0.17	0.03
13	-0.012	0.035	0.0832	-0.184	0.025
14	0.019	0.031	0.0602	-0.191	0.02
15	-0.015	0.034	0.0904	-0.196	0.015
16	0.021	0.036	0.0589	-0.194	0.009
17	-0.004	0.025	0.0687	-0.179	0.002
18	0.023	0.027	0.0761	-0.174	-0.004
19	-0.019	0.042	0.1038	-0.176	-0.011
20	0.028	0.047	0.0544	-0.161	-0.017
21	-0.017	0.045	0.1067	-0.156	-0.022
22	0.029	0.046	0.0584	-0.14	-0.027
23	-0.033	0.062	0.1035	-0.139	-0.031
24	0.014	0.047	0.0576	-0.139	-0.034
25	-0.01	0.024	0.0592	-0.123	-0.036
26	0.006	0.016	0.0627	-0.133	-0.037
27	-0.013	0.019	0.0802	-0.097	-0.037
28	0.017	0.03	0.0331	-0.089	-0.035
29	-0.025	0.042	0.0779	-0.091	-0.033
30	0.01	0.035	0.0709	-0.098	-0.03
31	-0.015	0.025	0.0718	-0.087	-0.025
32	0.01	0.025	0.14	0.39	0.54
33	-0.019	0.029	0.17	0.45	2.8
34	0.008	0.027	0.08	0.19	0.25
35	-0.027	0.035	0.13	0.77	2.55
36	0.018	0.045	0.17	0.21	0.31

Appendix table 3. Pitting (%) on flanks of worm wheel 1

Flank No.	Load cycles $M_L \cdot 10^6$										
	0.08	0.31	0.41	0.51	0.62	0.85	1.08	1.25	1.46	1.69	2.01
1	0	0.09	1.28	2.28	3.28	9.13	9.5	9.98	10.22	10.74	15.08
2	0	0.04	0.41	1.28	2.77	3.87	4.43	5.38	6.09	7.05	11.59
3	0	0.02	0.16	1.06	2.65	3.63	6.6	6.64	8.09	9.91	12.53
4	0.01	0.07	0.29	1.82	2.02	2.54	4.4	4.76	5.55	5.86	8.13
5	0	0.05	0.26	1.47	2.35	3.3	6.33	7.69	8.26	9.28	11.85
6	0.05	0.04	0.13	1.49	1.89	2.12	2.52	2.91	3.82	5.15	6.85
7	0.05	0.03	0.17	0.84	1.3	3.75	6.45	7.27	7.9	8.65	10.94
8	0	0.01	0.86	1	2.2	3.06	4.38	5.18	5.28	5.37	7
9	0.02	0.05	0.23	0.52	0.91	2.67	5.89	6.03	7.66	8.13	8.75
10	0	0.01	0.1	0.23	0.39	0.92	2.95	3.72	3.93	4.19	5.4
11	0.03	0.04	0.31	1.43	2.14	3.48	6.47	7.42	8.82	9.2	11.19
12	0	0.02	0.07	0.49	2	3.61	4.52	4.83	5.14	5.28	5.95
13	0	0.01	0.05	0.6	1.58	4.57	6.83	8.14	8.56	8.85	10.21
14	0.06	0.07	0.07	0.2	0.65	2.77	3.84	4.46	4.84	5.07	6.86
15	0.03	0.04	0.32	1.4	2.27	2.69	6.45	6.69	7.1	7.65	8.23
16	0.03	0.02	0.08	0.4	0.69	1.84	2.47	2.91	3.48	4.65	5.98
17	0.01	0.03	0.13	0.35	1.66	2.82	5.22	6.28	7.51	7.83	9.91
18	0.01	0.03	0.06	0.26	1.98	2.01	3.26	3.64	4.14	4.5	5.43
19	0.01	0.06	0.23	0.48	1.63	2.76	4.08	5.2	6.56	7.38	10.01
20	0	0.03	0.25	0.6	1.7	4.14	4.74	5.27	5.4	5.58	6.77
21	0	0.04	0.42	1.37	2.13	3.11	4.98	6.86	7.74	8.37	11.11
22	0	0.15	0.26	1.21	2.13	2.53	4.02	4.28	5.21	6.74	12.46
23	0	0.03	0.13	1.33	5.1	6	6.93	9.35	10.92	11.65	12.49
24	0.03	0.04	0.17	0.76	1.79	3.05	4.82	5.05	6.17	7.37	8.33
25	0	0.04	0.14	0.33	0.61	3.79	5.45	5.88	6.6	8.74	11.17
26	0	0.15	0.27	1.05	1.34	2.56	3.27	3.69	3.95	4.32	7.52
27	0.03	0.04	1.35	2.54	3.19	5.04	9.31	10.26	10.23	10.65	14.2
28	0	0.07	0.2	0.34	1.42	2.26	3.89	4.69	4.99	6.04	7.96
29	0	0.07	0.37	2.51	3.25	4.03	6.07	6.79	7.48	8.6	11.12
30	0	0.06	0.7	1.38	1.83	2.78	3.74	4.27	5.39	6.92	8.09
31	0	0.56	1.78	2.25	4.02	5.41	6.04	6.71	7.34	7.73	8.66
32	0.02	1.47	1.52	2.13	2.93	3.78	4.49	5.36	5.99	7.28	9.33
33	0	0.16	1.17	2.21	4.11	4.73	7.57	8.15	8.76	9.58	10.9
34	0	0.03	0.11	0.57	2.69	3.12	4.09	5.38	5.76	6.54	9.55
35	0	0.28	0.86	2.84	4.51	5.73	6.43	7.38	10.63	11.9	17.9
36	0	0.09	0.48	0.87	1.77	2.85	4.36	5.19	6.68	8.38	12.16

Appendix table 4. Worm wheel 2 - deviations

Flank No.	Deviation, mm				
	f_{p2}	f_{u2}	F_{u2}	F_{r2}	F_{ax2}
1	0.024	0.042	0.0785	-0.139	-0.012
2	-0.013	0.037	0.1115	-0.134	-0.013
3	0.028	0.041	0.0859	-0.123	-0.014
4	0	0.028	0.1035	-0.081	-0.014
5	0.026	0.026	0.0933	-0.087	-0.014
6	-0.028	0.054	0.0813	-0.103	-0.013
7	0.02	0.048	0.082	-0.083	-0.012
8	-0.021	0.041	0.126	-0.077	-0.011
9	0.038	0.059	0.1162	-0.058	-0.009
10	-0.033	0.071	0.1365	-0.026	-0.007
11	0.023	0.056	0.1275	-0.05	-0.005
12	-0.044	0.067	0.1123	-0.063	-0.003
13	0.005	0.049	0.1008	-0.056	-0.001
14	-0.029	0.034	0.093	-0.074	0.002
15	0.016	0.045	0.0747	-0.089	0.004
16	-0.028	0.044	0.0962	-0.079	0.006
17	0.016	0.044	0.0792	-0.059	0.009
18	-0.023	0.039	0.0939	-0.08	0.01
19	0.006	0.029	0.073	-0.083	0.012
20	-0.028	0.034	0.0856	-0.086	0.013
21	0.018	0.046	0.0565	-0.103	0.014
22	-0.007	0.025	0.0638	-0.092	0.014
23	0.006	0.013	0.0777	-0.114	0.014
24	-0.014	0.02	0.0777	-0.118	0.013
25	0.005	0.019	0.0673	-0.141	0.012
26	-0.011	0.016	0.1032	-0.146	0.011
27	0.039	0.05	0.0785	-0.121	0.009
28	-0.005	0.044	0.1008	-0.1	0.007
29	0.011	0.016	0.0942	-0.133	0.005
30	-0.021	0.032	0.1215	-0.152	0.003
31	0.019	0.04	0.066	-0.163	0.001
32	-0.016	0.035	0.1023	-0.152	-0.002
33	0.033	0.049	0.0595	-0.124	-0.004
34	-0.006	0.039	0.0841	-0.142	-0.006
35	0.013	0.019	0.0665	-0.16	-0.009
36	-0.018	0.031	0.1002	-0.155	-0.01

Appendix table 5. Pitting (%) on flanks of worm wheel 3

Flank No.	Load cycles $N_L \cdot 10^6$									
	0.19	0.42	0.64	0.81	1.02	1.21	1.44	1.59	1.80	2.0
1	0.05	0.08	0.12	0.17	0.17	0.3	0.34	0.38	0.53	1.25
2	0.01	0.05	0.04	0.04	0.08	0.1	0.17	0.22	0.31	0.89
3	0.01	0.02	0.09	0.12	0.11	0.15	0.26	0.26	0.38	1.02
4	0	0.02	0.07	0.21	0.22	0.16	0.25	0.32	0.4	0.61
5	0.01	0.02	0.06	0.11	0.17	0.2	0.26	0.39	0.44	0.92
6	0	0.09	0.09	0.07	0.1	0.08	0.14	0.21	0.37	0.91
7	0.01	0.04	0.1	0.11	0.16	0.25	0.3	0.42	0.59	1.2
8	0	0.01	0.03	0.04	0.08	0.21	0.24	0.43	0.54	1.01
9	0.03	0.05	0.11	0.1	0.1	0.18	0.2	0.3	0.49	1.19
10	0	0.01	0.05	0.04	0.06	0.11	0.15	0.15	0.29	0.69
11	0.01	0.04	0.03	0.05	0.06	0.22	0.24	0.44	0.59	1.35
12	0	0.06	0.07	0.15	0.08	0.13	0.23	0.33	0.55	1.15
13	0.01	0.02	0.08	0.11	0.15	0.3	0.62	0.62	0.85	1.67
14	0	0	0.03	0.05	0.05	0.15	0.19	0.27	0.59	1.07
15	0.01	0.02	0.12	0.13	0.22	0.28	0.33	0.43	0.96	1.69
16	0.01	0.01	0.1	0.1	0.08	0.17	0.26	0.44	0.6	1.22
17	0.01	0.01	0.08	0.11	0.12	0.35	0.42	0.48	0.76	1.63
18	0	0.05	0.11	0.16	0.16	0.11	0.27	0.37	0.54	1.06
19	0.03	0.04	0.09	0.15	0.19	0.42	0.57	0.5	0.72	1.57
20	0.02	0.02	0.08	0.08	0.1	0.19	0.19	0.31	0.45	0.99
21	0.02	0.01	0.09	0.12	0.11	0.28	0.28	0.41	0.75	1.61
22	0.01	0	0.08	0.1	0.1	0.19	0.11	0.19	0.27	0.6
23	0.02	0.04	0.07	0.09	0.1	0.33	0.26	0.37	0.58	1.4
24	0.01	0.02	0.07	0.1	0.1	0.15	0.21	0.28	0.47	1.03
25	0.02	0.06	0.22	0.24	0.24	0.37	0.4	0.47	0.78	1.55
26	0.02	0.01	0.08	0.08	0.09	0.14	0.18	0.36	0.46	0.76
27	0.01	0.02	0.04	0.08	0.07	0.11	0.24	0.34	0.49	1.16
28	0	0.01	0.05	0.05	0.08	0.12	0.12	0.23	0.37	1.12
29	0.03	0.03	0.04	0.05	0.05	0.09	0.23	0.27	0.56	1.21
30	0.01	0.05	0.07	0.14	0.1	0.14	0.2	0.27	0.52	1.16
31	0.02	0.03	0.09	0.09	0.09	0.15	0.15	0.24	0.4	1.33
32	0.01	0.01	0.03	0.04	0.05	0.07	0.13	0.19	0.28	0.74
33	0.01	0.03	0.04	0.13	0.13	0.16	0.25	0.3	0.53	1.54
34	0	0.01	0.03	0.05	0.03	0.07	0.1	0.11	0.23	0.69
35	0.03	0.03	0.09	0.09	0.19	0.19	0.32	0.39	0.55	1.28
36	0.01	0	0.01	0.02	0.03	0.04	0.11	0.14	0.28	0.71

Appendix table 6. Worm wheel 3 - deviations

Flank No.	Deviation, mm				
	f_{p2}	f_{u2}	F_{u2}	F_{r2}	F_{ax2}
1	0.015	0.045	0.08	-0.255	-0.037
2	-0.006	0.021	0.107	-0.24	-0.04
3	0.042	0.048	0.108	-0.217	-0.041
4	-0.012	0.054	0.1168	-0.212	-0.042
5	0.024	0.036	0.093	-0.219	-0.041
6	-0.017	0.041	0.1104	-0.218	-0.039
7	0.014	0.031	0.0945	-0.215	-0.036
8	-0.02	0.034	0.1235	-0.193	-0.031
9	0.048	0.068	0.1128	-0.143	-0.026
10	-0.008	0.056	0.1225	-0.118	-0.02
11	-0.012	0.02	0.1076	-0.129	-0.013
12	-0.03	0.042	0.1032	-0.148	-0.006
13	0.013	0.043	0.0935	-0.187	0.001
14	-0.021	0.034	0.1321	-0.176	0.008
15	0.004	0.025	0.0836	-0.193	0.015
16	-0.029	0.033	0.1145	-0.208	0.022
17	0.02	0.049	0.107	-0.205	0.028
18	-0.021	0.041	0.1269	-0.204	0.033
19	0.015	0.036	0.137	-0.198	0.037
20	-0.025	0.04	0.1537	-0.204	0.04
21	0.028	0.053	0.1425	-0.19	0.041
22	-0.015	0.043	0.1464	-0.18	0.042
23	0.017	0.032	0.1294	-0.184	0.041
24	-0.029	0.046	0.1803	-0.2	0.039
25	-0.005	0.034	0.0963	-0.231	0.036
26	-0.025	0.03	0.1054	-0.235	0.031
27	0.009	0.034	0.0818	-0.248	0.026
28	-0.024	0.033	0.113	-0.25	0.02
29	0.026	0.05	0.0713	-0.246	0.013
30	-0.018	0.044	0.1	-0.253	0.006
31	0.025	0.043	0.0694	-0.259	-0.001
32	0	0.025	0.1224	-0.237	-0.008
33	0.047	0.047	0.1188	-0.221	-0.015
34	-0.007	0.054	0.1266	-0.197	-0.022
35	0.005	0.012	0.1059	-0.208	-0.028
36	-0.03	0.035	0.1075	-0.237	-0.033

Appendix table 7. Pitting (%) on flanks of worm wheel 4

Flank No.	Load cycles $N_L \cdot 10^6$						
	0.17	0.22	0.28	0.46	0.63	0.78	1.00
1	0.15	0.41	2.76	3.55	8.47	11.03	11.98
2	0.16	0.42	1.62	3.96	8.85	10.4	11.61
3	0.11	0.15	0.87	4.46	7.39	10.3	10.75
4	0.29	0.57	0.83	3.81	9.22	11.58	11.59
5	0.14	0.29	0.79	2.87	6.5	9.41	10.98
6	0.2	0.66	3.39	4.73	6.55	8.99	9.98
7	0.31	0.58	3.47	6.82	7.86	8.71	12.11
8	0.2	2.56	4.1	8.64	10.9	11.07	11.84
9	0.1	1.4	1.49	4.55	7	9.23	10.44
10	0.2	0.56	3.27	4.54	8.66	10.2	15.19
11	0.39	1.12	2.94	5.51	9.58	10	12.4
12	0.29	1.08	2.86	7.38	11.05	11.95	14.16
13	0.42	1.91	4.98	8.65	11.43	12.32	14.8
14	0.95	1.08	2.65	8.02	9.87	13.92	21.31
15	0.23	2.06	4.35	7.58	15.39	16.2	16.4
16	0.5	1.29	6.73	7.77	10.42	10.82	15.04
17	0.15	0.9	6.14	8.17	9.59	9.7	11.67
18	0.31	0.74	2.81	5.24	5.54	9.43	10.81
19	0.69	0.83	1.14	7.31	8.12	11.03	14.16
20	0.36	0.75	7.48	7.9	11.73	12.13	13.13
21	0.2	0.78	2.11	6.38	6.69	8.35	10.09
22	0.67	1.12	1.8	4.36	7.15	9.62	12.66
23	0.17	0.43	3.01	6.11	8.48	11.4	14.23
24	1.29	1.1	2.05	4.78	6.02	8.13	10.47
25	0.33	0.57	1.69	7.21	7.98	10.02	12.13
26	0.32	1.65	2.31	9.51	11.93	12.03	13.99
27	0.07	0.05	0.54	6.06	8	9.54	14.21
28	0.06	0.32	2.28	3.1	8.32	8.61	10.9
29	0.84	0.86	3.55	4.93	7.23	10.06	11.73
30	0.19	1	2.02	5.6	6.59	7.23	8.31
31	0.02	0.08	0.64	2.69	7.61	11.02	11.97
32	0.45	1.2	1.07	4.49	6.44	7.14	10.31
33	0.07	0.17	0.58	3.42	4.1	8.12	9.4
34	0.28	0.67	4.87	7.09	8.49	9.99	10.63
35	0.1	0.42	0.57	3.02	5.06	8.84	9.99
36	0.14	1.25	1.4	4.02	6.28	7.94	9.5

Appendix table 8. Worm wheel 4 - deviations

Flank No.	Deviation, mm				
	f_{p2}	f_{u2}	F_{u2}	F_{r2}	F_{ax2}
1	-0.014	0.025	0.0564	-0.16	0.042
2	-0.009	0.023	0.0658	-0.165	0.039
3	-0.013	0.022	0.0651	-0.148	0.034
4	0.011	0.024	0.0606	-0.135	0.029
5	-0.024	0.035	0.074	-0.17	0.022
6	-0.01	0.034	0.0569	-0.167	0.015
7	0	0.01	0.0533	-0.175	0.007
8	-0.005	0.005	0.0508	-0.228	-0.001
9	-0.016	0.021	0.0617	-0.222	-0.009
10	-0.009	0.025	0.0435	-0.22	-0.016
11	-0.012	0.021	0.0724	-0.197	-0.023
12	-0.002	0.014	0.0359	-0.24	-0.03
13	-0.005	0.007	0.0698	-0.228	-0.035
14	0.004	0.009	0.0506	-0.239	-0.04
15	-0.009	0.013	0.0654	-0.225	-0.043
16	0.024	0.033	0.0509	-0.259	-0.045
17	-0.016	0.04	0.0444	-0.261	-0.045
18	0.009	0.025	0.0531	-0.237	-0.045
19	0.014	0.023	0.0647	-0.233	-0.042
20	0.002	0.016	0.0585	-0.281	-0.039
21	0.015	0.017	0.0614	-0.257	-0.034
22	-0.004	0.019	0.0682	-0.234	-0.029
23	0.018	0.022	0.0633	-0.214	-0.022
24	0.013	0.031	0.0384	-0.243	-0.015
25	-0.008	0.021	0.0592	-0.223	-0.007
26	0.008	0.016	0.0679	-0.204	0.001
27	0.013	0.021	0.0605	-0.197	0.009
28	0.014	0.027	0.0514	-0.205	0.016
29	-0.003	0.017	0.0632	-0.2	0.023
30	-0.008	0.011	0.061	-0.179	0.03
31	0.005	0.013	0.0458	-0.186	0.035
32	0.019	0.024	0.0549	-0.184	0.04
33	-0.026	0.045	0.0721	-0.182	0.043
34	0.011	0.037	0.0426	-0.153	0.045
35	-0.003	0.014	0.0612	-0.127	0.045
36	0.011	0.014	0.0547	-0.161	0.045